Thèse de Faten Farhat, Université de Lille, 2018

Université de Lille

Laboratoire de Mécanique, Multiphysique, Multiéchelle (FR2016)

École Doctorale Science Pour l'Ingenieur Lille Nord-de-France

Année 2018

THESE

Pour l'obtention du grade de

Docteur de l'Université de Lille

Discipline : Génie Civil

présentée par:

Faten Farhat

Modélisation multiéchelle du comportement mécanique des gaz shales

Soutenue publiquement le 5 Avril 2018 devant le jury:

A. Giraud	Professeur, Université de Lorraine	Rapporteur
D. Kondo	Professeur, Université Paris VI	Rapporteur
B. Ledesert	Professeur, Université de Cergy-Pontoise	Examinateur
K. Su	Ingénieur de recherche, HDR, TOTAL	Examinateur
J.F. Shao	Professeur, Université de Lille, LaMcube	Directeur de thèse
W.Q. Shen	Maître de conférences, Université de Lille, LaMcube	Co-encadrant

© 2018 Tous droits réservés.

lilliad.univ-lille.fr

© 2018 Tous droits réservés.

lilliad.univ-lille.fr

Acknowledgements

Essentially, I would like to kindly thank and appreciate my supervisor Professor Jian-Fu Shao who gave me the opportunity to complete my higher studies and have guided me during my master's training and the years of thesis. I am lucky to work with this patient and serene person.

I express my extreme thanks to Dr. Wanqing Shen, my co-supervisor, who guided and motivated me widely to continue my work and for the prosperous scientific informations.

I would like to thank Professors Albert Giraud and Djimedo Kondo who accepted to be the reviewers of my dissertation manuscript. I would like to evenly be grateful to Professor Beatrice Ledesert as the president and Mr. Kun Su as examiner of the jury.

I want to thank Mr. Hamid Pourpak for his advices during my thesis.

My thesis could not have been done without TOTAL finance and the support of its members, especially: Claire Fialips, Alain Lejay and Atef Onaisi. I would like to thank them.

I would like to show my courtesy to Mr. Shouyi Xie, who performed some experimental tests that I used in my thesis and for many helpful discussions. Special thanks to Yajun Cao for his help in Abaqus.

Finally, I show my gratitude to my family and my husband for their unconditional support and encouragement throughout the development of this work and during my academic career.

© 2018 Tous droits réservés.

lilliad.univ-lille.fr

© 2018 Tous droits réservés.

lilliad.univ-lille.fr

Abstract

The main objective of this thesis is to study the influence of microstructure on the macroscopic mechanical behavior of heterogeneous rocks, particularly Vaca Muerta shale rock. In this context, micromechanical models are developed by well-adapted homogenization techniques. The microstructure of this rock has been extensively studied in order to define the representative elementary volume indispensable for the implementation of a micromechanical approach. The studied material is modeled as a heterogeneous medium, made up, at mesoscale, of a composite matrix in which are dipped different types of inclusions. On a smaller scale, fine grains of calcite and kerogen are immersed in a porous clay matrix. The homogenization of non-linear instantaneous behavior is established in the context of clay matrix elastoplasticity and the progressive debonding of mineral inclusions: the nano-micro transition leads to the strength domain of the porous clay phase where the solid phase is considered to be a cohesive-frictional material that obeys to the classic Drucker-Prager criterion. Hill's incremental method is used as a homogenization means at micro-meso and meso-macro transitions. Next, the long-term behavior of the studied material is defined in terms of microstructure degradation. Finally, a simplified micromechanical model is developed to study long-term behavior of clayey and shale rocks in the context of clay matrix viscoplasticity. Based on this model, for the industrial application of the thesis, we study the interaction between Vaca Muerta shale rock and spherical grains of proppants.

Keywords: Micromechanics; Homogenization; Multiscale; Shale; Vaca Muerta; Differed behavior; Viscoplasticity; Damage; Degradation.

Résumé

L'objectif principal de cette thèse est d'étudier l'influence de la microstructure sur le comportement mécanique macroscopique des roches hétérogènes, particulièrement, la roche shale de Vaca Muerta. Dans ce contexte, des modèles micromécaniques sont développés par des techniques d'homogénéisation bien adaptées. La microstructure de cette roche a été profondément étudiée afin de définir le volume élémentaire représentatif indispensable pour la mise en œuvre d'une approche micromécanique. Le matériau étudié est modélisé comme un milieu hétérogène, constitué à l'échelle mésoscopique d'une matrice composite dans laquelle sont plongés différents types d'inclusions. À une échelle plus petite, des fins grains de calcite et kérogène sont immergés dans une matrice argileuse poreuse. L'homogénéisation du comportement instantané non linéaire est établie dans le contexte de l'élastoplasticité de la matrice

© 2018 Tous droits réservés.

lilliad.univ-lille.fr

argileuse et de la décohésion progressive des inclusions: la transition d'échelle nano-micro aboutit au domaine de résistance de la phase argileuse poreuse où la phase solide est considérée comme un matériau cohésif-frottant obéissant au critère classique de Drucker-Prager. La méthode incrémentale de Hill est utilisée comme moyen d'homogénéisation pour les transitions micro-méso et méso-macro. Ensuite, le comportement à long terme du matériau étudié est défini en terme de la dégradation de la microstructure et en particulier, de la matice argileuse. Finalement, un modèle micromécanique simplifié est développé pour étudier le comportement à long terme, des roches argileuses et shales, dans le contexte de la viscoplasticité de la matrice argileuse. En se basant sur ce modèle, pour l'application industrielle de la thèse, nous étudions l'interaction entre la roche shale de Vaca Muerta et les grains sphériques de proppants.

Mots clés: Micromécanique; Homogénéisation; Multi-échelle; Shale; Vaca Muerta; Comportement différé; Viscoplasticité; Endommagement; Dégradation.

© 2018 Tous droits réservés.

lilliad.univ-lille.fr

© 2018 Tous droits réservés.

lilliad.univ-lille.fr

Contents

© 2018 Tous droits réservés.

lilliad.univ-lille.fr

© 2018 Tous droits réservés.

lilliad.univ-lille.fr

© 2018 Tous droits réservés.

lilliad.univ-lille.fr

Principal Notations

- **Tensorial notations:**

.	Simple contraction
:	Double contraction
$\otimes$	Tensor product
$< f >$	Average of field f
Σ	Scalar
$\mathbf{\Sigma}$	Second-order tensor
$\mathbb{C}$	Fourth-order tensor
δ_{ij}	Kronecker's symbol: δ_{ij}=1 if $i = j$ and δ_{ij}=0 if $i \neq j$
$\mathbf{1}$	Second-order unit tensor
$\mathbb{I}$	Fourth-order symmetric unit tensor $\quad I_{ijkl} = \frac{1}{2}(\delta_{ik}\delta_{jl} + \delta_{il}\delta_{jk})$
$\mathbb{J}$	Spherical projection tensor of isotropic fourth-order tensors $\quad \mathbb{J} = \frac{1}{3}(\mathbf{1} \otimes \mathbf{1})$
$\mathbb{K}$	Deviatoric projection tensor of isotropic fourth-order tensors $\quad \mathbb{K} = \mathbb{I} - \mathbb{J}$
tr$\mathbf{\Sigma}$	Trace of tensor $\mathbf{\Sigma}$
$\mathbf{\Sigma}'$	Deviatoric part of tensor $\mathbf{\Sigma}$
sgn(Σ)	Signum function: sgn(Σ)=*1* if $\Sigma > 0$, *0* if $\Sigma = 0$ and *-1* if $\Sigma < 0$

- **Common notations:**

$\boldsymbol{\sigma}$	Nanoscopic stress tensor
$\tilde{\boldsymbol{\sigma}}$	Microscopic stress tensor
$\tilde{\boldsymbol{d}}$	Microscopic strain rate
$\tilde{\mathbf{\Sigma}}$	Mesoscopic stress tensor
$\mathbf{\Sigma}$	Macroscopic stress tensor
E	Young's modulus
ν	Poisson's ratio
κ	Bulk modulus
μ	Shear modulus
ρ_m	Mineral density
P_c	Confining pressure
P_a	Axial stress

© 2018 Tous droits réservés.

lilliad.univ-lille.fr

© 2018 Tous droits réservés.

lilliad.univ-lille.fr

General introduction

In recent years, the knowledge of shale rock thermo-hydro-mechanical behavior is quickly becoming one of the most important issues in modern geomechanics due to its importance in nuclear waste geological storage, extraction of shale hydrocarbon and sequestration of carbon dioxide. For instance, the history of shale gas production prospers with the success of Barnett shale in the United States in 1980. Shales constitute about 75% of the clastic fill of sedimentary basins [Jones and Wang, 1981]. They are one of the most heterogeneous rocks having a multiphase and multiscale composition which evolves continually due to diagenesis over various scales of length and time. The heterogeneities distinguish themselves from nanoscopic scale to macroscopic scale. In this work, we are more interested to shale rock in the context of hydrocarbon extraction. Shale hydrocarbon reservoirs, as geologically and petrophysically complex source rocks of variable mineralogy with natural oil and gas production potential, organic-rich and fine-grained mudrocks, evoke researchers to study their petrophysical, geological, geophysical, geomechanical and geochemical properties. Despite the significance of shale hydrocarbon reservoirs, microstructural characterization and theoretical mechanical modeling are limited due to their heterogeneous microstructure and multiscale properties.

A shale hydrocarbon formation can be subjected to various mechanical, hydraulic, thermal and chemical solicitations; in this work, we are limited to mechanical solicitations. Mechanical modeling of shale hydrocarbon reservoirs can be envisaged according to two main ways: phenomenological or micromechanical approaches. Classically, macroscopic triaxial testing methods and phenomenological models are used to measure and predict macroscopic mechanical properties of materials. From an experimental point of view, these macroscopic methods require expensive material sampling from high depths. As well as, the high degree of heterogeneity makes difficult the extrapolation between samples. Otherwise, theoretical phenomenological models are not able to take into account the influence of microstructure heterogeneity on macroscopic behavior. In this case, model's parameters identified for a certain depth, are not valid for other depths with different mineralogy, which requires its identification for each geomechanical zone characterized by certain mechanical properties. On the other side, the purpose of micromechanical approaches is to derive, through a suitable scale transition steps, the macroscopic behavior of the studied material from the description of its microstructure and the knowledge of its local constituent behavior. Micromechanical approaches take into consideration the influence of rock microstructural aspects on the macroscopic behavior and thus, avoid the identification of parameters for each geomechanical zone.

© 2018 Tous droits réservés.

lilliad.univ-lille.fr

After having exposed the advantages and limits of phenomenological and micromechanical approaches, we propose, in this work, to build multiscale models based on constituents behavior and microstructural data of clayey and shale rocks. Most micromechanical models, devoted to shale, study its elastic behavior ([Hornby et al., 1994], [Jakobsen et al., 2003], [Delafargue, 2004], and [Abedi et al., 2016a,b]). We can cite, as well, [Gathier, 2008] which proposes a two-scale non-linear procedure for the homogenization of shale yield design strength properties based on the linear comparison composite theory ([Ponte-Castaneda, 1992] and [Ponte-Castaneda, 1996]). Concerning Vaca Muerta shale rock, [Vallade, 2016] supposed that the latter has a brittle elastic behavior. Thus, [Vallade, 2016] had studied the material cracking by means of a numerical approach, Enhanced Finite Element Method (EFEM). The particularity of this method is that it takes into account the discontinuity of displacement related to the crack in an element. Differently, in this thesis, apart from the study of macroscopic elastic properties, the main objective is to establish theoretical analytical and semi-analytical micromechanical approaches to treat plasticity (since shales are rocks that exhibit plastic deformations due to the presence of clay) and to take into account microstructure degradation at long term which generate differed deformations. Another mechanism is envisaged to treat time-dependent behavior: viscosity of clay matrix. Thus, we develop micromechanical models based on nonlinear homogenization techniques with microstructural hypotheses on the porosity and concentration of mineral inclusions.

This thesis dissertation is divided into four chapters and organized as follows:

In the first chapter, a general overview of unconventional shale hydrocarbons is exposed. We present the main characteristics of unconventional resources, the principle of hydraulic fracturing technique as production means of shale hydrocarbons and the different mechanisms that contribute to hydraulic fracture conductivity deterioration. Afterward, a review of some shale rock microstructures is displayed. Shale rocks from different formations are seen as heterogeneous material with multiphase and multiscale composition. In the second subsection, the industrial context and objective of the thesis are exhibited. The general goal of TOTAL, in the 'Unconventional' program, is to create modeling and simulation tools that guide to formation areas with best production potential. Our work is part of the problem of analyzing and predicting instantaneous and time-dependent mechanical behavior of shale hydrocarbon reservoir by developing a micromechanical model that takes into account the heterogeneities of shale material such as clay porosity, organic matter and different types of inclusions at separated scales. In the last subsection, we present the microstructure and behavior of the material that interests us: Vaca Muerta shale rock. The knowl-

© 2018 Tous droits réservés.

lilliad.univ-lille.fr

edge of material microstructure is crucial in the perspective of multiscale modeling.

In the second chapter, we develop a micromechanical elastoplastic damage model for Vaca Muerta shale rock. In the first part, the representative elementary volume of the latter material is suggested based on the different observations of microstructure given in the first chapter. In the second part, the homogenization of Vaca Muerta shale behavior in elastic regime is studied. After having identified the elastic properties of different Vaca Muerta constituents, macroscopic elastic ones are predicted by using an appropriate linear homogenization scheme. Then, a sensitivity study in elastic regime is established to study the influence of kerogen elastic properties and fine inclusions on effective elastic ones. In the third part, the homogenization of non linear behavior is elaborated in the context of elastoplasticity and damage evolution. The non-linear homogenization procedure is summarized as follows: a first step of homogenization yields the strength domain of the porous clay phase where its solid phase is considered as a cohesive-frictional material obeying to the classical Drucker-Prager criterion. In the second homogenization step, fine inclusions are taken into account and the last step adds the different types of inclusions yielding to the macroscopic strength response. Interfacial debonding between matrix and inclusions is envisaged through a damage process. After having exposed the numerical implementation of the proposed model, a sensitivity assessment is realized to show the influence of damage evolution and microstructural aspects on macroscopic behavior. Then, the calibration and experimental validation of the micromechanical model are performed. Finally, to reduce the number of model's parameters, we consider the case of associated perfectly plastic clay solid phase.

In the third chapter, we study the time-dependent behavior of Vaca Muerta shale rock. Particularly, for a successful stimulation of a shale hydrocarbon formation, it is essential evenly to study the long term behavior of rock which controls the progressive closure of fractures and then contributes to the loss of productivity. The formulation of long term constitutive model is established in terms of material degradation. The evolution of microstructure, leading to the degradation of material failure strength, contributes to the development of a delayed plastic deformation. After having exposed the formulation of the model in long term, we present the algorithm for local integration of the clay phase. Then, a sensitivity evaluation of the proposed model is exhibited. Finally, a phase of experimental validation is performed.

In the fourth chapter, a simplified micromechanics based viscoplastic model is proposed to describe the time-dependent deformation for a class of clayey and shale rocks. At first, we present the simplified microstructure representing these heterogeneous materials. The heterogeneous rock is represented as a composite material

© 2018 Tous droits réservés.

lilliad.univ-lille.fr

containing a porous clay matrix and mineral inclusions at mesoscopic scale. Afterwards, the non linear homogenization procedure, established by [Shen et al., 2013] to obtain the effective plastic yield criterion, is summarized. The viscoplastic model is obtained by extending the latter criterion to obtain the viscoplastic loading function. In this model, the origin of time-dependent deformation is supposed the viscosity of clay matrix. Then, a series of numerical assessments are presented to investigate the influence of porosity and mineral inclusions on the time-dependent deformation of clayey rocks. Finally, comparisons between numerical simulations and experimental data for Callovo-Oxfordian argillites and Vaca Muerta shale are carried out and presented for different loading paths. Finally, the industrial application of the thesis is exhibited to study the interaction between Vaca Muerta shale rock and spherical grains of proppants.

© 2018 Tous droits réservés.

lilliad.univ-lille.fr

© 2018 Tous droits réservés.

lilliad.univ-lille.fr

Chapter 1

Problematic of the thesis

Contents

© 2018 Tous droits réservés.

lilliad.univ-lille.fr

1.1 General review of shale hydrocarbons

1.1.1 Shale hydrocarbons as unconventional resources

Historically, conventional natural hydrocarbon deposits have been the most practical and easiest layers to exploit. However, as technology and geological knowledge advance, unconventional natural hydrocarbon deposits are beginning to make up an increasingly large percent of exploitation demand. Unconventional hydrocarbons have the potential to contribute significantly to the replacement of conventional resources. The extremely high potential of unconventional hydrocarbons should extend for many more years the petroleum industry's capacity to meet global energy needs. For instance, over the last ten years, the economic success of shale hydrocarbon production in the United States have made an impact on North American oil and gas markets. In 2011, the natural gas shale output represented 34% of the total production compared to 1% in 2000 ([IHS, 2011] and [EIA, 2013]). Shale gas is expected to rise to 67% of the overall production by 2035, generating lower natural gas and electricity prices [Boyer et al., 2011].

Unconventional resources includes mainly three types: shale gas/oil, tight gas/oil and coalbed methane. Particularly, we are interested to shale gas/oil in this work. Shale resources have the same origin as all hydrocarbons; they are formed in the source rock, from the transformation of sediments rich in organic matter accumulated on the ocean. Over geological time, these sediments gradually sink into the underground; progressively, they solidify, while the organic matter contained therein is transformed into hydrocarbons under the combined effect of temperature and pressure. The major part of formed hydrocarbons is gradually expelled from the source rock and migrate to reach porous rock reservoirs. However, hydrocarbons, that remain confined in the source rock, constitute shale hydrocarbons. Thus, compared to conventional hydrocarbons, unconventional ones differ by the geological characteristics of its reservoir rock (figures 1.1 and 1.2). Note that both conventional and unconventional hydrocarbons are natural resources and have the same chemical compositions.

The low permeability of unconventional resource reservoirs prevents the extraction of hydrocarbons by conventional techniques such as simple digging. Therefore, it requires stimulation (hydraulic, chemical, electric or pneumatic) for the ascent of hydrocarbons from the bottom of wells to the surface. In recent years, the production of shale hydrocarbons has been stimulated by the widespread use of hydraulic fracturing technique (actually the most suitable method) to create the permeability that does not offer the nature. The extraction of shale hydrocarbons, particularly difficult, requires the use of the combined techniques of directional drilling and hy-

© 2018 Tous droits réservés.

lilliad.univ-lille.fr

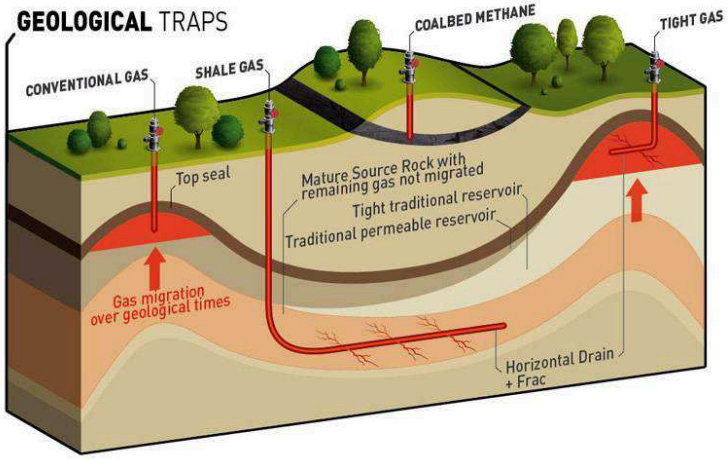

Figure 1.1: Geological section of conventional and unconventional hydrocarbons production area [TOTAL].

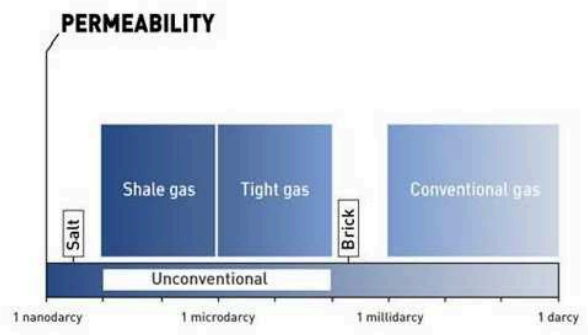

Figure 1.2: Conventional and unconventional reservoir permeability scale [TOTAL].

draulic fracturing. More specifically, the latter consists in injecting water at a high pressure which yields to the propagation of a large number of microfractures in the rock containing hydrocarbons, making it porous and allows shale hydrocarbons to move through the well and to be recovered at the surface. Due to the vertical variability in mineralogy of shale formation and the existence of natural cracks, hydraulic fractures will propagate through several different planes. The water which is injected contains various 'additives' (bactericides, gelling agents, and surfactants) to sterilize and prevent bacterial contamination of the reservoir, and 'proppant' (sand, lubricants, ceramics or cleanser) to improve the efficiency of fracturing and to keep the microfractures opened. On the other hand, directional drilling consists in digging a vertical well in the rock source at a depth of 5000-20000 ft below the surface [Hansen et al., 2013] and next, laterals extending from 1000-10000 ft are drilled horizontally ([Lhomme et al., 2005] and [Lecampion et al., 2013]). Hydraulic fracturing with only vertical wells will fracture the rock only in the closeness of drill, which will recover a very small amount of hydrocarbons. But with horizontal drilling, we create max-

© 2018 Tous droits réservés.
lilliad.univ-lille.fr

imum borehole surface area in contact with shale layer and we can fracture a larger amount of rock, therefore recover more hydrocarbons (figure 1.3). In order to limit water consumption and the impact of hydraulic fracturing on environment, alternative methods are being tested such as propane fracturing, electrical cracking or liquid helium injection.

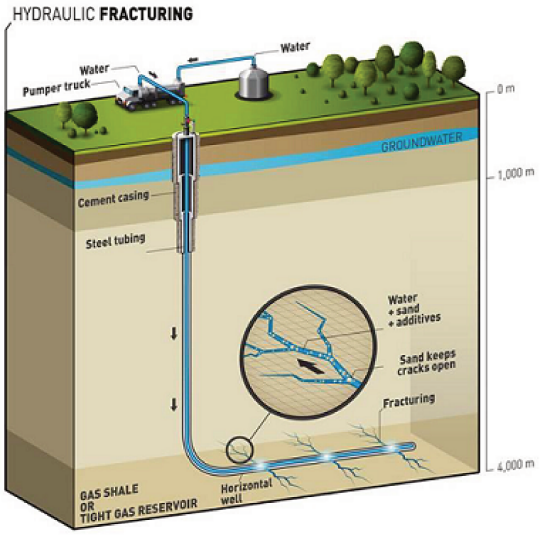

Figure 1.3: Hydraulic fracturing technique [TOTAL].

Wherefore, to reach an economic production, sufficient conductivity in hydraulic fractures must be sustained through the lifetime of wells. However, maintaining such conductivity could be challenging in some cases, especially in soft clay-rich formations. Different mechanisms could contribute to hydraulic fracture conductivity deterioration including fines migration ([Byrne et al., 2014], [Sameni et al., 2015] and [Tiab and Donaldson, 2015]), proppant diagenesis ([LaFollette and Carman, 2010] and [Duenckel et al., 2011]), proppant crushing, and reduction in fracture opening due to the embedment of proppant particles into the surface of the hydraulic fracture ([Veiga et al., 2005], [Morales et al., 2011], [Alramahi and Sundberg, 2012] and [Zhang et al., 2015]). Different variables influence the contribution of these mechanisms such as: mechanical properties, mineral content, temperature, proppant type, fracture fluid type and closure pressure.

1.1.2 Overview of shale rock microstructure in the literature

Shales are one of the most complex and complicated rocks due to its multiscale and multiphase composition. Therefore, characterizing shale rock formations is a challenge. The effects of the multiphase composition are amplified within organic-rich shales that contain varying amounts of organic matter (kerogen) dispersed within inorganic matrix [Ahmadov, 2011]. There is an intricate interplay between microtexture

© 2018 Tous droits réservés.
lilliad.univ-lille.fr

evolution and kerogen maturity ([Zargari et al., 2013], [Allan et al., 2015] and [Abedi et al., 2016a]). Thus, the heterogeneity of shale source rocks requires observations at multiple scales in order to characterize their microstructures. Usually, shales are made of submicron clay particles, nanoporosity and different inclusions.

Recently, [Curtis et al., 2010] have studied the microstructure of shale samples from different formations (Barnett, Woodford, Eagle Ford, Haynesville, Marcellus, Kimmeridge, Floyd, Fayetteville and Horn River) on the micro and nanoscales using a combination of Focused Ion Beam and Scanning Electron Microscopy techniques. They found a significant variations in the microstructure of the studied shale samples such as: mineral content, microtexture and porosity, and some similarities among different samples. ([Curtis et al., 2010] and [Akono and Kabir, 2016]) have predicated that the studied organic shales are composed essentially of quartz, clays, kerogen, carbonate and pyrite minerals in varying amounts. Shale hydrocarbon reservoirs possess extremely small-sized complex pore systems with organic and inorganic interparticle, intercrystalline and intraparticle pores ([Curtis et al., 2010], [Loucks et al., 2012], [King et al., 2015] and [Schieber et al., 2016]). The organic porosity changes from shale rock to another even inside the same shale rock: while some regions of kerogen can contain many pores, adjacent regions have no porosity. Besides, [Ahmadov, 2011] have studied hydrocarbon source rock samples from Kimmeridge, Bakken, Bazhenov, Monterey and Lockatong formations by using the combined Confocal Laser Scanning Microscopy and Scanning Electron Microscopy techniques. Special observations are made to notice spatial distribution of clay, pyrite and kerogen. Furthermore, [Ahmadov, 2011] has established spatial and temporal link between organic matter and corresponding maturity stages: in a mature stage, a strong anisotropy due to the organic matter is observed while no anisotropy within postmature sample. Other researches have been carried out to study heterogeneity of microstructural features by using advanced imaging by Scanning Electron Microscopy and Transmission Electron Microscopy ([Bennett et al., 1991] and [Hornby et al., 1994]) or by Synchrotron X-ray analysis [Lonardelli et al., 2007]. Recently, [Abedi et al., 2016a] has developed a method for the chemomechanical characterization of organic-rich shales at microscale and nanoscale using coupled nanoindentation and energy-dispersive X-ray spectroscopy. The method provides a means to identify pure material and mixture phases and interfaces between them.

As already seen, the microstructure of shale rock is quite complicated. Consequently, for micromechanical study, it is indispensable to make some hypothesis for its representation. According to [Dormieux et al., 2006] hypothesis, ([Delafargue, 2004], [Ulm and Abousleiman, 2006], [Bobko, 2008], [Akono and Kabir, 2016], [Abousleiman et al., 2016] and [Abedi et al., 2016a,b]) suppose that shale is a multiscale material

© 2018 Tous droits réservés.

lilliad.univ-lille.fr

with scales ranging from the scale of individual .clay minerals to macroscopic scale which is the one of millimetric rock sample. For instance, figure 1.4 shows the multi-scale structure model of organic-rich shale supposed by [Abedi et al., 2016a]. Level 0 is the scale of elementary clay particles at nanoscale. Level I is a porous clay/kerogen composite at microscale and level II is the scale of porous organic/inorganic hard inclusion composite at mesoscale. Macroscale is level III which is the level of shale specimens. According to [Abedi et al., 2016a], level I is of particular importance as the macroscopic behavior of organic-rich shales depends essentially on the porous clay and organic matter. Furthermore, [Abedi et al., 2016b] have studied the role of thermal maturity and organic matter on texture: they assumed that immature systems exhibit a matrix-inclusion morphology while mature ones display a polycrystalline microstructure.

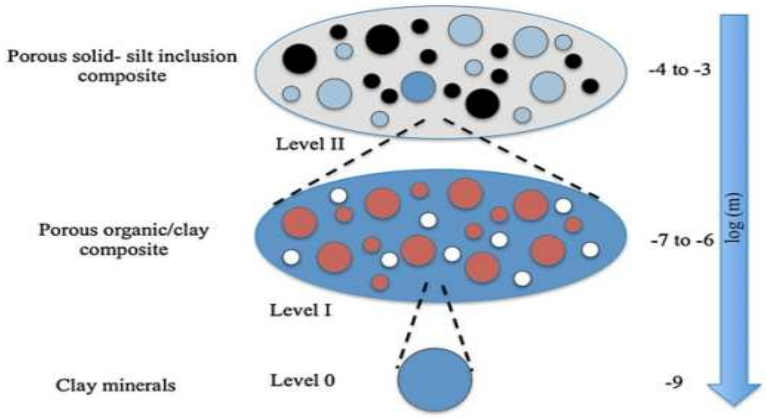

Figure 1.4: Multiscale structure model of organic-rich shale [Abedi et al., 2016a].

1.2 Industrial context and objective of the thesis

TOTAL's work in the 'Unconventional' program will lead to new methods of studying petroleum systems, but also to the creation of new simulation tools capable of reproducing the whole range of phenomena involved since the generation of hydrocarbons up to their production by specific processes. This complete simulation chain contributes to an extreme difficulty due to the implication of a large number of phenomena (mechanical, chemical, thermomechanical, kinetic, etc.) and their complex interactions. These modeling and simulation tools will guide, with a minimum of wells, to formation areas with the best production potential, 'sweet spots'. These zones are the most economically attractive because they are the most favorable to production due to their geological properties, their fluid content and their ability to be stimulated by hydraulic fracturing. Our work is part of the problem of analyzing and predicting instantaneous and time-dependent mechanical behavior of shale hydrocarbon reservoir. Different physical aspects and their coupled effects are required

© 2018 Tous droits réservés.

lilliad.univ-lille.fr

to be investigated for a comprehensive analysis of shale behavior; we are limited in this thesis to mechanical behavior.

Geomechanical and petrophysical factors such as total organic carbon content, thermal maturity and porosity are principal agents that influence the potential of shale play hydrocarbon production. Besides, a sustained productivity of a shale hydrocarbon layer depends substantially on geomechanical factors such as the network of natural fractures, the regime of in situ stresses, the elastic and rupture properties of hosted rock that control the geometry of hydraulic fractures, the connectivity and hydraulic conductivity of natural fractures networks [Su et al., 2014]. According to [Abousleiman et al., 2009], because of extreme low permeability of shale matrix, sustained productivity imposes that the main produced fractures and the natural ones remain open during production to contribute to the desired stimulated reservoir volume. Particularly, for a successful stimulation of a shale gas formation, it is essential evenly to study the time-dependent behavior of rock which controls the progressive closure of fractures. For this reason, characterization of short and long term mechanical properties of shale is a key issue.

Thus, the main objective of the thesis is to develop a micromechanical model, able to predict the instantaneous and time-dependent mechanical behavior of Vaca Muerta shale rock reservoir, which takes into account the heterogeneities of shale materials such as clay porosity, organic matter and different inclusions at separated scales. Figure 1.5 shows the basic concept to build a micromechanical model. At first, a representative elementary volume (REV) is defined according to microscopic observations, then an homogenization procedure is applied in order to predict the macroscopic response of the material. The industrial application of the thesis is to study the interaction between a fracture and a proppant grain in Vaca Muerta formation. Nevertheless, if time-dependent deformation of the rock is significant, the created fractures will be closed, contributing to the loss of hydrocarbon production.

1.3 Microstructure and behavior of Vaca Muerta shale rock

The exploitation of unconventional resources, trapped in source rocks, calls for fundamental knowledge of hosted rock functioning. Therefore, an important experimental program must be executed to characterize the shale rock and to understand how they operate from pore to basin scale. The objective of this section, is to study the microstructure and mechanical behavior of Vaca Muerta shale rock in order to be able to perform a micromechanical model capable to predict mechanical behavior

© 2018 Tous droits réservés.

lilliad.univ-lille.fr

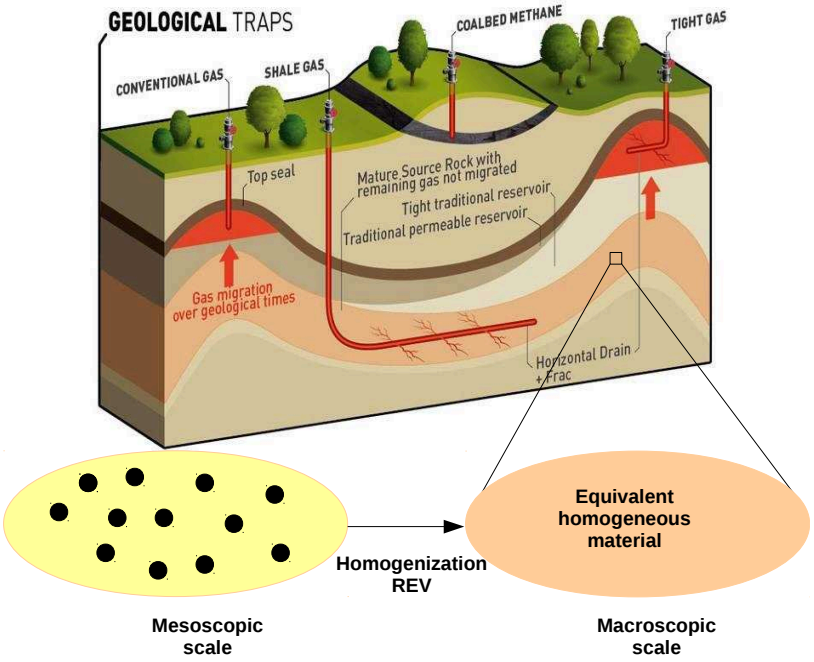

Figure 1.5: Application of homogenization concept in the context of a shale gas formation.

and especially creep behavior.

1.3.1 Microstructure

There are considered to be four main prospective basins in Argentina: Neuquén, Golfo San Jorge, Austral and Parana where the Neuquén basin is the most prolific oil and gas region. It is located in the west-central Argentina, covers 137 000 km^2 and contains both conventional and unconventional oil and gas plays. In recent years, Neuquén basin is facing a rapid decline in extraction levels, mainly due to the depletion of its mature deposits of conventional hydrocarbons. Thus, unconventional ones are the solution and the government has strongly supported their exploitation. First results of industrialists announce good indicators of depth, thickness (more than the double of Barnett, the largest exploitable reserve of shale gas in the United States), organic richness and thermal maturity [de la Terre, 2014]. The Lower and Upper Vaca Muerta formation are very organic where the total organic matter (TOC) can reach quite significant levels.

The Late Jurassic-Earliest Cretaceous Vaca Muerta formation, covering more than 30000 km^2, is the most interesting play of Neuquén basin beside Los Molles one and is the first unconventional development project in the country. It lies at a depth from 2000 to over 4000 m, with a thickness varying from 100 to over 500 m [Su et al., 2014]. As part of the study and evaluation of shale hydrocarbon potential of Vaca Muerta formation, many wells were drilled between 2011-2015. A series of experimental stud-

© 2018 Tous droits réservés.

lilliad.univ-lille.fr

ies have been carried out in order to study mineralogical, petrographical and textural characteristics of Vaca Muerta shale rock. Figure 1.6 shows two thin-section chemical/mineralogical maps of two depths from well S1, seen through Scanning Electron Microscope. Different mineralogical phases can be identified such as: calcite, quartz, pyrite, illite and others. Like most shale rocks and based on various microstructural observations, the main mineralogical phases of Vaca Muerta shale rock are supposed: clay, calcite and quartz. Many other minerals exist like: feldspar (albite), ankerite, pyrite and a significant proportion of insoluble organic matter (IOM). A small proportion of other minerals can be identified, like: barite, anastase and apatite. Five types of clay mineral phases occur in the studied samples: a kaolinite, an illite, a very poorly swelling interstratified illite-smectite type R1 or R3 (>80% illitic layers), a poorly swelling interstratified illite-smectite type R1 (75-80% illitic layers), and a corrensite [Fialips, 2014]. Calcite occurs as micritic mud (in black matrix associated with clay minerals and organic matter), mm-size bioclastic materials and μm-size calcified radiolarians (figure 1.7).

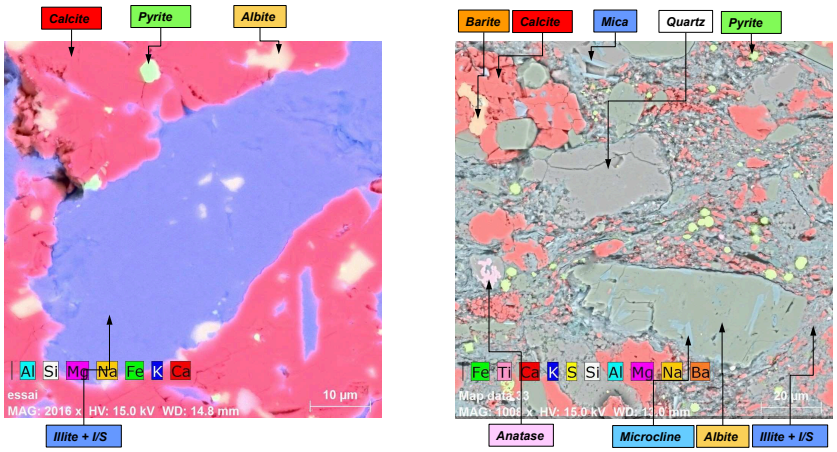

(a) 2542.98 m (b) 2538.13 m

Figure 1.6: Thin-section chemical/mineralogical maps for two depths from well S1 seen through Scanning Electron Microscope [Fialips, 2014].

[Askenazi et al., 2013] have invoked the mineralogical composition of Vaca Muerta shale. The proportion of carbonate and quartz varies extremely from 10 to 80% but clay proportion varies moderately from 5 to 35%. Concerning organic matter, the latter authors reported that insoluble organic matter reach up 12%, remaining typically within 3.5 and 7% in the basal section and normally between 2-4% uppermost part of the formation. There are levels in Vaca Muerta formation where total organic content (TOC) is less than 2% but it still contributes to shale hydrocarbon production. Figure 1.8 shows the variation of Vaca Muerta shale mineralogical composition in function of depth for three studied wells. Therefore, as we can see, the mineralogical composition changes substantially; observed variations in the bulk mineralogy do

© 2018 Tous droits réservés.

lilliad.univ-lille.fr

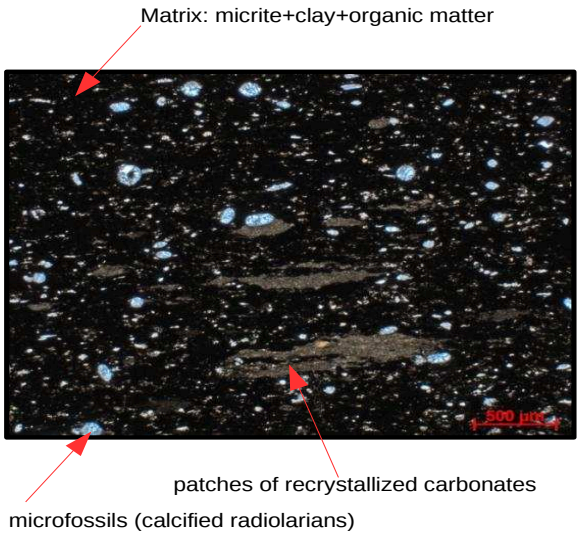

Figure 1.7: Petrographical microphotograph of a thin section of Vaca Muerta shale rock at a depth of 2646.32 m from well S1 [Fialips, 2014].

not show any particular systematic evolution with depth. Only quartz volumetric fraction tends to increase in the base of wells.

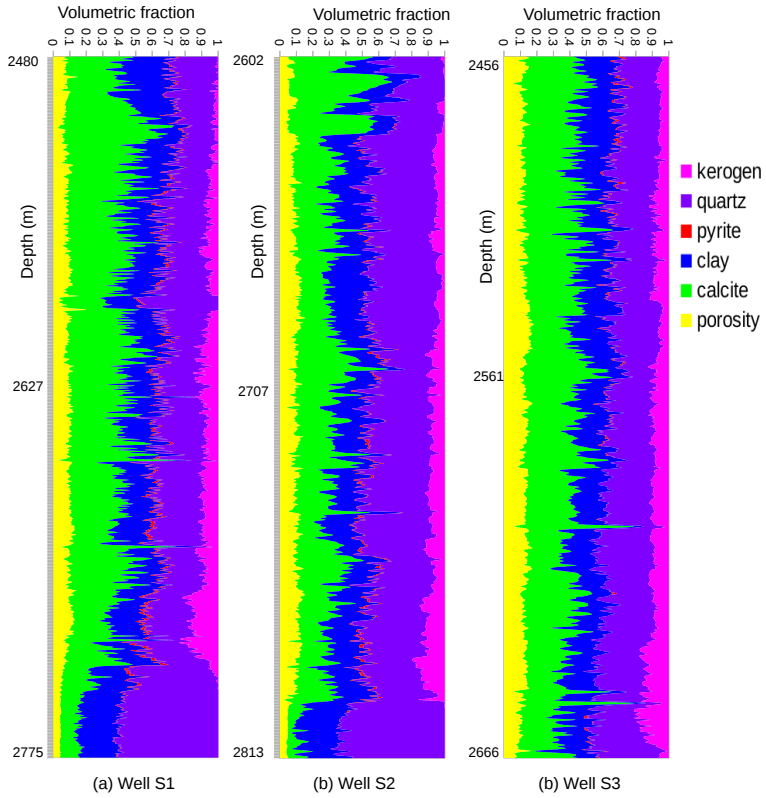

Figure 1.8: Mineralogical composition of Vaca Muerta shale formation in function of depth for three studied wells [TOTAL].

Following various observations and studies, we found that Vaca Muerta shale formation is primarily composed of silt-dominated mudstones, with variable content in

© 2018 Tous droits réservés.

lilliad.univ-lille.fr

calcareous (calcimicrite, bioclasts and micro-fossils) and illitic clay [Su et al., 2014]. Figure 1.9 is a ternary diagram of Vaca Muerta formation in two studied intervals of well S1. It illustrates mineralogical variability in the studied samples within the formation. A sub-linear compositional trend is clearly visible from a clayey-silty mudstone/clayey-siltstone with a moderate carbonate content pointing towards the nearly pure carbonate apex. Based on the previous observations, we can recognize that Vaca Muerta formation exhibits a strong vertical heterogeneity; there is several lithofacies with different texture and mineralogical composition.

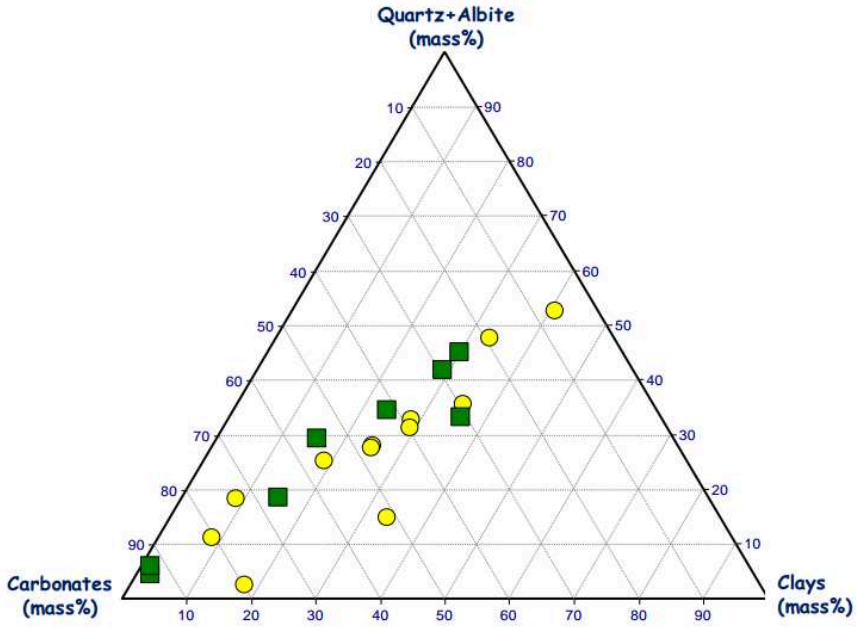

Figure 1.9: Ternary compositional plot of Vaca Muerta formation in well S1 [Fialips, 2014].

The knowledge of shale's porosity is very advantageous and enhances the capacity to locate and yield shale hydrocarbons. In most organic shale samples, pores are on the nanoscale, consequently, below the optical microscope resolution. Thus, alternative method must be used such as electronic microscopy. Recently, the introduction of combined Focused Ion Beam and Scanning Electron Microscopy technologies to the petroleum industry have allowed nanoscale pore structures imaging in 3D for the first time [Curtis et al., 2010]. Based on Focused Electron Beam (FEB-2D) and Focused Ion Beam (FIB-3D)-SEM images, two types of porosity are identified in Vaca Muerta shale samples: organic and mineral porosity (figure 1.10).

Figure 1.11 shows different types of porosity within organic and mineral composites: inter/intraparticle pores, organic hosted pores and interparticle pores between clay platelets. This identification is consistent with observation made by others works

© 2018 Tous droits réservés.

lilliad.univ-lille.fr

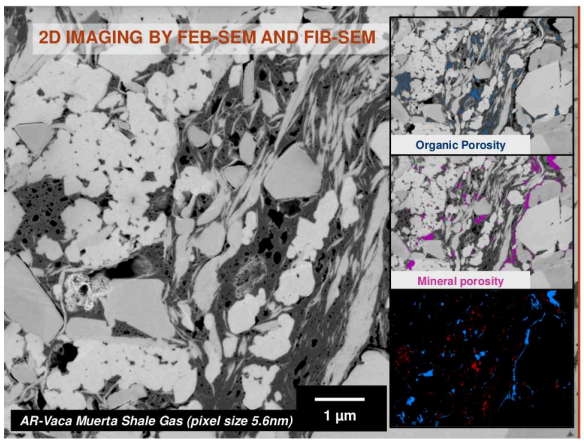

Figure 1.10: Distribution of two types of porosity inside Vaca Muerta shale rock: organic and mineral porosity [ISS/RGM, 2016].

that showed both an organic and mineral porosity within shale rock ([Curtis et al., 2010], [Loucks et al., 2012] and [King et al., 2015]). Figure 1.12 shows the distribution of different types of porosity inside a Vaca Muerta shale sample. As we can see that the size of different porosity varies from nano to microscale

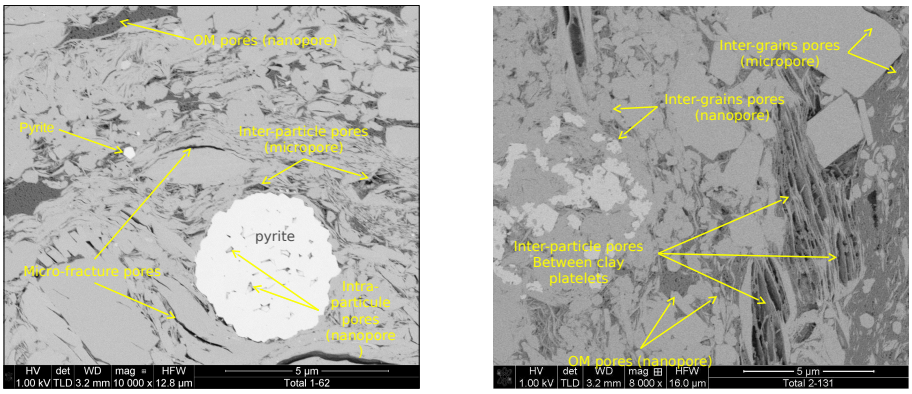

(a) (b)

Figure 1.11: Different types of porosity inside Vaca Muerta shale samples [ISS/RGM, 2016].

1.3.2 Mechanical behavior

To study the mechanical behavior in short and long term of Vaca Muerta shale rock, a series of triaxial compression and multistage creep tests was realized on selective shale samples. Other continuous laboratory measurements on the whole core are realized such as microindentation and scratch tests. Besides laboratory tests, drilling logs and in-situ experiments are carried out to study the mechanical behavior of the material. In this paragraph, we present some representative tests [TOTAL, 2012] and focus on the interactions between microstructure and mechanical behavior.

© 2018 Tous droits réservés.

lilliad.univ-lille.fr

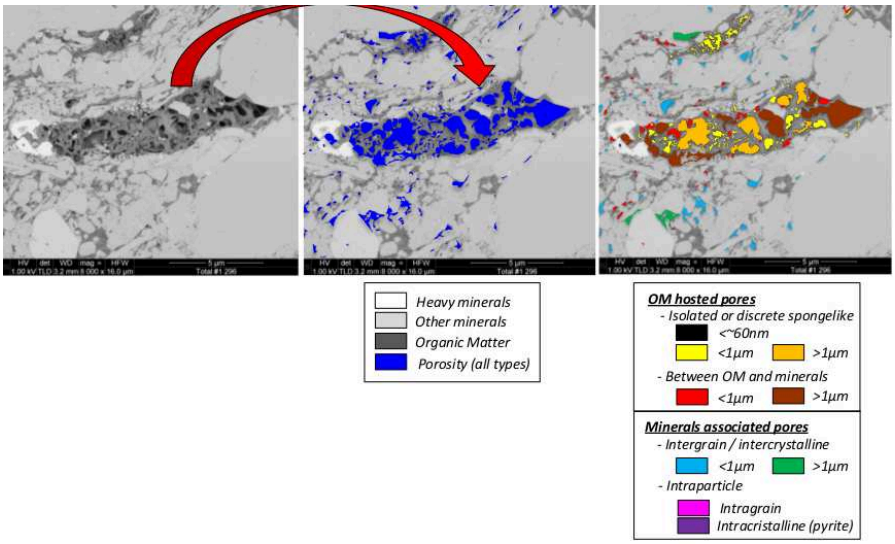

Figure 1.12: Distribution of different types of nano and micro porosity inside a Vaca-Muerta sample (FIB-SEM images) [ISS/RGM, 2016].

1.3.2.1 Instantaneous mechanical behavior

Several triaxial compression tests (simple, complex and multistage) are conducted according to TOTAL protocol in order to determine mechanical elastic properties, yield stress and the behavior after peak of samples taken from different depths of Vaca Muerta formation. Tests have been carried out, by TOTAL, on 2.5x5 cm cylindrical plugs with loading axis either perpendicular or parallel to bedding planes (figure 1.13). Tests are performed with an imposed strain rate in the range of 1 to $3x10^{-6}$/s in order to attain quasi-static tests. During the tests, axial and radial deformations are controlled as well as sonic compressive and shear wave velocities. Note that some triaxial compression tests are performed at our laboratory.

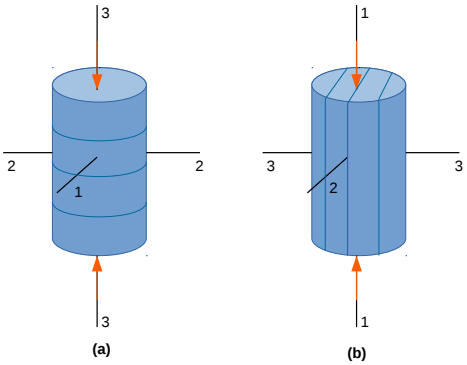

Figure 1.13: Orientation of loading axis which is (a) perpendicular (vertical sample) or (b) parallel (horizontal sample) to bedding planes.

Figure 1.14 shows stress-strain curves of two vertical samples from well S1 with a confining pressure of 10 MPa; one can notice that the macroscopic mechanical behavior depends on the mineralogical composition that varies with depth.

© 2018 Tous droits réservés.

lilliad.univ-lille.fr

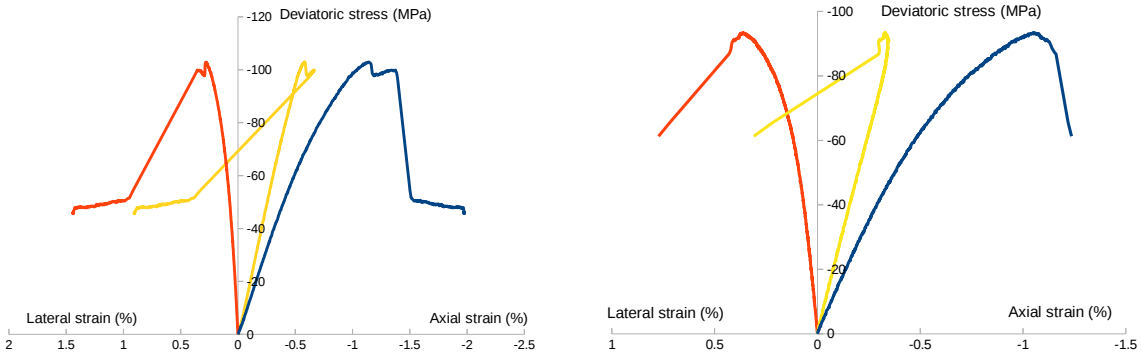

(a) 2649.23 m (b) 2530.23 m

Figure 1.14: Stress-strain curves of two Vaca Muerta vertical samples from well S1 with a confining pressure of 10 MPa.

Some multistage triaxial compression tests have been carried out on Vaca Muerta shale plugs. The principle is as follow: the same sample is used to successively perform several compression tests with successive confining pressures (figure 1.15). The axial loading is stopped just before failure, the confining pressure is increased and then, the new axial loading starts up and so on. Because of shale brittle behavior, the shale sample could be significantly damaged, at a confining pressure stage, without noticeable change of stress-strain slope which will affect the strength measured at the next stage. Thus, the control of multistage triaxial compression tests from one stage to the next is very delicate [TOTAL, 2012]. For this reason, these tests are limited.

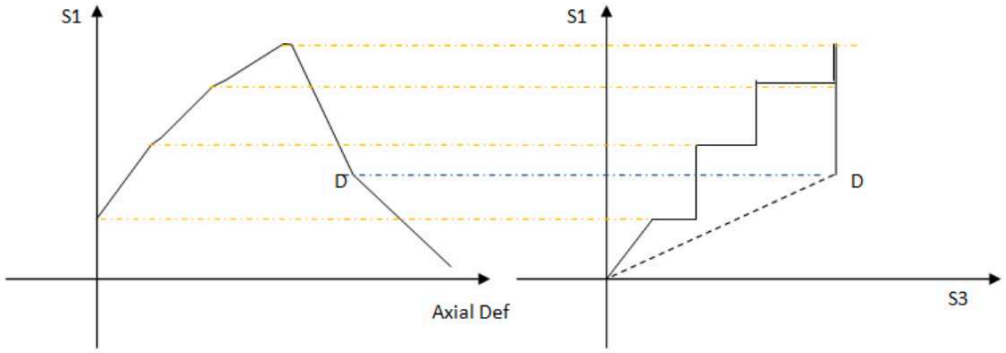

Figure 1.15: Loading path of a multistage triaxial compression test.

Figure 1.16 displays depth profile of Unconfined Compressive Strength (UCS) computed from sonic log [TOTAL, 2012] and mineralogical log of well S1. It is noted that Vaca Muerta shale strength is relatively high compared to other shale rocks due its mineralogical composition. As we can see, UCS varies greatly with depth.

© 2018 Tous droits réservés.

lilliad.univ-lille.fr

When the volumetric fraction of quartz and/or calcite inclusions is high, namely rigid inclusions, UCS is high as well; below 2730 m, quartz volumetric fraction increases considerably, therefore, UCS reaches a value of 110 MPa. Thus, the macroscopic mechanical behavior depends on the mineralogical composition that varies with depth.

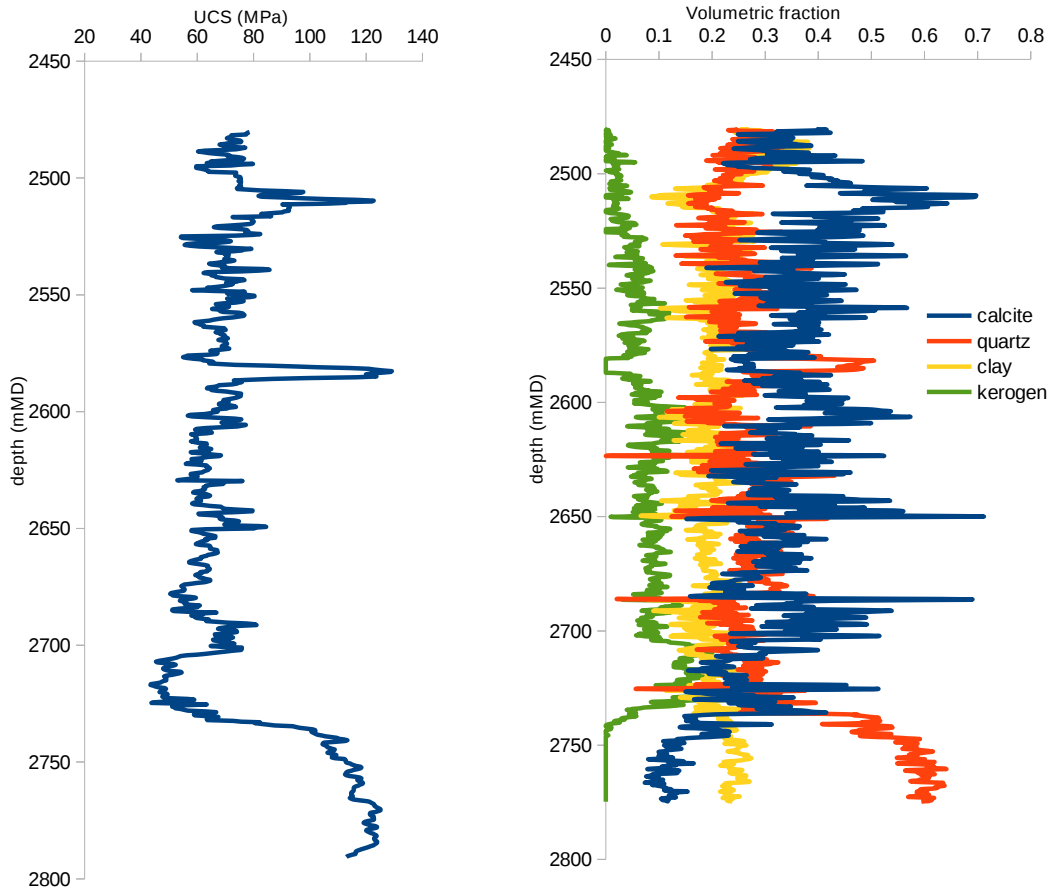

Figure 1.16: Depth profile of UCS computed from sonic log [TOTAL, 2012] and mineralogical log of well S1.

1.3.2.2 Time-dependent mechanical behavior

Different phenomena observed on shale rock, are the consequence of time effect such as: consolidation, aging, swelling, creep and relaxation. They are of mechanical, hydraulic, chemical and/or thermal origin. In this thesis, we are interested in the study of time-dependent behavior of mechanical origin (creep and relaxation). The understanding of creep and relaxation behavior is one of the keys for a successful stimulation of a shale hydrocarbon formation. Compared to instantaneous mechanical tests, a reduced number of long-term tests are performed on Vaca Muerta shale rock.

Two main loading types can be applied in the case of a creep test: monostage or multistage. The purpose of a multistage creep test is to study the influence of devi-

© 2018 Tous droits réservés.

lilliad.univ-lille.fr

atoric stress on strain rate with the same sample and a constant confining pressure. As if sample changes, then the mineralogical composition will change which can affect the material behavior. To evaluate the long term behavior of Vaca Muerta shale rock, several multistage triaxial compression creep tests are conducted by [Dusterloh, 2015]. Cylindrical samples (2.5x5 cm) are taken from different depths and orientations. Two test campaigns are realized with various conditions of temperature and stresses; the duration of each load stage is 30 days. Some tests are realized at a temperature of 100°C and others at 85°C. The confining pressure and the deviator are applied, simultaneously, with a rate of 1 MPa/min. The characteristic curves of two multistage creep tests are shown in figure 1.17; one can notice that only axial strain is measured. With the considered conditions of stresses, temperature and time, only transient and steady-state creep appear. The creep rate increases slightly with the increase of deviatoric stress. As we can see (figure 1.17), in principle, the amplitude of delayed deformation is small for all loading stages.

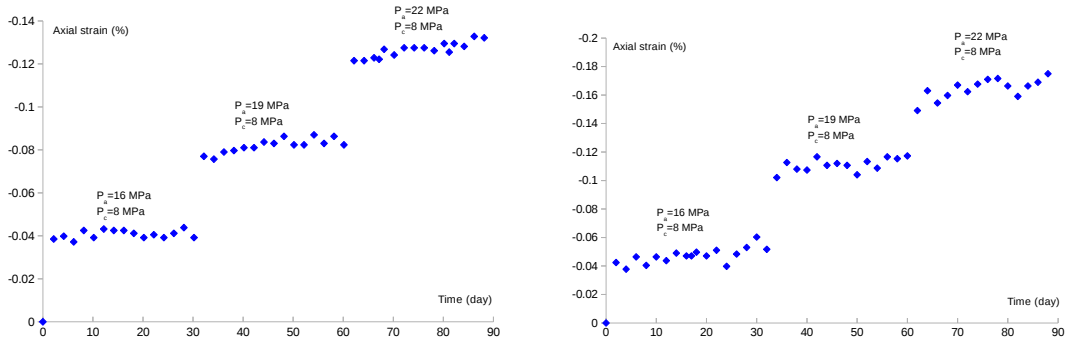

(a) 2537.14 m (b) 2537.24 m

Figure 1.17: Multistage triaxial compression creep curves for two Vaca Muerta shale samples [Dusterloh, 2015].

Some complementary multistage creep tests are realized in our laboratory in order to measure lateral deformations. Before any manipulation of samples, macroscopic cracks are visible. Tests are carried out at room temperature with different loading conditions; load stage is maintained between 15 and 20 days. Figure 1.18 illustrates the multistage triaxial creep curves for two Vaca Muerta shale samples. Apparently, creep deformation is low for the first two levels and then, suddenly, rupture occurs.

© 2018 Tous droits réservés.

lilliad.univ-lille.fr

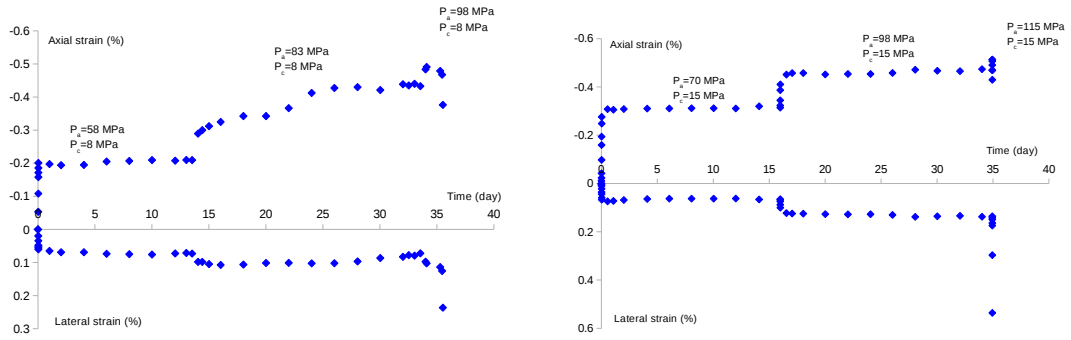

(a) 2668.84 m (b) 2768.44 m

Figure 1.18: Multistage triaxial compression creep curves for two Vaca Muerta shale samples performed in our laboratory.

1.4 Conclusion

In this chapter, firstly, we present a general bibliographic study of unconventional shale resources, hydraulic fracturing technique, as well as the principal mechanisms of hydraulic fracture conductivity deterioration. Then, we exhibit an overview of some shale rock microstructures from the literature. Shale rock from different formations is seen as a heterogeneous material with a multiscale and multiphase composition. The principle components of organic shales are: quartz, carbonate, pyrite, clay and kerogen minerals in varying amounts. In the second subsection, we discuss the industrial context and objective of the thesis. For a successful stimulation of a shale hydrocarbon formation, it is indispensable to characterize the short and long term mechanical properties of hosted rock. In this context, the main objective of the thesis is to develop a micromechanical model able to predict the instantaneous and time-dependent mechanical behavior of Vaca Muerta shale rock by taking into account the heterogeneities at different scales, such as, clay porosity, organic matter and different mineral inclusions. Finally, we study the microstructure and behavior of our interesting material, Vaca Muerta shale rock. A series of experimental studies have been carried out in order to study mineralogical, petrographical and textural characteristics of the studied material. According to microstructural observations, the main mineralogical phases are: calcite, quartz and clay; other minerals can exist: albite, ankerite, pyrite and insoluble organic matter. Based on log data, the mineralogical composition of Vaca Muerta shale varies, strongly, in function of depth with no particular systematic evolution. Following various observations, Vaca Muerta rock are supposed primarily composed of silt-dominated mudstones, with variable content in calcareous and illitic clay. Besides, two types of porosity are identified within Vaca Muerta samples: organic and mineral porosity. In the last paragraph, we present some short and long term representative tests and focus on the interactions between microstructure and mechanical behavior

© 2018 Tous droits réservés.

lilliad.univ-lille.fr

© 2018 Tous droits réservés.

lilliad.univ-lille.fr

Chapter 2

A micromechanical elastoplastic damage model for Vaca Muerta shale

Contents

© 2018 Tous droits réservés.

lilliad.univ-lille.fr

In the first chapter, based on experimental data, the microstructure and mechanical behavior of Vaca Muerta shale are studied, in particular, its highly heterogeneous character and the dependency of macroscopic mechanical behavior on the geological depth, i.e., mineralogical composition and porosity. In order to account for this dependency, a homogenization-based approach will be developed in this chapter. The macroscopic mechanical behavior of Vaca Muerta shale depends on the change of clay matrix porosity and the different types of fine and big organic/inorganic inclusions: the influence of porosity on clay matrix behavior will be obtained through a nano to micro upscaling procedure while the influence of fine and big inclusions are taken into account, respectively, through micro-meso and meso-macro upscaling steps. This chapter is structured as follows: in the first section, we describe the representative elementary volume of Vaca Muerta shale. In the second part, we study the linear elastic behavior of the studied material. Then, in the third section, the non linear instantaneous behavior of Vaca Muerta shale rock in the context of elastoplasticity and damage evolution is discussed.

2.1 Representative elementary volume

The formulation of a micromechanical model requires a simplified description of material microstructure. Thus, based on different observations of Vaca Muerta shale microstructure seen in the previous chapter, we have proposed the representative elementary volume (REV) of the studied material, given in figure 2.1, which will be the support for the construction of our micromechanical model.

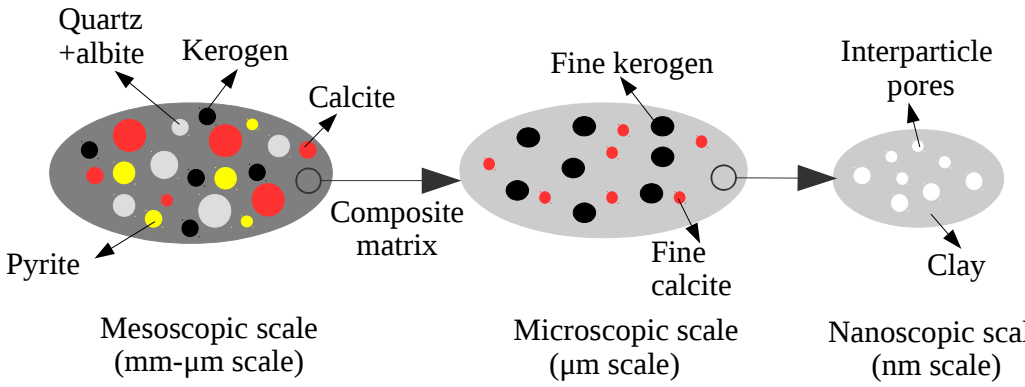

Figure 2.1: Representative elementary volume of Vaca Muerta shale rock.

As we can see, a scale separation is applied which is required for a homogenization procedure. Four relevant scales are considered where the heterogeneities are located on comparable scales:

- The nanoscale (∼nm): it is the scale of clay minerals fine matrix and its associated porosity. For simplicity, we assume that the pores are spherical and

© 2018 Tous droits réservés.

lilliad.univ-lille.fr

uniformly embedded in the clay matrix

- The microscale ($\sim \mu$m): where fine organic and inorganic inclusions are visible.
- The mesoscale (mm-μm) is the scale of big inclusions (quartz, albite, calcite, pyrite and kerogen).
- The macroscale (mm-cm) where the material can be considered as a homogeneous continuum medium.

The scale separability conditions, for the application of a micromechanical model, are satisfied in the different previous scales [Zaoui, 2000]:

1. the characteristic length of each scale is much smaller than that of the next scale;
2. the size of heterogeneities at each scale is sufficiently small compared to the characteristic length of the corresponding scale.

Thus, at the three homogenization scales, we suppose that the microstructure can be seen as a matrix-inclusion system. At mesoscale, the continuous phase is a composite matrix in which are embedded calcite (phase 1), quartz/albite (phase 2), pyrite (phase 3) and kerogen (phase 4) grains. At microscale, the composite matrix is a three-phase medium: fine kerogen (phase 5) and calcite (phase 6) are immersed in a porous clay matrix (phase 0). The mineral grains are assumed spherical and randomly distributed such that the macroscopic behavior of shale remains isotropic in nature. Calcite, quartz, kerogen and pyrite inclusions are supposed to have linear isotropic elastic behavior characterized by their elastic moduli. Whereas, the clay phase is considered as an elastoplastic damaged porous medium. The relative interparticle porosity (f), the relative volume fraction of fine kerogen (f_5) and calcite (f_6) are given, respectively, by the following:

$$f = \frac{\Omega_p}{\Omega_p+\Omega_a}; \quad f_5 = \frac{\Omega_5}{\Omega_6+\Omega_5+\Omega_p+\Omega_a}; \quad f_6 = \frac{\Omega_6}{\Omega_6+\Omega_5+\Omega_p+\Omega_a} \tag{2.1}$$

where Ω_p, Ω_a, Ω_5 and Ω_6 are the volume of interparticle pores, solid clay, fine kerogen and calcite respectively.

2.2 Linear homogenization

Measurement of shale elastic properties seems significant for: optimizing hydraulic fracture design, well stability study as well as to better predict seismic velocity. Thus, currently, with advanced experimental techniques, such as nanoindentation and Atomic Force Microscopy ([Zeszotarski et al., 2004], [Ahmadov, 2011], [Kumar et al.,

© 2018 Tous droits réservés.

lilliad.univ-lille.fr

2012] and [Bennett et al., 2015]), and theoretical micromechanical models ([Hornby et al., 1994], [Jakobsen et al., 2003], [Delafargue, 2004], [Bobko, 2008], [Gathier, 2008] and [Abedi et al., 2016a,b]), it becomes possible to determine intrinsic mechanical properties of heterogeneities, and then, use upscaling methods from submicroscale to macroscale to determine effective elastic properties. For instance, ([Delafargue, 2004] and [Abedi et al., 2016a,b]) used a combined experimental/nanoindentation - theoretical multiscale microporomechanics approach to determine either elastic or poroelastic properties of shale rocks. In this section, the effective elastic properties of Vaca Muerta shale are determined using a linear homogenization procedure in order to link the properties of constituents to shale elastic moduli at macroscopic scale. For linear homogenization study, we suppose that all phases have a linear elastic behavior.

2.2.1 Elastic properties of Vaca Muerta shale constituents

In order to predict effective elastic properties of Vaca Muerta shale by means of upscaling methods, it is essential to identify, at first, elastic properties of different phases and then, apply the appropriate homogenization scheme. As we will see, elastic properties of rigid inclusions (pyrite, quartz, albite and calcite) are explicitly known, whereas, those of clay and organic matter are not well recognized.

2.2.1.1 Elastic properties of rigid inclusions

Elastic properties of quartz, albite, calcite and pyrite constituents are well known and derived from the literature ([Lide, 2004] and [Brown et al., 2006]). In order to reduce the number of mesoinclusions, the grains of quartz and albite are supposed as a single equivalent inclusion phase. The effective elastic properties of the latter are calculated as the average values of the ones of quartz (E_q=101 GPa; ν_q=0.06) and albite (E_{al}=90 GPa; ν_{al}=0.25) inclusions [Jiang et al., 2009] and are given by: E_2=95.5 GPa and ν_2=0.155. The Young's modulus and Poisson's ratio of calcite, quartz+albite and pyrite are given respectively by: E_1=95 GPa; ν_1=0.27, E_2=95.5 GPa; ν_2=0.155 and E_3=311 GPa; ν_3=0.15 (table 2.1).

Table 2.1: Elastic properties of rigid inclusions.

	Calcite	Quartz+Albite	Pyrite
E (GPa)	95	95.5	311
ν	0.27	0.155	0.15

© 2018 Tous droits réservés.

lilliad.univ-lille.fr

2.2.1.2 Kerogen elastic properties

Elastic properties of shale formation are essentially affected by total organic content (TOC), porosity and total clay content [Kumar et al., 2012]. Well, the knowledge of kerogen mechanical properties appears to be important in this case; nevertheless, the elastic properties of kerogen as well as those of clay are not explicitly known . A wide range of values are widespread in the literature. [Zeszotarski et al., 2004] have estimated mechanical properties of kerogen in Woodford shale via modified Atomic Force Microscopy images and nanoindentation. They found that for immature kerogen, indentation modulus is equal approximately to 11 GPa. On the other hand, [Ahmadov, 2011] has estimated indentation modulus of organic matter through Atomic Force Microscopy based nanoindentation coupled with Scanning Electron and Confocal Laser-Scanning Microscopy. He found an indentation modulus for Bazhenov samples between 6-11 GPa and 12 GPa for Lockatong ones. For kerogen Poisson's ratio, [Ahmadov, 2011] inferred that if the latter varies in the range of 0.05 and 0.45, it has a minor dependence on shale Young's modulus. In the same framework, [Kumar et al., 2012] have estimated the elastic properties of Woodford shale organic matter through nanoindentation measurements. They estimated kerogen Young's modulus of samples with vitrinite reflectance between 0.5-6.36 % VR_o (vitrinite reflectance) and no porosity to be in the range of 6-15 GPa. But samples with significant organic porosity have a kerogen Young's modulus estimated between 1.9 and 2.2 GPa. Furthermore, [Yan and Han, 2013] have assessed bulk modulus of Green River mature kerogen from the measurements of ultrasonic velocities; from data measured on both dry and saturated samples, they inverted the bulk modulus of kerogen using [Gassmann, 1951] equation, Reuss and Voigt bounds. They found a bulk modulus of kerogen around 3.5-5 GPa and estimated shear modulus to be the half of bulk one. Besides, more recently, [Boulenouar et al., 2017] have performed nanoindentation experiments on Vaca Muerta shale samples from within oil window. They localized a population of softest nanoindentation measurement corresponding probably to the organic matter and estimated its average Young's modulus equal to 6 GPa. Furthermore, [Boulenouar et al., 2017] have noted that the nanoindentation measurements of the softest phase are very low compared to ones of source rock from the United States.

Regarding Vaca Muerta elastic properties of organic matter used in this study, we refer as well to literature since no direct experimental measurements are realized within the framework of thesis. As elastic properties of kerogen are linked to localized porosity and maturity which vary highly in shale formations, we distinguish, in our study, between organic matter within oil and gas windows. For organic matter in oil window where maturity varies between 0.8-1.1 % VR_o, we assume a Young's modulus and Poisson's ratio of solid organic matter equal respectively to: E_{om}=7 GPa and

© 2018 Tous droits réservés.

lilliad.univ-lille.fr

ν_{om}=0.3 ([Kumar et al., 2012] and [Boulenouar et al., 2017]). As we have seen in the first chapter, the organic matter is a porous medium; thus, its morphology is approximated as matrix-pore with spherical pores randomly distributed inside organic solid phase. To calculate elastic properties of porous organic matter, [Hashin and Shtrikman, 1963] upper bound is adopted as follows:

$$\kappa_4 = \kappa_5 = \frac{4(1-f_o)\kappa_{om}\mu_{om}}{4\mu_{om}+3f_o\kappa_{om}}; \quad \mu_4 = \mu_5 = \frac{(1-f_o)\mu_{om}}{1+6f_o\frac{\kappa_{om}+2\mu_{om}}{9\kappa_{om}+8\mu_{om}}} \tag{2.2}$$

where (κ_4 or κ_5;μ_4 or μ_5) and (κ_{om};μ_{om}) are respectively elastic properties of porous (phase 4 and 5) and solid organic matter in oil window. f_o is the relative organic porosity given by (with Ω_{op} and Ω_{om}, the volume of organic pores and solid kerogen respectively):

$$f_o = \frac{\Omega_{op}}{\Omega_{op}+\Omega_{om}} \tag{2.3}$$

For organic matter within gas window, where maturity is higher than 1.1 % VR_o, we use values obtained by ([Lucier et al., 2011] and [Qin et al., 2014]): E_{gm}=10.67 GPa and ν_{gm}=0.277 (κ_{gm}=7.98 GPa and μ_{gm}=4.18 GPa). Likewise, the same equations 2.2 are used to calculate elastic properties of porous organic matter, by knowing organic porosity f_o and those of solid phase (κ_{gm} and μ_{gm}).

Elastic properties and mineral density of organic matter within oil and gas windows are summarized in table 2.2.

Table 2.2: Elastic properties and mineral porosity of organic matter.

	Organic matter	
	(oil)	(gas)
E (GPa)	7	10.67
ν	0.3	0.277
ρ_m (g.cm^{-3})	1.3	1.5

2.2.1.3 Clay elastic properties

As have already been said, unlike quartz, pyrite and calcite minerals, clay elastic properties are not explicitly known in handbooks ([Mavko et al., 1998] and [Lide, 2004]). In [Mavko et al., 1998], the anisotropic elastic constants of large muscovite crystals are only directly known. The main difficulty of evaluating clay elastic properties is the fact that its particles are too small to be tested in pure solid form. Different experimental and theoretical studies have been devoted to investigate clay

© 2018 Tous droits réservés.

lilliad.univ-lille.fr

elastic properties, essential for interpreting and modeling the seismic response of clay-bearing formations ([Hornby et al., 1994], [Wang et al., 2001], [Prasad et al., 2002], [Vanorio et al., 2003], [Kopycinska-Müller et al., 2007] and [Wenk et al., 2007]). From the latter references, we can notice the large variability of clay elastic properties which highlights the difficulty to assess the intrinsic characteristics of single clay crystals.

In our study, to acquire clay matrix elastic properties, we do not refer to the literature and no direct experimental measurements are realized; however, an inverse approach [Guéry, 2007] is applied. For this reason, we have to choose an appropriate linear homogenization scheme. As already seen in the previous section, a matrix-inclusion/pore morphology is considered at the three homogenization levels. [Guéry, 2007] has compared the results of different homogenization schemes (dilute, Mori-Tanaka and self-consistent) with experimental data and concluded that [Mori and Tanaka, 1973] scheme appears to be the most suitable homogenization scheme in the case of a matrix-inclusion morphology. In the case of spherical inclusions and isotropy at both local and overall scales, [Mori and Tanaka, 1973] scheme yields the bulk κ^{hom} and shear μ^{hom} moduli of the homogenized medium, respectively, as follows:

$$\kappa^{hom} = \left(\sum_r f_r \frac{\kappa_r}{3\kappa_r + 4\mu_0} \right) \left(\sum_s \frac{f_s}{3\kappa_s + 4\mu_0} \right)^{-1} \tag{2.4}$$

$$\mu^{hom} = \frac{\sum_r f_r \frac{\mu_r}{\mu_0(9\kappa_0+8\mu_0)+6\mu_r(\kappa_0+2\mu_0)}}{\sum_s \frac{f_s}{\mu_0(9\kappa_0+8\mu_0)+6\mu_s(\kappa_0+2\mu_0)}} \tag{2.5}$$

where $(\kappa_r;\mu_r)$ denote, respectively, the bulk and shear moduli of phase r, $(\kappa_0;\mu_0)$ those of the matrix phase and f_r, the volume fraction of phase r.

As we have seen in the first chapter, Vaca Muerta shale rock is an anisotropic material like most shale rocks. According to microstructural observations, no aligned inclusions are detected. We suppose that the origin of inherent anisotropy is the presence of a set of bedding planes in clay matrix. For simplicity and as the expressions of macroscopic elastic moduli (equations 2.4 and 2.5) in the case of local and global isotropy are well known, we suppose that Vaca Muerta rocks, for the two principal orientations (figure 1.13), are two different isotropic materials with two different clay matrix; namely, clay matrix in the two cases has different elastic properties. We have only envisaged the two principal orientations seeing that most of experimental tests are carried out on samples with loading axis either parallel or perpendicular to bedding planes.

First, we calculate Young's modulus and Poisson's ratio of clay matrix solid phase for vertical samples ($E_s^{\perp}$ and $\nu_s^{\perp}$). Inverse procedure must be applied three times to

© 2018 Tous droits réservés.

lilliad.univ-lille.fr

obtain finally the elastic parameters of clay matrix solid phase (figure 2.1). But to avoid complexity, we suppose for this application that no fine calcite and kerogen exist at microscale. Thus, knowing elastic properties of constituents apart from clay matrix, experimental values of elastic coefficients of Vaca Muerta samples for a specified depth ($E^{hom^{\perp}}$=14130 MPa and $\nu^{hom^{\perp}}$=0.23, [TOTAL, 2012]) and the mineralogical composition for the same depth (f_1=0.41, f_2=0.23, f_3=0.017, f_4=0.12), the inverse use of non-linear equations 2.4 and 2.5 gives the elastic parameters of porous clay matrix ($\kappa_0^{\perp}$ and $\mu_0^{\perp}$). Next, we compute elastic properties of solid phase in clay matrix. Knowing the value of relative interparticle porosity (f=0.1) for the same previous depth and elastic parameters of porous clay matrix ($\kappa_0^{\perp}$ and $\mu_0^{\perp}$), [Hashin and Shtrikman, 1963] upper bound is applied to calculate those of clay matrix solid phase for vertical samples ($\kappa_s^{\perp}$ and $\mu_s^{\perp}$) as follows:

$$\kappa_0^{\perp} = \frac{4(1-f)\kappa_s^{\perp}\mu_s^{\perp}}{4\mu_s^{\perp} + 3f\kappa_s^{\perp}}; \quad \mu_0^{\perp} = \frac{(1-f)\mu_s^{\perp}}{1 + 6f\frac{\kappa_s^{\perp}+2\mu_s^{\perp}}{9\kappa_s^{\perp}+8\mu_s^{\perp}}} \tag{2.6}$$

Finally, our calculations lead to: $\kappa_s^{\perp}$=3565 MPa and $\mu_s^{\perp}$=1925 MPa ($E_s^{\perp}$=4894 MPa and $\nu_s^{\perp}$=0.27). The same steps are applied to obtain Young's modulus and Poisson's ratio of clay matrix solid phase for horizontal samples ($E_s^{\shortparallel}$ and $\nu_s^{\shortparallel}$). In this case, we choose a horizontal sample to apply the latter inverse procedure. Given (f_1=0.143, f_2=0.405, f_3=0.0044, f_4=0.12, f=0.1) and ($E^{hom^{\shortparallel}}$=20000 MPa and $\nu^{hom^{\shortparallel}}$=0.25, [TOTAL, 2012]), we obtain: $\kappa_s^{\shortparallel}$=10585 MPa and $\mu_s^{\shortparallel}$=3861 MPa ($E_s^{\shortparallel}$=10328 MPa and $\nu_s^{\shortparallel}$=0.34).

To avoid confusion, the elastic properties of clay phase, for perpendicular and parallel loadings, are summarized in table 2.3.

Table 2.3: Elastic properties of clay phase for perpendicular and parallel loadings.

	Porous clay (f=0.1)	Solid clay
$E^{\perp}$(GPa)	4	4.9
$\nu^{\perp}$	0.26	0.27
$E^{\shortparallel}$(GPa)	8.45	10.33
$\nu^{\shortparallel}$	0.32	0.34

2.2.2 Application and sensitivity study in elastic regime

2.2.2.1 Comparison with experimental elastic properties

Since the elastic properties of all constituents are now identified and the mineralogical composition of three wells (S1, S2 and S3) is known from mineralogical logs, Mori-

© 2018 Tous droits réservés.

lilliad.univ-lille.fr

Tanaka scheme (equations 2.4 and 2.5) can be applied to predict the macroscopic elastic properties as a function of depth for the three studied wells. The volumetric fraction of fine kerogen and calcite (f_5 and f_6) are not known continuously (known just at few depths), so we consider only the case without fine calcite and kerogen in this study. A sensitivity assessment is presented later to study the influence of fine calcite and kerogen on macroscopic effective elastic properties. Since the elastic properties of kerogen are dependent on maturity, it is necessary to specify whether the wells are located in gas or oil window. Wells S1 and S3 are within oil window while well S2 is in gas one. Experimental elastic moduli, with which we will compare our simulations, are measured from triaxial compression tests for different confining pressures. The latter are carried out on samples whose loading axis is either perpendicular or parallel to bedding planes (figure 1.13). The comparison between experimental data (points) and simulations (continuous lines) for the three wells (S1, S2 and S3) are given respectively in figures 2.2, 2.3 and 2.4. As we can see, macroscopic elastic properties relatively vary as a function of depth with the variation of mineralogy and porosity. In general, simulations of macroscopic Young's modulus E^{macro} are consistent with experimental data. It should be noted that experimental Poisson's coefficients are not displayed since its values vary widely (from 0.1 to 0.5). Thus, from these calculations, we can predict Young's modulus ($E^{macro\perp}$; $E^{macro//}$) and Poisson's coefficient ($\nu^{macro\perp}$; $\nu^{macro//}$) as function of depth for the two principal orientations.

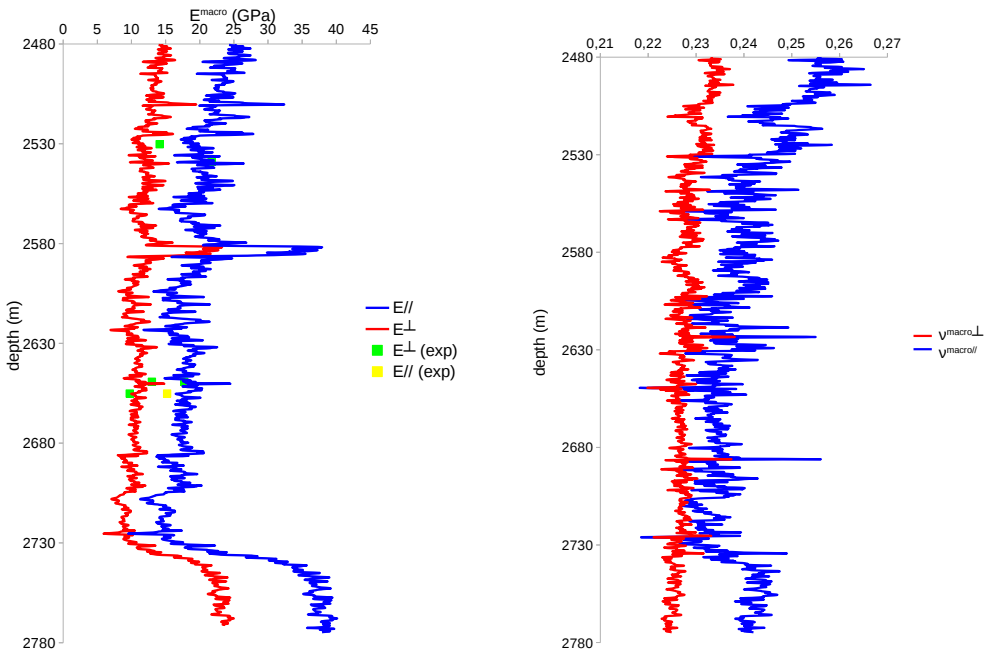

(a) Macroscopic Young's modulus (b) Macroscopic Poisson's ratio

Figure 2.2: Comparison between experimental (points) and calculated (continuous lines) elastic properties for well S1.

© 2018 Tous droits réservés.

lilliad.univ-lille.fr

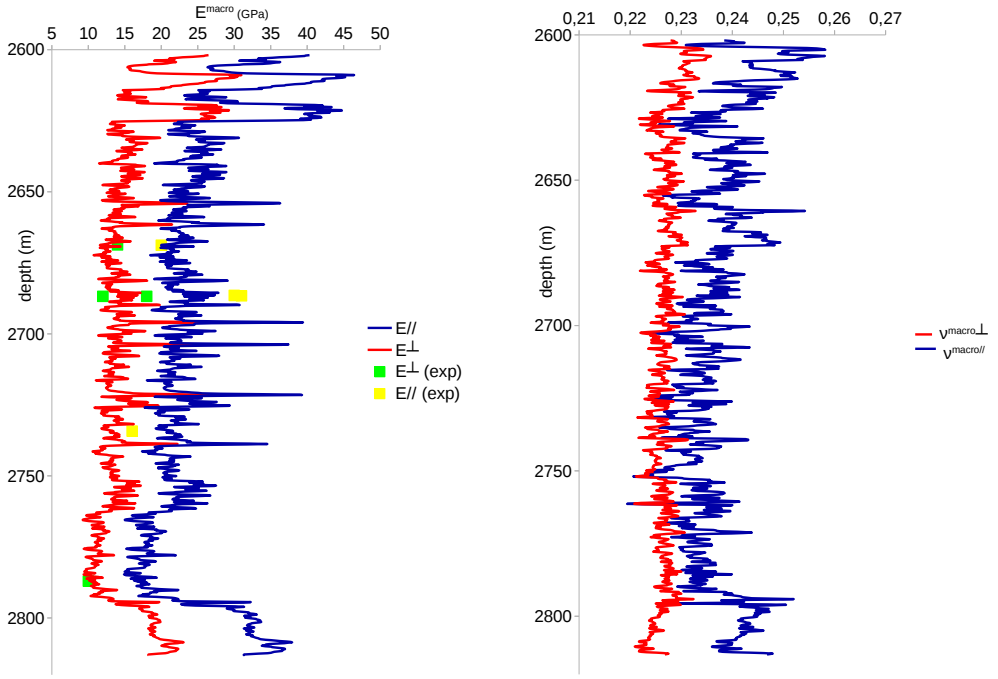

(a) Macroscopic Young's modulus (b) Macroscopic Poisson's ratio

Figure 2.3: Comparison between experimental (points) and calculated (continuous lines) elastic properties for well S2.

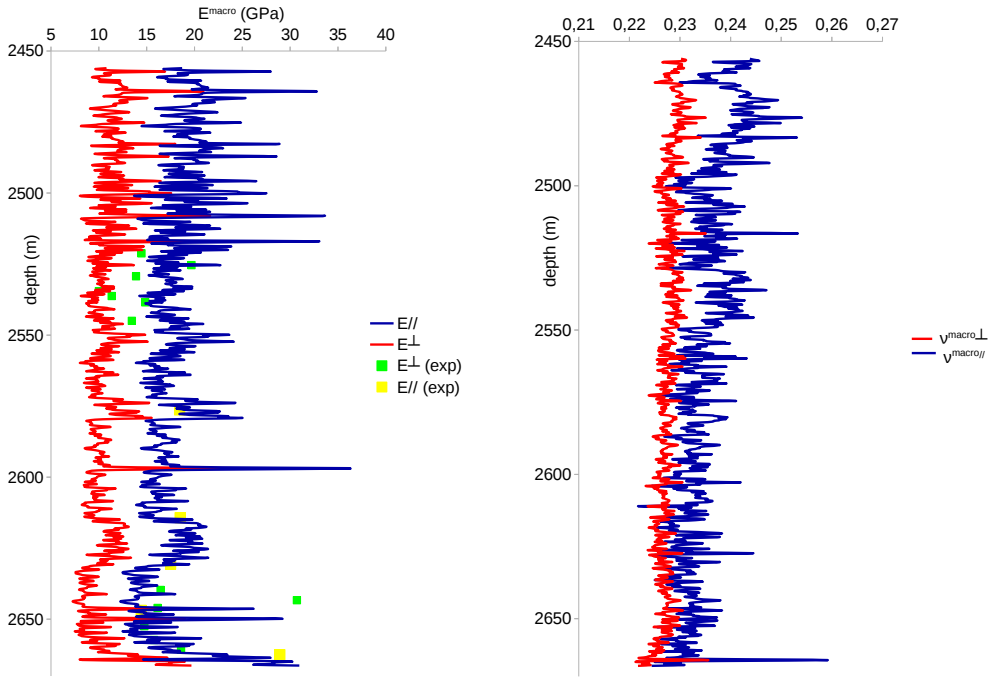

(a) Macroscopic Young's modulus (b) Macroscopic Poisson's ratio

Figure 2.4: Comparison between experimental (points) and calculated (continuous lines) elastic properties for well S3.

© 2018 Tous droits réservés.

lilliad.univ-lille.fr

2.2.2.2 Influence of kerogen elastic properties on effective elastic ones

Despite several researches to determine kerogen properties, the main question is how its intrinsic physical characteristics affect the macroscopic properties of the host rock ([Slim, 2008], [Zargari et al., 2013] and [Wilkinson et al., 2015]). [Sone, 2012], by observing the ductile creep behavior and brittle strength, has noticed that the deformational properties are influenced by the amount of soft components in the rock. Further, according to [Abousleiman et al., 2016], overall mechanical response of shale samples with only trace levels of organic material is little affected by the latter. In this paragraph, we study the influence of kerogen elastic properties on effective ones. As already seen, kerogen elastic properties are linked to localized porosity and maturity. Therefore, according to maturity level, three sets of kerogen elastic properties are considered (table 2.4) and we study its influence on macroscopic elastic response. The elastic properties of all other constituents are taken from the previous section (tables 2.1 and 2.3). The sensitivity study is realized in the case of vertical samples only. The typical mineralogical composition, used in this study, is given by: f_1=0.4, f_2=0.2, f_3=0.02, f_4=0.03/0.05/0.1/0.15 and f=0.1; as we can see, four different kerogen volumetric fraction is envisaged. The volumetric fraction of fine kerogen and calcite are supposed zero in this sensitivity study (we consider their effects on macroscopic elastic response in the next paragraph).

Table 2.4: Elastic properties and mineral density of kerogen with different maturity levels ([Vanorio et al., 2008], [Lucier et al., 2011], [Yan and Han, 2013] and [Qin et al., 2014]).

Maturity level	Hydrocarbon composition	κ_k (GPa)	μ_k (GPa)	ρ_m (g.cm^{-3})
Immature	oil	3.5	1.75	1.1
Mature	oil and gas	5	2.5	1.3
Overmature	gas	7.98	4.18	1.5

Figure 2.5.a shows the macroscopic bulk modulus as a function of kerogen one for the four volumetric fractions. One can notice that when κ_k becomes higher, κ^{macro} increases. The influence of κ_k on κ^{macro} is more pronounced when kerogen volumetric fraction is further significant. Figure 2.5.b exhibits the influence of kerogen shear modulus on macroscopic elastic one. The same observations, as in figure 2.5.a, can be noticed.

© 2018 Tous droits réservés.

lilliad.univ-lille.fr

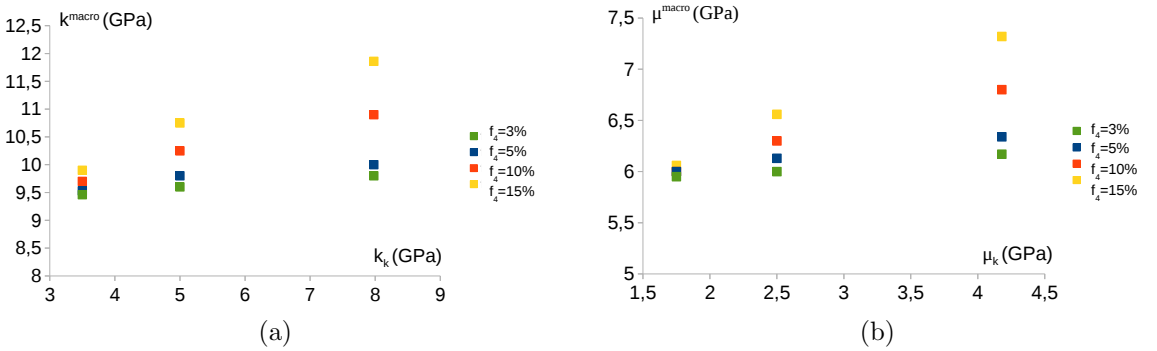

Figure 2.5: Influence of kerogen (a) bulk and (b) shear moduli on macroscopic elastic ones.

2.2.2.3 Influence of fine inclusions on effective elastic properties

According to the microstructure of Vaca Muerta shale, fine calcite and kerogen inclusions can be identified at microscale. In this paragraph, we study the influence of these fine grains on effective elastic properties. The sensitivity study is limited to the case of vertical samples and kerogen within oil window. The elastic properties of constituents are given in tables 2.1, 2.2 and 2.3. The typical mineralogical composition, used in this sensitivity study, is as follows: f_1=0.4; f_2=0.2; f_3=0.02; f_4=0.15; f=0.1; f_o=0.6. Figure 2.6.a shows the variation of macroscopic bulk and shear moduli as a function of macroscopic fine calcite volume Ω_6. The idea is to leave the total volume of calcite equal to 0.4 and to distribute the latter between the meso and microscales. For example, if f_1=0.4 then Ω_6=0 or if f_1=0.3 then Ω_6=0.1 (the same idea for fine kerogen). As we can notice, when Ω_6 increases, κ^{macro} and μ^{macro} increase. Through, when Ω_6 >0.2 (half of calcite total volume), the slope of the two curves becomes weak. Thus, with the same total volume of calcite, the distribution of calcite inclusions between meso and microscales has an influence on the macroscopic elastic properties. Regarding fine kerogen grains, as we can see in figure 2.6.b, κ^{macro} and μ^{macro} decrease when Ω_5 increases.

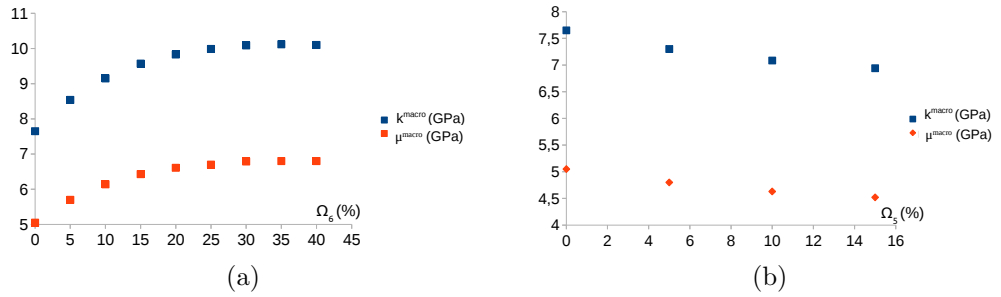

Figure 2.6: Influence of (a) fine calcite and (b) fine kerogen volume fractions on effective macroscopic elastic properties.

© 2018 Tous droits réservés.

lilliad.univ-lille.fr

2.3 Non-linear homogenization: Elastoplastic damage model

The aim of this section is to build a micromechanical model able to predict instantaneous mechanical behavior of Vaca Muerta shale rock. Clay matrix is assumed to have an elastoplastic behavior; all other phases have a linear elastic behavior. As already seen (figure 2.7), three homogenization representative scales are envisaged to account simultaneously for the interparticle porosity inside clay matrix, fine grains and meso inclusions. In the first main part, we discuss the homogenization of non linear behavior in the context of elastoplasticity: a first step of homogenization yields the strength domain of the porous clay phase where the solid clay phase is considered as a cohesive-frictional material obeying to the classical Drucker-Prager criterion. In the second homogenization step, fine inclusions are taken into account and the last homogenization step adds the different types of inclusions yielding to the macroscopic strength response. Thus, three transition levels are applied, simultaneously, to obtain the macroscopic mechanical behavior: at nano-micro transition, an analytical plastic criterion for porous medium is used to account for pores inside the clay matrix, then [Hill, 1965] incremental method is used at the micro-meso and meso-macro transitions as homogenization method (figure 2.7). In consequence, the model takes into account explicitly the influence of mineralogical composition as well as matrix porosity. At the second main part, we take into account in the modeling the complete interfacial debonding between the matrix and particles. It is assumed that the material damage process is related to progressive debonding of mineral inclusions (in our case, we suppose that mesocalcite inclusions are expected to interfacial debonding). Finally, comparisons between experimental data and simulations show the capacity of the micromechanical model to predict mechanical behavior of Vaca Muerta shale.

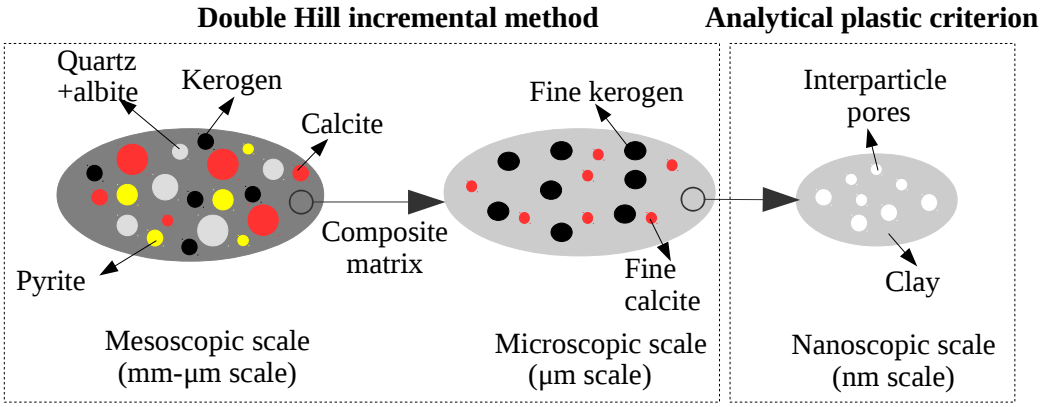

Figure 2.7: Representative elementary volume of Vaca Muerta shale rock.

© 2018 Tous droits réservés.

lilliad.univ-lille.fr

2.3.1 Elastoplastic model

2.3.1.1 First homogenization for the porous clay matrix

In this paragraph, a first level of modeling is proposed for the non linear behavior of the porous clay matrix. To this end, it is proposed to use an analytical plasticity criterion for a porous medium. Several studies have been devoted to determine plasticity criteria for a porous material with solid phase obeying to Von Mises ([Gurson, 1977], [Cheng et al., 2014] and [Shen et al., 2015a]) or Drucker-Prager criterion ([Guo et al., 2008], [Maghous et al., 2009] and [Shen et al., 2012]). Recently, [Shen et al., 2017] have formulated a theoretical macroscopic yield criteria for ductile porous materials consisting of a pressure sensitive matrix and spheroidal (prolate and oblate) voids. The closed form expression of the plastic criteria is determined by implementing an appropriate kinematical limit analysis with a relaxed plastic admissibility condition in an average sense. The resulting criterion takes into account the void shape effects and the plastic compressibility of the matrix. After a phase of improvement, the modified criterion is validated though comparison with numerical upper and lower bounds obtained by [Pastor et al., 2010] for a spherical void and by [Pastor and Kondo, 2014] for an oblate void. For a complete assessment of the approximate macroscopic yield criteria, comparisons between the latter and new Finite Element Method computations are realized for the case of prolate and oblate voids.

After this short review of porous material criteria, we return to the study of the clay matrix of our material. As already seen (figure 2.7), the latter is described by two phases: solid phase and spherical pores. The plastic deformation of the solid phase is assumed to be governed by an associated flow rule. As for most geomaterials, we assume, in this study, that the plastic deformation of Vaca Muerta shale is strongly pressure sensitive. Thus, the solid phase of the clay matrix is supposed obeying to the classical [Drucker and Prager, 1952] criterion, given as follows:

$$\phi(\sigma) = \sigma_{eq} + 3\alpha\sigma_m - \sigma_0 \leq 0 \tag{2.7}$$

where: $\sigma_{eq} = \sqrt{\frac{3}{2}\boldsymbol{\sigma}' : \boldsymbol{\sigma}'}$, $\boldsymbol{\sigma}' = \boldsymbol{\sigma} - \sigma_m \mathbf{1}$ and $\sigma_m = \frac{tr\boldsymbol{\sigma}}{3}$ are, respectively, the local equivalent, deviatoric and mean stresses inside the solid phase. σ_0 denotes the initial plastic threshold in pure shearing (σ_m=0) and α, the coefficient describing pressure sensitivity. The latter is related to the internal friction angle ψ by:

$$\tan\ \psi = 3\alpha \tag{2.8}$$

To describe the effective plastic behavior of the porous clay matrix, we use the analytical closed-form strength criterion, established by [Shen et al., 2017], for a porous

© 2018 Tous droits réservés.

lilliad.univ-lille.fr

medium with a Drucker-Prager type matrix and spherical pores, given as follows:

$$\Phi = \frac{\frac{\tilde{\sigma}_{eq}^2}{\sigma_0^2}}{\left[1-\frac{3\alpha}{(1-f)}\frac{\tilde{\sigma}_m}{\sigma_0}\right]^2} + 2f\cosh\left[\frac{2\alpha+sgn(\tilde{\sigma}_m)}{2\alpha}\ln\left(1-3\alpha\frac{\tilde{\sigma}_m}{\sigma_0}\right)\right] - 1 - f^2 = 0 \tag{2.9}$$

where f is the interparticle porosity in the clay matrix given in equation 2.1. $\tilde{\boldsymbol{\sigma}}$ denotes the stress in the porous clay matrix, $\tilde{\sigma}_m$=tr$\tilde{\boldsymbol{\sigma}}/3$ the hydrostatic stress, $\tilde{\sigma}_{eq} = \sqrt{\frac{3}{2}\tilde{\boldsymbol{\sigma}}' : \tilde{\boldsymbol{\sigma}}'}$ the equivalent deviatoric stress in which $\tilde{\boldsymbol{\sigma}}' = \tilde{\boldsymbol{\sigma}} - \tilde{\sigma}_m\mathbf{1}$ represents the deviatoric stress tensor.

The effective plastic yield function, given in equation 2.9, is now applied to describe the plastic behavior of the clay matrix by taking into account the effect of porosity. According to experimental observations of Vaca Muerta shale, one can notice that the material exhibits significant plastic hardening (figure 1.14). This process is treated by assuming that the yield stress of clay matrix solid phase increases with plastic deformation. Thus, the initial yield threshold stress σ_0 in equation 2.7 is substituted by $\bar{\sigma}$, the current yield stress. Therefore, the plastic criterion, given in equation 2.9, is rewritten as follows:

$$\Phi(\tilde{\boldsymbol{\sigma}}, \bar{\sigma}, f) = \frac{\frac{\tilde{\sigma}_{eq}^2}{\bar{\sigma}^2}}{\left[1-\frac{3\alpha}{(1-f)}\frac{\tilde{\sigma}_m}{\bar{\sigma}}\right]^2} + 2f\cosh\left(\frac{2\alpha+sgn(\tilde{\sigma}_m)}{2\alpha}\ln\left(1-3\alpha\frac{\tilde{\sigma}_m}{\bar{\sigma}}\right)\right) - 1 - f^2 = 0 \tag{2.10}$$

The continuous evolution of hardening is often described either by a hyperbolic or exponential law verifying the initial and asymptotic conditions. As in [Guéry, 2007] and [Shen et al., 2012], the following exponential form of the hardening law is adopted in our study:

$$\bar{\sigma} = \sigma_{0m} - (\sigma_{0m} - \sigma_{00})e^{-b\varepsilon^p} \tag{2.11}$$

where σ_{00} is the initial yield stress of clay and σ_{0m}, the asymptotic value of the yield stress. ε^p denotes the equivalent plastic strain of the solid clay phase.

As the plastic deformation of the solid phase is assumed to be governed by an associated flow rule, the plastic flow of the clay matrix is given by the normality rule as follows:

$$\tilde{\mathbf{d}}^p = \dot{\lambda}\frac{\partial\Phi}{\partial\tilde{\boldsymbol{\sigma}}}(\tilde{\boldsymbol{\sigma}}, \bar{\sigma}, f) \tag{2.12}$$

where $\tilde{\mathbf{d}}^p$ is the plastic strain rate of the porous clay matrix. The plastic multiplier $\dot{\lambda}$ is determined through the consistency condition (equation 2.13) and checks the loading-unloading conditions (equation 2.14):

$$\dot{\Phi} = \frac{\partial\Phi}{\partial\tilde{\boldsymbol{\sigma}}} : \dot{\tilde{\boldsymbol{\sigma}}} + \frac{\partial\Phi}{\partial f} : \dot{f} + \frac{\partial\Phi}{\partial\bar{\sigma}} : \frac{\partial\bar{\sigma}}{\partial\varepsilon^p}\dot{\varepsilon}^p = 0 \tag{2.13}$$

© 2018 Tous droits réservés.

lilliad.univ-lille.fr

$$\begin{cases} \dot{\lambda} = 0 \quad \text{if } \Phi < 0 \quad \text{or if } \Phi = 0 \quad \text{and} \quad \dot{\Phi} < 0 \\ \dot{\lambda} \geq 0 \qquad\qquad\qquad\qquad \text{if } \Phi = 0 \text{ and } \dot{\Phi} = 0 \end{cases} \tag{2.14}$$

To obtain the explicit expression of the equivalent plastic strain rate of the solid clay phase $\dot{\varepsilon}^p$, [Shen et al., 2012] have used an energy-based condition for the case of a Drucker-Prager solid phase, which relates the plastic strain rate of the clay matrix to that of the solid phase [Gurson, 1977]. One obtains:

$$(1-f)\bar{\sigma}\dot{\varepsilon}^p = \tilde{\boldsymbol{\sigma}} : \tilde{\mathbf{d}}^p \tag{2.15}$$

Thus, using the associated flow rule, one gets:

$$\dot{\varepsilon}^p = \frac{\tilde{\boldsymbol{\sigma}} : \frac{\partial \Phi}{\partial \tilde{\boldsymbol{\sigma}}}}{(1-f)\bar{\sigma}} \dot{\lambda} \tag{2.16}$$

The evolution law of the porosity is determined by imposing a kinematical compatibility [Shen et al., 2012] and is given as follows:

$$\dot{f} = (1-f)(\mathrm{tr}\tilde{\mathbf{d}}^p - 3\alpha\dot{\varepsilon}^p) \tag{2.17}$$

The explicit form of the plastic multiplier can now be identified by replacing equations 2.16 and 2.17 in the consistency condition 2.13. One obtains:

$$\dot{\lambda} = \frac{\frac{\partial \Phi}{\partial \tilde{\boldsymbol{\sigma}}} : \mathbb{C}_0 : \tilde{\mathbf{d}}}{\frac{\partial \Phi}{\partial \tilde{\boldsymbol{\sigma}}} : \mathbb{C}_0 : \frac{\partial \Phi}{\partial \tilde{\boldsymbol{\sigma}}} - \frac{\partial \Phi}{\partial f}(1-f)\left[\frac{\partial \Phi}{\partial \tilde{\sigma}_m} - 3\alpha \frac{\tilde{\boldsymbol{\sigma}} : \frac{\partial \Phi}{\partial \tilde{\boldsymbol{\sigma}}}}{(1-f)\bar{\sigma}}\right] - \frac{\partial \Phi}{\partial \bar{\sigma}} \frac{\partial \bar{\sigma}}{\partial \varepsilon^p} \frac{\tilde{\boldsymbol{\sigma}} : \frac{\partial \Phi}{\partial \tilde{\boldsymbol{\sigma}}}}{(1-f)\bar{\sigma}}} \tag{2.18}$$

where $\tilde{\mathbf{d}} = \tilde{\mathbf{d}}^e + \tilde{\mathbf{d}}^p$ is the total strain rate of the porous clay matrix. $\mathbb{C}_0 = 3\kappa_0 \mathbb{J} + 2\mu_0 \mathbb{K}$ is the effective elastic tensor of the porous clay matrix.

The effective tangent stiffness operator of the porous clay matrix $\mathbb{L}_0$ writes:

$$\mathbb{L}_0 = \begin{cases} \mathbb{C}_0 & \text{if } \Phi(\tilde{\boldsymbol{\sigma}}, f, \bar{\sigma}) \leq 0, \dot{\Phi}(\tilde{\boldsymbol{\sigma}}, f, \bar{\sigma}) < 0 \\ \mathbb{C}_0 - \frac{\mathbb{C}_0 : \frac{\partial \Phi}{\partial \tilde{\boldsymbol{\sigma}}} \otimes \frac{\partial \Phi}{\partial \tilde{\boldsymbol{\sigma}}} : \mathbb{C}_0}{H^d} & \text{if } \Phi(\tilde{\boldsymbol{\sigma}}, f, \bar{\sigma}) = 0, \dot{\Phi}(\tilde{\boldsymbol{\sigma}}, f, \bar{\sigma}) = 0 \end{cases} \tag{2.19}$$

H^d is given by:

$$H^d = \frac{\partial \Phi}{\partial \tilde{\boldsymbol{\sigma}}} : \mathbb{C}_0 : \frac{\partial \Phi}{\partial \tilde{\boldsymbol{\sigma}}} - \frac{\partial \Phi}{\partial f}(1-f)\left[\frac{\partial \Phi}{\partial \tilde{\sigma}_m} - 3\alpha \frac{\tilde{\boldsymbol{\sigma}} : \frac{\partial \Phi}{\partial \tilde{\boldsymbol{\sigma}}}}{(1-f)\bar{\sigma}}\right] - \frac{\partial \Phi}{\partial \bar{\sigma}} \frac{\partial \bar{\sigma}}{\partial \varepsilon^p} \frac{\tilde{\boldsymbol{\sigma}} : \frac{\partial \Phi}{\partial \tilde{\boldsymbol{\sigma}}}}{(1-f)\bar{\sigma}}$$

By calculating the derivatives of the yield function 2.10, the tangent stiffness tensor of the clay matrix can be rewritten as:

$$\mathbb{L}_0 = 3\kappa_1 \mathbb{J} + 2\kappa_2 \mathbb{K} - \kappa_3 \mathbf{1} \otimes \tilde{\boldsymbol{\sigma}}' - \kappa_4 \tilde{\boldsymbol{\sigma}}' \otimes \mathbf{1} - \kappa_5 \tilde{\boldsymbol{\sigma}}' \otimes \tilde{\boldsymbol{\sigma}}' \tag{2.20}$$

where κ_i, i=1-5, are equal to:

© 2018 Tous droits réservés.

lilliad.univ-lille.fr

$$\kappa_1 = \kappa_0 - \frac{9\kappa_0^2 B^2}{H^d}, \quad \kappa_2 = \mu_0, \quad \kappa_3 = \kappa_4 = \frac{6\kappa_0\mu_0 AB}{H^d} \quad \kappa_5 = \frac{4\mu_0^2 A^2}{H^d}$$

and:

$$A = \frac{3\left(1+\frac{3\tilde{\sigma}_m\alpha}{(1-f)\bar{\sigma}-3\tilde{\sigma}_m\alpha}\right)^2}{\bar{\sigma}^2} \tag{2.21}$$

$$B = \frac{-f[\bar{\sigma}(f-1)+3\tilde{\sigma}_m\alpha]^3[2\alpha+sgn(\tilde{\sigma}_m)]\sinh\left[\frac{(2\alpha+sgn(\tilde{\sigma}_m)\ln\left(1-\frac{3\alpha\tilde{\sigma}_m}{\bar{\sigma}}\right)}{2\alpha}\right]-2\tilde{\sigma}_{eq}^2\alpha(f-1)^2(\bar{\sigma}-3\tilde{\sigma}_m\alpha)}{[\bar{\sigma}(f-1)+3\tilde{\sigma}_m\alpha]^3(\bar{\sigma}-3\tilde{\sigma}_m\alpha)} \tag{2.22}$$

This associated plastic model is then incorporated in the micro-meso and meso-macro transitions.

Finally, we evaluate the influence of the two parameters (α and σ_0) and the porosity f on the microscopic mechanical response of the porous clay matrix. The reference values of the late parameters used are: f=0.1, α=0.1 and σ_0=10. Figures 2.8 and 2.9 show, respectively, the influence of pressure sensitivity coefficient α and strength parameter σ_0 of the solid phase on the microscopic response of the porous clay matrix. With the change of parameters, the hydrostatic and shear compression strengths are more influenced than the tensile ones.

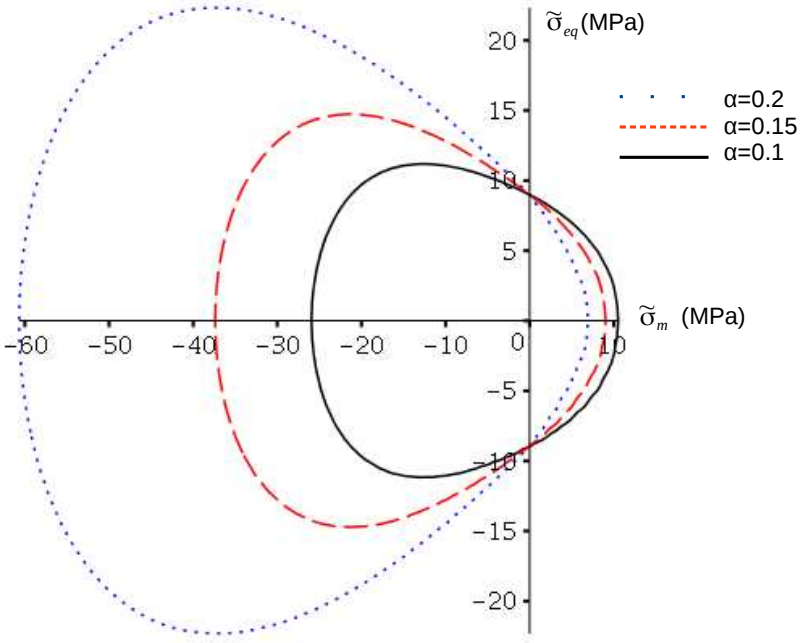

Figure 2.8: Effect of pressure sensitivity coefficient α on the microscopic failure criterion 2.10.

Figure 2.10 exhibits the influence of interparticle porosity f on the microscopic failure criterion 2.10. It is clearly shown that with the increase of porosity, the hydrostatic compression strength is substantially reduced. The effect of increasing porosity is less

© 2018 Tous droits réservés.

lilliad.univ-lille.fr

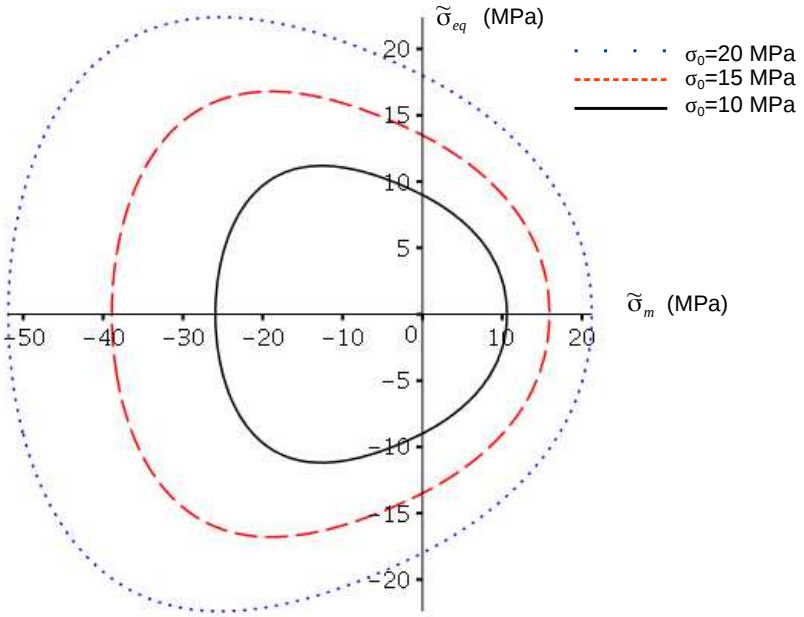

Figure 2.9: Effect of the matrix strength σ_0 on the microscopic failure criterion 2.10.

important on the microscopic hydrostatic tensile strength.

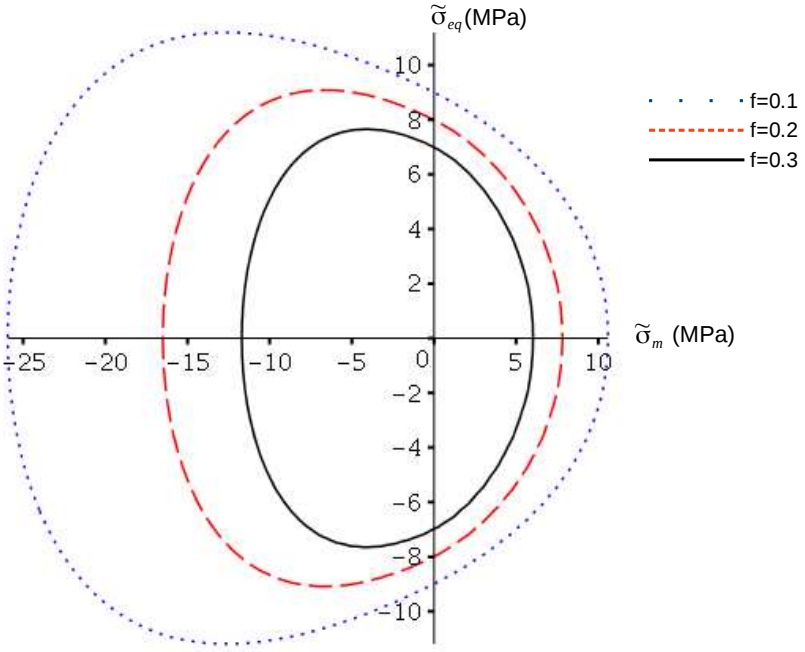

Figure 2.10: Effect of interparticle porosity f on the microscopic failure criterion 2.10.

It can be noted that the microscopic failure criterion 2.10, which is function of porosity f, is locked at the compression part of stress space (<0). This means that important plastic strain can be produced under hydrostatic compression loading. Thus, compared to the classical Drucker-Prager linear surface (figure 2.11), the microscopic plastic criterion 2.10 of the porous clay matrix is able to treat plasticity under hydrostatic loading that are experimentally observed in rocks with high porosity. Since

© 2018 Tous droits réservés.

lilliad.univ-lille.fr

these parameters directly influence the microscopic response of the clay matrix, then they will affect the macroscopic behavior of the studied material.

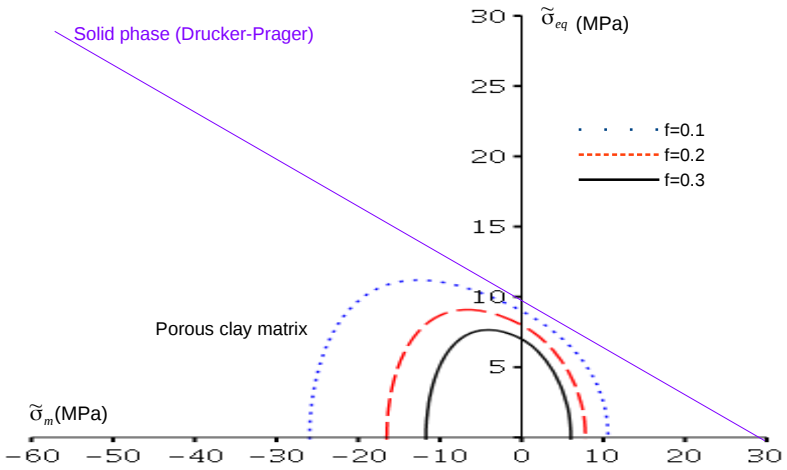

Figure 2.11: Comparison between Drucker-Prager solid phase and porous clay matrix criteria.

2.3.1.2 Effect of fine and meso inclusions

After having exposed the analytical plastic criterion, which describes the elastoplastic behavior of the porous clay matrix, the effects of fine and mesoinclusions on the macroscopic behavior of the studied shale will be considered. For the description of non-linear behavior of heterogeneous materials, various homogenization methods have been proposed, among them, [Hill, 1965] incremental method. The latter, which is based on the concept of "linear comparison composite", allows to incrementally linearize the problem of non linear homogenization and is based on linear homogenization scheme estimates. The method is able to figure different types of inclusions at the same scale (micro and meso scales, figure 2.7) and to be applied to arbitrary loading paths. According to Vaca Muerta microstructure, different types of inclusions, with scattered elastic properties, can be found at the same scale. In this case, it is difficult to establish an explicit criterion for this type of microstructure. Thus, Hill's incremental method is used twice in this model, to account firstly for fine grains at microscale and then, to consider the effect of various mesoinclusions at mesoscale. The principle of this method and the assumptions established for its application are first discussed. Then, we talk about its use for the formulation of our micromechanical model.

© 2018 Tous droits réservés.

lilliad.univ-lille.fr

[Hill, 1965] approach requires a rate formulation of constitutive relation for each constituent phase, as follows:

$$\dot{\boldsymbol{\sigma}}(\underline{z}) = \mathbb{L}(\underline{z}) : \dot{\boldsymbol{\varepsilon}}(\underline{z}) \tag{2.23}$$

Equation 2.23 links the strain rate $\dot{\boldsymbol{\varepsilon}}$ to the stress rate $\dot{\boldsymbol{\sigma}}$ by means of the tangent stiffness operator $\mathbb{L}$. As for the case of linear elasticity, a tangent localization tensor $\mathbb{A}$ of the linear comparison composite can be introduced, at each iteration step, to link the macroscopic strain rate $\dot{\mathbf{E}}$ to the local one $\dot{\boldsymbol{\varepsilon}}$:

$$\dot{\boldsymbol{\varepsilon}}(\underline{z}) = \mathbb{A}(\underline{z}) : \dot{\mathbf{E}} \tag{2.24}$$

Consequently, the rate form of the macroscopic constitutive relations reads:

$$\dot{\boldsymbol{\Sigma}} = \mathbb{L}^{hom} : \dot{\mathbf{E}} \tag{2.25}$$

where the effective tangent stiffness operator is given by:

$$\mathbb{L}^{hom} = < \mathbb{L} : \mathbb{A} > \tag{2.26}$$

The main steps of non linear homogenization for Hill's incremental method can be summarized in figure 2.12.

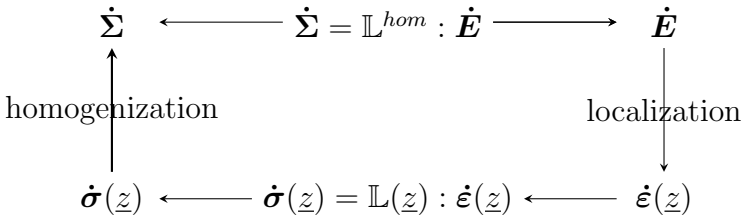

Figure 2.12: Diagram of non linear homogenization with Hill's incremental approach.

As we can see in equation 2.26, $\mathbb{L}^{hom}$ is obtained as the average over the representative elementary volume of the product of the local tangent stiffness and tangent strain localization tensor. As the local tangent stiffness is not uniform in each phase, [Hill, 1965] incremental method involves making some simplifications in order to fit out a closed-form expression of $\mathbb{L}^{hom}$. To this end, at any point $\underline{z}$ of a given phase (r), the local constitutive relation is approximated by:

$$\forall \underline{z} \in (r), \dot{\boldsymbol{\sigma}}(\underline{z}) = \mathbb{L}_r : \dot{\boldsymbol{\varepsilon}}(\underline{z}) \tag{2.27}$$

where $\mathbb{L}_r$ is the local tangent stiffness of a given phase (r), evaluated for a suitable chosen reference state of strain $\boldsymbol{\varepsilon}_r$ (mostly corresponding to the average local strain

© 2018 Tous droits réservés.
lilliad.univ-lille.fr

field of the phase (r)). This approximation leads to the assumption that each phase has a uniform tangent stiffness. Following this approximation, the incremental strain localization relation will be of the following form:

$$\dot{\bar{\boldsymbol{\varepsilon}}}_r = \mathbb{A}_r : \dot{\mathbf{E}} \tag{2.28}$$

where $\mathbb{A}_r$ is the tangent localization operator corresponding to the average strain per phase $\dot{\bar{\boldsymbol{\varepsilon}}}_r$.

Now, we determine the explicit form of the tangent localization operator $\mathbb{A}_r$ which makes it possible to deduce the homogenized tangent operator $\mathbb{L}^{hom}$, given by:

$$\mathbb{L}^{hom} = \sum_r f_r \mathbb{L}_r : \mathbb{A}_r \tag{2.29}$$

where f_r is the volumetric fraction of phase r.

To determine the expression of $\mathbb{A}_r$, a suitable linear homogenization method should be used. By assuming that the morphology of the linear comparison composite is similar to that of the studied Vaca Muerta shale, thus, [Mori and Tanaka, 1973] scheme is involved for the evaluation of the tangent strain localization operator $\mathbb{A}_r$. One obtains:

$$\mathbb{A}_r = [\mathbb{I} + \mathbb{P}^0_{I_r} : (\mathbb{L}_r - \mathbb{L}_0)]^{-1} : \left(\sum_{s=0}^{N} f_s \mathbb{A}^0_s \right)^{-1} \tag{2.30}$$

$\mathbb{P}^0_{I_r}$ denotes the fourth order Hill tensor which depends on the inclusion form I_r, its orientation as well as the tangent stiffness of the matrix phase of the linear comparison composite $\mathbb{L}_0$. The general expression of $\mathbb{P}^0_{I_r}$ is written using the Green function G^0_∞ in the form:

$$P^0_{I_{rinjk}} = -\left(\int_{I_r} G^0_{\infty ij}(\underline{x} - \underline{y}) dy \right)_{kl_{(il)(jk)}} \qquad \forall \underline{x} \in I_r \tag{2.31}$$

Besides, $\mathbb{P}^0_{I_r}$ can be written in function of Eshelby's tensor $\mathbb{S}^E$. As all inclusions for our material are supposed having the same morphology, Hill's tensor is given as follows:

$$\mathbb{P}^0_I = \mathbb{S}^E(\mathbb{L}_0) : \mathbb{L}_0^{-1} \tag{2.32}$$

$\mathbb{P}^0_I$ can be calculated either analytically or numerically. In the case of local and global isotropy, the analytical expression of $\mathbb{P}^0_I$ is explicitly known and given as follows:

$$\mathbb{P}^0_I = \frac{\beta_0}{2\mu_0}\mathbb{K} + \frac{\alpha_0}{3\kappa_0}\mathbb{J} \tag{2.33}$$

© 2018 Tous droits réservés.

lilliad.univ-lille.fr

with $\alpha_0 = \frac{3\kappa_0}{3\kappa_0+4\mu_0}$, $\beta_0 = \frac{6(\kappa_0+2\mu_0)}{5(3\kappa_0+4\mu_0)}$; κ_0 and μ_0 are respectively the bulk and shear moduli of the matrix phase. However, when the tangent stiffness of the matrix is anisotropic, the analytical expression of Green's function is not known. Thus $\mathbb{P}_I^0$ is evaluated numerically by using a Gauss type integration procedure (for more details, see [Guéry, 2007]). Note that, in our case, [Hill, 1965] homogenization procedure is applied twice: first, to homogenize the fine grains of calcite and kerogen, and then, the mesoinclusions.

The application of Hill's incremental method, in the framework of metals [Doghri and Ouaar, 2003] and geomaterials ([Guéry, 2007] and [Shen et al., 2012]), yields a too stiff macroscopic response compared to finite element simulations. As already seen, Hill's method is based on the hypothesis of uniform local tangent stiffness in each phase. Thus, the main reason of the stiff response would be the accumulation of errors at each increment caused by the failure to adequately take into account the strain heterogeneity within phases. ([Doghri and Ouaar, 2003] and [Guéry, 2007]) indicate that it is possible to relax the predictions of the incremental method by considering an Eshelby's tensor estimated from an isotropic approximation of the tangent operator of the matrix. The isotropization procedure has been confirmed by ([Guéry, 2007] and [Shen et al., 2012]) to reproduce the macroscopic response of Callovo-Oxfordian argillite. Therefore, the same isotropization procedure will be adopted in this model.

As already seen, the tangent stiffness tensor of the clay matrix is anisotropic (equation 2.20). To obtain its isotropic part, we use the general method of isotropization proposed by [Bornert et al., 2001a]:

$$\mathbb{L}_0^{iso} = (\mathbb{J} :: \mathbb{L}_0)\mathbb{J} + \frac{1}{5}(\mathbb{K} :: \mathbb{L}_0)\mathbb{K} = 3\kappa_i\mathbb{J} + 2\mu_i\mathbb{K} \tag{2.34}$$

where:

$$\kappa_i = \kappa_0(1 - \frac{9\kappa_0 B^2}{H^d}), \quad \mu_i = \mu_0(1 - \frac{2\mu_0 A^2}{5H^d}\tilde{\sigma}_{eq}^2) \tag{2.35}$$

Since we know the isotropic expression of $\mathbb{L}_0$ and as the inclusions are supposed to be spherical, the analytical expression of Eshelby's tensor can be written as follows:

$$\mathbb{S}^E(\mathbb{L}_0^{iso}) = \frac{3\kappa_i}{3\kappa_i + 4\mu_i}\mathbb{J} + \frac{6}{5}\frac{\kappa_i + 2\mu_i}{3\kappa_i + 4\mu_i}\mathbb{K} \tag{2.36}$$

Figure 2.13 shows the comparison between the macroscopic response without and with isotropization in the case of a uniaxial compression test. One can notice that the isotropization procedure makes it possible to obtain a soft macroscopic response. Given these recent results, it would seem that despite the above hypothesis, the incremental approach, via the implementation of an isotropization procedure, opens

© 2018 Tous droits réservés.

lilliad.univ-lille.fr

possibilities for the study of non-linear behavior of heterogeneous materials on multiaxial loading paths. Note that Hill's incremental method has the advantage to take into consideration several inclusions at a homogenization scale in line with the expectations related to our representative elementary volume.

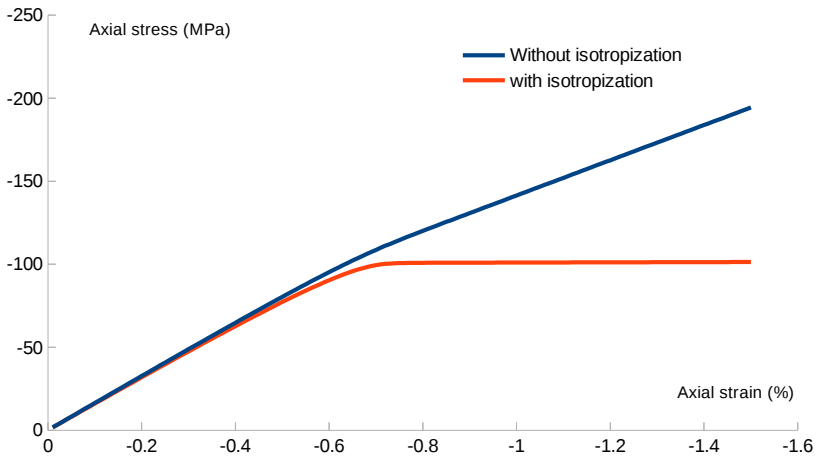

Figure 2.13: Macroscopic response in the case of a uniaxial compression test with and without isotropization of matrix tangent stiffness tensor.

2.3.2 Interfacial debonding between matrix and inclusions

After having exposed the micromechanical model of the elastoplastic behavior of the heterogeneous rock, we study in this paragraph the material damage at short term. We assumed that the instantaneous damage evolution is related to complete interfacial debonding between the matrix and inclusions. Initially, inclusions are supposed embedded firmly in the matrix with perfect interfaces. Several works have been dedicated to study the damage induced by the complete or partial progressive debonding between particles and matrix ([Tohgo and Weng, 1994], [Zhao and Weng, 1995], [Ju and Lee, 2000], [Dai and Huang, 2001] and [Shen and Shao, 2015]). Under the increase of external mechanical loading and since the material is heterogeneous, local stress concentrations may be developed at inclusion interfaces. In our study, we assume that some inclusions could undergo complete interfacial debonding and are assumed to become voids for the sake of simplicity. We consider that the spherical voids obtained from the debonding process are isotropically dispersed in the matrix. Thus, the interfacial debonding of mineral inclusions will significantly affect the overall macroscopic behavior of a heterogeneous material since completely debonded mineral inclusions will be replaced by pores. Therefore, the total porosity of the material increases and rigid inclusions volume decreases.

As we have evoked in figure 2.7, Vaca Muerta shale is seen as a heterogeneous material: at mesoscale, several mineral inclusions (quartz, calcite, pyrite and kerogen)

© 2018 Tous droits réservés.
lilliad.univ-lille.fr

are immersed in a composite matrix. The latter is constituted of fine calcite and kerogen which are embedded in a porous clay matrix. As we can see, several types of inclusions are considered at two different homogenization scales. Thus, all rigid inorganic inclusions can be subjected to interfacial debonding but probably the large inclusions more. Interfaces between organic matter and matrix will not undergo damage as organic matter is soft. For lack of microstructural observations of interfaces between inclusions and matrix, it is difficult to indicate which particles will be subjected to interfacial decohesion. In our model, by using Hill's incremental scheme as homogenization method, we are able to consider the interfacial debonding of several types of inclusions at the same time (a sensitivity study is shown later). For the sake of simplicity, since the calcite grains on the mesoscale are probably the most voluminous, it is assumed that the interfaces between the latter and matrix are damaged. Figure 2.14 shows the schematic representation of calcite debonding process at mesoscale. The left scheme correspond to the initial undamaged state where all calcite particles are perfectly bonded to the composite matrix. Under the increase of external macroscopic loading, some calcite particles are completely debonded and become voids (figure 2.14.b). The right scheme represents the state where all calcite grains are completely debonded.

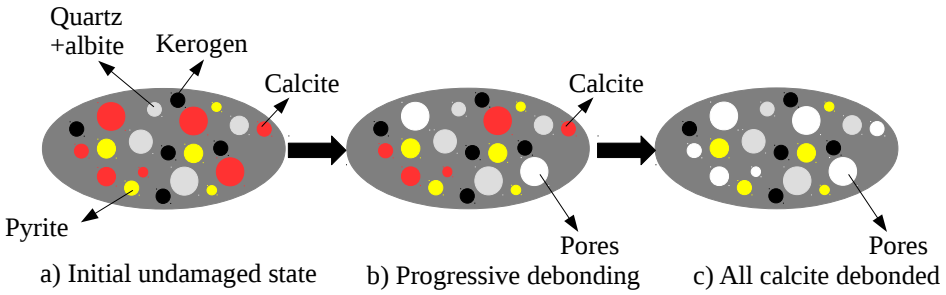

Figure 2.14: Schematic representation of calcite debonding process at mesoscale.

To describe the varying probability of inclusion debonding, [Weibull, 1951] statistical function is used. The equivalent plastic strain of the porous clay matrix ε_0^p will be used as the controlling factor of the particle-matrix debonding process. For compressive loading (civil engineering application), [Weibull, 1951] cumulative distribution function of particle debonding is given as follow:

$$P_d[\varepsilon_0^p] = 1 - \exp\left[-\left(\frac{\varepsilon_0^p}{S}\right)^M\right] \tag{2.37}$$

where $\varepsilon_0^p = \sqrt{\tilde{\boldsymbol{\varepsilon}}_0^p : \tilde{\boldsymbol{\varepsilon}}_0^p}$, $\tilde{\boldsymbol{\varepsilon}}_0^p$ is the plastic strain inside the porous clay matrix ; S and M are Weibull shape and scale parameters respectively. In this manner, this probability will monitor the volume fraction of completely debonded calcite particles which will

© 2018 Tous droits réservés.

lilliad.univ-lille.fr

be written as:

$$f_1^d = f_1^{ini} P_d[\varepsilon_0^p] = f_1^{ini} \left\{ 1 - \exp\left[- \left(\frac{\varepsilon_0^p}{S} \right)^M \right] \right\} \tag{2.38}$$

with f_1^{ini} the initial calcite volume fraction; f_1^d, the volume of completely debonded calcite which is equivalent to the current volume of obtained mesoscopic pores. Thus, the current volume of calcite particles is: $f_1 = f_1^{ini} - f_1^d$.

2.3.3 Numerical implementation and assessment

2.3.3.1 Numerical implementation

In this paragraph, the numerical implementation of the proposed micromechanical model is exposed. The model presented above is implemented in an integration code 'Valrock' developed in our laboratory. The loading path is divided into a limit number of steps. At the step n+1, the material point at the macroscopic scale is subjected to a macroscopic strain $E_{n+1} = E_n + \Delta E$, while the strain at the step n is known and the strain increment ΔE is given. The problem to be solved here is to find the corresponding macroscopic stress state at the end of the loading step by using Hill's incremental homogenization method. Note that mesopores (phase m) represent the pores created by the interfacial debonding of mesocalcite grains. The general algorithm for integrating the (n+1) load increment is as follows:

1. **Begin Hill 1**

   Input data: $\boldsymbol{E}_n$, $\Delta \boldsymbol{E}$;
   Calcite (phase 1): $\tilde{\boldsymbol{E}}_{1,n}$, $\tilde{\boldsymbol{\Sigma}}_{1,n}$;
   Quartz (phase 2): $\tilde{\boldsymbol{E}}_{2,n}$, $\tilde{\boldsymbol{\Sigma}}_{2,n}$;
   Pyrite (phase 3): $\tilde{\boldsymbol{E}}_{3,n}$, $\tilde{\boldsymbol{\Sigma}}_{3,n}$;
   Kerogen (phase 4): $\tilde{\boldsymbol{E}}_{4,n}$, $\tilde{\boldsymbol{\Sigma}}_{4,n}$;
   Mesopores (phase m): $\tilde{\boldsymbol{E}}_{m,n}$.
   Composite matrix (phase $0'$): $\tilde{\boldsymbol{E}}_{0',n}$;

2. Initially, the local strain increments in the phases (1), (2), (3), (4) and (m) are set equal to the macroscopic strain increment:

$$\Delta \tilde{\boldsymbol{E}}_1^0 = \Delta \boldsymbol{E}, \quad \Delta \tilde{\boldsymbol{E}}_2^0 = \Delta \boldsymbol{E}, \quad \Delta \tilde{\boldsymbol{E}}_3^0 = \Delta \boldsymbol{E}, \quad \Delta \tilde{\boldsymbol{E}}_4^0 = \Delta \boldsymbol{E}, \quad \Delta \tilde{\boldsymbol{E}}_m^0 = \Delta \boldsymbol{E}$$

3. Then, we calculate the local strains at the loading step (n+1) for phases (1), (2), (3), (4) and (m):

$$\tilde{\boldsymbol{E}}_{1,n+1} = \tilde{\boldsymbol{E}}_{1,n} + \Delta \tilde{\boldsymbol{E}}_1^i, \quad \tilde{\boldsymbol{E}}_{2,n+1} = \tilde{\boldsymbol{E}}_{2,n} + \Delta \tilde{\boldsymbol{E}}_2^i,$$

© 2018 Tous droits réservés.
lilliad.univ-lille.fr

$$\tilde{\boldsymbol{E}}_{3,n+1} = \tilde{\boldsymbol{E}}_{3,n} + \Delta\tilde{\boldsymbol{E}}_3^i, \quad \tilde{\boldsymbol{E}}_{4,n+1} = \tilde{\boldsymbol{E}}_{4,n} + \Delta\tilde{\boldsymbol{E}}_4^i \quad \tilde{\boldsymbol{E}}_{m,n+1} = \tilde{\boldsymbol{E}}_{m,n} + \Delta\tilde{\boldsymbol{E}}_m^i$$

As the mesoinclusions have elastic behavior, its local stiffness tensors: $\mathbb{L}_1$, $\mathbb{L}_2$, $\mathbb{L}_3$ and $\mathbb{L}_4$ are known and equal to the elastic ones. Note that for mesopores: κ_m=μ_m=0.

4. The average local strain in the composite matrix is given by:

$$\Delta\tilde{\boldsymbol{E}}_{0'}^i = \frac{\Delta\boldsymbol{E} - f_1\Delta\tilde{\boldsymbol{E}}_1^i - f_2\Delta\tilde{\boldsymbol{E}}_2^i - f_3\Delta\tilde{\boldsymbol{E}}_3^i - f_4\Delta\tilde{\boldsymbol{E}}_4^i - f_1^d\Delta\tilde{\boldsymbol{E}}_m^i}{1 - f_1 - f_2 - f_3 - f_4 - f_1^d}$$

where f_r is the volumetric fraction of phase (r).

5. Let $\Delta\tilde{\boldsymbol{\varepsilon}}$=$\Delta\tilde{\boldsymbol{E}}_{0'}^i$ (mesoscopic strain increment=local strain in the composite matrix).

6. **Begin Hill 2**

Input data: $\Delta\tilde{\boldsymbol{\varepsilon}}$;
Fine kerogen (phase 5): $\tilde{\boldsymbol{\varepsilon}}_{5,n}$, $\tilde{\boldsymbol{\sigma}}_{5,n}$;
Fine calcite (phase 6): $\tilde{\boldsymbol{\varepsilon}}_{6,n}$, $\tilde{\boldsymbol{\sigma}}_{6,n}$;
Clay matrix (phase 0): $\tilde{\boldsymbol{\varepsilon}}_{0,n}$, $\tilde{\boldsymbol{\varepsilon}}_{0,n}^p$, ε_n^p, $\tilde{\boldsymbol{\sigma}}_n$;

6.1. Initially, the local strain increments in the phases (5) and (6) are set equal to the mesoscopic strain increment:

$$\Delta\tilde{\boldsymbol{\varepsilon}}_5^0 = \Delta\tilde{\boldsymbol{\varepsilon}}, \quad \Delta\tilde{\boldsymbol{\varepsilon}}_6^0 = \Delta\tilde{\boldsymbol{\varepsilon}}$$

6.2. Then, we calculate the local strains at the loading step (n+1) for phases (5) and (6):

$$\tilde{\boldsymbol{\varepsilon}}_{5,n+1} = \tilde{\boldsymbol{\varepsilon}}_{5,n} + \Delta\tilde{\boldsymbol{\varepsilon}}_5^j, \quad \tilde{\boldsymbol{\varepsilon}}_{6,n+1} = \tilde{\boldsymbol{\varepsilon}}_{6,n} + \Delta\tilde{\boldsymbol{\varepsilon}}_6^j$$

6.3. Thus, the average local strain in the clay matrix is given by:

$$\Delta\tilde{\boldsymbol{\varepsilon}}_0^j = \frac{\Delta\tilde{\boldsymbol{\varepsilon}} - f_5\Delta\tilde{\boldsymbol{\varepsilon}}_5^j - \Delta\tilde{\boldsymbol{\varepsilon}}_6^j}{1 - f_5 - f_6}$$

6.4. At the iteration j for the phase 0, the values of $\Delta\tilde{\boldsymbol{\varepsilon}}_0^j$, $\tilde{\boldsymbol{\varepsilon}}_{0,n}$, $\tilde{\boldsymbol{\varepsilon}}_{0,n}^p$ and ε_n^p are known, $\tilde{\boldsymbol{\varepsilon}}_{0,n+1}$, $\tilde{\boldsymbol{\varepsilon}}_{0,n+1}^p$, ε_{n+1}^p, $\mathbb{L}_0^j$ and $\mathbb{L}_0^{iso,j}$ are calculated according to analytical plastic model given in paragraph 2.3.1.1. The algorithm for local integration of the elastoplastic clay phase is given in Appendix A.

6.5. Since the fine calcite and kerogen grains have the same morphology, thus Hill's tensor is given by:

$$\mathbb{P}_{I_5}^{0,j} = \mathbb{P}_{I_6}^{0,j} = \mathbb{P}_I^{0,j} = \mathbb{S}^E(\mathbb{L}_0^{iso,j}) : \mathbb{L}_0^j$$

Note that we use the isotropic form of clay tangent stiffness tensor ($\mathbb{L}_0^{iso}$), thus Eshelby's tensor can be calculated as in equation 2.36.

© 2018 Tous droits réservés.
lilliad.univ-lille.fr

6.6. The tangent strain localization tensors $\mathbb{A}_r^j$ for phases (0), (5) and (6) are given respectively as follows:

$$\mathbb{A}_0^j = [f_0\mathbb{I} + f_5\mathbb{A}_5^{0,j} + f_6\mathbb{A}_6^{0,j}]^{-1}; \quad \mathbb{A}_5^j = \mathbb{A}_5^{0,j} : \mathbb{A}_0^j; \quad \mathbb{A}_6^j = \mathbb{A}_6^{0,j} : \mathbb{A}_0^j$$

where $\mathbb{A}_r^{0,j} = [\mathbb{I} + \mathbb{P}_I^{0,j} : (\mathbb{L}_r^j - \mathbb{L}_0^j)]^{-1}$ for r=5, 6.

6.7. We check the compatibility of local strains between two iterations for phases (5) and (6). If the compatibility is reached ($\|\boldsymbol{R}_5^j\| <$ tol5 and $\|\boldsymbol{R}_6^j\| <$ tol6; tol5=tol6=10^{-10}), we passed to step 6.8.; else, an additional iteration is needed (back to step 6.2. with j=j+1) with:

$$\Delta\tilde{\boldsymbol{\varepsilon}}_5^{j+1} = \Delta\tilde{\boldsymbol{\varepsilon}}_5^j + \boldsymbol{R}_5^j; \quad \Delta\tilde{\boldsymbol{\varepsilon}}_6^{j+1} = \Delta\tilde{\boldsymbol{\varepsilon}}_6^j + \boldsymbol{R}_6^j$$

where the errors $\boldsymbol{R}_r$ are given by: $\boldsymbol{R}_5^j = \mathbb{A}_5^j : \Delta\tilde{\boldsymbol{\varepsilon}} - \Delta\tilde{\boldsymbol{\varepsilon}}_5^j$ and $\boldsymbol{R}_6^j = \mathbb{A}_6^j : \Delta\tilde{\boldsymbol{\varepsilon}} - \Delta\tilde{\boldsymbol{\varepsilon}}_6^j$

6.8. Determination of the tangent stiffness tensor of the composite matrix (phase $0^{'}$) by using Mori-Tanaka homogenization scheme:

$$\mathbb{L}_{0'} = [f_0\mathbb{L}_0 + f_5\mathbb{L}_5 : \mathbb{A}_5^0 + f_6\mathbb{L}_6 : \mathbb{A}_6^0] : \mathbb{A}_0$$

We calculate then the isotropic part of tensor $\mathbb{L}_{0'}$, which is denoted $\mathbb{L}_{0'}^{iso}$.

End Hill 2

7. As all mesoinclusions have the same morphology, their Hill's tensor is the same and given by:

$$\mathbb{P}_I^{0^{'},i} = \mathbb{S}^E(\mathbb{L}_{0'}^{iso,i}) : \mathbb{L}_{0'}^i$$

8. Then, the tangent strain localization tensors $\mathbb{A}_r^i$ for phases ($0^{'}$), (1), (2), (3), (4) and (m) are given, respectively, as follows:

$$\mathbb{A}_{0'}^i = [f_{0'}\mathbb{I} + f_1\mathbb{A}_1^{0^{'},i} + f_2\mathbb{A}_2^{0^{'},i} + f_3\mathbb{A}_3^{0^{'},i} + f_4\mathbb{A}_4^{0^{'},i} + f_1^d\mathbb{A}_m^{0^{'},i}]^{-1}$$

$\mathbb{A}_1^i = \mathbb{A}_1^{0^{'},i} : \mathbb{A}_{0'}^i$; $\mathbb{A}_2^i = \mathbb{A}_2^{0^{'},i} : \mathbb{A}_{0'}^i$; $\mathbb{A}_3^i = \mathbb{A}_3^{0^{'},i} : \mathbb{A}_{0'}^i$; $\mathbb{A}_4^i = \mathbb{A}_4^{0^{'},i} : \mathbb{A}_{0'}^i$; $\mathbb{A}_m^i = \mathbb{A}_m^{0^{'},i} : \mathbb{A}_{0'}^i$

where: $\mathbb{A}_r^{0^{'},i} = [\mathbb{I} + \mathbb{P}_I^{0^{'},i} : (\mathbb{L}_r^i - \mathbb{L}_{0'}^i)]^{-1}$.

9. We check the compatibility of local strain between to iterations for phases (1), (2), (3), (4) and (m) and evaluate the errors $\boldsymbol{R}_r^i$:

$$\boldsymbol{R}_1^i = \mathbb{A}_1^i : \Delta E - \Delta\tilde{\boldsymbol{E}}_1^i$$

$$\boldsymbol{R}_2^i = \mathbb{A}_2^i : \Delta E - \Delta\tilde{\boldsymbol{E}}_2^i$$

$$\boldsymbol{R}_3^i = \mathbb{A}_3^i : \Delta E - \Delta\tilde{\boldsymbol{E}}_3^i$$

© 2018 Tous droits réservés.

lilliad.univ-lille.fr

$$\boldsymbol{R}_4^i = \mathbb{A}_4^i : \Delta E - \Delta\tilde{\boldsymbol{E}}_4^i$$

$$\boldsymbol{R}_m^i = \mathbb{A}_m^i : \Delta E - \Delta\tilde{\boldsymbol{E}}_m^i$$

If $\|\boldsymbol{R}_1^j\| <$ tol1 and $\|\boldsymbol{R}_2^j\| <$ tol2 and $\|\boldsymbol{R}_3^j\| <$ tol3 and $\|\boldsymbol{R}_4^j\| <$ tol4 and $\|\boldsymbol{R}_m^j\| <$ tolm, then compatibility is reached and we pass to step 10; otherwise, an additional iteration (back to step 3 with i=i+1) is needed until the convergence conditions are verified:

$$\Delta\tilde{\boldsymbol{E}}_1^{i+1} = \Delta\tilde{\boldsymbol{E}}_1^i + \boldsymbol{R}_1^i; \quad \Delta\tilde{\boldsymbol{E}}_2^{i+1} = \Delta\tilde{\boldsymbol{E}}_2^i + \boldsymbol{R}_2^i$$

$$\Delta\tilde{\boldsymbol{E}}_3^{i+1} = \Delta\tilde{\boldsymbol{E}}_3^i + \boldsymbol{R}_3^i; \quad \Delta\tilde{\boldsymbol{E}}_4^{i+1} = \Delta\tilde{\boldsymbol{E}}_4^i + \boldsymbol{R}_4^i; \quad \Delta\tilde{\boldsymbol{E}}_m^{i+1} = \Delta\tilde{\boldsymbol{E}}_m^i + \boldsymbol{R}_m^i$$

End Hill 1

10. The macroscopic stress tensor at the increment (n+1) is given by:

$$\boldsymbol{\Sigma}_{n+1} = f_1\tilde{\boldsymbol{\Sigma}}_{1,n+1} + f_2\tilde{\boldsymbol{\Sigma}}_{2,n+1} + f_3\tilde{\boldsymbol{\Sigma}}_{3,n+1} + f_4\tilde{\boldsymbol{\Sigma}}_{4,n+1} + f_{0'}\tilde{\boldsymbol{\Sigma}}_{0',n+1}$$

where:

$$\tilde{\boldsymbol{\Sigma}}_{0',n+1} = f_0\tilde{\boldsymbol{\sigma}}_{n+1} + f_5\tilde{\boldsymbol{\sigma}}_{5,n+1} + f_6\tilde{\boldsymbol{\sigma}}_{6,n+1};$$

$$\tilde{\boldsymbol{\sigma}}_{n+1} = \tilde{\boldsymbol{\sigma}}_n + \Delta\tilde{\boldsymbol{\sigma}}_{n+1} = \tilde{\boldsymbol{\sigma}}_n + \mathbb{L}_0 : (\mathbb{A}_0 : \Delta\tilde{\boldsymbol{\varepsilon}});$$

$$\tilde{\boldsymbol{\sigma}}_{r,n+1} = \tilde{\boldsymbol{\sigma}}_{r,n} + \Delta\tilde{\boldsymbol{\sigma}}_{r,n+1} = \tilde{\boldsymbol{\sigma}}_{r,n} + \mathbb{L}_r : (\mathbb{A}_r : \Delta\tilde{\boldsymbol{\varepsilon}}) \quad \text{for i=5-6;}$$

$$\tilde{\boldsymbol{\Sigma}}_{r,n+1} = \tilde{\boldsymbol{\Sigma}}_{r,n} + \Delta\tilde{\boldsymbol{\Sigma}}_{r,n+1} = \tilde{\boldsymbol{\Sigma}}_{r,n} + \mathbb{L}_r : (\mathbb{A}_r : \Delta\boldsymbol{E}) \quad \text{for i=1-4;}$$

2.3.3.2 Numerical assessment of the proposed model

Sensitivity study of damage evolution

In this paragraph, some sensitivity studies are performed in order to show the influence of some parameters and conditions of interfacial damage on the macroscopic mechanical behavior of the studied heterogeneous material. At first, we have considered a simple case of the representative elementary volume given in figure 2.15. Two scale of study are assumed: calcite grains are seen immersed in a porous clay matrix. Then, we envisage the debonding of calcite particles by using elastic and plastic parameters given in table 2.5.

Figure 2.16 shows the elastoplastic damage response of a two-phase composite in uniaxial compression tests and different values of Weibull parameter S. In figure 2.16.a, the influence of strength parameter S is clearly displayed: a higher value of S leads to a higher failure strength before all calcite particles are completely debonded. In figure 2.16.b, the evolution of volume fraction of completely debonded calcite in function of axial strain is presented. Note that in all figures, the curves of the same color

© 2018 Tous droits réservés.

lilliad.univ-lille.fr

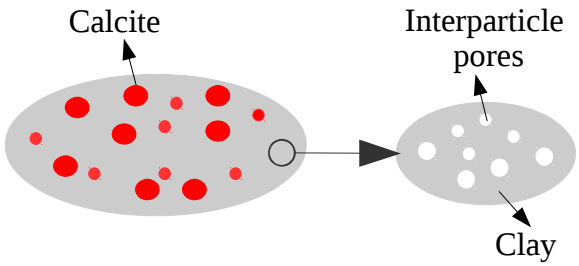

Figure 2.15: Simplified representative elementary volume.

Table 2.5: Typical values of parameters for the model with associated flow rule.

	Phase (0) clay	Phase (1) calcite
Elastic properties	E_0=5 GPa	E_1=95 GPa
	ν_0=0.27	ν_1=0.27
Plastic properties	σ_{0m}=50	
	σ_{00}=1	
	b=650	
	α=0.24	
Porosity/volume fraction	0.1	0.3

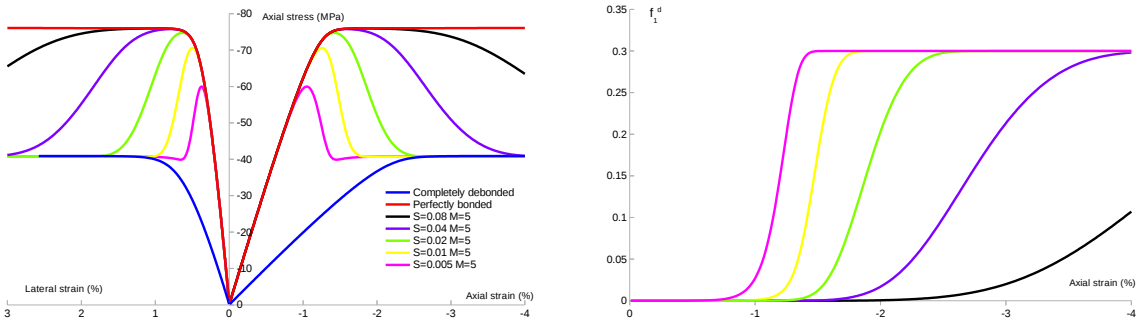

(a) (b)

Figure 2.16: (a) The predicted elastoplastic responses of two-phase composite with evolutionary debonding damage under uniaxial compression test with M=5 and various values of S; (b) the predicted volume fraction of completely debonded calcite particles.

correspond to the same value of S.

Figure 2.17 illustrates the influence of Weibull parameter M on the macroscopic response (continuous lines for M=2 and dashed ones for M=5). As we can see, M controls the debonding evolution rate.

Now, we return to our original complex case given in figure 2.7 and make some sen-

© 2018 Tous droits réservés.

lilliad.univ-lille.fr

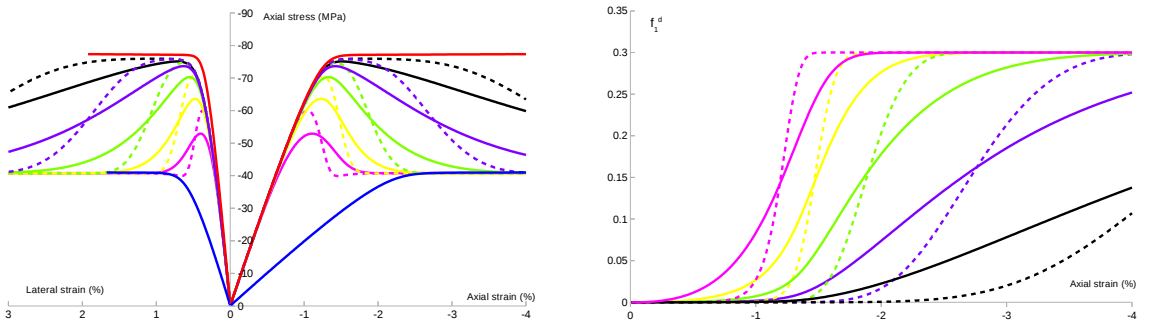

(a) (b)

Figure 2.17: (a) Influence of Weibull parameter M on the predicted elastoplastic responses of two-phase composite with evolutionary debonding damage under uniaxial compression test with various values of S; (b) the predicted volume fraction of completely debonded calcite particles (continuous lines-M=2; dashed lines-M=5).

sitivity study. Elastic properties of all constituents are given in tables 2.1, 2.2 and 2.3 (case of perpendicular sample in oil window). The same plastic parameters, given in table 2.5, are used. A typical mineralogical composition is considered: f_1^{ini}=0.3, f_2=0.2, f_3=0.01, f_4=0.05, f_5=0.11, f_6=0.23 and f=0.1. Figure 2.18 exhibits the predicted elastoplastic responses of the studied complex material with evolutionary damage of mesocalcite under uniaxial compression test with M=2 and various values of S. Comparing figures 2.17 (simple case) and 2.18, it can be noted that the micromechanical model is able to take into consideration the mineralogical composition on the macroscopic response.

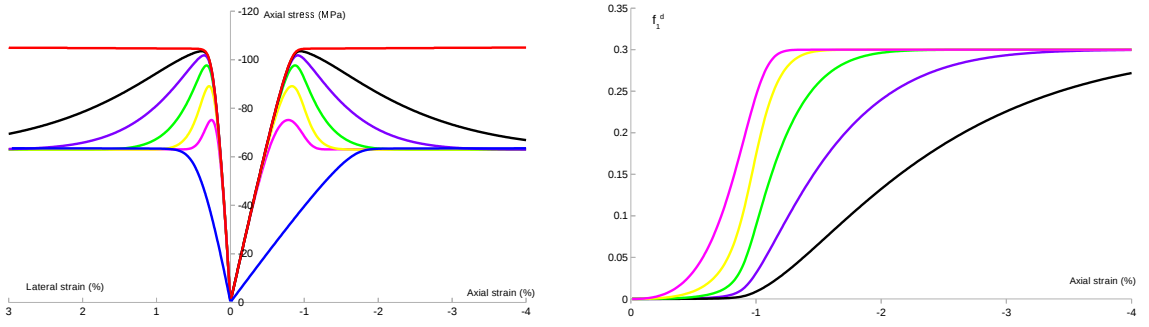

(a) (b)

Figure 2.18: (a) The predicted elastoplastic responses of the studied heterogeneous material with evolutionary debonding damage under uniaxial compression test with M=2 and various values of S; (b) the predicted volume fraction of completely debonded calcite particles.

As already said, for simplicity and the lack of experimental data, we have supposed that only interfaces between mesocalcite and matrix are subjected to debonding pro-

© 2018 Tous droits réservés.

lilliad.univ-lille.fr

cess. However, the model is able to treat interfacial debonding of many inclusions at the same time. Wherefore, in figure 2.19, we have study two cases: 1- debonding of only mesocalcite grains (continuous lines) and 2- debonding of mesocalcite and mesoquartz grains at the same time (dashed lines). It is obvious that the micromechanical model is able to accounts for debonding of several particles at the same time and reproduce the material softening related to progressive interfacial debonding process.

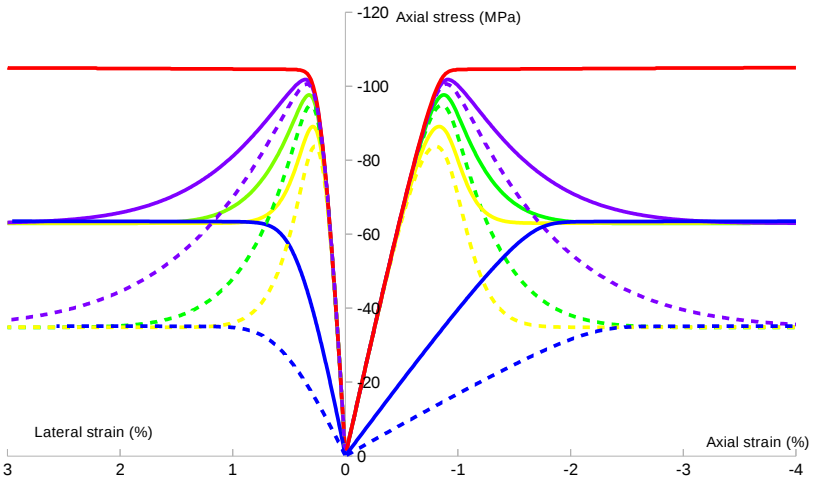

Figure 2.19: Comparison between the macroscopic elastoplastic response in the case of interfacial damage of mesocalcite (continuous line) and mesocalcite+mesoquartz (dashed lines) for different values of S and M=2.

Influence of fine inclusions on macroscopic behavior

In this section, we investigate the influence of fine kerogen and calcite volume fractions (f_5 and f_6 respectively) on the macroscopic mechanical behavior. The used plastic parameters of the solid clay phase are: α=0.1 and σ_0=15. A considered typical mineralogical composition is used: f_1=0.4, f_2=0.25, f_3=0.03 and f_4=0.1. The elastic properties of all phases are given in tables 2.1, 2.2 and 2.3 for the case of perpendicular samples in oil window. In figure 2.20, we study the influence of fine kerogen grains on the macroscopic behavior. As we can see, the volume fraction of fine kerogen has an effect on the macroscopic behavior. When f_5 increases (f_4 decreases and the total volume fraction of kerogen is kept constant=0.1), the failure strength decreases as kerogen phase has elastic properties lower than that of the porous matrix thus it decreases its rigidity. Note that the response in compression loading is more affected than that in traction one.

Figure 2.21 shows the effect of fine calcite volume fraction f_6 on the macroscopic mechanical behavior. The total volume fraction of calcite is kept constant=0.4 (we increase f_6 and decrease f_1). As we can spot, when f_6 increases, the failure strength

© 2018 Tous droits réservés.

lilliad.univ-lille.fr

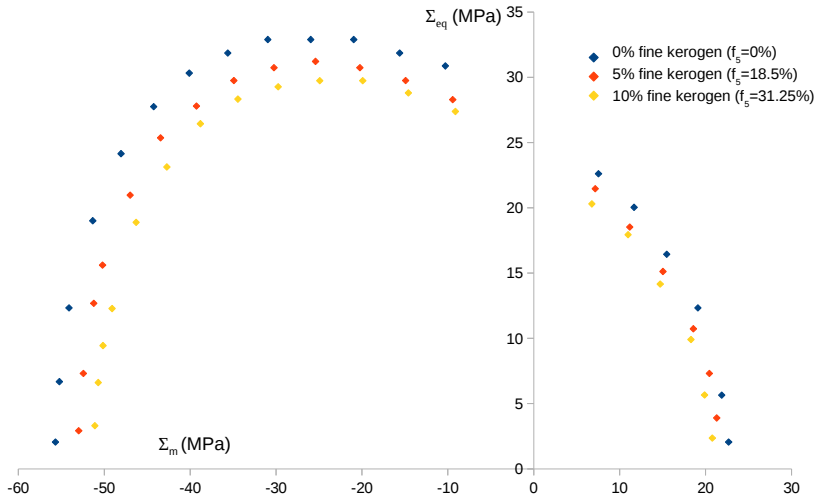

Figure 2.20: Influence of fine kerogen grains on the macroscopic mechanical behavior.

is enhanced. Therefore, fine calcite grains boost the material rigidity. As in the case of fine kerogen, the response in compression loading is more affected than that in traction one.

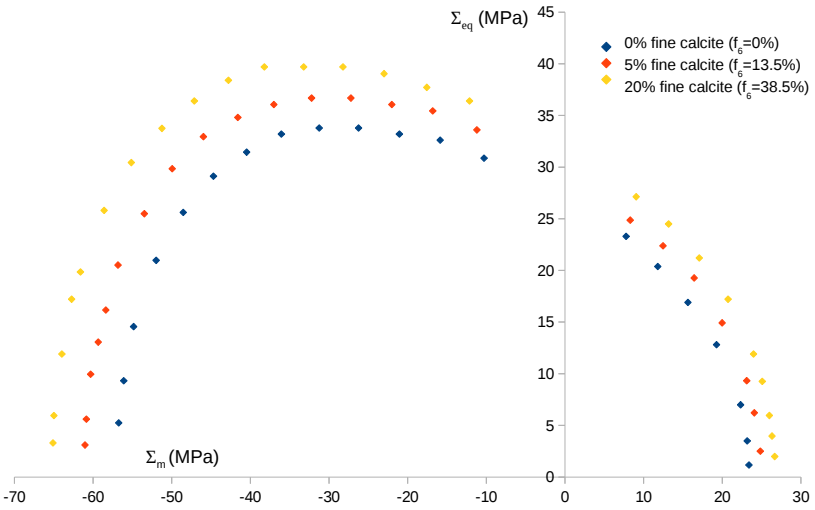

Figure 2.21: Influence of fine calcite grains on the macroscopic mechanical behavior.

2.3.4 Calibration and experimental validation of the model

After having formulated the semi-analytical micromechanical model, the purpose of this section is to evaluate its predictive capabilities and in particular, its ability to reproduce the instantaneous mechanical behavior of Vaca Muerta shale rock. As seen earlier, an associated flow rule is used to describe the plastic deformation of clay solid phase. However, as we will see hereafter, the proposed associated model overestimates the lateral and volumetric strains. Thus, in order to improve the accuracy of model predictions to reproduce Vaca Muerta shale behavior, a non-associated plastic model

© 2018 Tous droits réservés.

lilliad.univ-lille.fr

will be considered for clay matrix solid phase. Note that in all graphs, continuous red curves represent numerical simulations and symbolic blue ones feature experimental data.

2.3.4.1 Identification of model's parameters

The proposed model involves many elastic and plastic parameters, in addition to Weibull's constants. Elastic ones of various phases are already given in tables 2.1, 2.2 and 2.3 for vertical and horizontal samples in oil or gas window. As for the case of elastic parameters, plastic and Weibull's constants are first identified for a given mineralogical composition and then, validated against other compositions with the same set of values. The four plastic parameters of clay matrix and the two Weibull's constants are identified, step by step, from direct calibration of numerical results and experimental data, similar to that proposed in [Guéry, 2007]. For our studied material, plastic as well as debonding parameters are optimized from stress-strain curves of a simple triaxial compression test (confining pressure=5 MPa) on a horizontal sample (parallel loading) from well S2 at the depth of 2686.49 m. Identified plastic parameters are as follows: α=0.245, σ_{00}=1, σ_{0m}=50, b=650. Besides, Weibull's parameters of particle debonding are given by: S=0.04 and M=1. Note that mineralogical composition is available from mineral logs (figure 1.8). Plastic and debonding parameters for vertical and horizontal samples are the same since, according to experimental data, there is no significant difference in terms of strength peak between the two principal orientations. According to latter parameters and elastic ones given previously, figure 2.22 shows comparison between associated model simulations and experimental data for the sample at the depth 2686.49 m. As we can notice, the axial strain is well reproduced, however, the proposed associated model overestimates the lateral and volumetric strains. Mainly, this is due to the fact that an associated flow rule is used to describe the plasticity of clay matrix.

2.3.4.2 Formulation of the non-associated model

As we have seen in the previous section, the use of an associated flow rule for clay matrix yields an overestimated lateral and volumetric strain responses. Thus, to improve the accuracy of model's predictions, a non-associated plastic model is considered for clay matrix solid phase. Due to the difficult to formulate analytically a plastic potential and for the sake of simplicity, the plastic potential of a porous medium G is assumed having the same form as the plastic criterion (equation 2.10) and is given as

© 2018 Tous droits réservés.

lilliad.univ-lille.fr

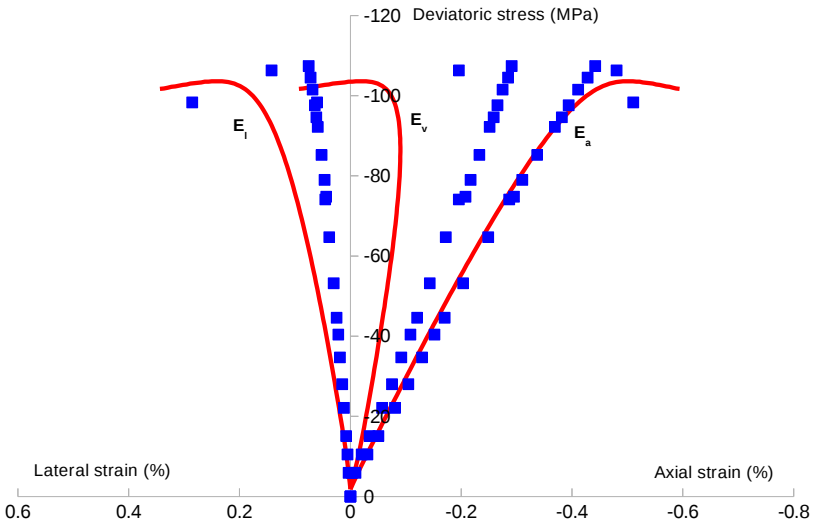

Figure 2.22: Comparison between associated model simulations and experimental data in a triaxial compression test on a Vaca Muerta shale sample (confining pressure=5 MPa; depth=2686.49 m; well S2; horizontal; f_1=0.2275, f_2=0.431, f_3=0.0164, f_4=0.1, f_6=0.05, f=0.08).

follows:

$$G = \frac{\frac{\tilde{\sigma}_{eq}^2}{\bar{\sigma}^2}}{\left[1 - \frac{3\alpha_2}{(1-f)}\frac{\tilde{\sigma}_m}{\bar{\sigma}}\right]^2} + 2f\cosh\left(\frac{2\alpha_2 + sgn(\tilde{\sigma}_m)}{2\alpha_2}\ln\left(1 - 3\alpha_2\frac{\tilde{\sigma}_m}{\bar{\sigma}}\right)\right) - 1 - f^2 \quad (2.39)$$

Note that compared to the plastic criterion, the latter potential is function of a dilatancy coefficient α_2. Then, the plastic flow rule (equation 2.12) of the clay matrix turns into:

$$\tilde{\mathbf{d}}^p = \dot{\lambda}\frac{\partial G}{\partial \tilde{\boldsymbol{\sigma}}}(\tilde{\boldsymbol{\sigma}}, \bar{\sigma}, f) \quad (2.40)$$

The equivalent plastic strain of the clay matrix (equation 2.16) becomes:

$$\dot{\varepsilon}^p = \frac{\tilde{\boldsymbol{\sigma}} : \tilde{\mathbf{d}}^p}{(1-f)\left[\bar{\sigma} + 3(\alpha_2 - \alpha)\frac{\tilde{\sigma}_m}{1-f}\right]} \quad (2.41)$$

The evolution law of porosity (equation 2.17) will get the following form:

$$\dot{f} = (1-f)\left[\mathrm{tr}\tilde{\mathbf{d}}^p - 3\alpha_2\dot{\varepsilon}^p\right] \quad (2.42)$$

Finally, the effective tangent stiffness operator of the porous clay matrix (equation 2.19) turns into:

$$\mathbb{L}_0 = \begin{cases} \mathbb{C}_0 & \text{if } \Phi(\tilde{\boldsymbol{\sigma}}, \bar{\sigma}, f) \leq 0, \dot{\Phi}(\tilde{\boldsymbol{\sigma}}, \bar{\sigma}, f) < 0 \\ \mathbb{C}_0 - \frac{\mathbb{C}_0 : \frac{\partial G}{\partial \tilde{\boldsymbol{\sigma}}} \otimes \frac{\partial \Phi}{\partial \tilde{\boldsymbol{\sigma}}} : \mathbb{C}_0}{H^D} & \text{if } \Phi(\tilde{\boldsymbol{\sigma}}, \bar{\sigma}, f) = 0, \dot{\Phi}(\tilde{\boldsymbol{\sigma}}, \bar{\sigma}, f) = 0 \end{cases} \quad (2.43)$$

© 2018 Tous droits réservés.

lilliad.univ-lille.fr

with:

$$H^D = \frac{\partial \Phi}{\partial \tilde{\boldsymbol{\sigma}}} : \mathbb{C}_0 : \frac{\partial G}{\partial \tilde{\boldsymbol{\sigma}}} - \frac{\partial \Phi}{\partial f}\left[(1-f)\frac{\partial G}{\partial \tilde{\sigma}_m} - 3\alpha_2 \frac{\tilde{\boldsymbol{\sigma}} : \frac{\partial G}{\partial \tilde{\boldsymbol{\sigma}}}}{\bar{\sigma}+3(\alpha_2-\alpha)\frac{\tilde{\sigma}_m}{1-f}}\right] - \frac{\partial \Phi}{\partial \bar{\sigma}}\frac{\partial \bar{\sigma}}{\partial \varepsilon^p}\frac{\tilde{\boldsymbol{\sigma}} : \frac{\partial G}{\partial \tilde{\boldsymbol{\sigma}}}}{(1-f)\left[\bar{\sigma}+3(\alpha_2-\alpha)\frac{\tilde{\sigma}_m}{1-f}\right]}$$

To complete the formulation in the case of a non-associated model, the same isotropization procedure as that used for the associated model is here used. The tangent moduli κ_i and μ_i (equation 2.35) will get the following form respectively:

$$\kappa_i = \kappa_0\left(1 - \frac{9\kappa_0 B B^{'}}{H^D}\right), \quad \mu_i = \mu_0\left(1 - \frac{2\mu_0 A A^{'}}{5H^D}\tilde{\sigma}_{eq}^2\right) \tag{2.44}$$

where coefficients A and B are given in equations 2.21 and 2.22 respectively; $A^{'}$ and $B^{'}$ take the later forms:

$$A^{'} = \frac{3\left(1+\frac{3\tilde{\sigma}_m\alpha_2}{(1-f)\bar{\sigma}-3\tilde{\sigma}_m\alpha_2}\right)^2}{\bar{\sigma}^2}$$

$$B^{'} = \frac{-f[\bar{\sigma}(f-1)+3\tilde{\sigma}_m\alpha_2]^3[2\alpha_2+sgn(\tilde{\sigma}_m)]\sinh\left[\frac{(2\alpha_2+sgn(\tilde{\sigma}_m)\ln\left(1-\frac{3\alpha_2\tilde{\sigma}_m}{\bar{\sigma}}\right)}{2\alpha_2}\right]-2\tilde{\sigma}_{eq}^2\alpha_2(f-1)^2(\bar{\sigma}-3\tilde{\sigma}_m\alpha_2)}{[\bar{\sigma}(f-1)+3\tilde{\sigma}_m\alpha_2]^3(\bar{\sigma}-3\tilde{\sigma}_m\alpha_2)}$$

Note that if α_2=α, the associated flow rule is recovered.

2.3.4.3 Experimental validation

The purpose of this section is to evaluate the capacity of the non-associated model, defined previously, by comparing numerical simulations with Vaca Muerta experimental data. Considering the same parameter identification procedure that in section 2.3.4.1, an additional parameter α_2 is supplemented compared to the associated model. The set of plastic and debonding parameters of the non-associated model for Vaca Muerta shale is summarized in table 2.6.

Table 2.6: Set of parameters of the non-associated model for Vaca Muerta shale.

Plastic parameters	Debonding parameters
α=0.245	S=0.04
α_2=0.1	M=1
σ_{0m}=50	
σ_{00}=1	
b=650	

Using the values given in tables 2.1, 2.2, 2.3 and 2.6 (elastic properties are chosen according to whether the sample is horizontal or parallel and if taken from a gas or oil well), a set of numerical simulations are carried out for triaxial compression tests at

© 2018 Tous droits réservés.

lilliad.univ-lille.fr

different confining pressures and on samples from various wells and at different depths. Figures 2.23-2.28 show comparisons between non-associated model simulations and Vaca Muerta experimental data. Several comments can be withdrawn:

- In general, there is a good agreement between numerical results and experimental data.
- The non-associated model describes suitably the transition from volumetric compressibility to dilatancy with the increase of the deviatoric stress.
- The lateral and volumetric strains are less pronounced compared to the associated model.
- The proposed micromechanical model can consistently account for the effect of mineralogical composition (fine grains, mesoinclusions and porosity) on the macroscopic response of Vaca Muerta shale. This represents an advantage regarding phenomenological macroscopic models.
- The proposed model is able to account for the effect of confining pressure on macroscopic behavior.
- The micro-macro model takes into account the material softening related to progressive interfacial debonding process.

Some important differences can be observed between numerical results and experimental data for some samples. One note that many factors can influence the results. The most important one is that the mineralogical composition and microstructure of Vaca Muerta shale are very complex. The interparticle porosity is approximated to be the quarter of total one. Even, the volume fraction of fine inclusions are not well known for all samples. For horizontal samples (parallel loading), it is obvious to obtain a difference between numerical and experimental curves for lateral strain (therefore, volumetric strain) given that experimental values do not represent the true values since lateral deformation is not isotropic (there is two values in two directions). Besides, according to our observations, most withdrawn samples are cracked before any loading which can affect the macroscopic response. But in general, apart from the comparison between experimental data and simulations, the proposed micromechanical model is able to capture the main features of heterogeneous rocks mechanical behavior.

Some complex triaxial compression tests are realized: a number of hydrostatic loading-unloading cycles is performed before applying the deviatoric stress. With the proposed micromechanical model since the plasticity surface is no longer a straight line (Drucker-Prager criterion) but rather it is a closed surface (figure 2.11), thus, during

© 2018 Tous droits réservés.

lilliad.univ-lille.fr

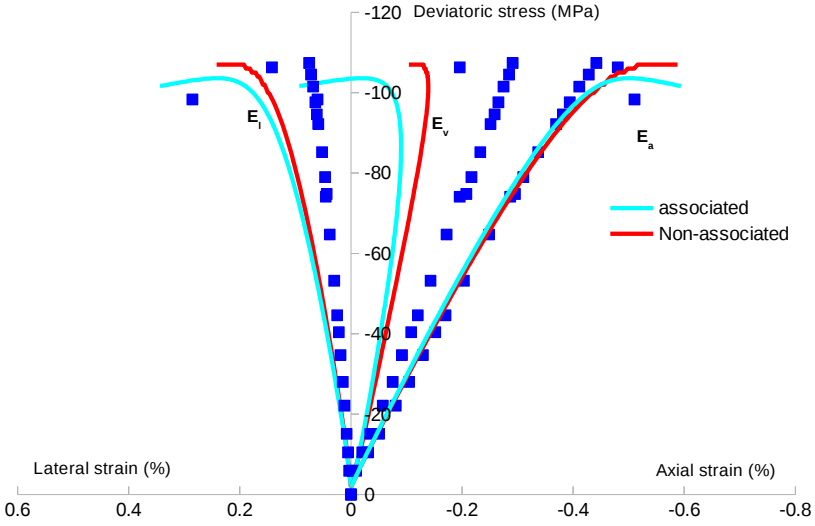

Figure 2.23: Comparison between associated/non-associated model simulations and experimental data in a simple triaxial compression test on a Vaca Muerta shale sample (confining pressure=5 MPa; depth=2686.49 m; well S2; horizontal; f_1=0.2275, f_2=0.431, f_3=0.0164, f_4=0.1, f_6=0.05, f=0.08).

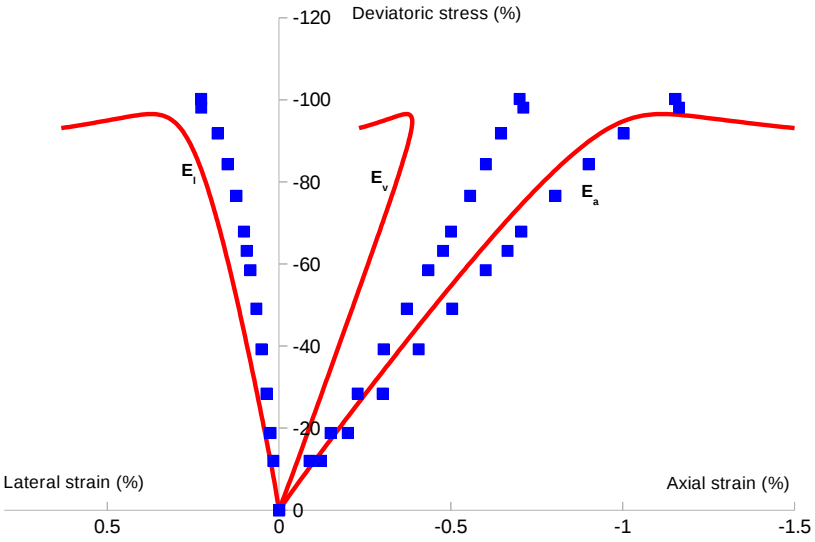

Figure 2.24: Comparison between non-associated model simulations and experimental data in a simple triaxial compression test on a Vaca Muerta shale sample (confining pressure=5 MPa; depth=2668.71 m; well S2; vertical; f_1=0.15, f_2=0.412, f_3=0.0033, f_5=0.23, f=0.09).

© 2018 Tous droits réservés.

lilliad.univ-lille.fr

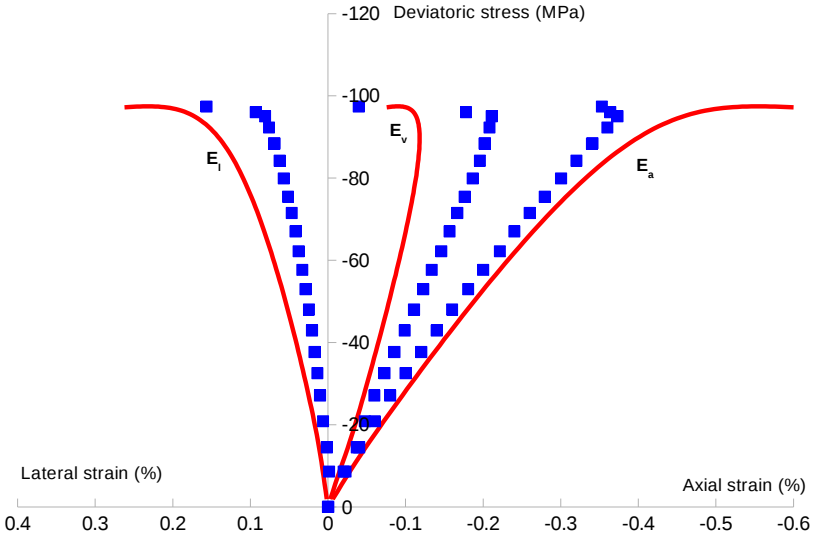

Figure 2.25: Comparison between non-associated model simulations and experimental data in a simple triaxial compression test on a Vaca Muerta shale sample (confining pressure=8 MPa; depth=2668.78 m; well S2; horizontal; f_1=0.143, f_2=0.35, f_3=0.0044, f_4=0.12, f_6=0.13, f=0.13).

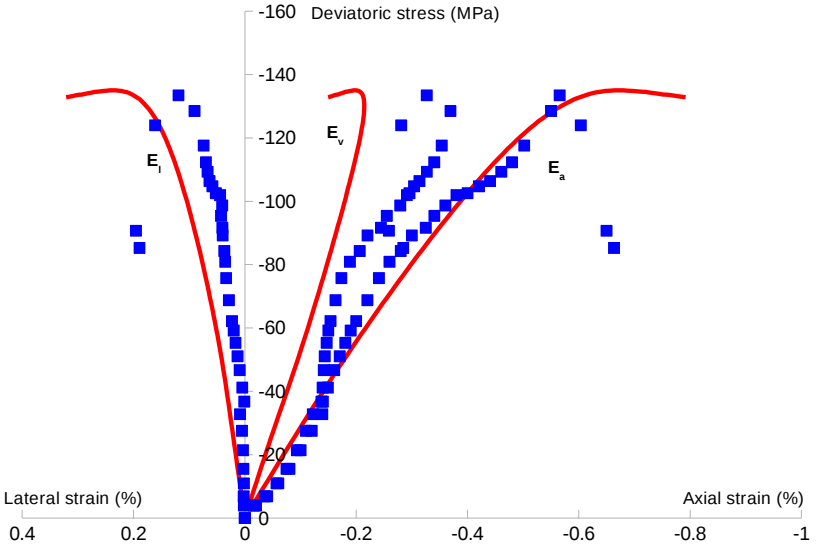

Figure 2.26: Comparison between non-associated model simulations and experimental data in a simple triaxial compression test on a Vaca Muerta shale sample (confining pressure=25 MPa; depth=2686.55 m; well S2; horizontal; f_1=0.2275, f_2=0.431, f_3=0.0164, f_4=0.1, f_6=0.05, f=0.08).

© 2018 Tous droits réservés.

lilliad.univ-lille.fr

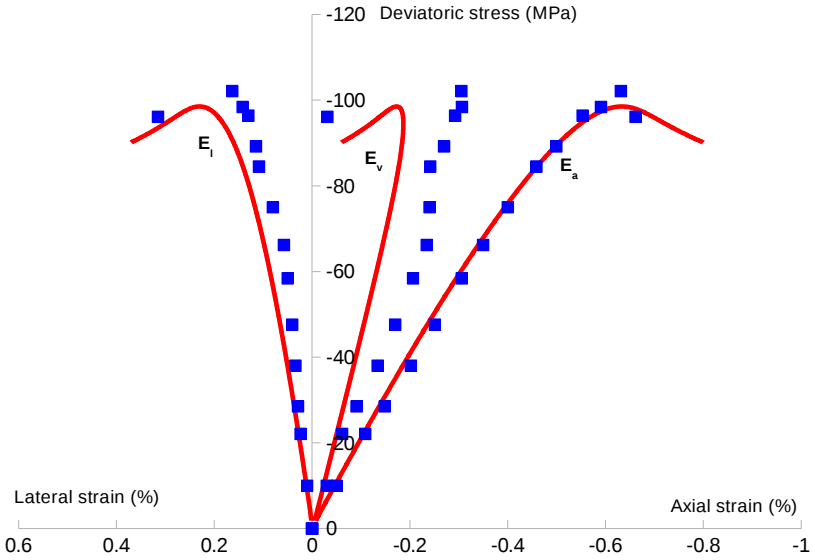

Figure 2.27: Comparison between non-associated model simulations and experimental data in a simple triaxial compression test on a Vaca Muerta shale sample (confining pressure=2 MPa; depth=2639.73 m; well S3; vertical; f_1=0.4, f_2=0.3, f_4=0.257, f_6=0.05, f=0.05).

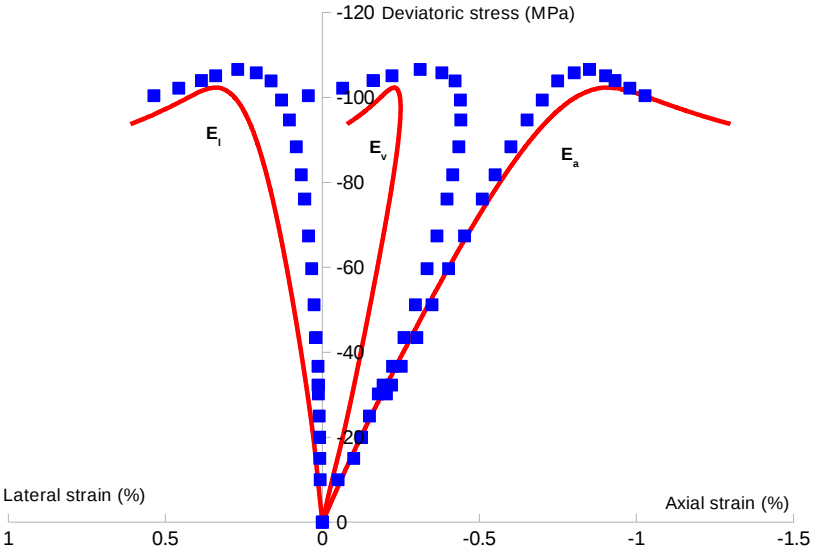

Figure 2.28: Comparison between non-associated model simulations and experimental data in a simple triaxial compression test on a Vaca Muerta shale sample (confining pressure=10 MPa; depth=2652.46 m; well S3; vertical; f_1=0.2415, f_2=0.173, f_4=0.264, f_6=0.25, f=0.08).

© 2018 Tous droits réservés.

lilliad.univ-lille.fr

hydrostatic loading, if the applied stress exceeds the elasticity threshold, the material enters into a state of plasticity. Therefore, interfacial debonding process and plastic strain can occur even during hydrostatic loading. The loading path of complex triaxial tests, applied to the samples from two wells S1 and S3, is illustrated in figure 2.29. For samples from well S1, during hydrostatic loading, firstly, axial and lateral stresses are increased to -80 MPa and then, a unloading phase is applied to reach a stress state of -10 MPa. Finally, the deviatoric phase starts up where axial stress increases and lateral one is kept constant. Figures 2.30-2.33 exhibit comparisons between non-associated model simulations and experimental data in some complex triaxial compression tests on Vaca Muerta shale samples (confining pressure=10 MPa; vertical; different depths). One can see a very good accordance between numerical results and experimental data.

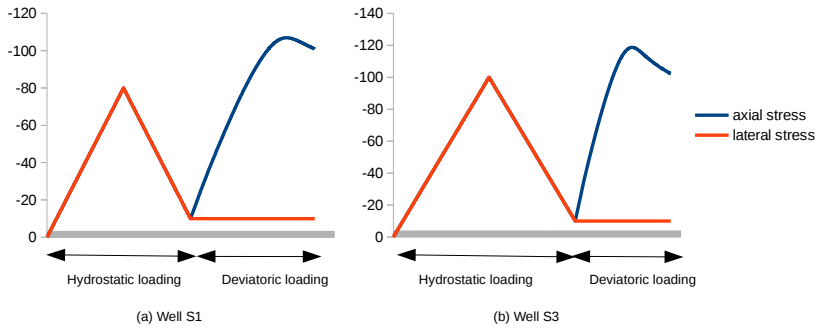

Figure 2.29: Illustration of the loading path for complex triaxial tests for wells S1 and S3.

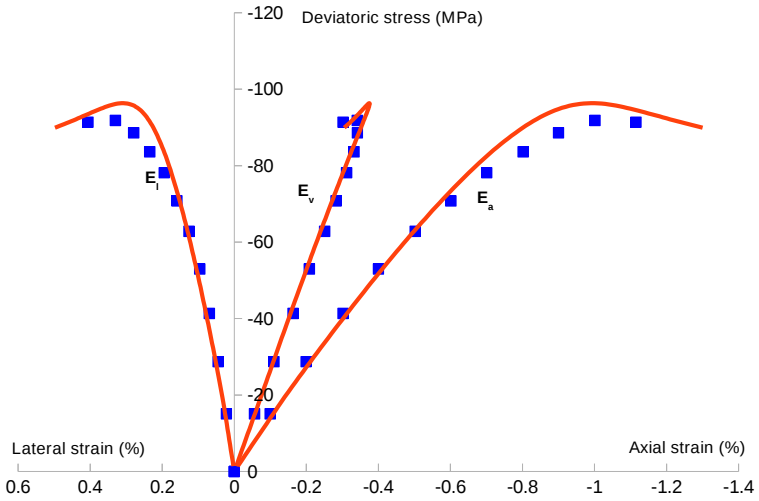

Figure 2.30: Comparison between non-associated model simulations and experimental data in a complex triaxial compression test on a Vaca Muerta shale sample (confining pressure=10 MPa; depth=2530.23 m; well S1; vertical; f_1=0.423, f_2=0.215, f_3=0.0173, f_5=0.23, f=0.094).

© 2018 Tous droits réservés.

lilliad.univ-lille.fr

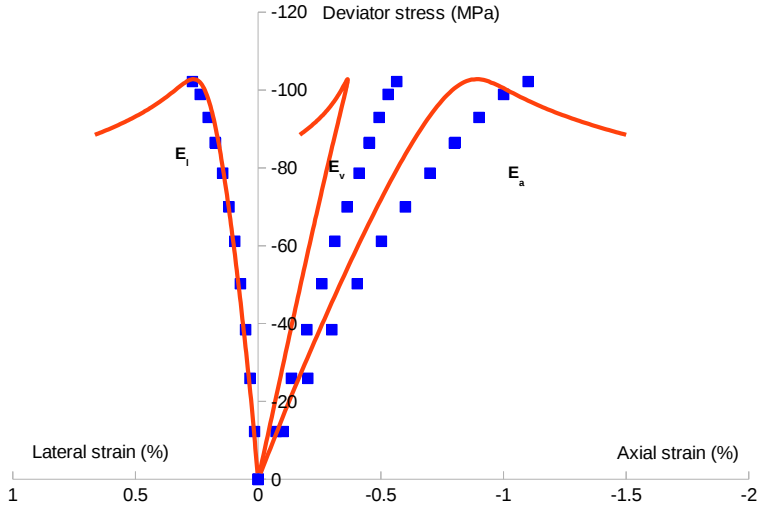

Figure 2.31: Comparison between non-associated model simulations and experimental data in a complex triaxial compression test on a Vaca Muerta shale sample (confining pressure=10 MPa; depth=2649.23 m; well S1; vertical; f_1=0.39, f_2=0.3, f_3=0.024, f_4=0.15, f=0.1).

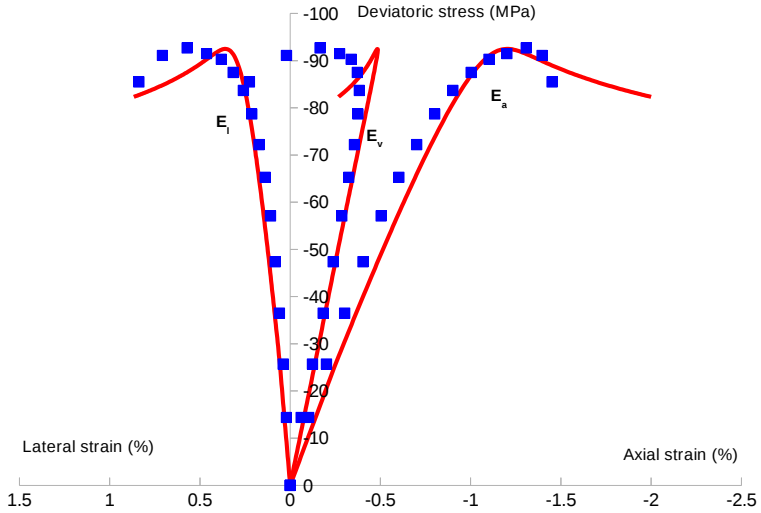

Figure 2.32: Comparison between non-associated model simulations and experimental data in a complex triaxial compression test on a Vaca Muerta shale sample (confining pressure=10 MPa; depth=2536.23 m; well S3; vertical; f_1=0.26, f_2=0.3075, f_3=0.0068, f_4=0.172, f=0.14).

© 2018 Tous droits réservés.

lilliad.univ-lille.fr

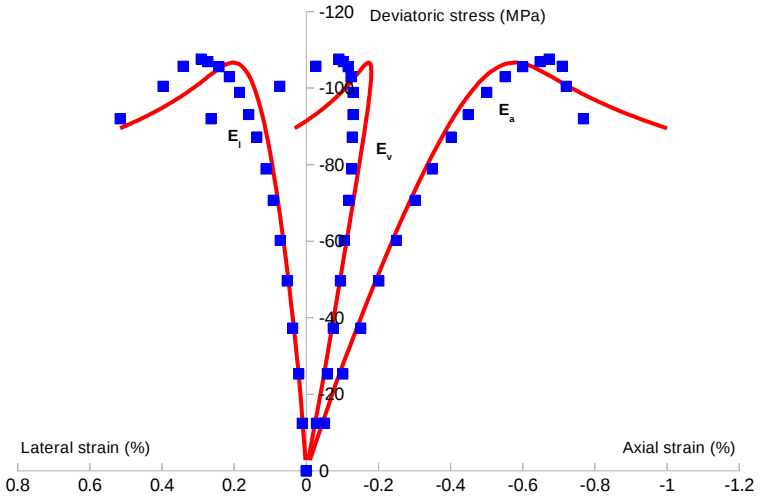

Figure 2.33: Comparison between non-associated model simulations and experimental data in a complex triaxial compression test on a Vaca Muerta shale sample (confining pressure=10 MPa; depth=2576.21 m; well S3; vertical; f_1=0.53, f_2=0.21, f_4=0.153, f_5=0.05, f_6=0.05, f=0.08).

Figures 2.34 and 2.35 exhibit the variation of perfectly bonded calcite volume fraction f_1 during hydrostatic loading phase of a complex triaxial test for two samples from wells S1 and S3. One can observe that the variation is quite small; nevertheless, it can be noticed that the debonding process starts as early as the hydrostatic loading phase.

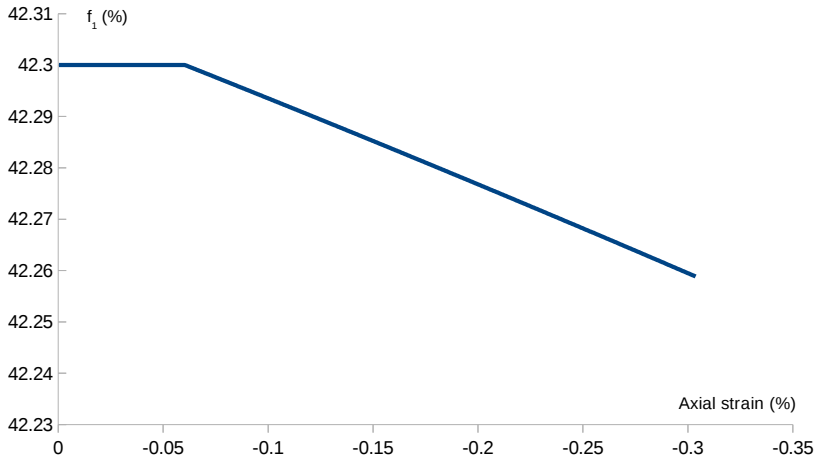

Figure 2.34: Evolution of perfectly bonded calcite volume fraction f_1 with axial strain during hydrostatic loading phase of a complex triaxial test on a Vaca Muerta shale sample (depth=2530.23 m; well S1).

2.3.5 Case of associated perfectly plastic clay solid phase

For the industrial application of the thesis, it is more appropriate to use a model with the least possible number of parameters. For this purpose, we consider a simplified

© 2018 Tous droits réservés.

lilliad.univ-lille.fr

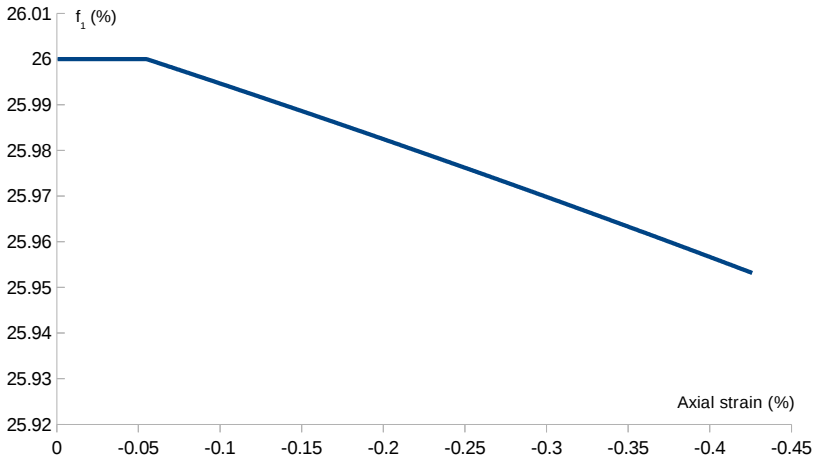

Figure 2.35: Evolution of perfectly bonded calcite volume fraction f_1 with axial strain during hydrostatic loading phase of a complex triaxial test on a Vaca Muerta shale sample (depth=2536.23 m; well S3).

modeling case where the solid clay phase is assumed to have a perfectly plastic behavior and follows an associated flow law. In this case, the number of plastic parameters is reduced to two only: $\bar{\sigma} = \sigma_{0m}$=50, α=α_2= 0.245. For these conditions, the comparison between simulations and experimental data will not be very satisfactory. But if we are interested only to the value of peak stress, the simulations can be sufficient. The goal was to use as few parameters as possible. Some examples of simulations are presented below (figures 2.36 and 2.37) and others in appendix B.

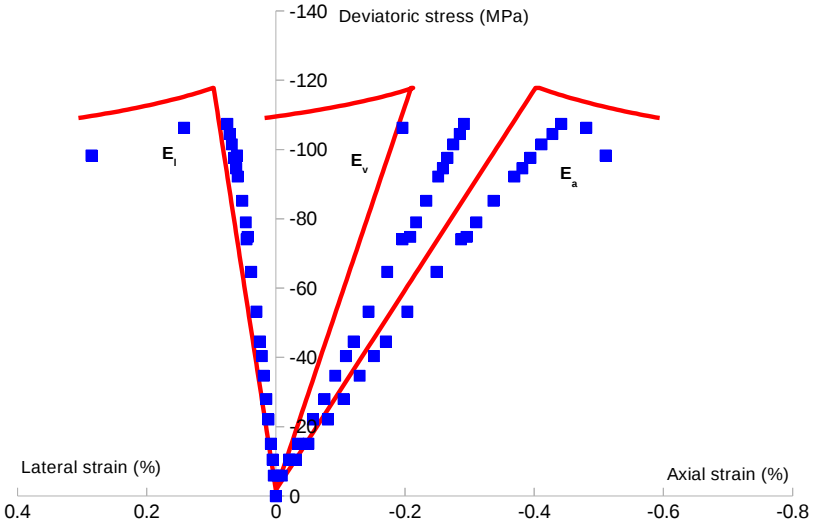

Figure 2.36: Comparison between associated perfectly plastic simulations and experimental data in a simple triaxial compression test on a Vaca Muerta shale sample (confining pressure=5 MPa; depth=2686.49 m; well S2; horizontal; f_1=0.2275, f_2=0.431, f_3=0.0164, f_4=0.1, f_6=0.05, f=0.08).

© 2018 Tous droits réservés.

lilliad.univ-lille.fr

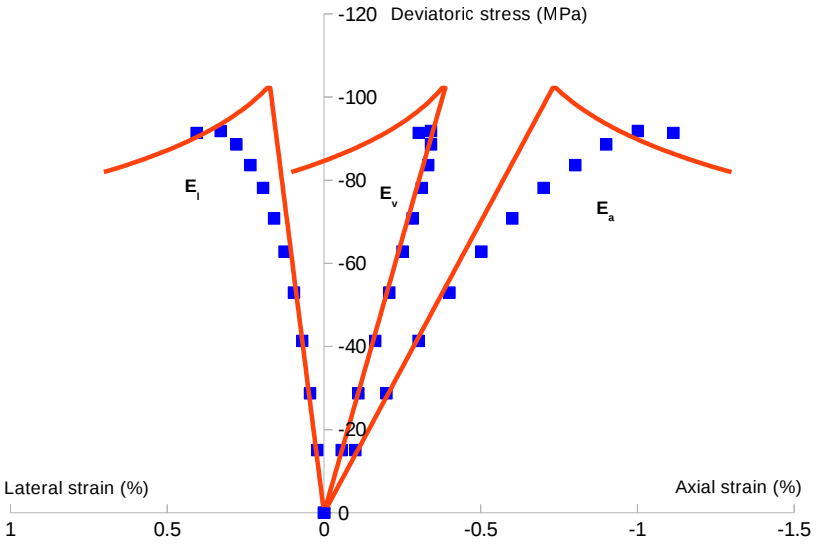

Figure 2.37: Comparison between associated perfectly plastic simulations and experimental data in a complex triaxial compression test on a Vaca Muerta shale sample (confining pressure=10 MPa; depth=2530.23 m; well S1; vertical; f_1=0.423, f_2=0.215, f_3=0.0173, f_5=0.23, f=0.094).

2.4 Conclusion

In this chapter, a micromechanical elastoplastic damage model is developed to study the instantaneous mechanical behavior of Vaca Muerta shale. Firstly, based on microstructure observations, the representative elementary volume of this material is illustrated. This illustration seems indispensable in a scale modeling approach. In the second section, we have discussed the elastic behavior of the studied material. At first, elastic properties of all Vaca Muerta constituents are identified and afterward, Mori-Tanaka scheme has been used as the linear homogenization method to predict macroscopic elastic properties, which are compared to experimental data. In general, the comparison seems satisfactory. Then, a sensitivity study in elastic regime is established to show the influence of kerogen elastic properties and fine inclusions on effective elastic ones.

In the third section, the elastoplastic damage behavior of Vaca Muerta shale has been formulated by using a non-linear homogenization procedure. The sliding between clay sheets is supposed as the origin of plasticity. A first step of homogenization yields the strength domain of the porous clay phase where its solid phase is considered as a cohesive-frictional material obeying to Drucker-Prager criterion. At the second and third homogenization steps, the effects of fine and meso inclusions are taken into account simultaneously by using Hill's incremental method. In the second main part, interfacial debonding between composite matrix and mesocalcite inclusions is considered as the damage process. Later, the algorithm of numerical implementation

© 2018 Tous droits réservés.

lilliad.univ-lille.fr

is exposed. Afterward, the influence of damage evolution and some microstructural aspects on macroscopic mechanical behavior is investigated. Finally, the calibration and experimental validation of the proposed model are performed. In general, comparisons between experimental data and numerical simulations seem favorable. For industrial application of the model, a simplified case is studied where clay solid phase is supposed to have an associated perfectly plastic behavior.

© 2018 Tous droits réservés.

lilliad.univ-lille.fr

© 2018 Tous droits réservés.

lilliad.univ-lille.fr

Chapter 3

Constitutive model for long term behavior of Vaca Muerta shale

Contents

© 2018 Tous droits réservés.

lilliad.univ-lille.fr

The previous chapter was devoted to the formulation of instantaneous mechanical behavior of Vaca Muerta shale rock in the context of elastoplasticity and damage evolution. By applying three homogenization levels, the macroscopic constitutive law was obtained by means of Hill's incremental method. By using an isotropic version of matrix tangent operator for Eshelby's tensor calculation, the micromechanical model is shown capable to reproduce the mechanical behavior of the studied material. As we have demonstrated, the model has the advantage of taking into consideration the influence of mineralogical composition, porosity and plastic compressibility of the solid phase on the macroscopic response.

Based on laboratory tests ([Cristescu, 1993], [Martin and Chandler, 1994], [Maranini and Brignoli, 1999], [Hunsche and Hampel, 1999] and [Li and Xia, 2000]), it is obvious to consider that most geomaterials, like rocks and concrete, exhibit both instantaneous and time-dependent irreversible deformations. Thus, after having formulated the short term behavior, the aim of this chapter is to model the time dependent behavior of Vaca Muerta shale rock by counting on the effect of porosity and mineralogical composition. This study is indispensable in shale hydrocarbon stimulation to control the progressive closure of fractures and the loss of well productivity. In most existing time-dependent models ([Shao et al., 2003], [Shao et al., 2006], [Zhou et al., 2008] and [Zhao et al., 2016]), the influence of microstructural constituents is not explicitly taken into account or envisaged through empirical relations. Although, others consider the material heterogeneity ([Bikong et al., 2015] and [Xu et al., 2017]). In our study, the creep behavior is modeled in terms of material degradation: we consider that the time-dependent deformation is a macroscopic consequence of microstructure evolution ([Pietruszczak et al., 2002], [Shao et al., 2003] and [Pietruszczak et al., 2004]). Particularly, in our model, we assume that the origin of macroscopic time-dependent deformation is the damage of clay solid phase. Thus, the evolution of microstructure is considered as the time dependent progressive damage process.

3.1 Formulation of time-dependent behavior

Classically, the time-dependent inelastic deformation of materials is described by the phenomenological viscoplastic theory ([Perzyna, 1966], [Cristescu, 1989], [Simo and Hughes, 1998] and [Lemaitre and Chaboche, 1998]) where the time dependent deformation is attributed to the inherent viscous effect of material. This approach provides a mathematical description of the time dependent behavior: a loading function is defined using the over-stress concept and the viscoplastic strain rate is determined by a corresponding flow rule ([Fodil et al., 1997], [Jin and Cristescu, 1998], [Maranini and Yamaguchi, 2001], [Voyiadjis et al., 2012] and [Zhu and Sun, 2013]). In other studies, the time-dependent deformation is attributed to the progressive degradation of mi-

© 2018 Tous droits réservés.

lilliad.univ-lille.fr

crostructure, such as the dissolution of grain interfaces due to chemical-mechanical coupling ([Gerard et al., 1998] and [Lydzba et al., 2007]), the subcritical propagation of microcracks in hard rocks ([Huang and Shao, 2012] and [Bikong et al., 2015]) and pore collapse in highly porous rocks ([Dahou et al., 1995] and [Xie, 2005]). In this model, we consider that the time-dependent deformation is a macroscopic consequence of microstructure evolution. We suppose that the microcraking inside clay matrix is the time-dependent progressive damage process, leading to the degradation of failure strength of clay matrix solid phase. Thus, the material is now considered constituted of an elastoplastic damage clay matrix and elastic inclusions. Therefore, our goal is to develop a unified approach for the description of both, short and long term elastoplastic damage behavior of material. Thereby, the long term behavior will be an extension of the instantaneous one presented in chapter 2.

As in ([Pietruszczak et al., 2002] and [Shao et al., 2003]), an internal variable ζ is introduced to quantify the microstructural evolution inside the clay matrix. ζ will be function of clay plastic deformation which, in turn, evolves in time t. Thus, the idea is to assume that when $t \to \infty$, $\zeta \to \bar{\zeta}$, where $\bar{\zeta}$ represents a stationary state corresponding to microstructure equilibrium ($\zeta = \bar{\zeta}$). Therefore, the microstructure evolves in time until $\zeta = \bar{\zeta}$ when a equilibrium state is reached. The kinetics of microstructure evolution can be described in terms of the deviation from the equilibrium state given by $(\bar{\zeta} - \zeta)$. A simple linear form of the evolution law is considered as follows:

$$\dot{\zeta} = \gamma(\bar{\zeta} - \zeta) \tag{3.1}$$

where γ is a material constant that controls the rate of primary creep, $\bar{\zeta} \in [0, 1]$ and $\zeta \in [0, \bar{\zeta}]$. As we know, a general creep response is decomposed into three stages: primary, secondary and tertiary creep where the latter corresponds to material failure. Thus, according to our formulation, material failure will occur, when $\bar{\zeta}$ increases very fast compared to ζ so that the latter cannot reach an equilibrium state.

By using Laplace transform, convolution theorem and integration by parts with $\zeta(0)$=0 [Pietruszczak et al., 2004], the definition of ζ becomes:

$$\zeta(t) = \int_0^t \gamma\bar{\zeta}(\tau)\ e^{-\gamma(t-\gamma)}\mathrm{d}\tau = \bar{\zeta}(t) - \int_0^t \frac{\partial\bar{\zeta}}{\partial\tau}\mathrm{e}^{-\gamma(t-\tau)}d\tau \tag{3.2}$$

For computational efficiency, a fast explicit integral algorithm established by [Zhao et al., 2016] is used here to solve numerically the integral (3.2) for the calculation of an explicit form of time dependent variable ζ. For a time increment $\mathrm{d}t_{n+1}$ at a step

© 2018 Tous droits réservés.

lilliad.univ-lille.fr

(n+1), ζ_{n+1} is given as follows:

$$\zeta_{n+1} = \zeta_n \mathrm{e}^{-\gamma \mathrm{d}t_{n+1}} + \gamma \left(\frac{\bar{\zeta}_{n+1} + \bar{\zeta}_n}{2} \right) \mathrm{e}^{-\frac{1}{2}\gamma \mathrm{d}t_{n+1}} \mathrm{d}t_{n+1} \tag{3.3}$$

where $\bar{\zeta}_{n+1}$ and $\bar{\zeta}_n$ are respectively the stationary state variables at actual (n+1) and previous (n) steps.

In the present formulation, the parameter for stationary state of microstructure evolution $\bar{\zeta}$ is identified as:

$$\bar{\zeta} = \frac{\bar{\sigma}}{\sigma_{0m}} \tag{3.4}$$

where $\bar{\sigma}$ is the plastic hardening function (equation 2.11) and σ_{0m}, the asymptotic value of clay solid phase yield stress.

Physically, when coherent materials (cement paste and clay rocks) are leached or completely destroyed under the effect of external factors, they become a granular material; thereby, its cohesion decreases. Thus, based on the concept of damage mechanics, we assume that the time-dependent damage of the clay matrix affects the failure surface (equation 2.7) through the plastic hardening function $\bar{\sigma}$. The latter turns into:

$$\bar{\sigma}^d = \bar{\sigma}(1 - \beta\zeta) \tag{3.5}$$

where β is a model parameter.

A unified model is considered, in this chapter, to study the instantaneous and time-dependent behavior of Vaca Muerta shale rock. The same set of plastic and degradation parameters is used to simulate both, short and long term tests. As we have already presented, the irreversible plastic deformation can take place in an instantaneous manner due to loading variations, or, in a delayed way due to microstructural evolution inside clay matrix. Note that the plastic deformation (either instantaneous or time-dependent) occurs only in the clay phase so the macroscopic plastic strain is equivalent to clay phase microscopic one. The total macroscopic strain rate $\dot{E}_{ij}$ is decomposed into elastic $\dot{E}^e_{ij}$ and plastic $\dot{E}^p_{ij}$ parts:

$$\dot{E}_{ij} = \dot{E}^e_{ij} + \dot{E}^p_{ij} \tag{3.6}$$

The elastic strain rate can be calculated by using Hooke's law and macroscopic elastic properties (section 2.2). In the case of an instantaneous loading, the plastic strain rate is determined according to the definition of the microscopic yield function and plastic flow rule of the clay matrix, given in paragraph 2.3.4.2. Besides, in the case of

© 2018 Tous droits réservés.

lilliad.univ-lille.fr

long term loading, the plastic strain is calculated according to the latter formulation of long term behavior, the definition of the microscopic yield function and plastic flow rule of the clay matrix. The idea is as follows: at the end of instantaneous plastic computation, the clay plastic criterion checks the plastic equilibrium condition ($\Phi < 0$). Then, once the plastic hardening law is degraded (equation 3.5), the plastic criterion may be degraded and the plastic equilibrium condition will no longer be verified ($\Phi > 0$). Thus, a plastic deformation will take place. To understand the formulation of the constitutive model for long term behavior, let's take the example of a creep path. As we know, a creep test consists into two stages: a loading application phase (confining and deviatoric stress) and then a load maintenance one. During the stage of loading application, since its duration is very short, elastic $\dot{E}^e_{ij}$ or plastic $\dot{E}^p_{ij}$ strain takes place depending on stress variations. The effect of time is insignificant in this stage. However, during the load maintenance phase, since the holding time is quite important compared to the duration of application, plastic strain occurs due to the degradation inside clay matrix.

3.2 Algorithm for local integration of the clay phase

The numerical implementation of micromechanical model for short term behavior, given in section 2.3.3.1, remains the same for long term behavior. Only the algorithm for local integration of the elastoplastic damage clay phase will change (step 6.4.) and is presented in this paragraph for a step (n+1) or at time $t_{n+1} = t_n + dt_{n+1}$ as follows:

1. Input data : $\tilde{\boldsymbol{\varepsilon}}_{0,n}$, $\tilde{\boldsymbol{\varepsilon}}^p_{0,n}$, ε^p_n, $\Delta\tilde{\boldsymbol{\varepsilon}}_0$, $\bar{\zeta}_n$, ζ_n and dt_{n+1};

2. Calculating the deformation at step $n+1$: $\tilde{\boldsymbol{\varepsilon}}_{0,n+1} = \tilde{\boldsymbol{\varepsilon}}_{0,n} + \Delta\tilde{\boldsymbol{\varepsilon}}_0$;

3. Initialize (elastic prediction): For $i = 0$

$$\begin{cases} \tilde{\boldsymbol{\varepsilon}}^{p,0}_{0,n+1} = \tilde{\boldsymbol{\varepsilon}}^p_{0,n} \\ \tilde{\boldsymbol{\sigma}}^0_{n+1} = \mathbb{C}_0 : (\tilde{\boldsymbol{\varepsilon}}_{0,n+1} - \tilde{\boldsymbol{\varepsilon}}^{p,0}_{0,n+1}) \\ \bar{\zeta}^0_{n+1} = \bar{\zeta}_n = \frac{\bar{\sigma}_n}{\sigma_{0m}} \\ \zeta^0_{n+1} = \zeta_n \mathrm{e}^{-\gamma \mathrm{d}t_{n+1}} + \gamma \left(\frac{\bar{\zeta}^0_{n+1} + \bar{\zeta}_n}{2} \right) \mathrm{e}^{-\frac{1}{2}\gamma \mathrm{d}t_{n+1}} \mathrm{d}t_{n+1} \\ \bar{\sigma}^{d,0}_{n+1} = \bar{\sigma}_n (1 - \beta \zeta^0_{n+1}) \\ \Phi(\tilde{\boldsymbol{\sigma}}^i_{n+1}, \varepsilon^{p,i}_{n+1}, f) = \Phi^i_{n+1} \end{cases}$$

4. If $\Phi^i_{n+1} \leq 0$ then: go to step 7; else go to step 5 for plastic correction:

5. $$\delta(\Delta\lambda) = \frac{\Phi^i_{n+1}}{\frac{\partial\Phi}{\partial\tilde{\boldsymbol{\sigma}}} : \mathbb{C}_0 : \frac{\partial G}{\partial\tilde{\boldsymbol{\sigma}}} - \frac{\partial\Phi}{\partial f}\left[\frac{\partial G}{\partial\bar{\sigma}_m}(1-f) - 3\alpha_2 \frac{\tilde{\boldsymbol{\sigma}} : \frac{\partial G}{\partial\tilde{\boldsymbol{\sigma}}}}{\bar{\sigma} + 3(\alpha_2 - \alpha)\frac{\bar{\sigma}_m}{1-f}}\right] - \frac{\partial\Phi}{\partial\bar{\sigma}} \frac{\partial\bar{\sigma}}{\partial\varepsilon^p} \frac{\tilde{\boldsymbol{\sigma}} : \frac{\partial G}{\partial\tilde{\boldsymbol{\sigma}}}}{(1-f)\left[\bar{\sigma} + 3(\alpha_2 - \alpha)\frac{\bar{\sigma}_m}{1-f}\right]}}$$

© 2018 Tous droits réservés.

lilliad.univ-lille.fr

6. Calculate new values for each iteration:

$$\begin{cases} \tilde{\boldsymbol{\sigma}}_{n+1}^{i+1} = \tilde{\boldsymbol{\sigma}}_{n+1}^{i} - \delta(\Delta\lambda)\mathbb{C}_0 : \frac{\partial G_{n+1}^{i}}{\partial \tilde{\boldsymbol{\sigma}}}(\tilde{\boldsymbol{\sigma}}_{n+1}^{i}, \varepsilon_{n+1}^{p,i}, f) \\ \varepsilon_{n+1}^{p,i+1} = \varepsilon_{n+1}^{p,i} + \delta(\Delta\lambda)\frac{\tilde{\boldsymbol{\sigma}} : \frac{\partial G}{\partial \tilde{\boldsymbol{\sigma}}}}{(1-f)\left[\bar{\sigma} + 3(\alpha_2 - \alpha)\frac{\tilde{\sigma}_m}{1-f}\right]} \\ \Delta\lambda^{i+1} = \lambda^{i} + \delta(\Delta\lambda) \\ \tilde{\boldsymbol{\varepsilon}}_{n+1}^{p,i+1} = \tilde{\boldsymbol{\varepsilon}}_{n+1}^{p,i} + \delta(\Delta\lambda)\frac{\partial G}{\partial \tilde{\boldsymbol{\sigma}}} \\ \bar{\zeta}^{i+1}_{n+1} = \frac{\bar{\sigma}_{n+1}^{i+1}}{\sigma_{0m}} = \frac{\sigma_{0m} - (\sigma_{0m} - \sigma_{00})\mathrm{e}^{-b\varepsilon_{n+1}^{p,i+1}}}{\sigma_{0m}} \\ \zeta_{n+1}^{i+1} = \zeta_n \mathrm{e}^{-\gamma \mathrm{d}t_{n+1}} + \gamma\left(\frac{\bar{\zeta}_{n+1}^{i+1} + \bar{\zeta}_n}{2}\right)\mathrm{e}^{-\frac{1}{2}\gamma \mathrm{d}t_{n+1}}\mathrm{d}t_{n+1} \\ \bar{\sigma}_{n+1}^{d,i+1} = \bar{\sigma}_{n+1}^{i+1}(1 - \beta\zeta_{n+1}^{i+1}) \end{cases}$$

Set $i = i + 1$ and return to step 4

7. End of Algorithm

3.3 Sensitivity assessment for long term behavior

In this paragraph, a qualitative study is carried out to show different characteristics of the proposed model for long term behavior. For this sensitivity study, we use a typical mineralogical composition of Vaca Muerta shale rock: $f_1 = 0.2$; $f_2 = 0.3$; $f_3 = 0.01$; $f_4 = 0.1$; $f_5 = 0.05$; $f_6 = 0.05$; $f = 0.1$ and the same set of plastic and debonding parameters identified in section 2.3.4.1 in the case of an associated flow rule (table 3.1). In figure 3.1.a, one illustrates the influence of degradation parameter β on creep response: when β increases, the creep deformation is more considerable. In figure 3.1.b, we show the influence of model's parameter γ on creep response. As we can see, γ influences the transition rate from primary to secondary creep: when γ increases, the transition will take place more quickly.

Table 3.1: Set of parameters used in model's qualitative study for time dependent behavior.

Plastic parameters	Debonding parameters
α=0.245	S=0.04
σ_{0m}=50	M=1
σ_{00}=1	
b=650	

© 2018 Tous droits réservés.

lilliad.univ-lille.fr

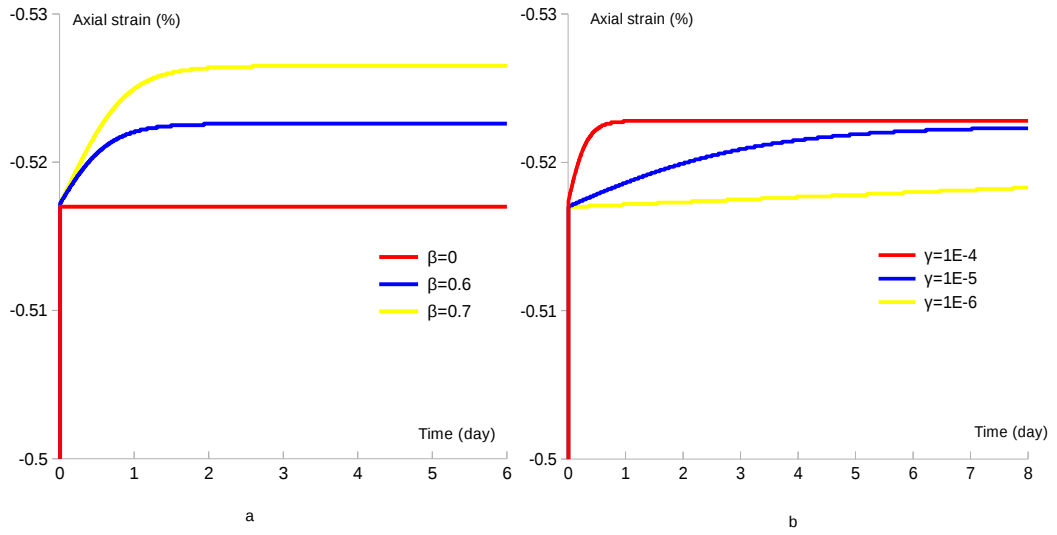

Figure 3.1: a. Influence of creep parameters β ($\gamma = 5.10^{-5}/s$) and b. γ (β=0.6) on creep response (P_a=50 MPa; P_c=0 MPa).

Figure 3.2.a shows the influence of applied axial stress on uniaxial creep response: when the applied axial stress is 60 MPa, only primary and secondary creep are observed. However, when the axial stress reaches 65 or 70 MPa, tertiary creep (failure) occurs. Figure 3.2.b exhibits the variation of microstructural parameter ζ (continuous lines) and stationary state parameter $\bar{\zeta}$ (dashed lines) as function of time for the latter stress conditions. As we can see, for axial stress=60 MPa, after a while, $\zeta \rightarrow \bar{\zeta}$, i.e. the microstructure is in an equilibrium state and the failure does not occur. Whereas, for the case of axial stress=65 or 70 MPa, $\bar{\zeta}$ varies too fast compared to ζ and reaches the limit value ($\bar{\zeta}$=1), implying a spontaneous failure.

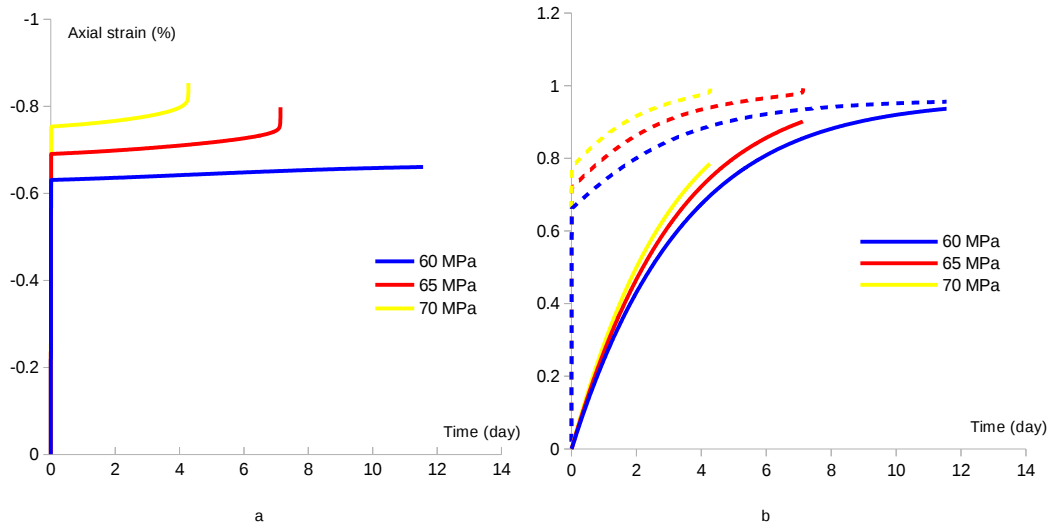

Figure 3.2: a. Influence of applied axial stress on uniaxial creep response; b. Variation of ζ (continuous lines) and $\bar{\zeta}$ (dashed lines) as function of time for the different stress intensities (β=0.7 and γ=$5.10^{-6}/s$).

© 2018 Tous droits réservés.

lilliad.univ-lille.fr

In figure 3.3, one illustrates the simulations of a uniaxial and triaxial multistage creep tests. One can notice that the creep deformation becomes more significant when the axial stress increases. Particularly, in the right simulation, its clear that failure occurs at the second stage.

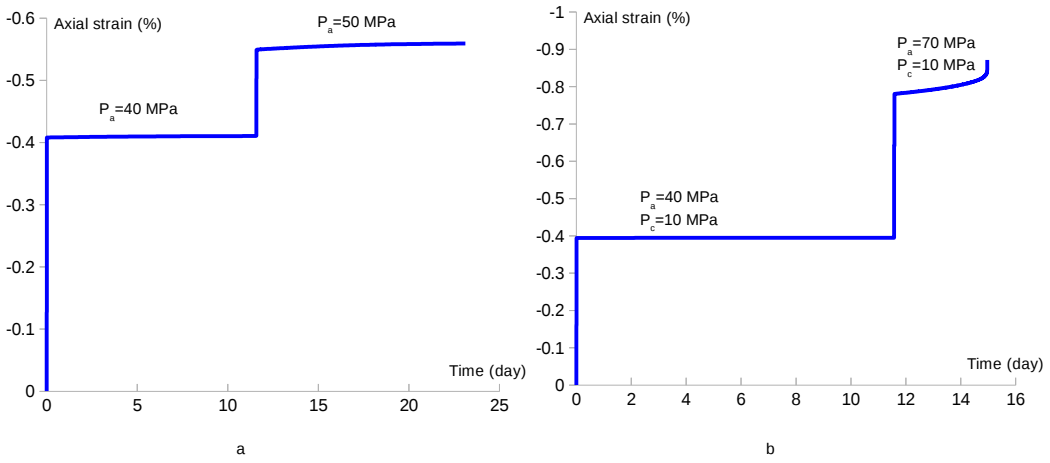

Figure 3.3: a. A multistage uniaxial and b. triaxial creep simulations (β=0.7 and γ=$5.10^{-6}/s$).

In figure 3.4, we show the influence of degradation parameters β and γ on relaxation response. As we can see, the higher the value β, more relaxation is pronounced. As well, when the value of γ increases, the relaxation rate is faster. Notably, the model is able to reproduce relaxation tests.

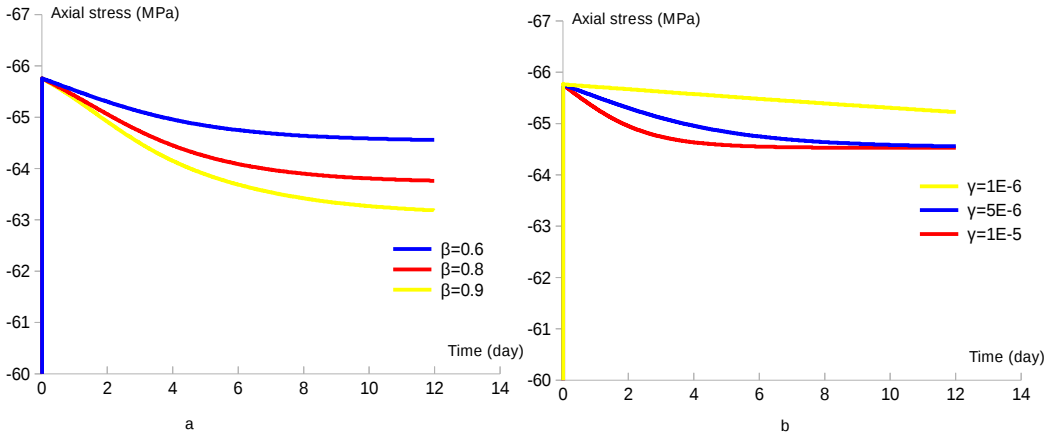

Figure 3.4: a. Influence of degradation parameters β ($\gamma = 5.10^{-6}/s$) and b. γ ($\beta = 0.6$) on relaxation response (axial strain=0.7 % and P_c=0 MPa).

Figure 3.5 exhibits the simulations of a multistage uniaxial and triaxial relaxation tests. One can notice the influence of confining pressure on macroscopic response and the capacity of the model to reproduce multistage relaxation tests.

© 2018 Tous droits réservés.

lilliad.univ-lille.fr

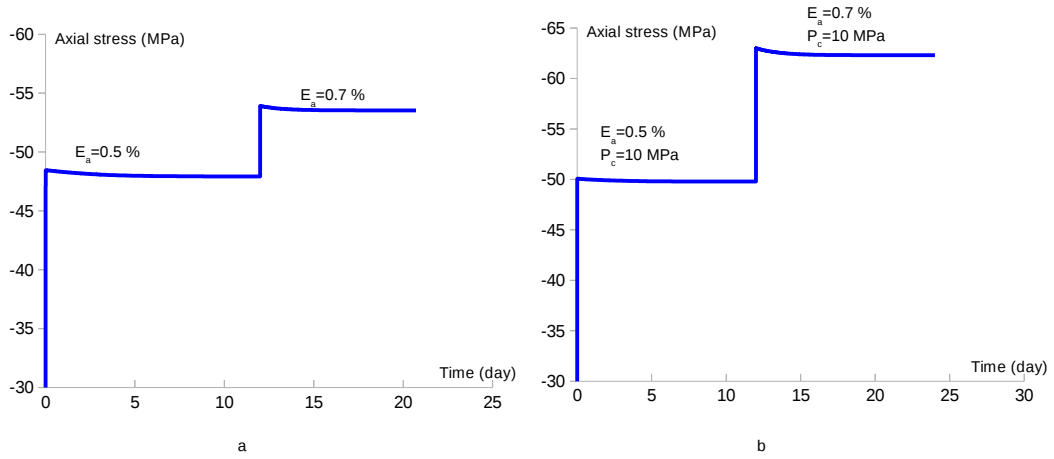

Figure 3.5: a. A multistage uniaxial and b. triaxial relaxation simulations (β=0.7 and $\gamma = 10^{-5}/s$).

Figure 3.6 illustrates stress-strain curves in uniaxial compression tests with different axial strain rates. Apparently, when the axial strain rate is very slow ($< 10^{-6}/s$), a time-dependent deformation takes place which leads to the decrease of the peak strength. As we have already seen in this paragraph, the proposed model is able to reproduce different time dependent loading paths (creep, relaxation and triaxial compression tests with different axial loading rates). Therefore, on a qualitative level, the model is quite rich.

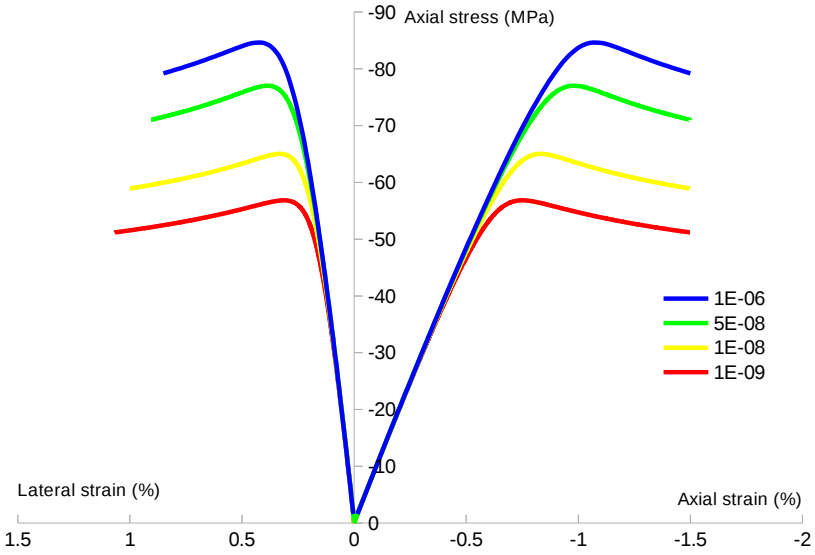

Figure 3.6: Stress-strain curves in a uniaxial compression test with various axial strain rates (β=0.5 and γ=5.$10^{-6}/s$).

© 2018 Tous droits réservés.

lilliad.univ-lille.fr

3.4 Experimental validation of the proposed model

The aim of this paragraph is to simulate creep tests performed on Vaca Muerta shale rock by applying the proposed model. Note that the comparison is done only between creep data and numerical simulations. Relaxation tests on Vaca Muerta shale are in progress and could not be completed before the completion of the thesis. With the same elastic (tables 2.1, 2.2 and 2.3) and plastic parameters (table 2.6) used for the validation of short-term triaxial compression tests, the proposed micromechanical model is applied to simulate creep tests by using the following degradation parameters: $\beta = 0.6$ and $\gamma = 5.10^{-5}$. Figures 3.7 and 3.8 show the comparison between non-associated model simulations and experimental data in two multistage triaxial (P_c=8 MPa and P_c=15 MPa, respectively) compression creep tests on two Vaca Muerta shale samples with different loading conditions. Note that these creep tests are carried out in our laboratory. The results of numerical simulations are quite consistent with the experimental data in quantitative sense. Both axial and lateral deformations are predicted quite accurately. In the two figures, spontaneous failure occurs at the third stage of loading due to unstable degradation process, leading to an accelerated creep deformation. According to experimental curves, for this studied material, the level of creep deformation is weak for the considered stress conditions and then, failure will take place spontaneously when axial stress exceeds a certain limit. Besides, as for the case of instantaneous mechanical behavior, the model is able to take into account the influence of mineralogical composition on the macroscopic behavior.

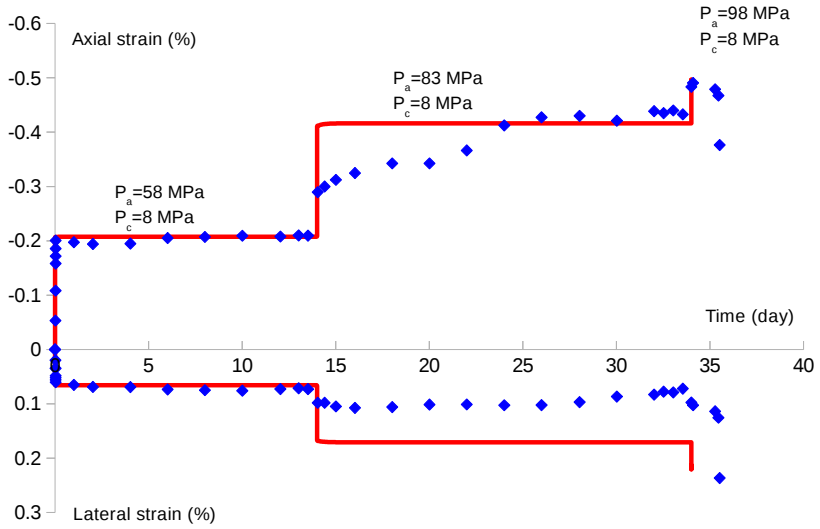

Figure 3.7: Comparison between non-associated model simulations and experimental data in a multistage triaxial compression creep test on a Vaca Muerta shale sample (confining pressure=8 MPa; depth=2668.84 m; well S2; horizontal; f_1=0.143, f_2=0.3, f_3=0.0044, f_4=0.12, f_6=0.13, f=0.1).

© 2018 Tous droits réservés.

lilliad.univ-lille.fr

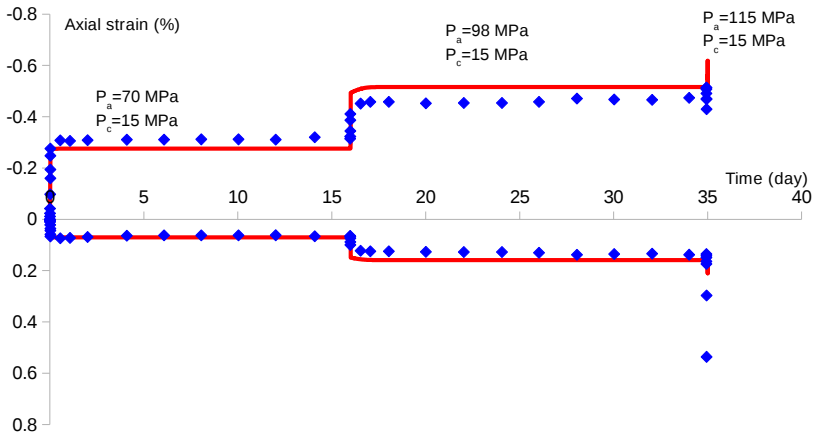

Figure 3.8: Comparison between non-associated model simulations and experimental data in a multistage triaxial compression creep test on a Vaca Muerta shale sample (confining pressure=15 MPa; depth=2768.44 m; well S2; horizontal; f_1=0.249, f_2=0.294, f_3=0.0133, f_4=0.12, f_6=0.12, f=0.15).

According to [Li and Xia, 2000], in a multistage triaxial compression creep test, the effect of strain history, on further evolution of rock deformation by means of irreversible plastic strains cumulated during all previous load levels, has to be taken into account properly. To show the influence of loading path history, we simulate a triaxial compression creep test with a confining pressure of 15 MPa and an axial stress of 115 MPa (figure 3.9). We can clearly distinguish in this figure the three phase of a creep response: transient, stationary and tertiary creep. Failure takes place approximately after few hours of loading retention where $\bar{\zeta} \to 1$ and ζ is smaller (figure 3.10). The purpose is to compare the duration before failure in figure 3.9 with that of the last loading stage of figure 3.8. As we can see, in the latter figure, failure occurs directly during the application of last load. Thereby, the notice of [Li and Xia, 2000] is well verified: a material subjected to multistage loading will suffer a cumulation of creep damage between all stress levels.

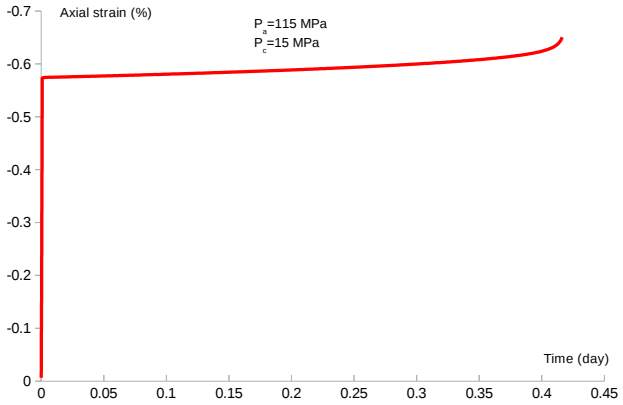

Figure 3.9: Simulation of a triaxial compression creep test with a confining pressure of 15 MPa and a deviatoric stress of 100 MPa.

© 2018 Tous droits réservés.

lilliad.univ-lille.fr

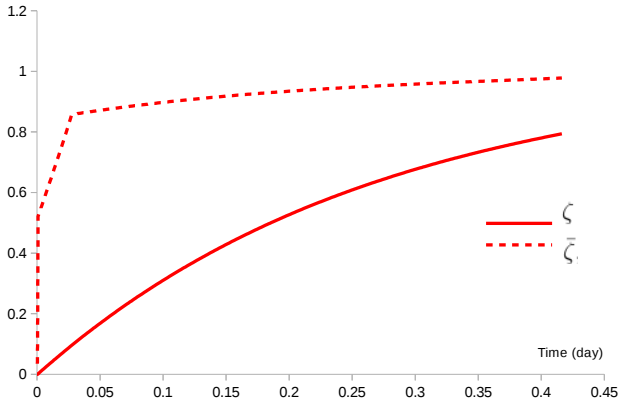

Figure 3.10: Variation of microstructure evolution parameters ζ and $\bar{\zeta}$ as function of time for test given in figure 3.9.

Other multistage creep tests are realized by [Dusterloh, 2015]. Some comparisons between these experimental data and numerical simulations are given in figures 3.11-3.14. It may well be remarked that the comparison seems satisfactory for most cases. Even if the comparison is not perfect, the most importantly is that the model takes into account the effect of mineralogical composition on the macroscopic response.

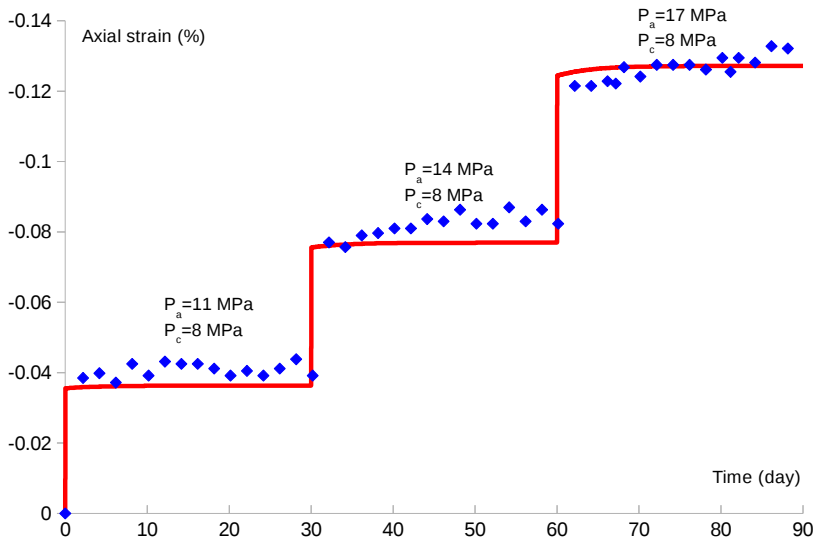

Figure 3.11: Comparison between non-associated model simulations and experimental data in a multistage triaxial compression creep test on a Vaca Muerta shale sample (confining pressure=8 MPa; depth=2537.14 m; well S1; vertical; f_1=0.19, f_2=0.237, f_3=0.016, f_4=0.13, f_6=0.194, f=0.1).

© 2018 Tous droits réservés.

lilliad.univ-lille.fr

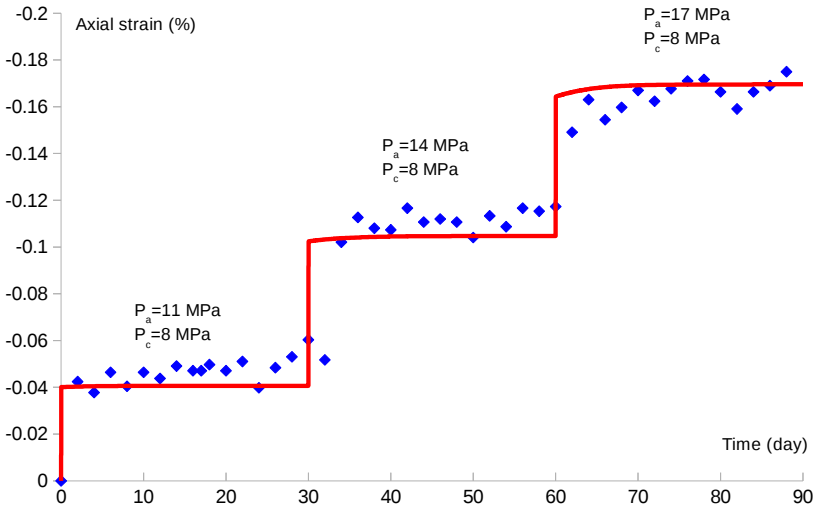

Figure 3.12: Comparison between non-associated model simulations and experimental data in a multistage triaxial compression creep test on a Vaca Muerta shale sample (confining pressure=8 MPa; depth=2537.24 m; well S1; horizontal; f_1=0.2374, f_2=0.236, f_3=0.019, f_4=0.13, f_6=0.337, f=0.087).

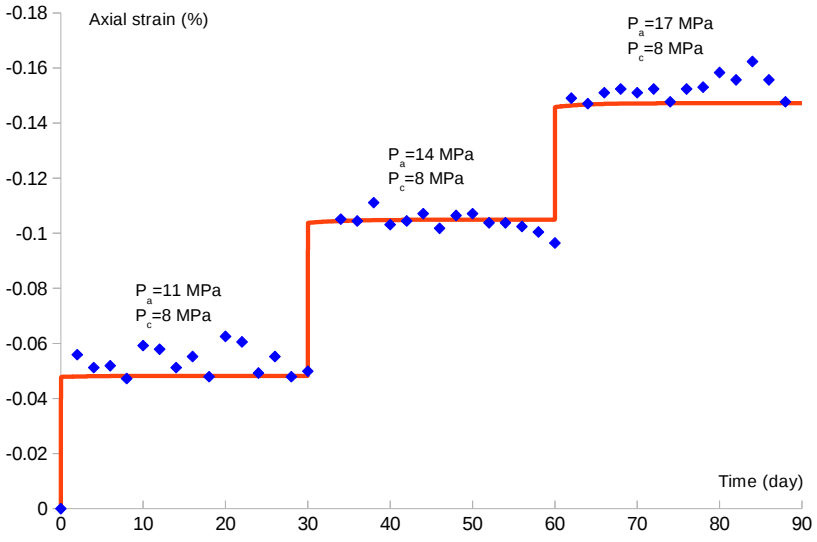

Figure 3.13: Comparison between non-associated model simulations and experimental data in a multistage triaxial compression creep test on a Vaca Muerta shale sample (confining pressure=8 MPa; depth=2546 m; well S1; horizontal; f_1=0.099, f_2=0.55, f_3=0.014, f_4=0.108, f_6=0.05, f=0.095).

© 2018 Tous droits réservés.

lilliad.univ-lille.fr

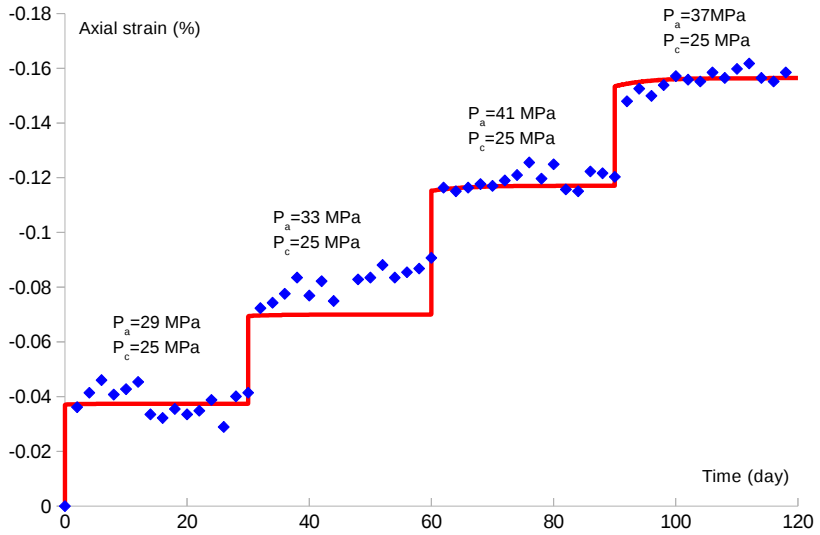

Figure 3.14: Comparison between non-associated model simulations and experimental data in a multistage triaxial compression creep test on a Vaca Muerta shale sample (confining pressure=25 MPa; depth=2568.11 m; well S3; horizontal; f_1=0.208, f_2=0.35, f_3=0.007, f_4=0.191, f=0.15).

3.5 Conclusion

In this chapter, we have studied the time-dependent behavior of Vaca Muerta shale. The differed deformation is described in terms of microstructure evolution, inducing the progressive degradation of material failure strength. The formulation, established by ([Pietruszczak et al., 2002] and [Shao et al., 2003]), is applied to submit a unified model for both instantaneous and long term elastoplastic damage behavior of Vaca Muerta shale. Firstly, the formulation of the constitutive model is presented. Afterward, the algorithm for local integration of the elastoplastic damage clay phase is exposed. Then, a sensitivity study is realized to show the ability of the model to reproduce the different loading paths such as: creep, relaxation and triaxial compression tests with different axial strain rates. Finally, an experimental validation is carried out: a number of comparison between creep experimental data and simulations is performed. Numerical simulations are quite consistent with experimental data in a quantitative sense. Note that the main advantage of this micromechanical model is that it takes into account the effect of mineralogical composition and porosity on the macroscopic response.

© 2018 Tous droits réservés.

lilliad.univ-lille.fr

© 2018 Tous droits réservés.

lilliad.univ-lille.fr

Chapter 4

A simplified viscoplastic model for clayey and shale rocks

Contents

© 2018 Tous droits réservés.

lilliad.univ-lille.fr

In this chapter, a simplified micromechanics based formulation is proposed for clayey and shale rocks. Clayey and shale rocks are considered as a composite material with two scales. At microscale, the clay matrix is a porous medium composed of a solid phase and pores. At mesoscale, the homogenized porous clay matrix is reinforced by different types of inclusions. For simplicity and in order to build an analytical micromechanical model, these inclusions will be replaced by an effective one. The analytical macroscopic plastic criterion of this composite material has been determined using a non linear homogenization method as in [Shen et al., 2013]. This macroscopic criterion is here extended to define the viscoplastic loading function. A unified formulation is proposed to describe both plastic and viscoplastic strains through two distinct yield surfaces. A non-associated potential is introduced to respectively determine the plastic and viscoplastic flow rules. A series of numerical assessment is performed in order to investigate the influence of porosity and mineral composition on both plastic and viscoplastic deformations. Comparisons between numerical results and experimental data on Callovo-Oxfordian argillites and Vaca Muerta shale are also presented to show the capability of the proposed model in reproducing the main features of clayey and shale rocks deformational behavior. Finally, for the industrial application of the thesis, the proposed model is used to study the interaction between Vaca Muerta shale rock and the grains of proppants in order to see if the deferred deformation of the rock will induce a decrease in cracks conductivity.

4.1 Simplified microstructure

In order to obtain an analytical form of macroscopic plastic criterion, the microstructure of clayey and shale rocks is simplified; only two scales are considered. At mesoscopic scale (hundreds of μm to mm), the rock is seen as a composite material with a continuous clay matrix which is reinforced by a random distribution of spherical inclusions. For clayey rock, quartz and carbonates are the mesoinclusions but for shale rock, we consider quartz, carbonates, pyrite and kerogen. The mechanical behavior of all these mesoinclusions can be described by a linear isotropic elastic model. At microscopic scale ($\sim \mu$m), the clay matrix is considered as an assembly of clay particles and interparticle pores. The latter are supposed spherical and having a size smaller than that of mineral inclusions. Therefore, the clay matrix is approximated by a porous medium with a continuous solid phase and spherical pores. As a first approximation, for clayey and shale rocks, we suppose that all mesoinclusions are merged into one family of inclusions at mesoscale. According to [Shen et al., 2013], the representative volume element (RVE) of the simplified material is illustrated in figure 4.1.

One denotes, Ω_p, Ω_i and Ω_m, the volume of pores, mineral inclusions and solid clay matrix respectively. Then, the relative porosity of the clay matrix f and the volume

© 2018 Tous droits réservés.

lilliad.univ-lille.fr

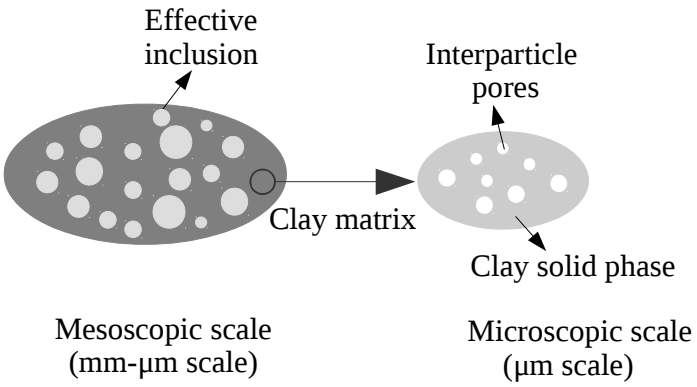

Figure 4.1: A simplified representation of typical clayey and shale rocks [Shen et al., 2013].

fraction of inclusions ρ are given by the following relations:

$$f = \frac{\Omega_p}{\Omega_p + \Omega_m}; \quad \rho = \frac{\Omega_i}{\Omega_i + \Omega_m + \Omega_p} \tag{4.1}$$

4.2 A unified plastic and viscoplastic model

The plastic deformation in clayey and shale rocks is mainly related to the irreversible evolution of clay matrix such as sliding along clay sheets and to the growth of microcracks at grain-matrix interfaces and eventually inside the matrix. The plastic deformation can take place in an instantaneous way due to stress variations and other external loads, and also in a delayed manner due to viscous sliding and subcritical propagation of microcracks. At the macroscopic scale, this leads to both instantaneous and time-dependent plastic deformations. Differently than classical approaches where separate models are used to describe plastic and viscoplastic deformations, a unified formulation will be developed here. The same physical processes are considered and the viscoplastic deformation is seen as a delayed plastic deformation. The plastic and viscoplastic deformations are described by the same form of yield function and flow potential. The loading surface of viscoplastic deformation is inside the yield surface of plastic deformation, as shown in figure 4.2. The stress state, verifying the plastic equilibrium condition but being outside the viscoplastic loading surface, may produce time-dependent creep deformation. Therefore, the total macroscopic strain rate is decomposed into an elastic part $\dot{E}^e_{ij}$, an instantaneous plastic part $\dot{E}^p_{ij}$ and a time-dependent viscoplastic part $\dot{E}^{vp}_{ij}$:

$$\dot{E}_{ij} = \dot{E}^e_{ij} + \dot{E}^p_{ij} + \dot{E}^{vp}_{ij} \tag{4.2}$$

The elastic strain can be calculated by using the macroscopic elastic properties. The plastic strain rate should be determined by the definition of a macroscopic yield

© 2018 Tous droits réservés.
lilliad.univ-lille.fr

function and a plastic flow rule while the viscoplastic strain rate by a viscoplastic loading function and a flow rule.

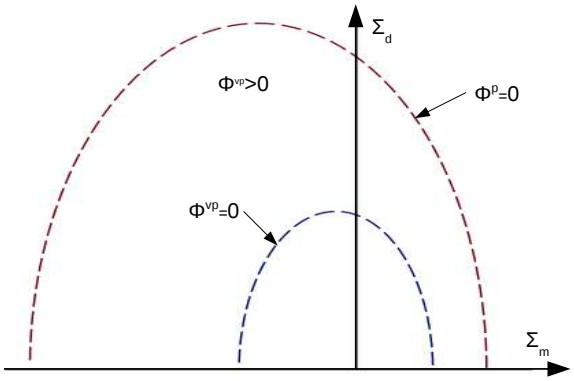

Figure 4.2: Illustration of instantaneous macroscopic plastic yield surface ϕ^p and viscoplastic loading surface ϕ^{vp}.

4.2.1 Macroscopic plastic yield criterion

Following the definition of two material scales shown in figure 4.1, the macroscopic plastic yield criterion can be obtained from a two-step non linear homogenization procedure. As the macroscopic plastic deformation in clayey and shale rocks is generated by the solid clay grains, the starting point is to define its local behavior. As for most cohesive-frictional materials, it is assumed that local plastic behavior is described by the classical Drucker-Prager criterion (we used the same notations as in [Shen et al., 2013]):

$$\phi^m(\tilde{\sigma}) = \tilde{\sigma}_d + T(\tilde{\sigma}_m - h) \leq 0 \tag{4.3}$$

where $\tilde{\sigma}$ is the local stress tensor in the solid clay phase, $\tilde{\sigma}_m$ the corresponding mean stress and $\tilde{\sigma}_d = \sqrt{\tilde{\sigma}' : \tilde{\sigma}'}$ the equivalent shear stress, related to the deviatoric stress tensor $\tilde{\sigma}'$. The parameter h defines the hydrostatic tensile strength and T the frictional coefficient. It is useful to point out that Drucker-Prager criterion contains two stress invariants only and does not consider the effect of third invariant or Lode angle.

By using the modified secant method proposed by [Maghous et al., 2009] or equivalently the variational approach by [Suquet, 1995], an analytical form of the macroscopic plastic yield function for a porous medium reinforced by rigid inclusions has been obtained by [Shen et al., 2013] and expressed in the following form:

$$\Phi^p(\Sigma, f, \bar{T}) = \Theta\Sigma_d^2 + \left(\frac{3f}{2\bar{T}^2} - 1\right)\Sigma_m^2 + 2(1-f)h\Sigma_m - \frac{3+2f+3f\rho}{3+2f}(1-f)^2h^2 = 0 \tag{4.4}$$

© 2018 Tous droits réservés.

lilliad.univ-lille.fr

with:

$$\Theta = \frac{\frac{1+2f/3}{\bar{T}^2} + \frac{2}{3}\rho\left(\frac{3f}{2\bar{T}^2} - 1\right)}{\frac{4\bar{T}^2-12f-9}{6\bar{T}^2-13f-6}\rho + 1}$$

Σ is the macroscopic stress tensor, Σ_m the corresponding mean stress and $\Sigma_d = \sqrt{\Sigma' : \Sigma'}$, the equivalent shear stress related to the macroscopic deviatoric stress Σ'. Experimental data of geomaterials show that the solid clay phase could exhibit significant plastic hardening. In order to account for this process, it is assumed that the frictional coefficient T varies with the equivalent plastic strain of the solid clay phase ϵ^p to be identified later. The following exponential hardening law is here proposed:

$$\bar{T} = T_m - (T_m - T_0)e^{-b_1\epsilon^p} \tag{4.5}$$

where T_0 is the initial threshold of the frictional coefficient, T_m its asymptotic value and b_1 the parameter which controls the kinetics of hardening.

4.2.2 Macroscopic viscoplastic loading function

Following the unified concept proposed here and as shown in figure 4.2, the viscoplastic loading surface is delayed with respect to the instantaneous plastic yield surface. The plastic yield surface evolution is controlled by both the porosity change and the variation of frictional coefficient $\bar{T}$ defined in equation 4.5. As the porosity has a common effect on both plastic yield and viscoplastic loading surfaces, it is assumed that the delay of the viscoplastic loading function is controlled by a viscoplastic hardening function $\bar{T}_{vp}(\epsilon^p)$ with the following condition: $\bar{T}_{vp}(\epsilon^p) \leq \bar{T}_p(\epsilon^p)$. Note that when $\bar{T}_{vp} = \bar{T}_p$, the two surfaces coincide and the viscoplastic flow vanishes. The viscoplastic hardening function is expressed in the following form:

$$\bar{T}_{vp} = T_m - (T_m - T_0)e^{-b_{vp}\epsilon^p} \tag{4.6}$$

The parameter b_{vp} controls the kinetics of viscoplastic loading surface evolution. By comparing the two hardening functions 4.5 and 4.6, one gets the following condition $b_{vp} < b_1$. Replacing $\bar{T}_p$ by $\bar{T}_{vp}$ in equation 4.4, the viscoplastic loading function Φ^{vp} is expressed as follows:

$$\Phi^{vp}(\Sigma, f, \bar{T}_{vp}) = \Theta\Sigma_d^2 + \left(\frac{3f}{2\bar{T}_{vp}^2} - 1\right)\Sigma_m^2 + 2(1-f)h\Sigma_m - \frac{3+2f+3f\rho}{3+2f}(1-f)^2h^2 \geq 0 \tag{4.7}$$

with:

$$\Theta = \frac{\frac{1+2f/3}{\bar{T}_{vp}^2} + \frac{2}{3}\rho\left(\frac{3f}{2\bar{T}_{vp}^2} - 1\right)}{\frac{4\bar{T}_{vp}^2-12f-9}{6\bar{T}_{vp}^2-13f-6}\rho + 1}$$

© 2018 Tous droits réservés.

lilliad.univ-lille.fr

4.2.3 Plastic and viscoplastic flow rules

In most geomaterials, a transition from volumetric compressibility to dilatancy is generally observed under high deviatoric loading. In order to take into account this transition, a non-associated flow rule is needed. Inspired by the previous studies ([Maghous et al., 2009] and [Shen et al., 2013]), a heuristic method is here adopted. The plastic potential is defined by modifying the plastic yield criterion and by introducing a dilatancy coefficient $\bar{t}$ as follows:

$$G^p(\Sigma, f, \bar{T}, \bar{t}) = \Theta\Sigma_d^2 + \left(\frac{3f}{2\bar{T}\bar{t}} - 1\right)\Sigma_m^2 + 2(1-f)h\Sigma_m - \frac{3+2f+3f\rho}{3+2f}(1-f)^2h^2 \quad (4.8)$$

with:

$$\Theta = \frac{\frac{1+2f/3}{\bar{T}\bar{t}} + \frac{2}{3}\rho\left(\frac{3f}{2\bar{T}\bar{t}} - 1\right)}{\frac{4\bar{T}\bar{t}-12f-9}{6\bar{T}\bar{t}-13f-6}\rho + 1}$$

Further, it is assumed that the dilatancy coefficient $\bar{t}$ evolves with plastic deformation and it is also a function of the equivalent plastic strain ϵ^p:

$$\bar{t} = t_m - (t_m - t_0)e^{-b_2\epsilon^p} \quad (4.9)$$

t_m, t_0 and b_2 are three parameters used for the evolution of the dilatancy coefficient. If $\bar{t} = \bar{T}$, the associated flow rule is recovered. Accordingly, the plastic flow rule is given by:

$$\dot{E}^p = \dot{\lambda}^p \frac{\partial G^p}{\partial \Sigma}(\Sigma, f, \bar{T}, \bar{t}) \quad (4.10)$$

$\dot{\lambda}^p$ is the positive plastic multiplier verifying the following loading-unloading conditions:

$$\begin{cases} \dot{\lambda}^p = 0 & \text{if} \quad \Phi^p < 0 \quad \text{or} \quad \text{if} \quad \Phi^p = 0 \quad \text{and} \quad \dot{\Phi}^p < 0 \\ \dot{\lambda}^p \geq 0 & \text{if} \quad \Phi^p = 0 \quad \text{and} \quad \dot{\Phi}^p = 0 \end{cases} \quad (4.11)$$

The equivalent plastic strain rate in the solid clay phase $\dot{\epsilon}^p$ is defined according to the energy condition during the upscaling procedure ([Gurson, 1977], [Maghous et al., 2009] and [Shen et al., 2013]). In the absence of viscoplastic flow, one gets:

$$\dot{\epsilon}^p = \frac{\Sigma : \dot{E}^p}{(1-f)(1-\rho)\left[\bar{T}h + (\bar{t} - \bar{T})\frac{\Sigma_m}{1-f}\right]} \quad (4.12)$$

Then, the variation of porosity is determined from the kinematical compatibility and is given by:

$$\dot{f} = \frac{1-f}{1-\rho} tr\dot{E}^p - (1-f)\bar{t}\dot{\epsilon}^p \quad (4.13)$$

© 2018 Tous droits réservés.

lilliad.univ-lille.fr

In a similar way that for the plastic potential, the non-associated viscoplastic potential is defined in the following form:

$$G^{vp}(\Sigma, f, \bar{T}_{vp}, \bar{t}) = \Theta\Sigma_d^2 + \left(\frac{3f}{2\bar{T}_{vp}\bar{t}} - 1\right)\Sigma_m^2 + 2(1-f)h\Sigma_m - \frac{3+2f+3f\rho}{3+2f}(1-f)^2h^2 \quad (4.14)$$

with:

$$\Theta = \frac{\frac{1+2f/3}{\bar{T}_{vp}\bar{t}} + \frac{2}{3}\rho\left(\frac{3f}{2\bar{T}_{vp}\bar{t}} - 1\right)}{\frac{4\bar{T}_{vp}\bar{t}-12f-9}{6\bar{T}_{vp}\bar{t}-13f-6}\rho + 1}$$

The viscoplastic flow rule is determined by the over-stress concept [Perzyna, 1966] and expressed by the following power law:

$$\dot{E}^{vp} = \dot{\lambda}^{vp}\frac{\partial G^{vp}}{\partial \Sigma}(\Sigma, f, \bar{T}_{vp}, \bar{t}) \quad (4.15)$$

The viscoplastic multiplier $\dot{\lambda}^{vp}$ is calculated by:

$$\begin{cases} \dot{\lambda}^{vp} = 0 & \text{if} \quad \Phi^{vp} \leq 0 \\ \dot{\lambda}^{vp} = \frac{h}{\eta}\left(\frac{\Phi^{vp}}{h}\right)^m & \text{if} \quad \Phi^{vp} > 0 \end{cases} \quad (4.16)$$

Two parameters are introduced to calculate the viscoplastic strain rate. η corresponds to the viscosity of materials and determines the initial viscoplastic strain rate while the power m controls the evolution of viscoplastic strain rate.

In the absence of instantaneous plastic deformation, the variations of equivalent plastic strain $\dot{\epsilon}^p$ and of porosity $\dot{f}$ are given by:

$$\dot{\epsilon}^p = \frac{\Sigma : \dot{E}^{vp}}{(1-f)(1-\rho)\left[\bar{T}_{vp}h + (\bar{t} - \bar{T}_{vp})\frac{\Sigma_m}{1-f}\right]} \quad (4.17)$$

$$\dot{f} = \frac{1-f}{1-\rho}tr\dot{E}^{vp} - (1-f)\bar{t}\dot{\epsilon}^p \quad (4.18)$$

When both instantaneous plastic and viscoplastic deformations occur, the variations of equivalent plastic strain $\dot{\epsilon}^p$ and of porosity $\dot{f}$ are given by:

$$\dot{\epsilon}^p = \frac{\Sigma:\dot{E}^p}{(1-f)(1-\rho)\left[\bar{T}h + (\bar{t}-\bar{T})\frac{\Sigma_m}{1-f}\right]} + \frac{\Sigma:\dot{E}^{vp}}{(1-f)(1-\rho)\left[\bar{T}_{vp}h + (\bar{t}-\bar{T}_{vp})\frac{\Sigma_m}{1-f}\right]} \quad (4.19)$$

$$\dot{f} = \frac{1-f}{1-\rho}(tr\dot{E}^p + tr\dot{E}^{vp}) - (1-f)\bar{t}\dot{\epsilon}^p \quad (4.20)$$

4.3 Numerical assessment

4.3.1 Influence of microstructure on macroscopic criterion

In this section, a series of numerical simulations are presented in order to show the influence of microstructure on macroscopic plastic criterion. In figure 4.3, one il-

© 2018 Tous droits réservés.

lilliad.univ-lille.fr

lustrates the macroscopic plastic yield surface for different values of porosity f and volumetric fraction of mineral inclusions ρ, using the representative parameters given in table 4.1. One can clearly see that the macroscopic yield surface is strongly influenced by the porosity of material. Both hydrostatic compression and shear yield stresses significantly increase with the decrease of porosity. The hydrostatic tensile yield stress also increases with the decrease of porosity but with a more moderated manner than the previous ones. However, it seems that the influence of inclusion volumetric fraction on the macroscopic yield surface is less significant than that of the porosity, in particular for the yield stresses under hydrostatic compression and tension. Only the shear yield stress is significantly influenced by the inclusion volume fraction.

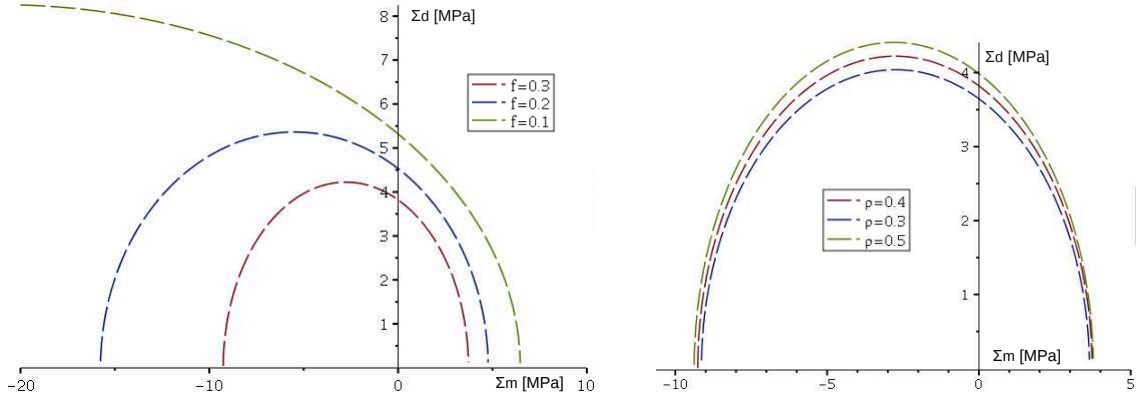

(a) (b)

Figure 4.3: Influence of (a) porosity f and (b) volumetric fraction of inclusions ρ on macroscopic instantaneous yield surface Φ^p.

Table 4.1: Reference parameters for the sensitivity analysis.

T	f	ρ	h
0.3	0.3	0.4	16 MPa

4.3.2 Influence of microstructure on typical loading paths

In the following, the response of the proposed micromechanics based model is evaluated for some typical loading paths, namely, instantaneous triaxial compression, creep, relaxation and lateral extension tests with constant mean stress. Elastic, plastic and viscoplastic parameters, given in table 4.2, are used for this sensitivity study. An associated flow rule is supposed.

© 2018 Tous droits réservés.

lilliad.univ-lille.fr

Table 4.2: Typical values of parameters used in sensitivity analysis.

	Phase (0) clay	Phase (1) inclusion
Elastic parameters	E_s=5.5 GPa	E_i=98 GPa
	ν_s=0.34	ν_i=0.15
Plastic parameters	T_0=0	
	T_m=0.78	
	b_1=150	
	h=16 MPa	
Viscoplastic parameters	$\eta = 10^{13}$	
	b_{vp}=90	
	m=2	

In figure 4.4, the mechanical response in a uniaxial compression test with an axial strain rate of $10^{-6}/s$ is presented, respectively for three values of porosity and inclusion volume fraction. One can logically see that both the macroscopic elastic modulus and failure strength increase with the increase of mineral inclusion fraction and with the decrease of porosity. Compared with classical phenomenological models, by using the proposed micromechanics based model, the macroscopic elastic properties and the macroscopic yield stresses are explicitly dependent on porosity and inclusion volume fraction. Furthermore, it is also possible to directly calculate the evolutions of porosity and inclusion volume fraction together with those of plastic strains from the relation 4.20.

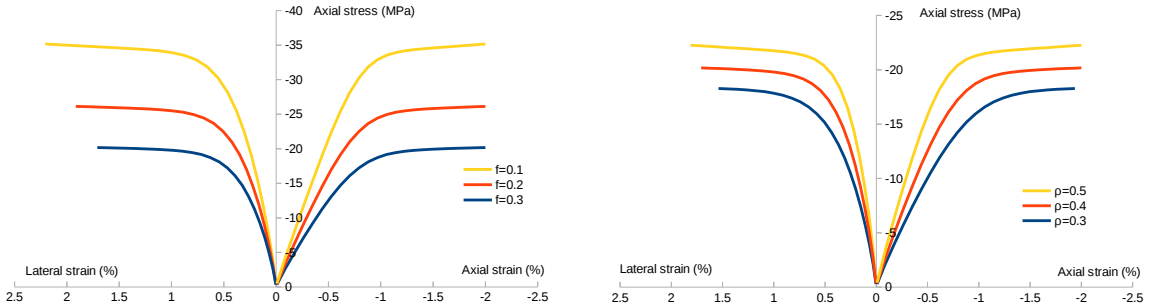

(a) (b)

Figure 4.4: Stress-strain curves in an uniaxial compression test with (a) different values of porosity f and (b) inclusion volume fraction ρ .

In figure 4.5, the evolution of axial strain, during a uniaxial creep test with an axial stress of 5 MPa, is illustrated in function of time. The axial strain contains two stages: the instantaneous strain due to the application of axial stress and the creep

© 2018 Tous droits réservés.

lilliad.univ-lille.fr

strain. As in a uniaxial compression test, the instantaneous strain is significantly affected by the porosity and inclusion fraction. The creep strain rate increases with the increase of porosity and the decrease of inclusion fraction. In figure 4.6, one also shows the axial stress evolution during a uniaxial relaxation test (axial strain=0.3 %) for different values of porosity and inclusion volume fraction; we can well notice the influence of microstructure on the macroscopic relaxation response.

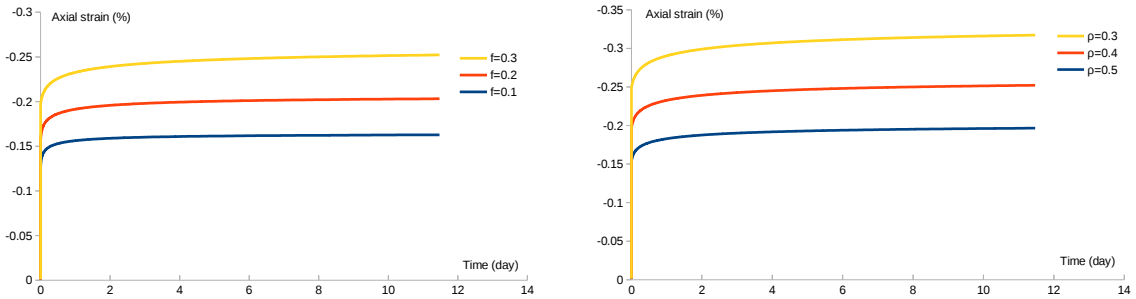

(a) (b)

Figure 4.5: Evolution of axial strain with time in an uniaxial creep test (axial stress= 5 MPa) for (a) different values of porosity f and (b) inclusion's volumetric fraction ρ.

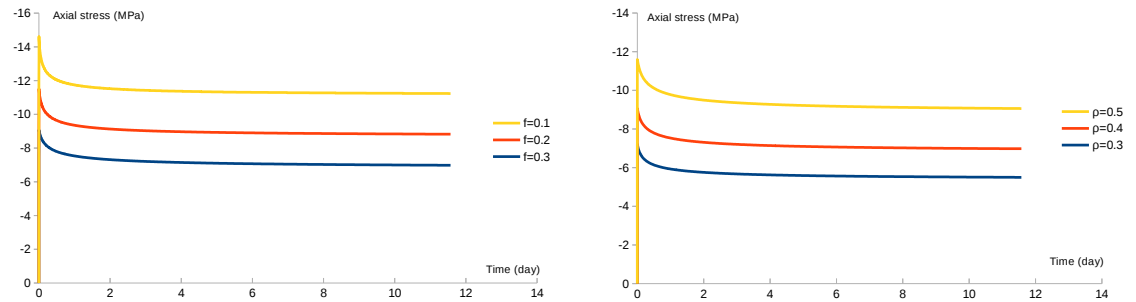

(a) (b)

Figure 4.6: Evolution of axial stress in an uniaxial relaxation test (axial strain=0.3%) for (a) different values of porosity f and (b) inclusion's volumetric fraction ρ.

To complete this sensitivity study, the response in a lateral extension test with constant mean stress is here studied. In this loading path, starting from a hydrostatic stress state, the lateral stress (confining pressure) is decreased while the axial stress is increased to keep the mean stress constant. This loading path is seen as representative of stress evolution in surrounding rock around an underground cavity during excavation. In figure 4.7, one shows the stress-strain curves during a lateral extension test with an initial confining pressure of 12 MPa. From this sensitivity study, it can be concluded that the mechanical strength is reduced by the increase of porosity; however, the material is reinforced by the increase of inclusion volume fraction. Further,

© 2018 Tous droits réservés.

lilliad.univ-lille.fr

it is interesting to note that even if the inclusion volume fraction has a relatively less important effect on the macroscopic yield surface than the porosity, as shown in figure 4.3, it still has a significant effect on the macroscopic deformation of the material. This is due to the fact that the evolutions of porosity and inclusion volume fraction are inherently coupled according to relations 4.19 and 4.20.

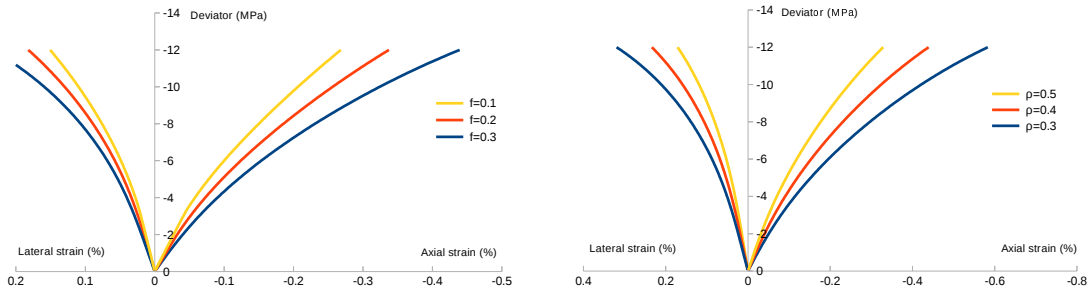

(a) (b)

Figure 4.7: Stress-strain curves in a lateral extension test with constant mean stress: (a) influence of porosity f and (b) inclusion's volumetric fraction ρ.

4.4 Experimental validation of the non-associated model

To check the performance of the proposed micromechanical model, a series of experimental validation is realized on Callovo-Oxfordian argillite and Vaca Muerta shale rock. The model seems able to predict the main instantaneous and time-dependent mechanical behaviors of clayey and shale rocks.

4.4.1 Callovo-Oxfordian argillites

In this section, numerical results are compared with experimental data obtained on a typical Callovo-Oxfordian claystone, studied in the framework of radioactive waste in France [Conil and Armand, 2015]. The mineralogical composition and porosity of this clayey rock vary with geological depth. Only a representative layer is considered here. The layer is in an average way composed of 54% of clay matrix and 46 % of elastic mineral grains (carbonate and quartz). The overall porosity varies from 14.72% to 17.08%. For this material, the porosity is assumed totally embedded in the clay matrix. Thus, with the given mineralogical composition, the average relative porosity of the clay matrix is about $f = 30\%$. In the first part of this paragraph, four elastic, seven plastic and three viscoplastic parameters for Callovo-Oxfordian argillites are identified. Then, a series of comparisons between experimental data and numerical

© 2018 Tous droits réservés.

lilliad.univ-lille.fr

simulations is carried out to check the performance of the proposed model.

4.4.1.1 Identification of model parameters for clayey rocks

The effective elastic properties are determined by performing two steps of linear homogenization. At the first step, the effective elastic properties of the porous clay matrix are determined. One assumes that the isotropic elastic behavior of the solid clay phase is characterized by its bulk and shear moduli noted as κ_s and μ_s. Considering that pores are embedded into the solid clay matrix, it is convenient to apply the classical Mori-Tanaka scheme [Mori and Tanaka, 1973], which is equivalent to the Hashin's upper bound [Hashin and Shtrikman, 1963]. The effective bulk and shear moduli of the porous clay matrix, noted as κ_0 and μ_0, are given by:

$$\kappa_0 = \frac{4(1-f)\kappa_s\mu_s}{4\mu_s + 3f\kappa_s}; \quad \mu_0 = \frac{(1-f)\mu_s}{1 + 6f\frac{\kappa_s+2\mu_s}{9\kappa_s+8\mu_s}} \tag{4.21}$$

At the second step, the effective macroscopic elastic properties of Callovo Oxfordian claystone are determined. At mesoscopic scale, mineral grains are embedded into the porous clay matrix which is homogenized at the first step. Again, one applies Mori-Tanaka homogenization scheme due to matrix-inclusion morphology. The homogenized bulk and shear moduli, noted as κ^{hom} and μ^{hom}, are given by the following relations:

$$\kappa^{hom} = \frac{\sum_{r=0} f_r \frac{\kappa_r}{3\kappa_r+4\mu_0}}{\sum_{s=0} \frac{f_s}{3\kappa_s+4\mu_0}} \tag{4.22a}$$

$$\mu^{hom} = \frac{\sum_{r=0} f_r \frac{\mu_r}{\mu_0(9\kappa_0+8\mu_0)+6\mu_r(\kappa_0+2\mu_0)}}{\sum_{s=0} \frac{f_s}{\mu_0(9\kappa_0+8\mu_0)+6\mu_s(\kappa_0+2\mu_0)}} \tag{4.22b}$$

with: f_r is the volumetric fraction of phase (r); (κ_r, μ_r) are respectively bulk and shear moduli of phase (r).

In practice, in order to apply the relations 4.22, it is necessary to know the elastic properties of solid clay matrix and mineral grains, as well as, the mineralogical composition. The elastic properties of carbonate and quartz can be found in many published literatures, for instance, the handbook of Chemistry and Physics [Lide, 2004]. As an example, Young's modulus and Poisson coefficient of carbonate grains and those of quartz grains are respectively about: $E_c = 95$ GPa and $\nu_c = 0.27$, $E_q = 101$ GPa and $\nu_q = 0.06$. In the present work, as we have already said, for the sake of simplicity and in order to find an analytical expression of macroscopic plastic

© 2018 Tous droits réservés.

lilliad.univ-lille.fr

yield criterion of clayey and shale rocks, the two families of mineral grains are mixed into an equivalent inclusion phase. As in [Jiang et al., 2009], the elastic properties of the equivalent inclusion phase are given by the average of those of quartz and carbonates: $E_i = 98$ GPa and $\nu_i = 0.165$. However, it is a hard task to determine the elastic properties of clay matrix. Some attempts have been made to directly measure the local elastic properties of clay particles using different techniques such as nanoindentation. But large scatters have been found and it is not easy to obtain representative values. An alternative way is used here, based on an inverse approach. Given the values of porosity and volume fraction of inclusions, as well as, the experimental macroscopic Young's modulus E^{hom} and Poisson's ratio ν^{hom} (obtained from a uniaxial compression test on a representative sample), then, by the inversion of the homogenized relations 4.22, it will be possible to get the elastic properties of the porous clay matrix E_0 and ν_0 (or equivalently κ_0 and μ_0). As an example, according to some studies on Callovo-Oxfordian claystone ([Abou-Chakra Guéry et al., 2008] and [Shen et al., 2012]) with a porosity f=0.3, one has obtained the elastic properties of the porous clay matrix: $E_0 = 3$ GPa and $\nu_0 = 0.3$, and then, those of the solid clay grains: $E_s = 5.57$ GPa and $\nu_2 = 0.34$.

As for elastic parameters, the direct identification of plastic and viscoplastic ones from local measurements is so far an open issue; an alternative indirect method is used. For a selected mineralogical composition and stress conditions, the plastic and viscoplastic parameters are identified, respectively, by numerical fitting on a triaxial compression and creep tests. The obtained values are then validated for other mineralogical compositions and stress states. To identify plastic and viscoplastic parameters, we used, respectively, a triaxial compression test with a confining pressure of 6 MPa (figure 4.9) and a triaxial creep test with a confining pressure of 6 MPa and a deviatoric stress of 7 MPa (figure 4.11-50 % of peak differential stress). The identified parameters for Callovo-Oxfordian argillites are summarized in table 4.3 and used in all numerical simulations presented below. In all following figures, continuous curve represent numerical simulations and symbolic ones correspond to experimental data.

4.4.1.2 Triaxial compression tests

In figures 4.8, 4.9 and 4.10, one shows the comparisons between simulations and experimental data on Callovo-Oxfordian argillites for three triaxial compression tests with three confining pressures (2, 6 and 12 MPa). These tests were performed with a constant axial strain rate of 10^{-6}/s. In a general way, there is a good agreement for both axial and lateral strains and for all values of confining pressure. However, some

© 2018 Tous droits réservés.

lilliad.univ-lille.fr

Table 4.3: Typical values of parameters for Callovo-Oxfordian argillites.

	Phase (0) clay	Phase (i) inclusion
Elastic parameters	E_s=5.5 GPa	E_i=98 GPa
	ν_s=0.34	ν_i=0.165
Plastic parameters	T_0=0	
	T_m=0.78	
	b_1=150	
	t_0=0	
	t_m=0.45	
	b_2=150	
	h=16 MPa	
Viscoplastic parameters	$\eta = 10^{15}$	
	b_{vp}=60	
	m=2	

differences are obtained, especially for the volumetric strain. Several explanations can be given. The studied claystone is a strongly heterogeneous rock; the mineralogical composition may be quite different between samples, while averaged values are used in all simulations. Besides, the mechanical behavior of claystone is further very sensitive to water content, which can be significantly modified during core drilling, core transportation and sample preparation. Finally, microcracks can be induced in samples during preparation and due to drying-saturation process. However, the main features of the instantaneous mechanical behavior of the studied claystone is well reproduced by the proposed model.

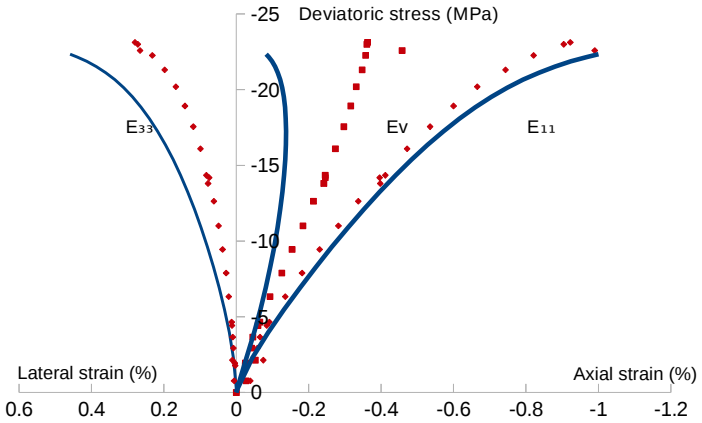

Figure 4.8: Comparison between numerical results and experimental data in a triaxial compression test with a confining pressure of 2 MPa.

© 2018 Tous droits réservés.

lilliad.univ-lille.fr

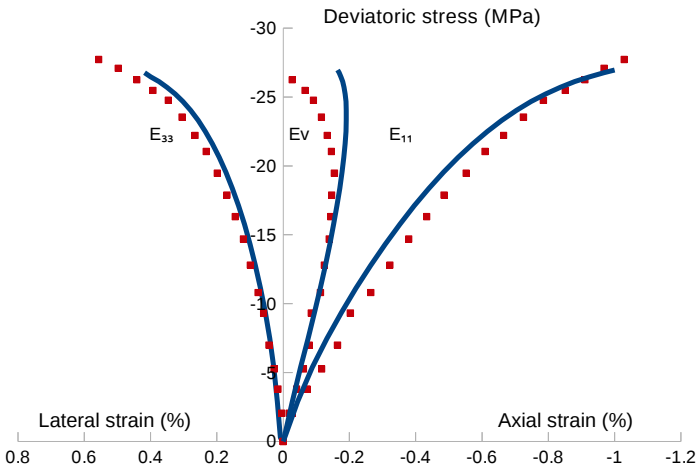

Figure 4.9: Comparison between numerical results and experimental data in a triaxial compression test with a confining pressure of 6 MPa.

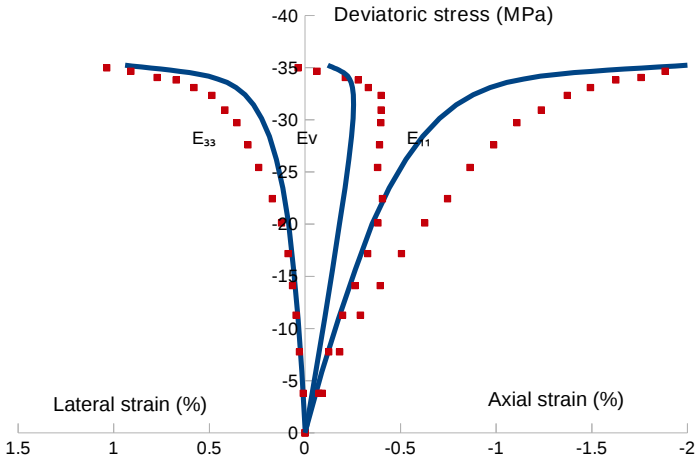

Figure 4.10: Comparison between numerical results and experimental data in a triaxial compression test with a confining pressure of 12 MPa.

4.4.1.3 Triaxial creep tests

In figure 4.11, one can see the comparison between numerical and experimental results for three creep tests performed on Callovo-Oxfordian argillites, with a confining pressure of 6 MPa and different levels of stress (50, 75 and 90% of peak differential stress). An overall good agreement is obtained. For the considered stress and duration conditions, only primary creep is obtained. Creep tests with longer time duration are still necessary to evaluate the long term behavior of rock. With the same confining pressure, the creep strain rate increases with the applied differential stress level. There is a large difference of lateral strain between the experimental data and calculated values for the test with 90% of peak differential stress. The numerical result provides a much larger lateral strain than the experimental data. Due to experimental uncertainties in creep tests, further tests are required to define the degree of uncertainty and to identify the shortcoming of the proposed model. Based on this, a modification of the plastic potential can be envisaged to improve the prediction of

© 2018 Tous droits réservés.

lilliad.univ-lille.fr

lateral strain under high differential stress.

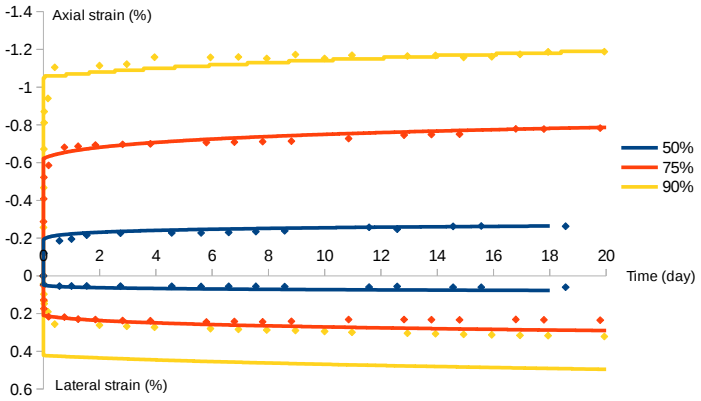

Figure 4.11: Comparison between simulation and experimental data of axial and lateral strains in triaxial creep tests with a confining pressure of 6 MPa and respectively at 50, 75, 90% of peak differential stress.

In the context of geological disposal of radioactive waste, it is necessary to consider time-dependent deformation for a very long duration. However, laboratory and in situ tests are generally limited in time duration; for instance, creep tests used above were performed for 20 days only. For a further experimental validation, some triaxial compression creep tests reported in previous studied have also been considered here ([Chanchole, 2004] and [Abou-Chakra Guéry et al., 2009]). Those tests have also been performed on Callovo-Oxfordian claystone under uniaxial and triaxial compression conditions on samples with different mineralogical composition. The duration of some creep tests was up to 600 days. Unfortunately, only axial strains were measured in those tests. Using the same parameters as those given in table 4.2, but with different mineralogical composition, the evolution of viscoplastic axial strain with time is calculated by using the proposed micromechanics based model for some selected tests. Comparisons between numerical results and experimental data are shown in figures 4.12 to 4.17. Despite some scatters, one can see that the proposed model is able to reproduce the time-dependent strains obtained in experimental tests.

4.4.1.4 Triaxial relaxation tests

Parameters of viscoplastic model are generally identified from creep tests. Relaxation tests provide an interesting way to verify the model performance. In figures 4.18, 4.19 and 4.20, the evolutions of axial stress (or differential stress q as confining pressure being kept constant) are simulated and compared with experimental results for three relaxation tests, with different confining pressures (2, 6 and 12 MPa) and different values of initial differential stress (q_0=20.8, 25 and 32.8 MPa). In a quantitative manner, the proposed model is able to well reproduce the progressive decrease of the axial stress due to relaxation process.

© 2018 Tous droits réservés.

lilliad.univ-lille.fr

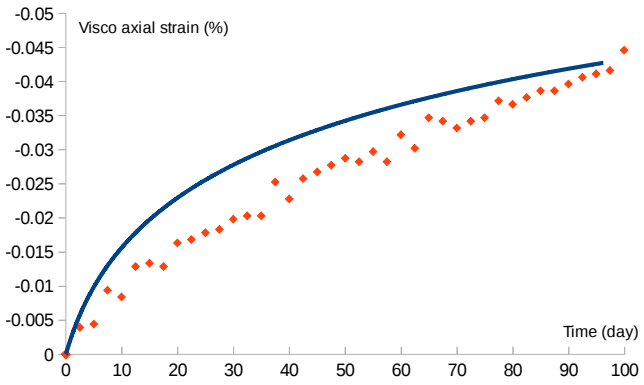

Figure 4.12: Comparison between simulation and experimental data of viscoplastic axial strain in a uniaxial creep test (axial stress=9.9 MPa; f_0=30.4% f_1=69.6%).

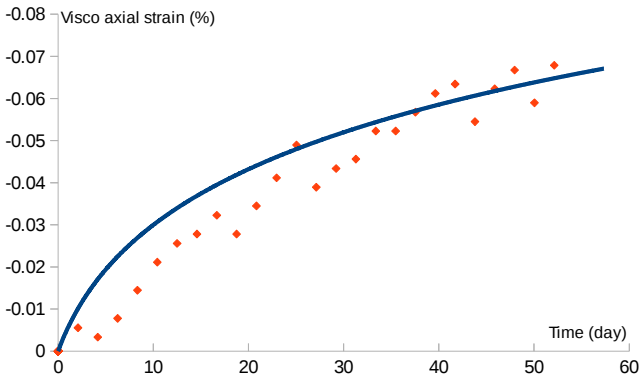

Figure 4.13: Comparison between simulation and experimental data of viscoplastic axial strain in a uniaxial creep test (axial stress=8 MPa; f_0=56.2% f_1=43.8%).

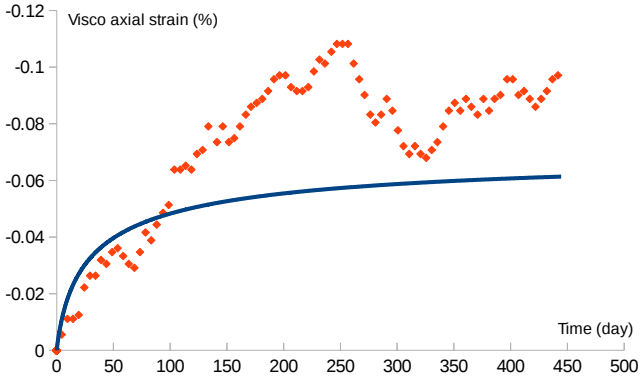

Figure 4.14: Comparison between simulation and experimental data of viscoplastic axial strain in a triaxial creep test (axial stress=22 MPa; confining pressure=12 MPa; f_0=57% f_1=43%).

© 2018 Tous droits réservés.

lilliad.univ-lille.fr

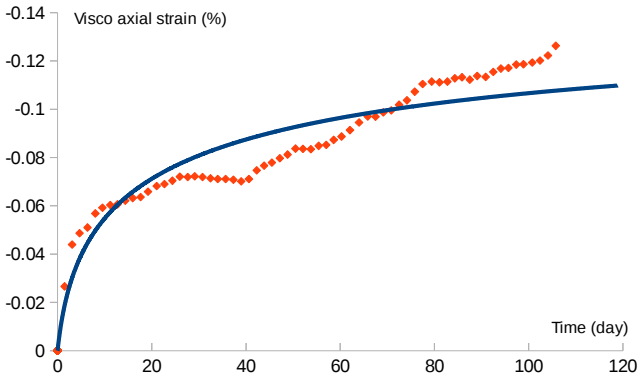

Figure 4.15: Comparison between simulation and experimental data of viscoplastic axial strain in a triaxial creep test (axial stress=24 MPa; confining pressure=12 MPa; f_0=57% f_1=43%).

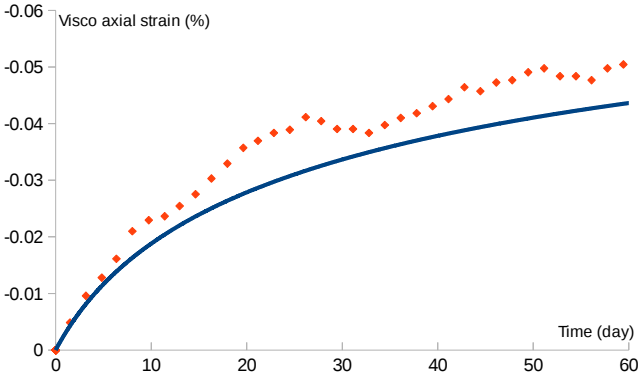

Figure 4.16: Comparison between simulation and experimental data of viscoplastic axial strain in a triaxial creep test (axial stress=22 MPa; confining pressure=12 MPa; f_0=56.9% f_1=43.1%).

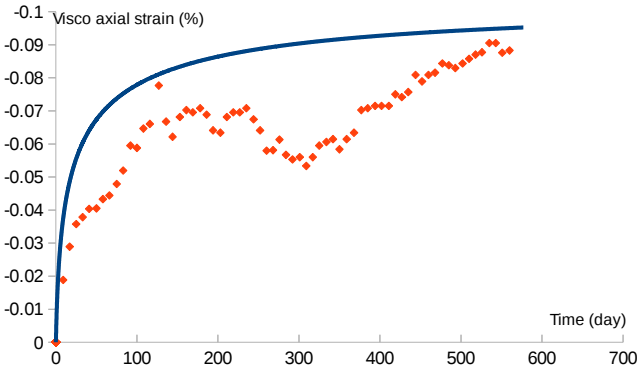

Figure 4.17: Comparison between simulation and experimental data of viscoplastic axial strain in a triaxial creep test (axial stress=22 MPa; confining pressure=12 MPa; f_0=61% f_1=39%).

© 2018 Tous droits réservés.

lilliad.univ-lille.fr

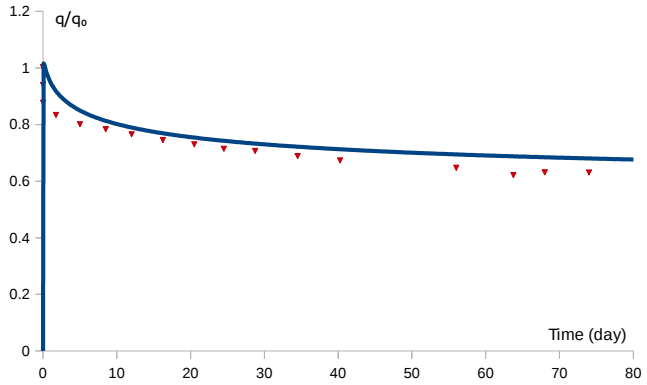

Figure 4.18: Comparison between simulation and experimental data for a relaxation test (confining pressure=2 MPa; q_0=20.81 MPa).

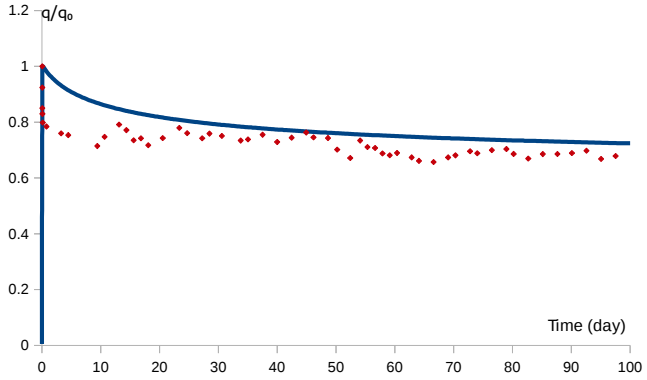

Figure 4.19: Comparison between simulation and experimental data for a relaxation test (confining pressure=6 MPa; q_0=25 MPa).

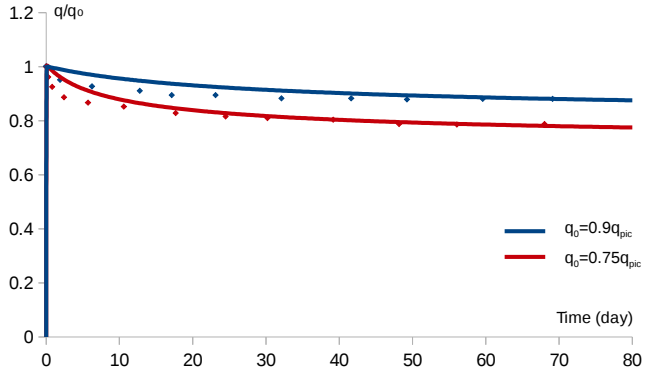

Figure 4.20: Comparison between simulation and experimental data for a relaxation test (confining pressure=12 MPa; q_0=32.8 MPa).

© 2018 Tous droits réservés.

lilliad.univ-lille.fr

Three kinds of tests are considered here, triaxial compression, creep and relaxation tests. The claystone is a rock with very low permeability (between 10^{-19} and 10^{-21} m^2). The variation of interstitial pressure is an important factor for both short and long term deformational processes. As the period to obtain a fully saturation state of samples is very long and it is difficult to make continuous measurement of interstitial pressure evolution, the samples, used in the tests considered here, were not fully saturated, but they were stabilized under a relative humidity of 90 %; the initial saturation state of samples was estimated between 80 and 95 %. Further, all tests were realized under pseudo-drained conditions without measurement of interstitial pressure. A small strain rate (10^{-6}/s) was used in triaxial compression tests and stress loading phases in creep and relaxation tests; small size samples (20x40mm) were used. With all these precautions, it is thought that the effect of interstitial pressure was significantly reduced. Therefore, in all numerical calculations presented here, total stresses are considered and interstitial pressure is neglected. However, for future applications of the proposed model to saturated situations, effects of pore pressure on plastic and viscoplastic deformation can be taken into account without theoretical difficulties, as discussed in previous studies ([Lydzba and Shao, 2002], [Xie and Shao, 2012] and [Xie and Shao, 2015]).

4.4.2 Vaca Muerta shale rock

For further validation of the proposed elastoviscoplastic micromechanics-based model, other numerical simulations are carried out to predict instantaneous and time-dependent mechanical behaviors of Vaca Muerta shale. Note that experimental data of Vaca Muerta shale, used below, are the same as those in chapters 2 and 3.

4.4.2.1 Identification of model parameters for shale rocks

In this section, as for the case of Callovo-Oxfordian argillites, we determine elastic, plastic and viscoplastic parameters of the proposed model for Vaca Muerta shale. To determine the elastic properties, in the case of Callovo-Oxfordian argillite, two linear homogenization steps are applied where the inclusions of calcite and quartz are considered as an equivalent inclusion with average elastic properties. In the case of Vaca Muerta shale, for elastic calculations, to avoid the calculation of equivalent inclusion elastic properties, we consider the microstructure given in chapter 2 (figure 2.1) and not the simplified one (figure 4.1). Namely, several types of inclusions are represented at micro and meso scales. In this case, for the calculation of macroscopic elastic properties (κ^{hom} and μ^{hom}), three homogenization steps are yet considered (section 2.2). Then, for the non linear computation, where one needs to know the volume fraction of equivalent inclusion (ρ), which is considered as the sum of all

© 2018 Tous droits réservés.

lilliad.univ-lille.fr

volume fractions of all inclusions at micro and mesoscales:

$$\rho = f_1 + f_2 + f_3 + f_4 + (f_5 + f_6).(1 - f_1 - f_2 - f_3 - f_4) \tag{4.23}$$

Thus, elastic properties of all Vaca Muerta constituents, used in this model are given in tables 2.1, 2.2 and 2.3.

The procedure for identifying plastic and viscoplastic parameters is the same as for the case of Callovo-Oxfordian argillite presented above. A triaxial compression test with a confining pressure of 5 MPa (figure 4.21) and a triaxial compression creep test (figure 4.31) are used, respectively, to identify plastic and viscoplastic parameters of viscoplastic model for the case of Vaca Muerta shale (table 4.4).

Table 4.4: Typical values of parameters for Vaca Muerta shale.

Plastic parameters	Viscoplastic parameters
T_0=t_0=0	$\eta = 10^{16}$
T_m=0.74	b_{vp}=150
t_m=0.3	m=1.5
b_1=b_2=600	
h=30 MPa	

4.4.2.2 Triaxial compression tests

We present in this paragraph the comparisons between numerical simulations (continuous red curves) and experimental data (symbolic blue curves) of triaxial compression tests with different confining pressure (2, 5, 10 and 25 MPa). According to figures 4.21-4.30, in general, numerical simulations seem satisfactory compared to experimental data. The model is able to reproduce the main features of instantaneous behavior of Vaca Muerta shale, comprising non-linear deformation, volumetric dilatancy and pressure sensitivity. The main advantage of the proposed model, compared to a phenomenological model, is that it takes into account the effect of mineralogical composition on the macroscopic response; thus, the same set of parameters is used for all depths.

© 2018 Tous droits réservés.

lilliad.univ-lille.fr

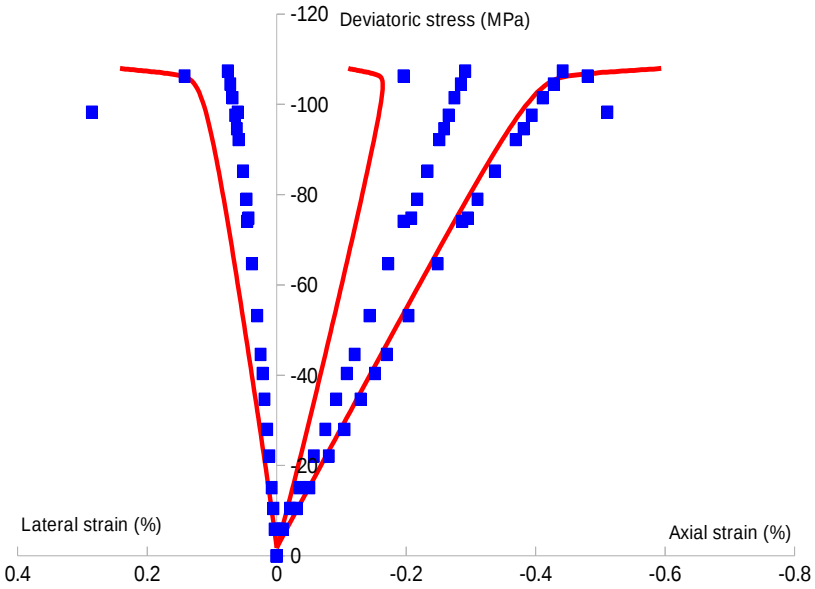

Figure 4.21: Comparison between viscoplastic model simulations and experimental data in a simple triaxial compression test on a Vaca Muerta shale sample (confining pressure=5 MPa; depth=2686.49 m; well S2; horizontal; f_1=0.2275, f_2=0.431, f_3=0.0164, f_4=0.1, f_6=0.05, f=0.08).

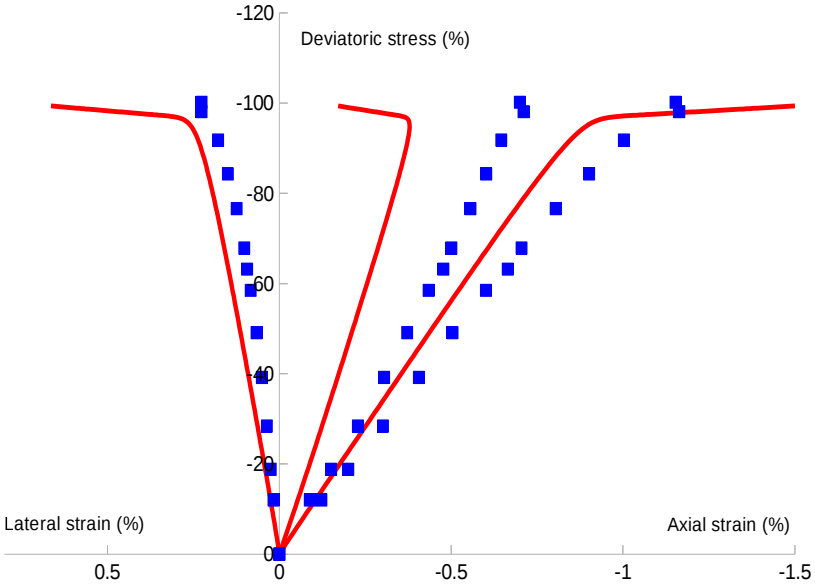

Figure 4.22: Comparison between viscoplastic model simulations and experimental data in a simple triaxial compression test on a Vaca Muerta shale sample (confining pressure=5 MPa; depth=2668.71 m; well S2; vertical; f_1=0.15, f_2=0.412, f_3=0.0033, f_5=0.23, f=0.09).

© 2018 Tous droits réservés.

lilliad.univ-lille.fr

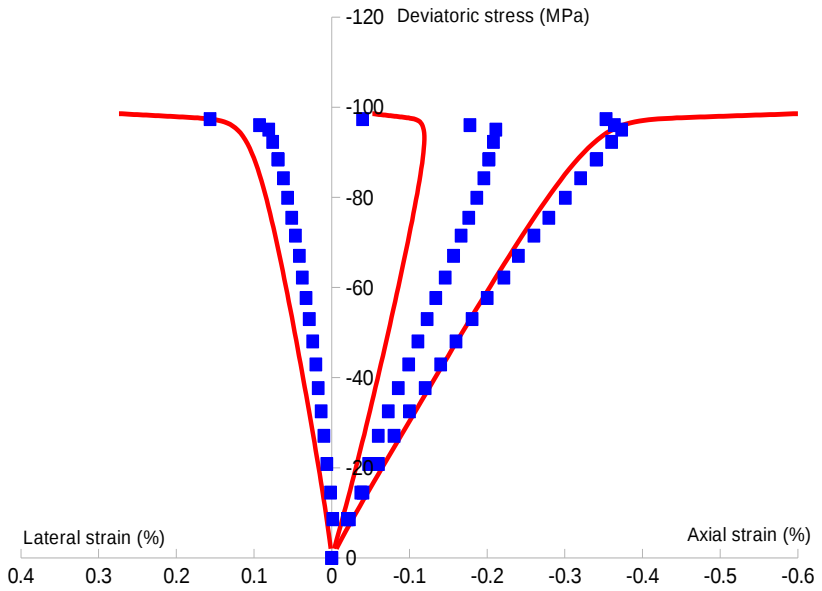

Figure 4.23: Comparison between viscoplastic model simulations and experimental data in a simple triaxial compression test on a Vaca Muerta shale sample (confining pressure=8 MPa; depth=2668.78 m; well S2; horizontal; f_1=0.143, f_2=0.35, f_3=0.0044, f_4=0.12, f_6=0.13, f=0.13).

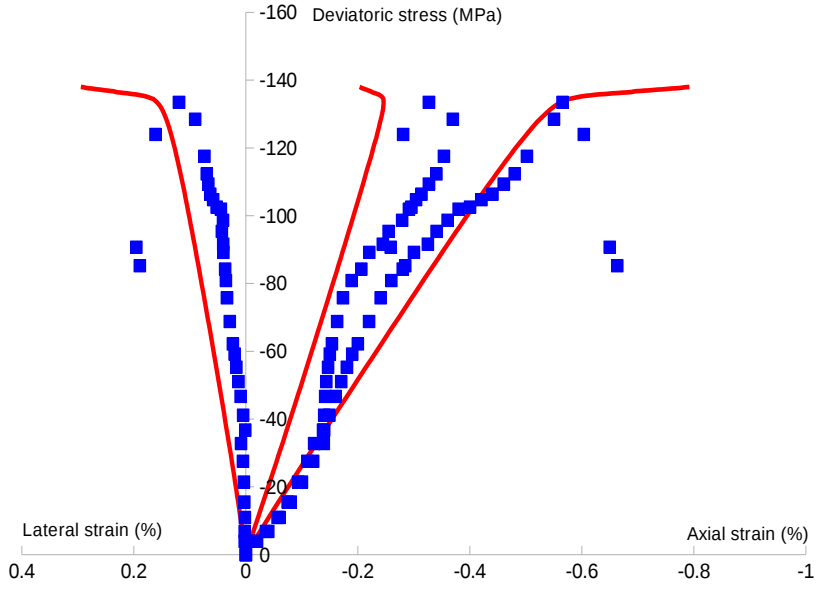

Figure 4.24: Comparison between viscoplastic model simulations and experimental data in a simple triaxial compression test on a Vaca Muerta shale sample (confining pressure=25 MPa; depth=2686.55 m; well S2; horizontal; f_1=0.2275, f_2=0.431, f_3=0.0164, f_4=0.1, f_6=0.05, f=0.08).

© 2018 Tous droits réservés.

lilliad.univ-lille.fr

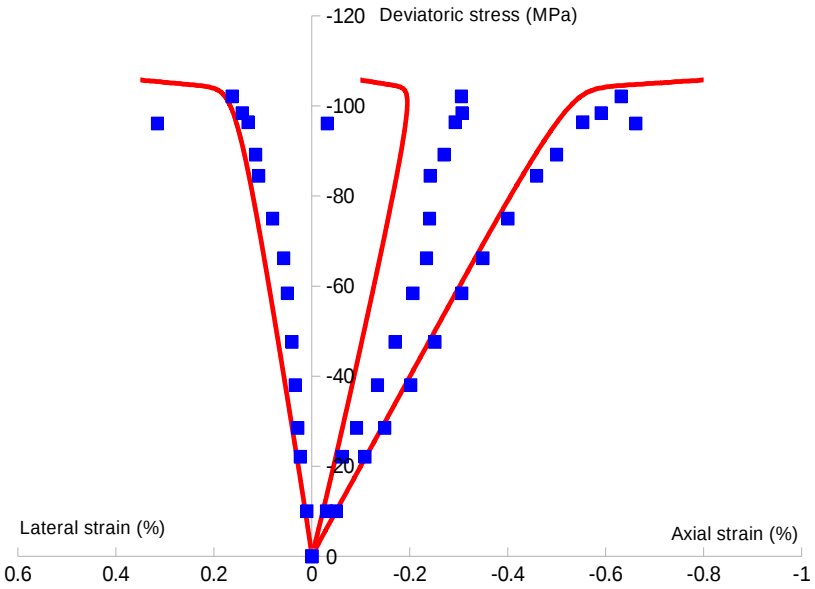

Figure 4.25: Comparison between viscoplastic model simulations and experimental data in a simple triaxial compression test on a Vaca Muerta shale sample (confining pressure=2 MPa; depth=2639.73 m; well S3; vertical; f_1=0.4, f_2=0.3, f_4=0.257, f_6=0.05, f=0.05).

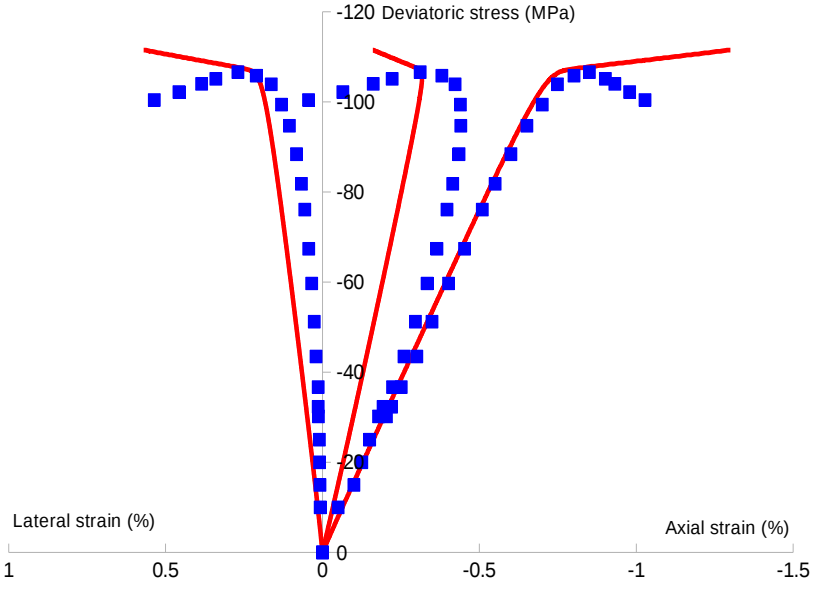

Figure 4.26: Comparison between viscoplastic model simulations and experimental data in a simple triaxial compression test on a Vaca Muerta shale sample (confining pressure=10 MPa; depth=2652.46 m; well S3; vertical; f_1=0.2415, f_2=0.173, f_4=0.264, f_6=0.25, f=0.08).

© 2018 Tous droits réservés.

lilliad.univ-lille.fr

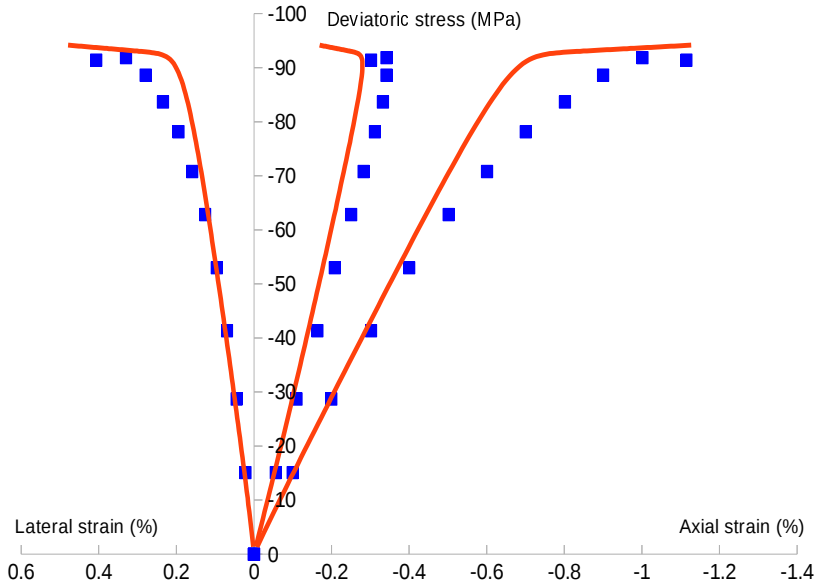

Figure 4.27: Comparison between viscoplastic model simulations and experimental data in a complex triaxial compression test on a Vaca Muerta shale sample (confining pressure=10 MPa; depth=2530.23 m; well S1; vertical; f_1=0.423, f_2=0.215, f_3=0.0173, f_5=0.23, f=0.094).

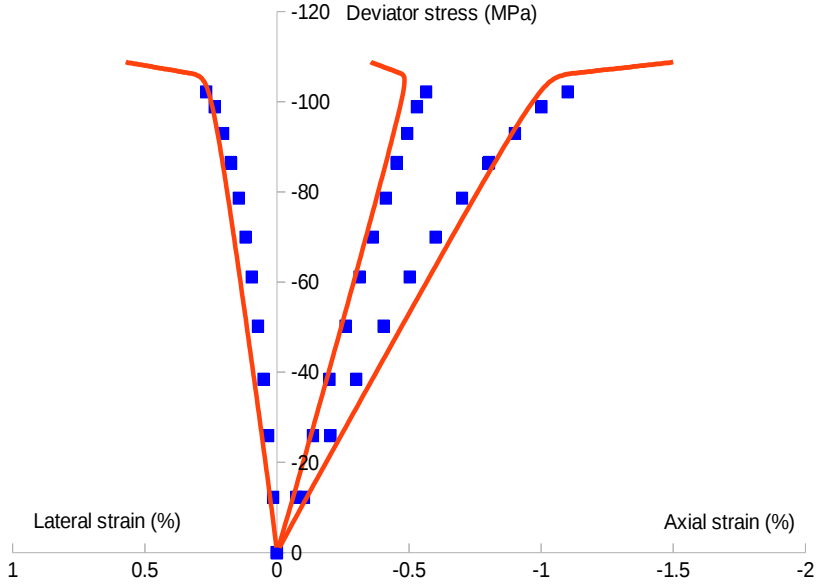

Figure 4.28: Comparison between viscoplastic model simulations and experimental data in a complex triaxial compression test on a Vaca Muerta shale sample (confining pressure=10 MPa; depth=2649.23 m; well S1; vertical; f_1=0.39, f_2=0.3, f_3=0.024, f_4=0.15, f=0.1).

© 2018 Tous droits réservés.

lilliad.univ-lille.fr

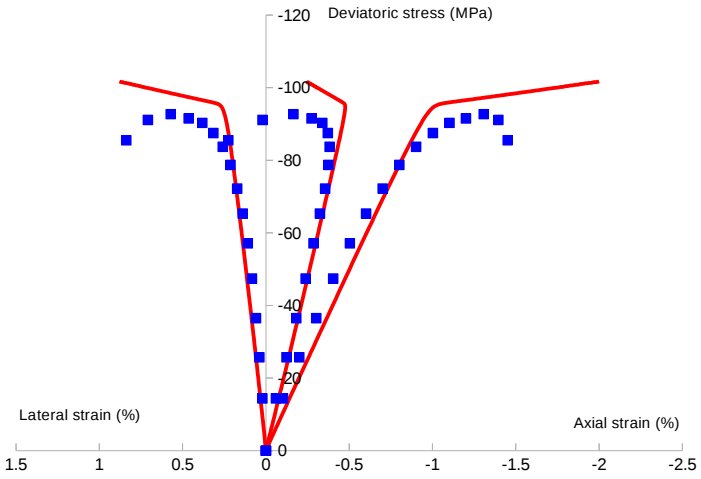

Figure 4.29: Comparison between viscoplastic model simulations and experimental data in a complex triaxial compression test on a Vaca Muerta shale sample (confining pressure=10 MPa; depth=2536.23 m; well S3; vertical; f_1=0.26, f_2=0.3075, f_3=0.0068, f_4=0.172, f=0.14).

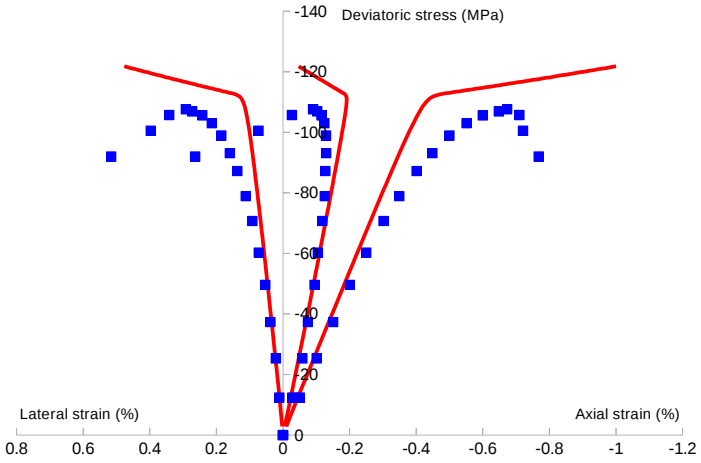

Figure 4.30: Comparison between viscoplastic model simulations and experimental data in a complex triaxial compression test on a Vaca Muerta shale sample (confining pressure=10 MPa; depth=2576.21 m; well S3; vertical; f_1=0.53, f_2=0.21, f_4=0.153, f_5=0.05, f_6=0.05, f=0.08).

4.4.2.3 Triaxial creep tests

In this paragraph, the proposed model is used to simulate triaxial compression creep tests performed on Vaca Muerta shale, by using the same set of parameters given in tables 2.1, 2.3, 2.2 and 4.4. Figures 4.31-4.36 exhibit comparison between experimental data and numerical simulations for different depths and stress conditions. It is obvious that numerical results are in accordance with experimental data and the viscoplastic model is able to describe the multistage creep behavior of Vaca Muerta shale.

© 2018 Tous droits réservés.

lilliad.univ-lille.fr

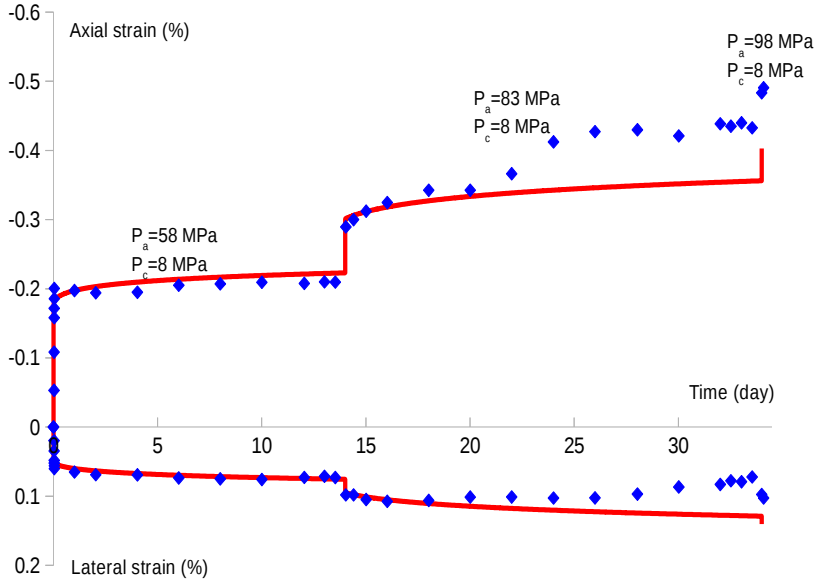

Figure 4.31: Comparison between viscoplastic model simulations and experimental data in a multistage triaxial compression creep test on a Vaca Muerta shale sample (confining pressure=8 MPa; depth=2668.84 m; well S2; horizontal; f_1=0.143, f_2=0.3, f_3=0.0044, f_4=0.12, f_6=0.13, f=0.1).

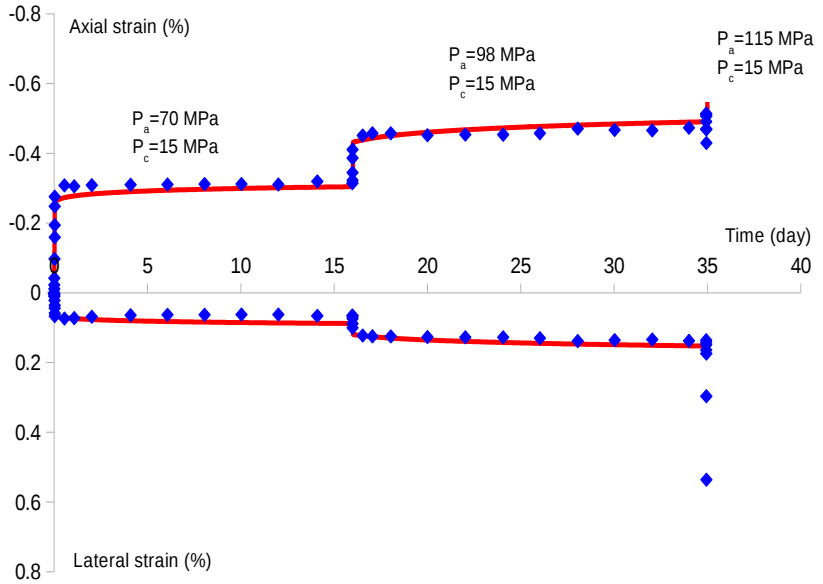

Figure 4.32: Comparison between viscoplastic model simulations and experimental data in a multistage triaxial compression creep test on a Vaca Muerta shale sample (confining pressure=15 MPa; depth=2768.44 m; well S2; horizontal; f_1=0.249, f_2=0.294, f_3=0.0133, f_4=0.12, f_6=0.12, f=0.15).

© 2018 Tous droits réservés.

lilliad.univ-lille.fr

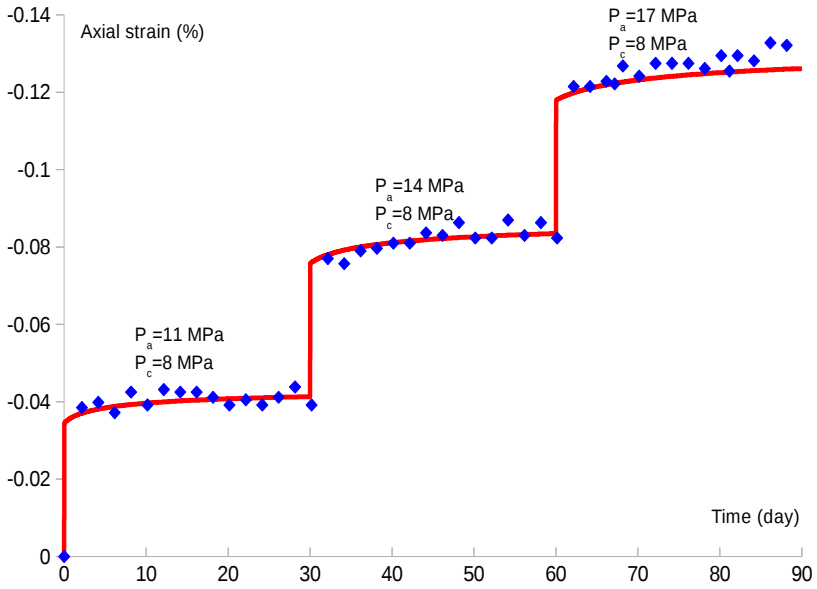

Figure 4.33: Comparison between viscoplastic model simulations and experimental data in a multistage triaxial compression creep test on a Vaca Muerta shale sample (confining pressure=8 MPa; depth=2537.14 m; well S1; vertical; f_1=0.19, f_2=0.237, f_3=0.016, f_4=0.13, f_6=0.194, f=0.1).

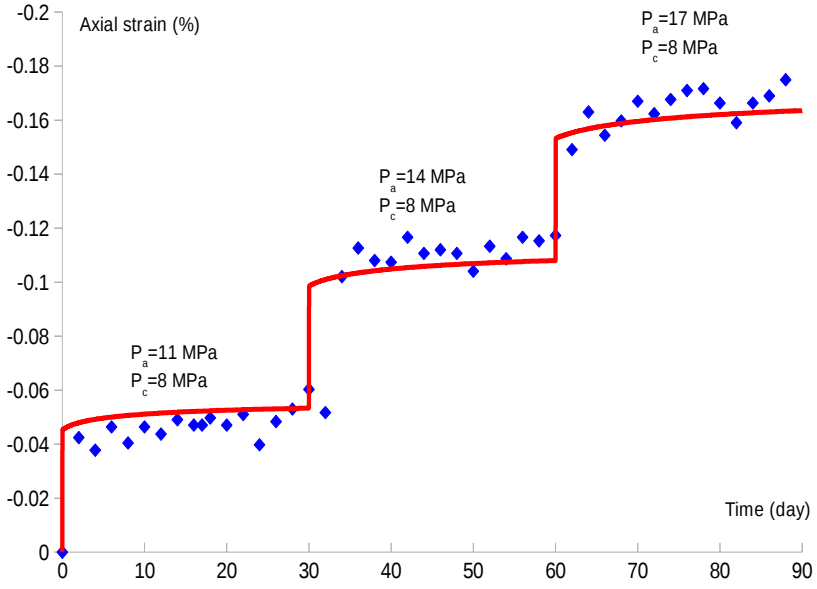

Figure 4.34: Comparison between viscoplastic model simulations and experimental data in a multistage triaxial compression creep test on a Vaca Muerta shale sample (confining pressure=8 MPa; depth=2537.24 m; well S1; horizontal; f_1=0.2374, f_2=0.236, f_3=0.019, f_4=0.13, f_6=0.337, f=0.087).

© 2018 Tous droits réservés.

lilliad.univ-lille.fr

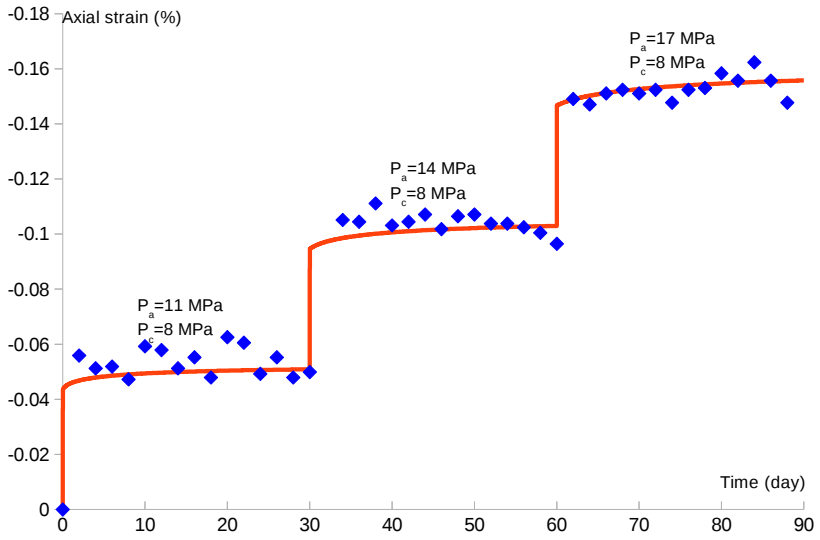

Figure 4.35: Comparison between viscoplastic model simulations and experimental data in a multistage triaxial compression creep test on a Vaca Muerta shale sample (confining pressure=8 MPa; depth=2546 m; well S1; horizontal; f_1=0.099, f_2=0.55, f_3=0.014, f_4=0.108, f_6=0.05, f=0.095).

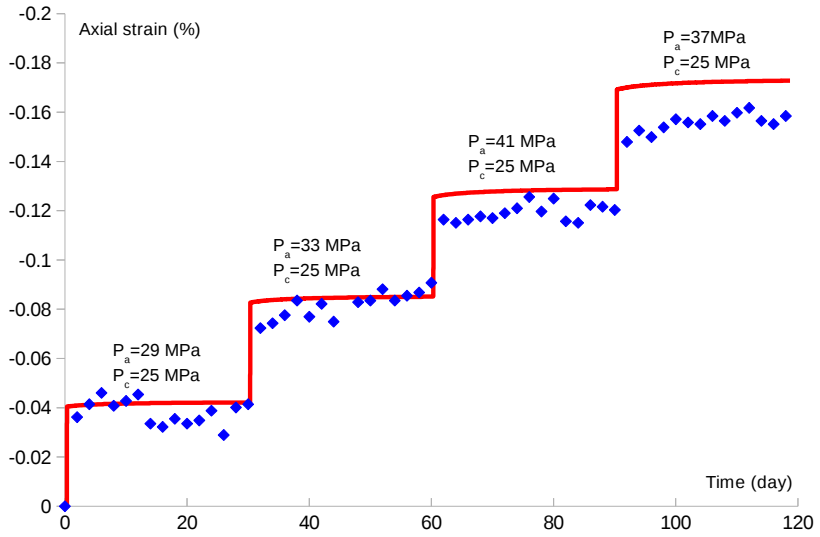

Figure 4.36: Comparison between viscoplastic model simulations and experimental data in a multistage triaxial compression creep test on a Vaca Muerta shale sample (confining pressure=25 MPa; depth=2568.11 m; well S3; horizontal; f_1=0.208, f_2=0.35, f_3=0.007, f_4=0.191, f=0.15).

4.5 Industrial application

The productivity of a shale hydrocarbon layer depends substantially on geomechanical factors such as the natural fracture network, the in situ stress regime, the elastic and rupture properties and time-dependent behavior of the hosted rock. The operational objective of the thesis is to examine whether the deferred or time-dependent behavior

© 2018 Tous droits réservés.

lilliad.univ-lille.fr

of Vaca Muerta shale rock influences the reclosing of fractures created by hydraulic fracturing. For the industrial application of the thesis, we study the interaction between a fracture surface (rock) and a spherical grain of proppant in Vaca Muerta shale formation. Thus, the goal is to show if the time-dependent mechanical behavior of Vaca Muerta shale can influence the mechanism of cracks propagation. If the hosted shale rock exhibits a significant creep deformation, this leads to the embedment of proppant grains into the rock. Therefore, the conductivity of fractures will be reduced over time which can cause a steeper decline of hydrocarbon production rate.

4.5.1 The state of problem

Figure 4.37 shows proppant grains with diameters between 300-600 µm in a natural or hydraulic fracture. To study the proppant-fracture contact, a fracture is modeled by two smooth and parallel surfaces containing a layer of medium sized proppants (450 µm in diameter) distributed in a uniform manner within a fracture. We study the interaction between one grain of proppant and the fracture. In this case, the proppant grain is considered as a spherical indenter. The illustration of a proppant spherical grain, in contact with a smooth surface of a fracture, is shown in figure 4.38.

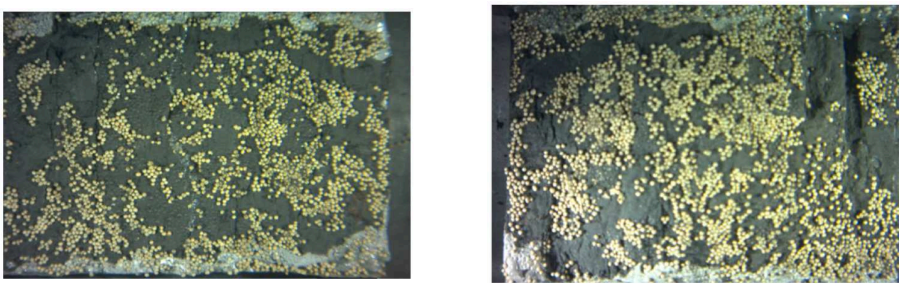

(a) (b)

Figure 4.37: Proppant grains with diameters between 300-600 µm in a natural or hydraulic fracture [TOTAL].

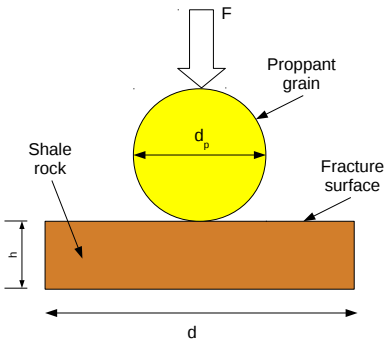

Figure 4.38: Illustration of a proppant spherical grain in contact with a fracture.

© 2018 Tous droits réservés.

lilliad.univ-lille.fr

Where: $F=\frac{\sigma_h^{'}.\pi.d^2}{4}$; $\sigma_h^{'}$=minor horizontal effective in-situ stress=10 MPa (in our case); d_p=diameter of a proppant grain; d is function of proppant concentration (defined later) and h is the thickness of rock chosen according to the zone of influence (defined later).

Three cases of proppants layer are studied where the concentration of proppants varies: perfect, half and quarter layers. In the case of a perfect layer, the spherical grains of proppants are attached to each other. For a half-layer, the number of grains becomes half compared to a perfect layer. Thus, the voids between proppant grains will increase. For a quarter-layer, the number of proppants is now a quarter compared to a perfect layer. In this case, the voids between the grains increase further. For instance, assuming that for a perfect layer, we have 100000 grains of proppants, thus, for half and quarter layers, we have 50000 and 25000 proppant grains respectively. When the quantity of grains decreases, the void between two grains increases. The voids are distributed between grains in a uniform way. Thus, for our calculations, the value of d, which depends on proppants concentration, is: d_p, $2d_p$ and $4d_p$ for the cases of perfect, half and quarter layers respectively. Therefore, F, the concentrated force, will increase with the decrease of proppant number. The illustrations of the three cases: perfect, half and quarter layers are given, respectively, in figures 4.39, 4.40 and 4.41. White circles indicate the absence of proppant grains (voids).

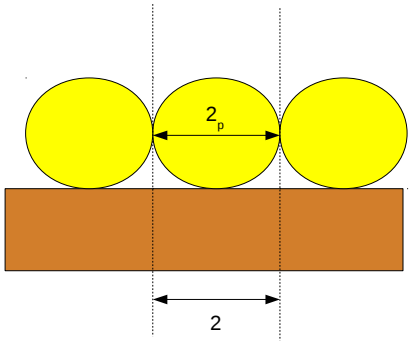

Figure 4.39: Illustration of perfect proppant layer.

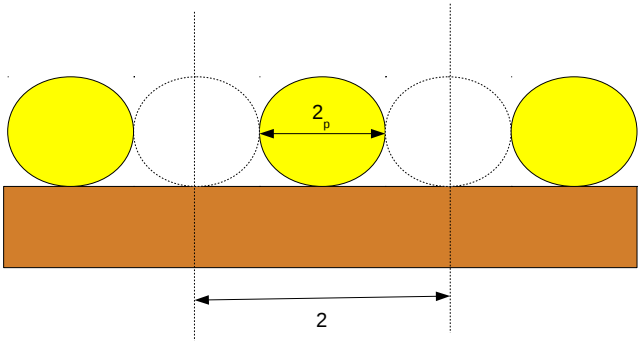

Figure 4.40: Illustration of half proppant layer.

© 2018 Tous droits réservés.

lilliad.univ-lille.fr

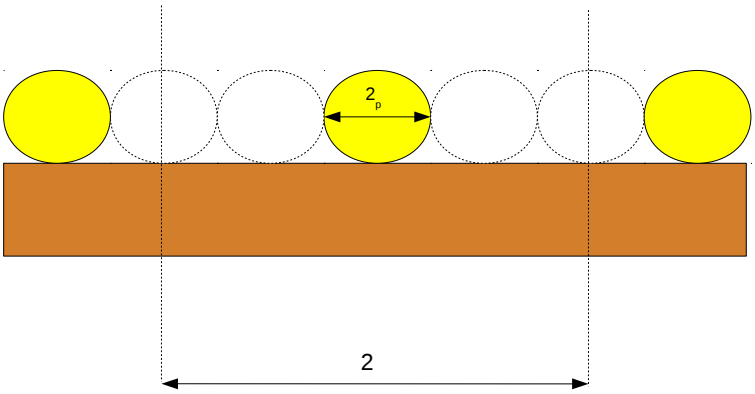

Figure 4.41: Illustration of quart proppant layer.

4.5.2 Geometry and mesh

To study the interaction between a proppant grain and Vaca Muerta rock, the micromechanical viscoplastic model described in section 4.2 has been integrated in the standard finite element code Abaqus in the form of a subroutine UMAT for a non linear finite element analysis. For the three cases of layer, the geometrical studied domain includes a 2D axisymmetric structure with boundary conditions, as shown in figure 4.42. For the sake of simplicity, the inclusion is considered as an axisymmetric discrete rigid part using the element type RAX2 divided with 24 elements and 25 nodes. A surface to surface interface was established between the inclusion and rock layer in order to simulate the contact effect during the deformation process. A concentrated force (F) is applied at the top of the inclusion. For the three rock layers, the detailed mesh informations of structure, used in this model, are presented in table 4.5. Figure 4.43 exhibits the mesh outline of the structure in 3D for the three layer cases.

Table 4.5: Mesh information of structure for the three cases of layer.

Layer	Height (h; µm)	Width ($d/2$; µm)	Element type	Element number	Node number	Concentrated force (N)
Perfect	450	225	CAX4	800	861	-1.58
Half	450	450	CAX4	2025	2116	-6.36
Quarter	450	900	CAX4	1800	1891	-25.45

4.5.3 Numerical results

In this paragraph, some numerical results from the non linear finite element analysis are presented. The used model parameters for Vaca Muerta shale rock are those given in tables 2.1, 2.2, 2.3 and 4.4 (vertical samples in oil window). It is recalled that the

© 2018 Tous droits réservés.
lilliad.univ-lille.fr

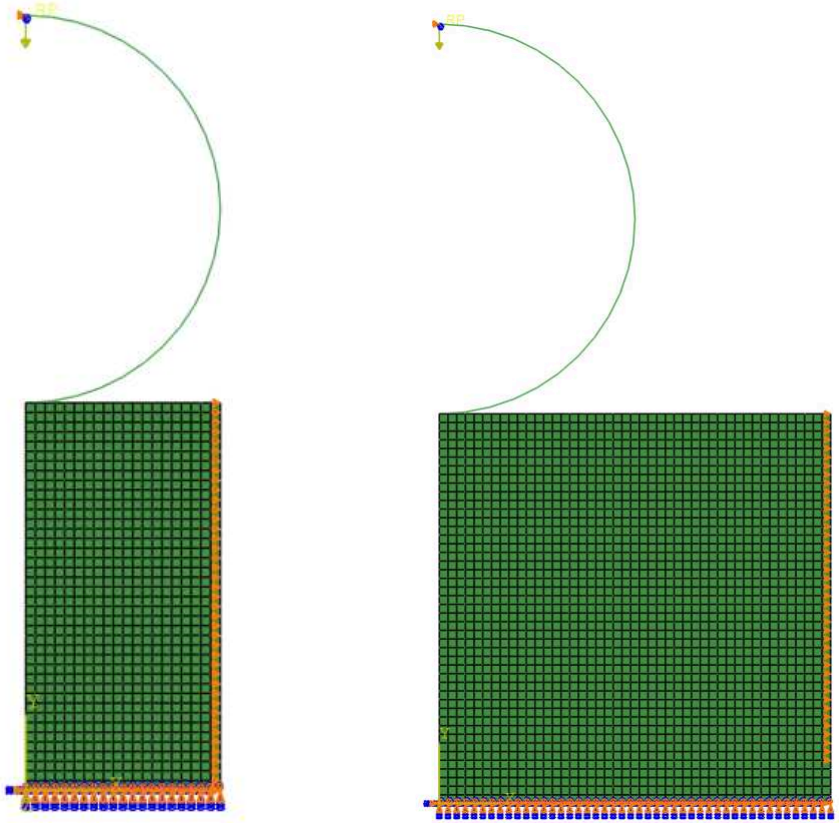

(a) Perfect layer

(b) Half layer

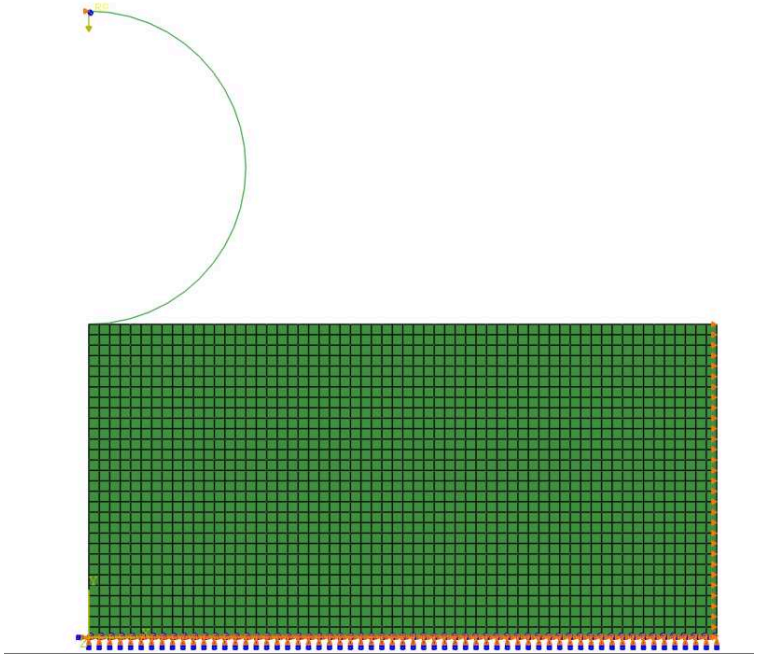

(c) Quarter layer

Figure 4.42: 2D axisymmetric structure with boundary conditions for the three layers.

© 2018 Tous droits réservés.

lilliad.univ-lille.fr

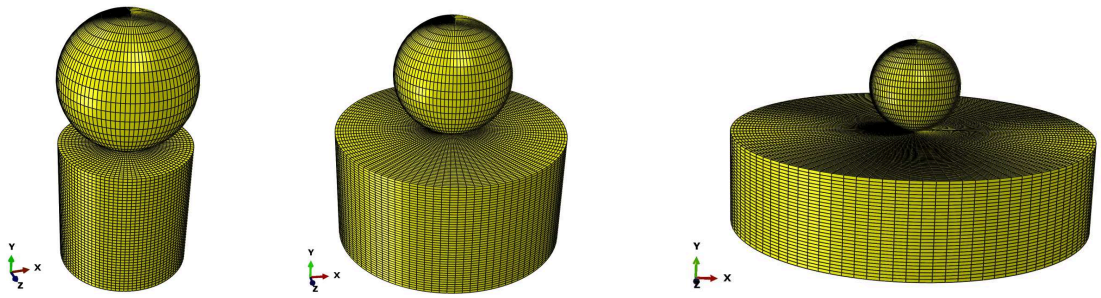

(a) Perfect layer (b) Half layer (c) Quarter layer

Figure 4.43: Mesh outline of the structure in 3D for the three layer cases.

main advantage of a micromechanical model, compared to a phenomenological model, is that it can take into consideration the variation of the mineralogical composition on the macroscopic response. Thus, for each layer case, calculations are performed for three mineralogical zones whose volume fraction of each phase and porosity are presented in table 4.6. From zone Z1 to Z3, the volume fractions of big/fine calcite and kerogen increase, as well as, the interparticle porosity. Contrariwise, the volume fraction of quartz/albite and pyrite decrease. Note that the notations for volume fractions and porosity are the same as those used in chapter 2.

Table 4.6: Approximate mineralogical composition for the three studied mineralogical zones.

Mineralogical zone	f_1	f_2	f_3	f_4	f_5	f_6	f
Z1	0.15	0.4	0.05	0.0825	0.063	0.1575	0.07
Z2	0.22	0.37	0.03	0.09	0.069	0.17	0.09
Z3	0.35	0.28	0.02	0.105	0.081	0.2	0.14

Figure 4.44 presents the variation of the equivalent stress of Von Mises for the three layers with mineralogical composition of zone Z1. Figures 4.45 and 4.46 show the variation of the deformation along X and Y axis, respectively, for the three layers with mineralogical composition of zone Z1. The calculations for zone Z2 and Z3 are given in Appendix C. In figure 4.47, we exhibits the variation of viscoplastic strain along Y axis at the contact point between the proppant grain and rock for the three layers and the three mineralogical compositions. As we have already said, with a micromechanical approach, we are able to take into consideration the mineralogical composition in calculations which makes it possible to avoid calibrating the model for each mineralogical zone. For perfect and half layers, the influence of mineralogical composition on macroscopic response is minimal compared with that of quarter layer. In figure 4.48, we show the influence of proppant distribution on the variation of

© 2018 Tous droits réservés.

lilliad.univ-lille.fr

viscoplastic strain along Y axis for the three mineralogical zones. As we can see, for the three mineralogical zones, the viscoplastic deformation along Y axis for the case of quarter layer is the most significant. Thus, as a first conclusion, according to the results, the higher the concentration of proppants, the less time-dependent deformation, then, the embedment of proppant grains is less significant.

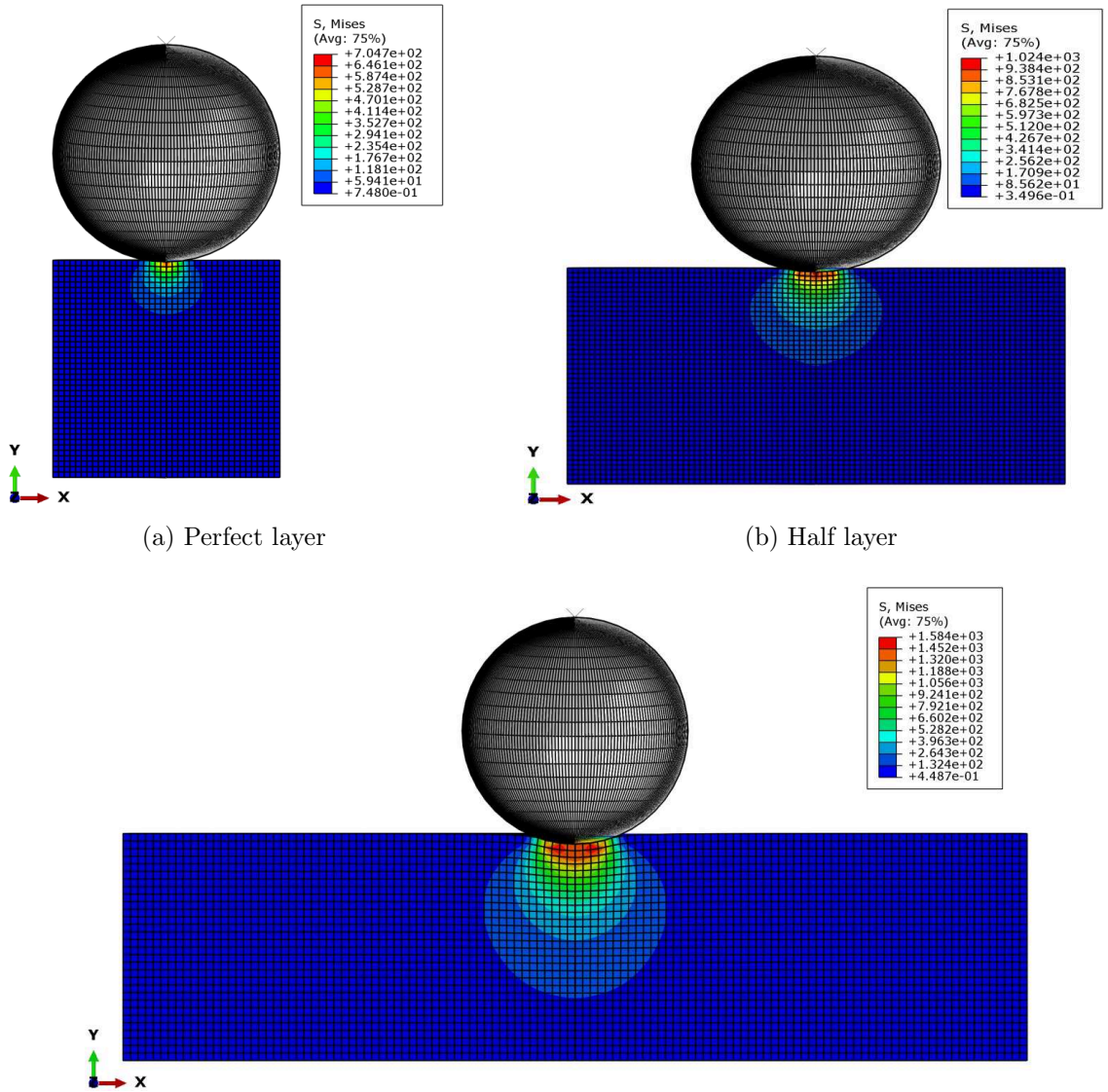

(a) Perfect layer

(b) Half layer

(c) Quarter layer

Figure 4.44: Variation of the equivalent stress of Von Mises for the three layers with mineralogical composition of zone Z1.

© 2018 Tous droits réservés.

lilliad.univ-lille.fr

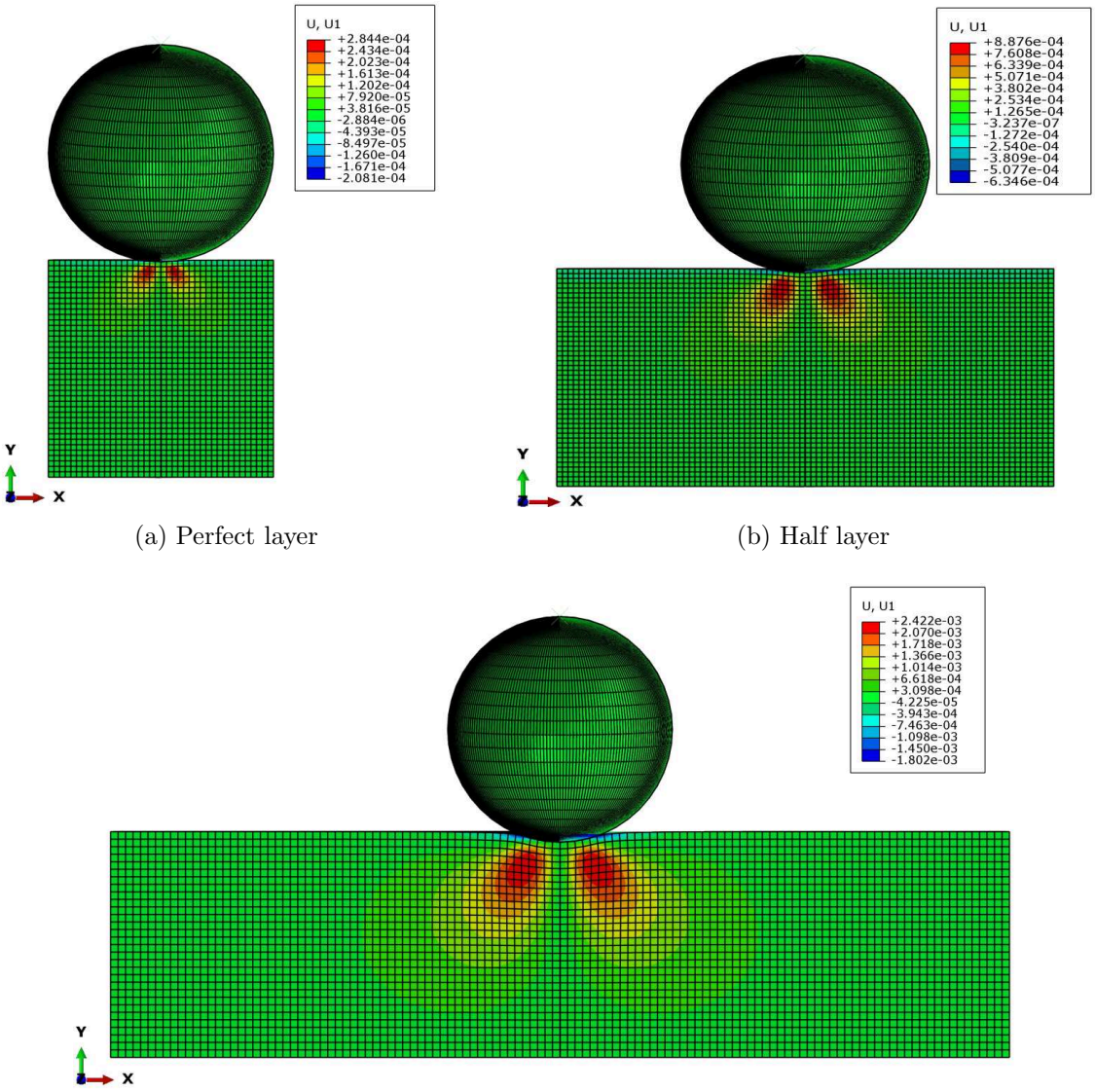

(a) Perfect layer

(b) Half layer

(c) Quarter layer

Figure 4.45: Variation of the deformation along X axis for the three layers with mineralogical composition of zone Z1.

© 2018 Tous droits réservés.

lilliad.univ-lille.fr

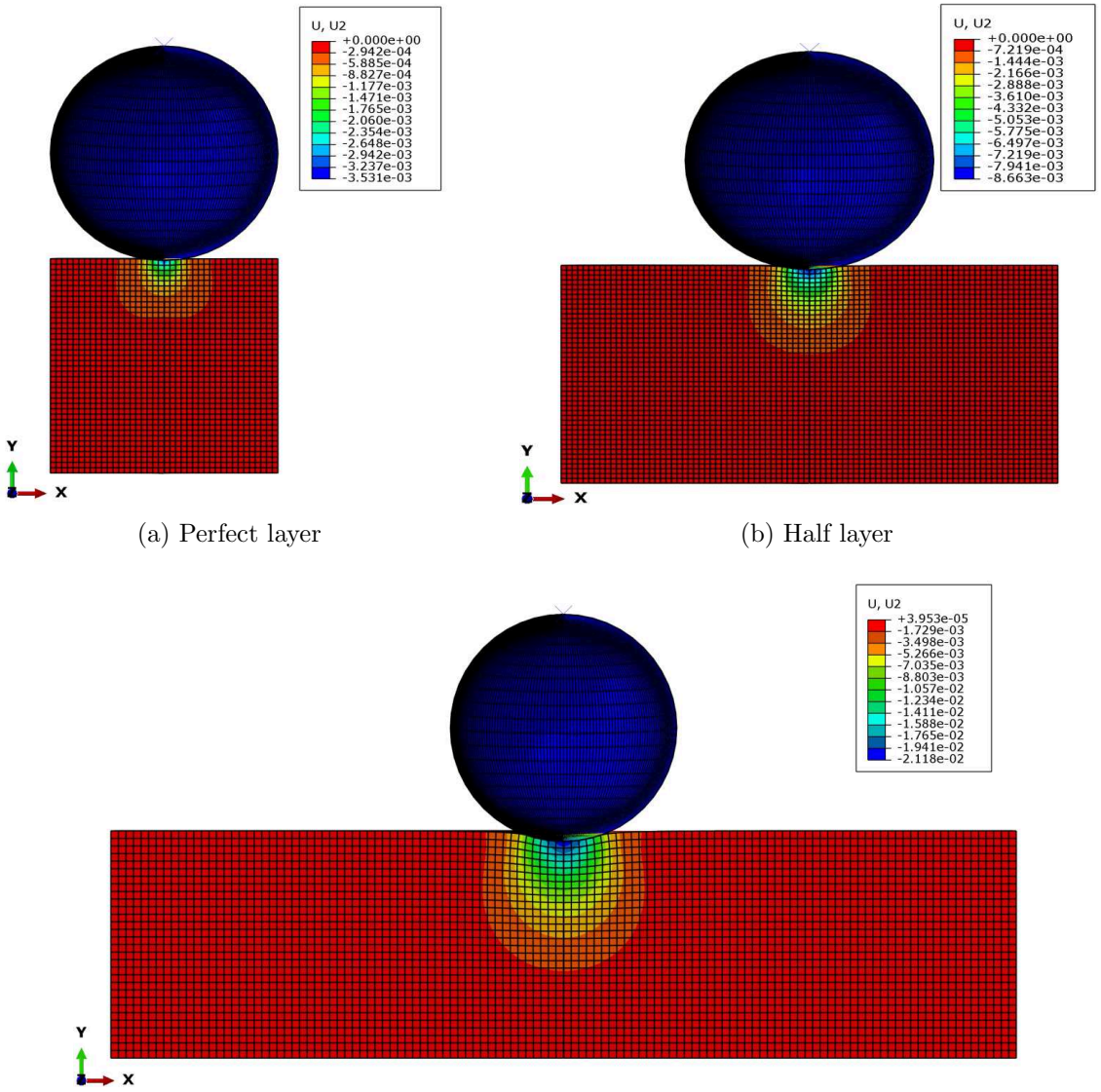

(a) Perfect layer

(b) Half layer

(c) Quarter layer

Figure 4.46: Variation of the deformation along Y axis for the three layers with mineralogical composition of zone Z1.

© 2018 Tous droits réservés.

lilliad.univ-lille.fr

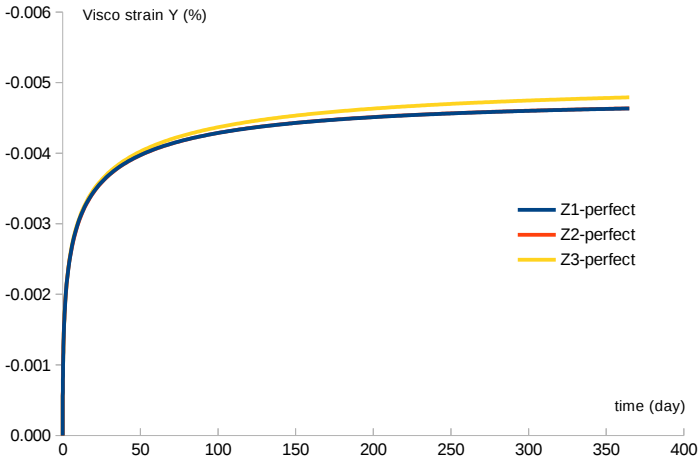

(a) Perfect layer

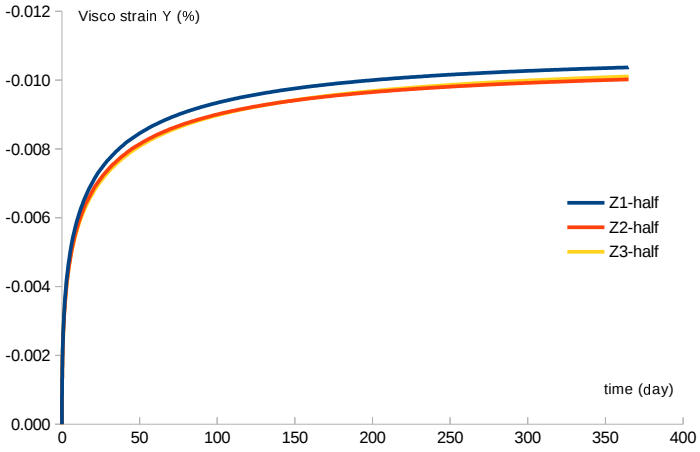

(b) Half layer

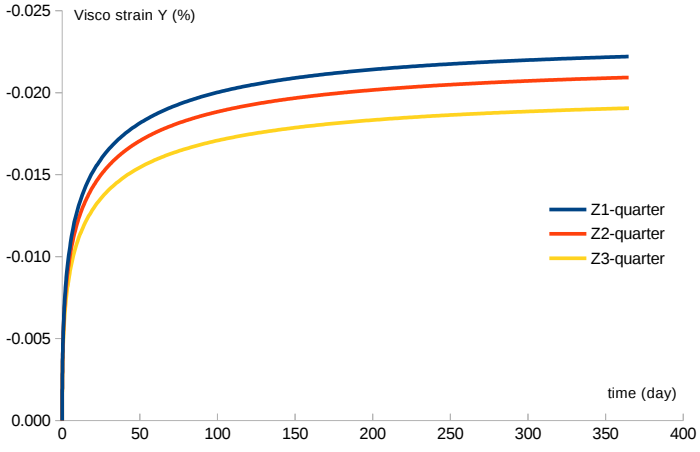

(c) Quarter layer

Figure 4.47: Variation of viscoplastic strain along Y axis at the contact point between the proppant grain and rock for the three layers and the three mineralogical compositions.

© 2018 Tous droits réservés.

lilliad.univ-lille.fr

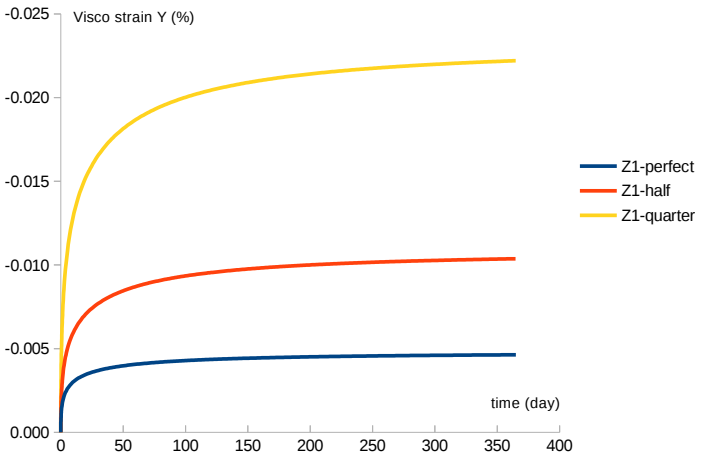

(a) Zone Z1

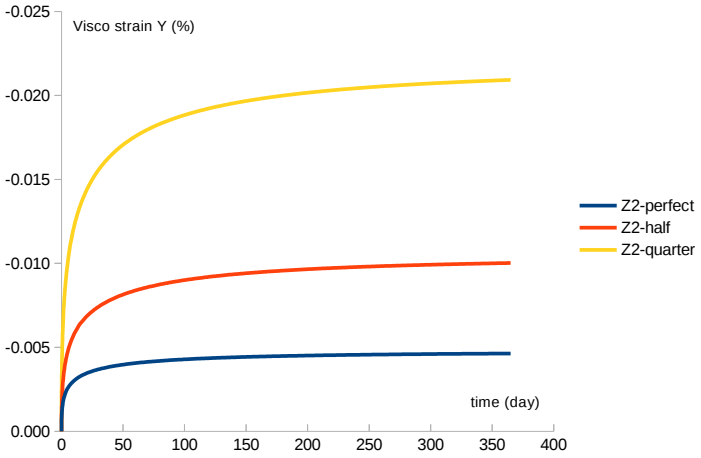

(b) Zone Z2

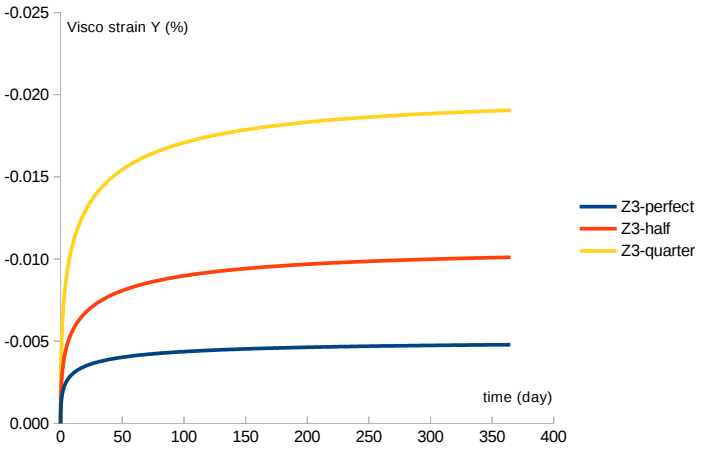

(c) Zone Z3

Figure 4.48: Influence of proppant distribution on the variation of viscoplastic strain along Y axis for the three mineralogical zones.

4.6 Conclusion

In this chapter, a micromechanics based model has been proposed to describe the elastic, plastic and viscoplastic strains in clayey and shale rocks. A unified approach

© 2018 Tous droits réservés.

lilliad.univ-lille.fr

has been developed for the instantaneous plastic and time-dependent delayed strains. The plastic yield and viscoplastic loading functions are derived from a non linear homogenization method and are able to explicitly account for the influences of porosity and mineral inclusions on macroscopic mechanical behavior. It has been clearly found that the increase of porosity significantly enhanced both instantaneous and time-dependent strains while the elastic mineral grains (carbonate and quartz) lead to a reduction of those strains. The failure strength of clayey and shale rocks is reduced with the increase of porosity and reinforced by the presence of mineral grains. The numerical predictions provided by the proposed model have been compared with experimental data for Callovo-Oxfordian argillites and Vaca Muerta shale. In a quantitative manner, the proposed model is able to describe the main features of mechanical behavior of clayey and shale rocks. Further laboratory tests will be welcome for a deep characterization of the complex behavior of clayey and shale rocks and in order to identify the improvement needed for the proposed model. In the last section, we have presented an example of application of the micromechanical model to study the interaction of a proppant grain in contact with Vaca Muerta shale rock. The goal is to estimate if the long-term deformation of the rock will lead to the embedment of proppant grain in the rock inducing the decrease of cracks conductivity. We have studied three cases of layer (perfect, quarter and half) in order to estimate if the concentration of proppant has an influence on the embedment process. As a first conclusion, according to numerical results, the higher the concentration of proppants, the less time-dependent deformation, then, the embedment of proppant grains is less significant.

© 2018 Tous droits réservés.

lilliad.univ-lille.fr

© 2018 Tous droits réservés.

lilliad.univ-lille.fr

General conclusion and perspectives

The main objective of the thesis is to build a micromechanical theoretical model to predict the instantaneous and time-dependent mechanical behavior of Vaca Muerta shale rock. Constructing this model, the operational application will be to study the interaction between a proppant grain and Vaca Muerta shale rock to estimate the embedment of a grain into the rock due to the effect of time-dependent deformations. Compared with macroscopic phenomenological models, a micromechanical modeling approach allows the microstructural aspects to be taken into account on the macroscopic response.

As a first step, a general review of shale hydrocarbons is presented. Shale hydrocarbons are seen as unconventional resources where its low permeability requires the use of hydraulic fracturing technique. Afterward, a short overview of many shale rock microstructure has been presented. In general, shale rock is seen as a complex material having a multiscale and multiphase microstructure. Usually, shales are constituted of submicron clay particles, nanoporosity and different types of inclusions. Before starting the mechanical behavior modeling of Vaca Muerta shale, it is essential to study its microstructure based on a series of experimental observations. The main mineralogical phases, identified within the studied material, are: quartz, calcite, pyrite, clay and organic matter. The proportion of different phases varies considerably with depth. Two types of porosity are distinguished within Vaca Muerta shale samples: organic and mineral porosity. Hereafter, we expose some representative triaxial and multistage creep tests that are realized on Vaca Muerta shale samples, by focusing on the interaction between microstructure and mechanical behavior.

In the second chapter, we have elaborated a micromechanical semi-analytical elasto-plastic damage model for Vaca Muerta shale rock. Initially, with a simplified description of material microstructure, the representative elementary volume is proposed. Four homogenization scales are considered with a matrix-inclusion system. At macroscale, the material is seen as a homogeneous continuum medium. At mesoscale, many types of inclusions are seen immersed in a composite matrix. At a smaller scale, the latter is composed of fine calcite and kerogen inclusions embedded in a porous clay matrix. Then, in the second part, by assuming that all material phases have a linear elastic behavior, we have studied the behavior of Vaca Muerta shale in elastic regime. After having differentiated the elastic properties of all Vaca Muerta shale constituents, we have predicted effective elastic properties of the studied material by an

© 2018 Tous droits réservés.

lilliad.univ-lille.fr

appropriate linear homogenization method. Note that to account for the anisotropy of clay matrix, for simplicity, we have supposed that Vaca Muerta rocks, for the two principal orientations, are two different isotropic materials with two different clay matrix (various elastic properties). In the second main part, we have leaded off the non-linear homogenization in the context of elastoplasticity and interfacial debonding damage process. We have supposed that the clay matrix has an elastoplastic behavior while all other phases are elastic. In this homogenization-based approach, the macroscopic mechanical behavior will depend on the change of clay matrix porosity and the different types of fine and big organic/inorganic inclusions. The influence of porosity on clay matrix behavior will be reached through a nano to micro upscaling procedure where an analytical plastic criterion for porous medium is used. Then, the influence of fine and big inclusions are taken into account through micro-meso and meso-macro upscaling steps simultaneously. For the later transitions, Hill's incremental method has been involved. An associated flow rule of the clay matrix is assumed at first time. Afterward, we have considered a damage process: the complete interfacial debonding between the composite matrix and mesocalcite. After having formulated the semi-analytical micromechanical elastoplastic damage model, it has been validated by comparing Vaca Muerta experimental data and numerical simulations. A non-associated plastic flow rule seems indispensable to well reproduce both axial and lateral strains. By applying a parameter identification procedure, plastic and debonding parameters are acquired. In general, there is a good agreement between numerical results and experimental data. At the end of this comparison, several remarks can be withdrawn. The non-associated model describes, suitably, the transition from volumetric compressibility to dilatancy with the increase of the deviatoric stress. Both lateral and axial strains are well reproduced. The proposed micromechanical model is able to account for the mineralogical aspects (porosity, fine and mesoinclusions) on the macroscopic response of Vaca Muerta shale. Furthermore, the model is able to account for the effect of confining pressure on macroscopic behavior. Additionally, it takes into account the material softening related to progressive interfacial debonding process. Finally, in order to reduce the number of material parameters, we have studied the case of an associated perfectly plastic clay solid phase. For these conditions, the comparison between simulations and experimental data are not very satisfactory but if we are interested to the value of peak stress only, it can be sufficient.

The third chapter has been devoted to study the time dependent behavior of Vaca Muerta shale rock in terms of progressive material degradation. The origin of macroscopic time-dependent deformation is assumed to be the microscopic damage of clay solid phase. By introducing an internal variable to quantify the microstructural evolution, an appropriate formulation is considered. A unified model is developed to study the instantaneous and time-dependent behavior of Vaca Muerta shale rock.

© 2018 Tous droits réservés.

lilliad.univ-lille.fr

Note that the long term constitutive formulation is an extension of the instantaneous one presented in the second chapter. The same set of elastic, plastic and degradation parameters is used to simulate both, short and long term tests. An experimental validation is carried out by comparing creep data and simulations. In a quantitative sense, numerical simulations are quite consistent with experimental data. Comparison with further experimental data, like relaxation and triaxial compression tests with different loading conditions, seems indispensable.

Eventually, in the last chapter, a simplified viscoplastic model for clayey and shale rocks has been developed. For practical applications, the aim of this chapter is to build an analytical micromechanics based model, easy to be implemented in a standard calculation code. For this reason, a simplified microstructure is considered where clayey and shale rocks are assumed to be a composite material with two scales. At microscale, the clay matrix is a porous medium composed of a solid phase and spherical pores. At mesoscale, the homogenized porous clay matrix is reinforced by an equivalent inclusion. As an approximation, the latter corresponds to the assembly of many types of inclusions. Note that if for industrial requirement, we demand to consider all types of inclusions, the semi-analytical model, presented in the second chapter, is used. In this model, we suppose that the origin of time-dependent deformation is the viscosity of clay matrix. For elastoviscoplastic formulation, an analytical macroscopic plastic criterion has been extended to define the viscoplastic loading function. A unified formulation is proposed to describe both, plastic and viscoplastic strains through two distinct hardening laws. To prove the capability of the proposed model in reproducing the main features of clayey and shale rocks mechanical behavior, the model is validated via comparisons between experimental data and numerical results on two types of rock: Callovo-Oxfordian argillites and Vaca Muerta shale. Finally, for the operational application of the thesis, we have study the interaction between a proppant grain and Vaca Muerta shale rock in order to examine if the time-dependent deformation of the later material is significant. If the hosted shale rock exhibits a considerable creep deformation, this leads to the embedment of proppant grain into the rock and then, the conductivity of the fracture will be reduced.

Finally, as perspectives for this work, we can mention: the inherent anisotropy of the rock, the viscoelastic behavior of the organic matter and the effects of cracks. We can cite many other perspectives like:

- Experimental study of delayed behavior involving a series of creep and relaxation tests under in situ conditions, and possibly the presence of a fracture and/or proppant grains. Our laboratory has an original experimental device to create a fracture in a cylindrical sample and to perform creep tests under normal and

© 2018 Tous droits réservés.

lilliad.univ-lille.fr

shear stresses.

- Triaxial compression and creep tests under microtomography are needed in ordered to identify the micromechanisms of deformation at each constituents of the material. The knowledge of grains geometric shape seems interesting as well.

- Extension of the mechanical model to hydromechanical and chemomechanical coupling. From the basic model, hydromechanical coupling will be considered by taking into account the effects of saturation and pore pressures. Therefore, a poromechanical version of the micro-macro model will be established. In particular, we will check the validity of effective stresses at different scales. Therefore, it is also important to perform creep tests at different degrees of saturation, interstitial pressures and under different stress levels.

- Simulate the embedment of a proppant grain in Vaca Muerta shale rock as a function of depth for several layer cases. This proppant embedment log indicates in which areas the drains will be placed.

© 2018 Tous droits réservés.

lilliad.univ-lille.fr

© 2018 Tous droits réservés.

lilliad.univ-lille.fr

Thèse de Faten Farhat, Université de Lille, 2018

Appendix A

Algorithm for local integration of the elastoplastic clay phase

The scheme of local integration of clay matrix elastoplastic constitutive law, described in paragraph 2.3.1.1, is presented in this appendix. This algorithm constitutes a subroutine (step 6.4.) of the numerical scheme given in paragraph 2.3.3.1. The problem can be summarized as following:

$$\begin{cases} \tilde{\boldsymbol{\sigma}}_{n+1} = \mathbb{C}_0 : (\tilde{\boldsymbol{\varepsilon}}_{0,n+1} - \tilde{\boldsymbol{\varepsilon}}^p_{0,n+1}); \\ \tilde{\boldsymbol{\varepsilon}}_{0,n+1} = \tilde{\boldsymbol{\varepsilon}}_{0,n} + \Delta\tilde{\boldsymbol{\varepsilon}}_0 \quad \text{known}; \\ \tilde{\boldsymbol{\varepsilon}}^p_{0,n+1} = \tilde{\boldsymbol{\varepsilon}}^p_{0,n} + \Delta\tilde{\boldsymbol{\varepsilon}}^p_0 = \tilde{\boldsymbol{\varepsilon}}^p_{0,n} + \Delta\lambda\frac{\partial\Phi}{\partial\tilde{\boldsymbol{\sigma}}}; \\ \varepsilon^p_{n+1} = \varepsilon^p_n + \Delta\varepsilon^p; \\ \Phi(\tilde{\boldsymbol{\sigma}}, \bar{\sigma}, f) = 0; \end{cases} \tag{A.1}$$

Knowing $\tilde{\boldsymbol{\varepsilon}}_{0,n+1}$, the plastic deformation $\tilde{\boldsymbol{\varepsilon}}^p_{0,n}$ and the equivalent plastic strain ε^p_n, the problem is to determine $\tilde{\boldsymbol{\varepsilon}}^p_{0,n+1}$, ε^p_{n+1} and $\tilde{\boldsymbol{\sigma}}_{n+1}$ where $\Delta\lambda$ is the unknown. This scheme is explicit and follows an algorithm type "cutting point algorithm" [Simo and Hughes, 1998].

A.1 Elastic prediction

It is primarily supposed that the increment is elastic, namely, $\Delta\lambda$=0; thus, $\tilde{\boldsymbol{\varepsilon}}^p_{0,n+1} = \tilde{\boldsymbol{\varepsilon}}^p_{0,n}$ and $\tilde{\boldsymbol{\sigma}}_{n+1} = \mathbb{C}_0 : (\tilde{\boldsymbol{\varepsilon}}_{0,n+1} - \tilde{\boldsymbol{\varepsilon}}^p_{0,n})$. If the trial stress verifies $\Phi(\tilde{\boldsymbol{\sigma}}, \bar{\sigma}, f) = 0$, then the hypothesis is valid and the procedure for current step is completed; otherwise, a phase of plastic correction is needed.

© 2018 Tous droits réservés.

lilliad.univ-lille.fr

A.2 Plastic correction

The plastic correction is carried out through an iterative procedure. For an iteration i, $\Delta\lambda^i$ is known, we have to determine $\Delta\lambda^{i+1}$. It is defined that:

$$\tilde{\boldsymbol{\sigma}}_{n+1}^{i+1} = \mathbb{C}_0 : (\tilde{\boldsymbol{\varepsilon}}_{0,n+1} - \tilde{\boldsymbol{\varepsilon}}_{0,n+1}^{p,i}) - \Delta\lambda^{i+1} : \mathbb{C}_0 : \frac{\partial \Phi}{\partial \tilde{\boldsymbol{\sigma}}} \tag{A.2}$$

$$\varepsilon_{n+1}^{p,i+1} = \varepsilon_n^{p,i} + \Delta\lambda^{i+1}\gamma, \quad \gamma = \frac{\tilde{\boldsymbol{\sigma}} : \frac{\partial \Phi}{\partial \tilde{\boldsymbol{\sigma}}}}{(1-f)\bar{\sigma}} \tag{A.3}$$

$$\Phi(\tilde{\boldsymbol{\sigma}}_{n+1}^{i+1}, \varepsilon_{n+1}^{p,i+1}, f) = \Phi_{n+1}^{i+1} \tag{A.4}$$

It is possible to solve this problem by using Taylor's series; we linearize equation A.4:

$$\Phi_{n+1}^{i+1} = \frac{\partial \Phi_{n+1}^i}{\partial \tilde{\boldsymbol{\sigma}}}\delta\tilde{\boldsymbol{\sigma}} + \frac{\partial \Phi_{n+1}^i}{\partial f}\delta f + \frac{\partial \Phi_{n+1}^i}{\partial \bar{\sigma}}\delta\bar{\sigma} + \Phi_{n+1}^i = 0 \tag{A.5}$$

$$\delta(\Delta\lambda)\left[-\frac{\partial \Phi}{\partial \tilde{\boldsymbol{\sigma}}} : \mathbb{C}_0 : \frac{\partial \Phi}{\partial \tilde{\boldsymbol{\sigma}}} + \frac{\partial \Phi}{\partial f}(1-f)\left(\frac{\partial \Phi}{\partial \tilde{\sigma}_m} - 3\alpha\gamma\right) + \frac{\partial \Phi}{\partial \bar{\sigma}}\frac{\partial \bar{\sigma}}{\partial \varepsilon^p}\gamma\right] + \Phi_{n+1}^i = 0 \tag{A.6}$$

Thus:

$$\delta(\Delta\lambda) = \frac{\Phi_{n+1}^i}{\frac{\partial \Phi}{\partial \tilde{\boldsymbol{\sigma}}} : \mathbb{C}_0 : \frac{\partial \Phi}{\partial \tilde{\boldsymbol{\sigma}}} - \frac{\partial \Phi}{\partial f}(1-f)\left(\frac{\partial \Phi}{\partial \tilde{\sigma}_m} - 3\alpha\gamma\right) - \frac{\partial \Phi}{\partial \bar{\sigma}}\frac{\partial \bar{\sigma}}{\partial \varepsilon^p}\gamma} \tag{A.7}$$

One obtains:

$$\Delta\lambda^{i+1} = \Delta\lambda^i + \delta(\Delta\lambda) \tag{A.8}$$

The corresponding algorithm is summarized as follows:

© 2018 Tous droits réservés.

lilliad.univ-lille.fr

1. Input data : $\tilde{\boldsymbol{\varepsilon}}_{0,n}, \tilde{\boldsymbol{\varepsilon}}^{p}_{0,n}, \varepsilon^{p}_{n}$ and $\Delta\tilde{\boldsymbol{\varepsilon}}_{0}$

2. Calculating the deformation at step $n+1$: $\tilde{\boldsymbol{\varepsilon}}_{0,n+1} = \tilde{\boldsymbol{\varepsilon}}_{0,n} + \Delta\tilde{\boldsymbol{\varepsilon}}_{0}$

3. Initialize : $i = 0, \tilde{\boldsymbol{\varepsilon}}^{p,0}_{0,n+1} = \tilde{\boldsymbol{\varepsilon}}^{p}_{0,n},\ \Delta\lambda^{0}{=}0$

$$\tilde{\boldsymbol{\sigma}}^{0}_{n+1} = \mathbb{C}_{0} : (\tilde{\boldsymbol{\varepsilon}}_{0,n+1} - \tilde{\boldsymbol{\varepsilon}}^{p,0}_{0,n+1})$$

$$\Phi(\tilde{\boldsymbol{\sigma}}^{i}_{n+1}, \varepsilon^{p,i}_{n+1}, f) = \Phi^{i}_{n+1}$$

4. IF $\Phi^{i}_{n+1} \leq$ Tolerance THEN: EXIT (end of algorithm)

ELSE (plastic correction):

5. $$\delta(\Delta\lambda) = \frac{\Phi^{i}_{n+1}}{\frac{\partial\Phi}{\partial\tilde{\boldsymbol{\sigma}}} : \mathbb{C}_{0} : \frac{\partial\Phi}{\partial\tilde{\boldsymbol{\sigma}}} - \frac{\partial\Phi}{\partial f}(1-f)\left(\frac{\partial\Phi}{\partial\tilde{\sigma}_{m}} - 3\alpha\gamma\right) - \frac{\partial\Phi}{\partial\tilde{\sigma}}\frac{\partial\tilde{\sigma}}{\partial\varepsilon^{p}}\gamma}$$

6. Calculate new values for each iteration:

$$\tilde{\boldsymbol{\sigma}}^{i+1}_{n+1} = \tilde{\boldsymbol{\sigma}}^{i}_{n+1} - \delta(\Delta\lambda)\mathbb{C}_{0} : \frac{\partial\Phi^{i}_{n+1}}{\partial\tilde{\boldsymbol{\sigma}}}(\tilde{\boldsymbol{\sigma}}^{i}_{n+1}, \varepsilon^{p,i}_{n+1}, f)$$

$$\varepsilon^{p,i+1}_{n+1} = \varepsilon^{p,i}_{n+1} + \delta(\Delta\lambda)\gamma$$

$$\Delta\lambda^{i+1} = \lambda^{i} + \delta(\Delta\lambda)$$

$$\tilde{\boldsymbol{\varepsilon}}^{p,i+1}_{n+1} = \tilde{\boldsymbol{\varepsilon}}^{p,i}_{n+1} + \delta(\Delta\lambda)\frac{\partial\Phi}{\partial\tilde{\boldsymbol{\sigma}}}$$

Set $i = i+1$ and return to step 4

ENDIF

7. EXIT

End of Algorithm

© 2018 Tous droits réservés.

lilliad.univ-lille.fr

Appendix B

Comparison between experimental data and simulations in the case of associated perfectly plastic clay solid phase

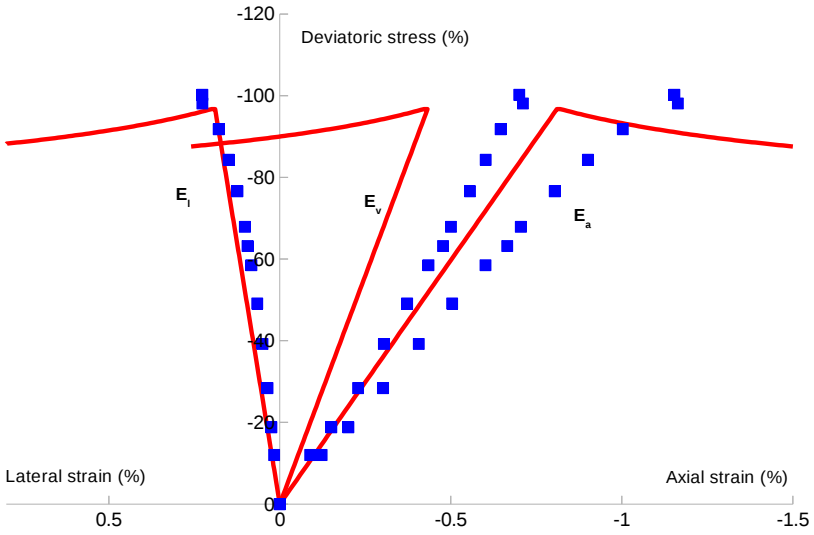

Figure B.1: Comparison between associated perfectly plastic simulations and experimental data in a simple triaxial compression test on a Vaca Muerta shale sample (confining pressure=5 MPa; depth=2668.71 m; well S2; vertical; f_1=0.15/f_2=0.412/f_3=0.0033/f_5=0.23/f=0.09).

© 2018 Tous droits réservés.

lilliad.univ-lille.fr

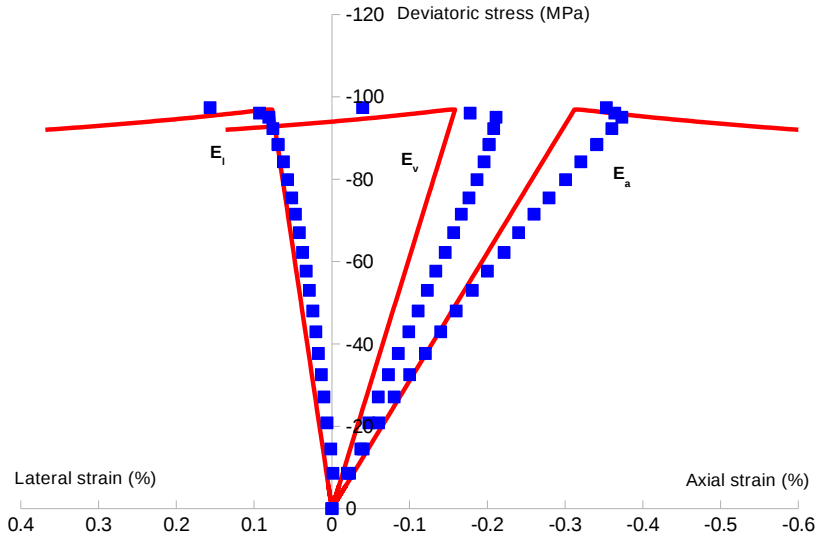

Figure B.2: Comparison between associated perfectly plastic simulations and experimental data in a simple triaxial compression test on a Vaca Muerta shale sample (confining pressure=8 MPa; depth=2668.78 m; well S2; horizontal; f_1=0.143/f_2=0.35/f_3=0.0044/f_4=0.12/f_6=0.13/f=0.13).

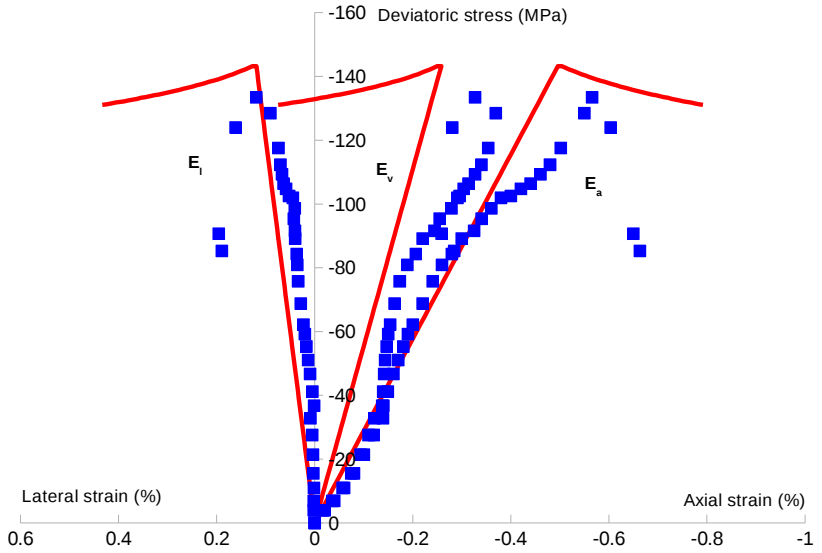

Figure B.3: Comparison between associated perfectly plastic simulations and experimental data in a simple triaxial compression test on a Vaca Muerta shale sample (confining pressure=25 MPa; depth=2686.55 m; well S2; horizontal; f_1=0.2275/f_2=0.431/f_3=0.0164/f_4=0.1/f_6=0.05/f=0.08).

© 2018 Tous droits réservés.

lilliad.univ-lille.fr

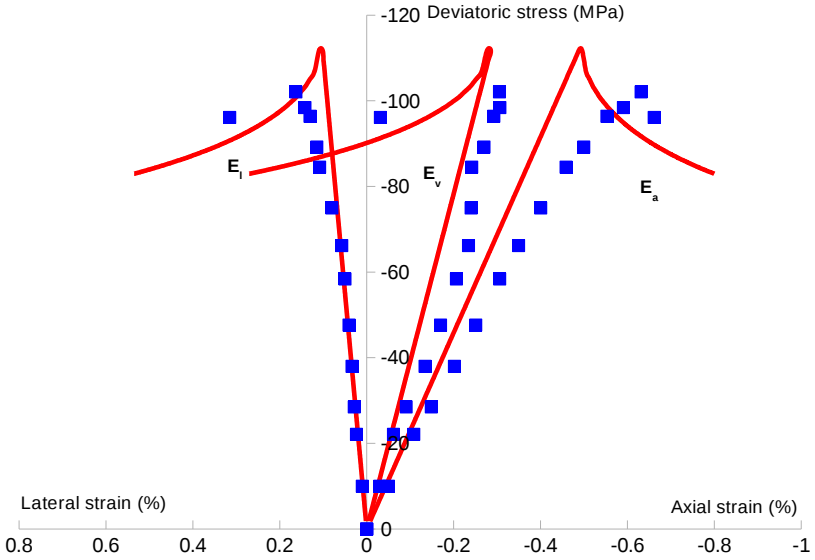

Figure B.4: Comparison between associated perfectly plastic simulations and experimental data in a simple triaxial compression test on a Vaca Muerta shale sample (confining pressure=2 MPa; depth=2639.73 m; well S3; vertical; f_1=0.4/f_2=0.3/f_4=0.257/f_6=0.05/f=0.05).

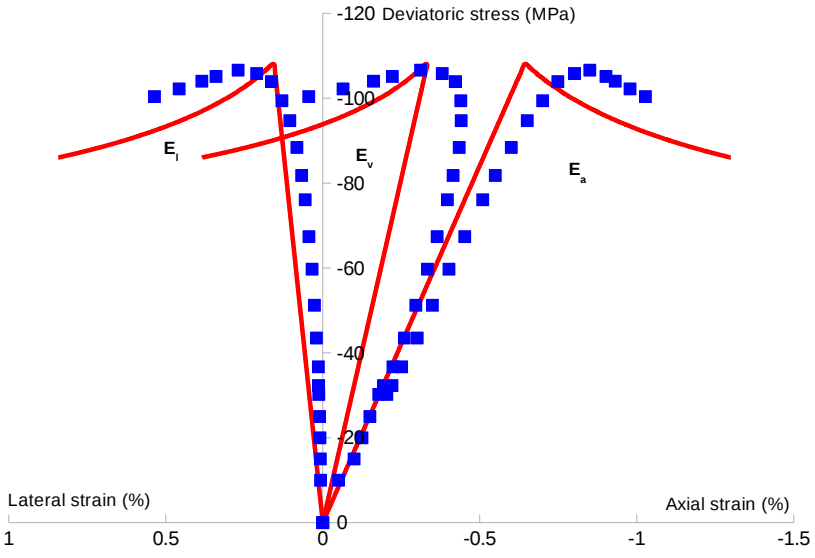

Figure B.5: Comparison between associated perfectly plastic simulations and experimental data in a simple triaxial compression test on a Vaca Muerta shale sample (confining pressure=10 MPa; depth=2652.46 m; well S3; vertical; f_1=0.2415/f_2=0.173/f_4=0.264/f_6=0.25/f=0.08).

© 2018 Tous droits réservés.

lilliad.univ-lille.fr

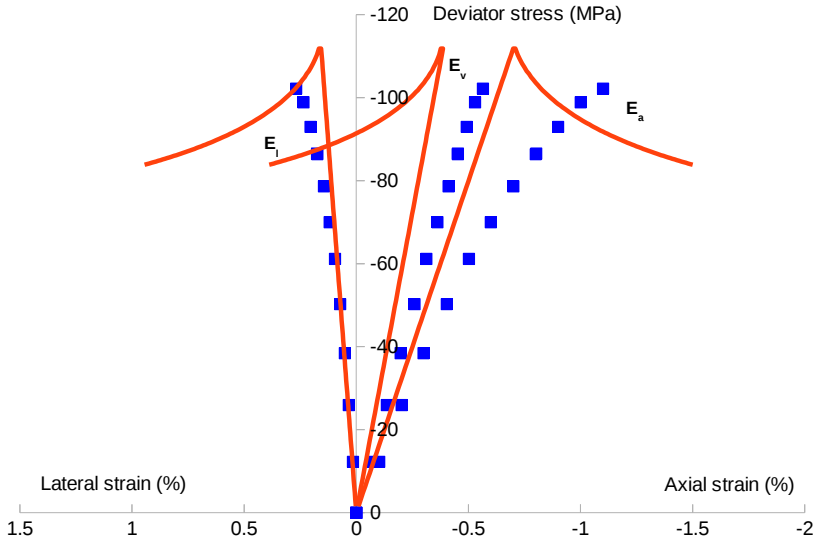

Figure B.6: Comparison between associated perfectly plastic simulations and experimental data in a complex triaxial compression test on a Vaca Muerta shale sample (confining pressure=10 MPa; depth=2649.23 m; well S1; vertical; f_1=0.39/f_2=0.3/f_3=0.024/f_4=0.15/f=0.1).

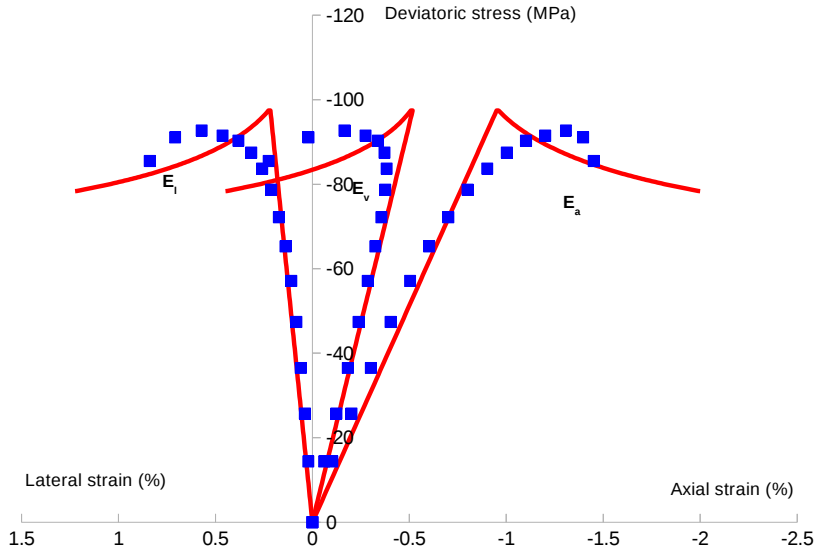

Figure B.7: Comparison between associated perfectly plastic simulations and experimental data in a complex triaxial compression test on a Vaca Muerta shale sample (confining pressure=10 MPa; depth=2536.23 m; well S3; vertical; f_1=0.26/f_2=0.3075/f_3=0.0068/f_4=0.172/f=0.14).

© 2018 Tous droits réservés.

lilliad.univ-lille.fr

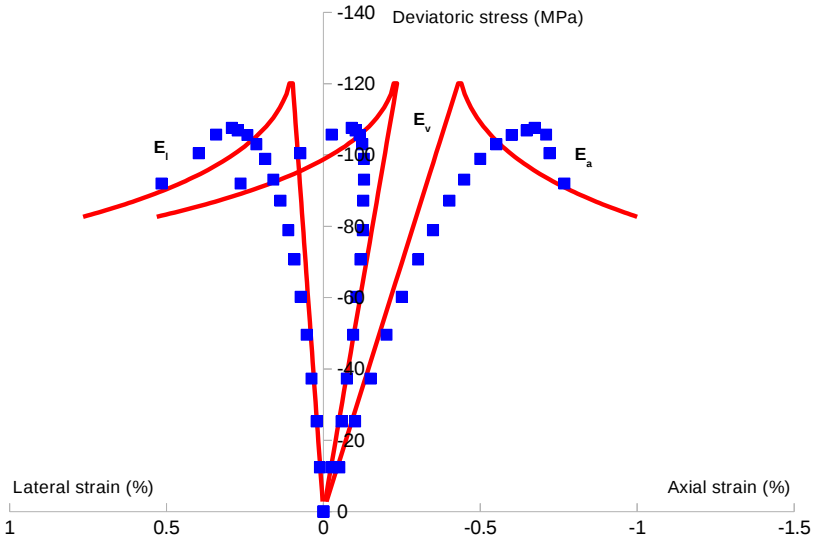

Figure B.8: Comparison between associated perfectly plastic simulations and experimental data in a complex triaxial compression test on a Vaca Muerta shale sample (confining pressure=10 MPa; depth=2576.21 m; well S3; vertical; f_1=0.53/f_2=0.21/f_4=0.153/f_5=0.05/f_6=0.05/f=0.08).

© 2018 Tous droits réservés.

lilliad.univ-lille.fr

Appendix C

Abaqus finite element results

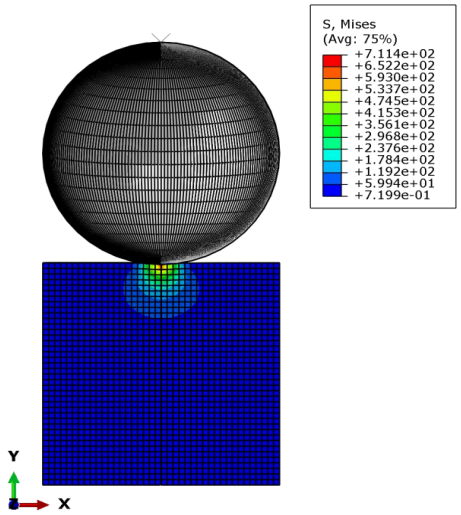

(a) Perfect layer

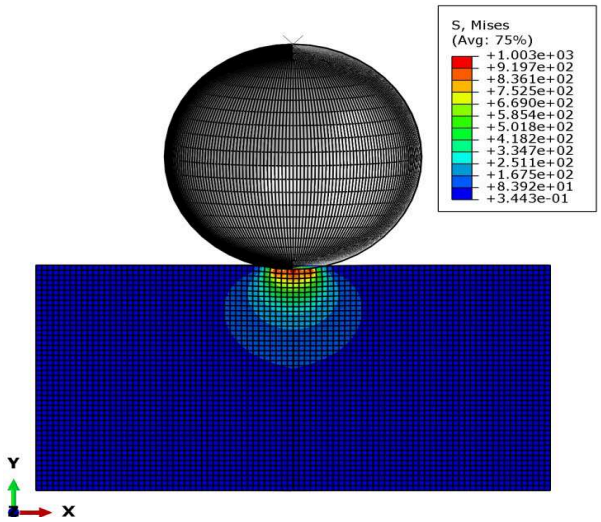

(b) Half layer

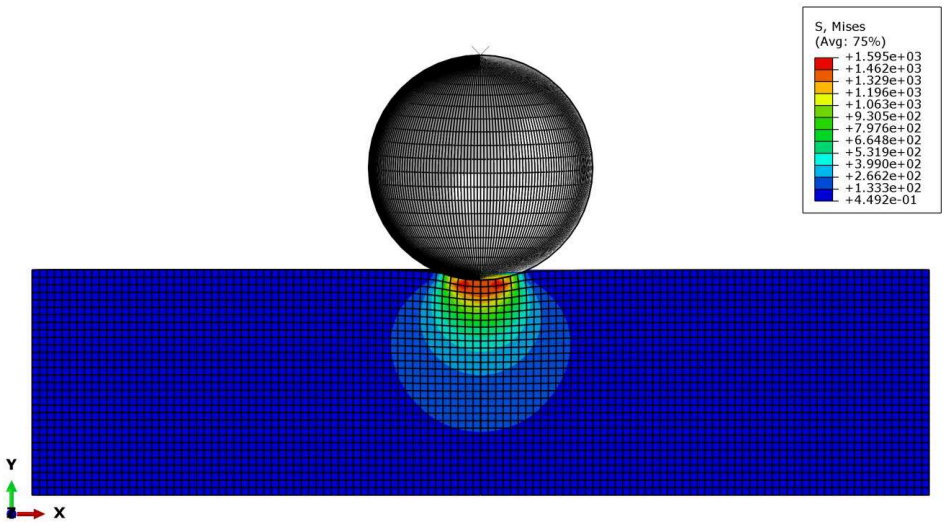

(c) Quarter layer

Figure C.1: Variation of the equivalent stress of Von Mises for the three layers with mineralogical composition of zone Z2.

© 2018 Tous droits réservés.

lilliad.univ-lille.fr

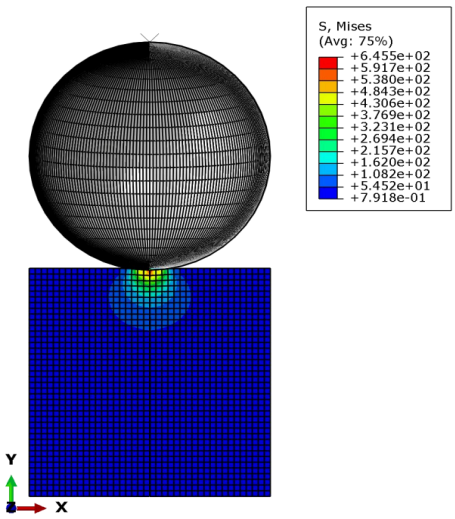

(a) Perfect layer

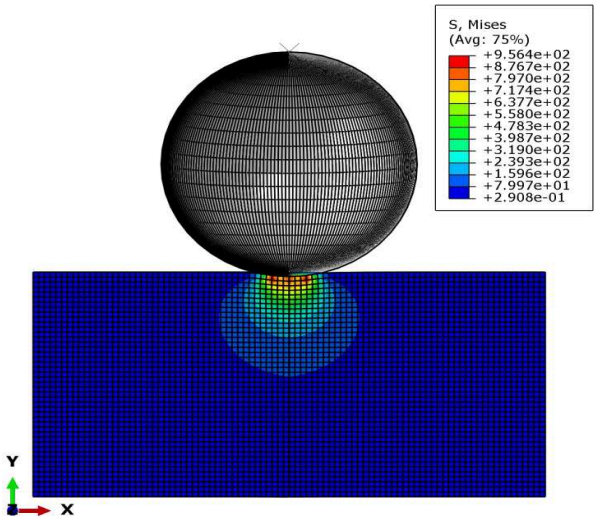

(b) Half layer

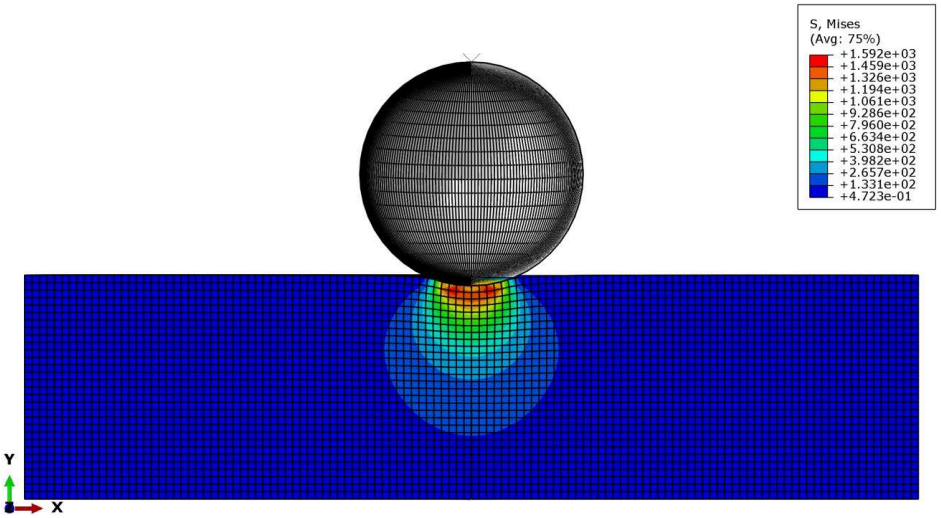

(c) Quarter layer

Figure C.2: Variation of the equivalent stress of Von Mises for the three layers with mineralogical composition of zone Z3.

© 2018 Tous droits réservés.

lilliad.univ-lille.fr

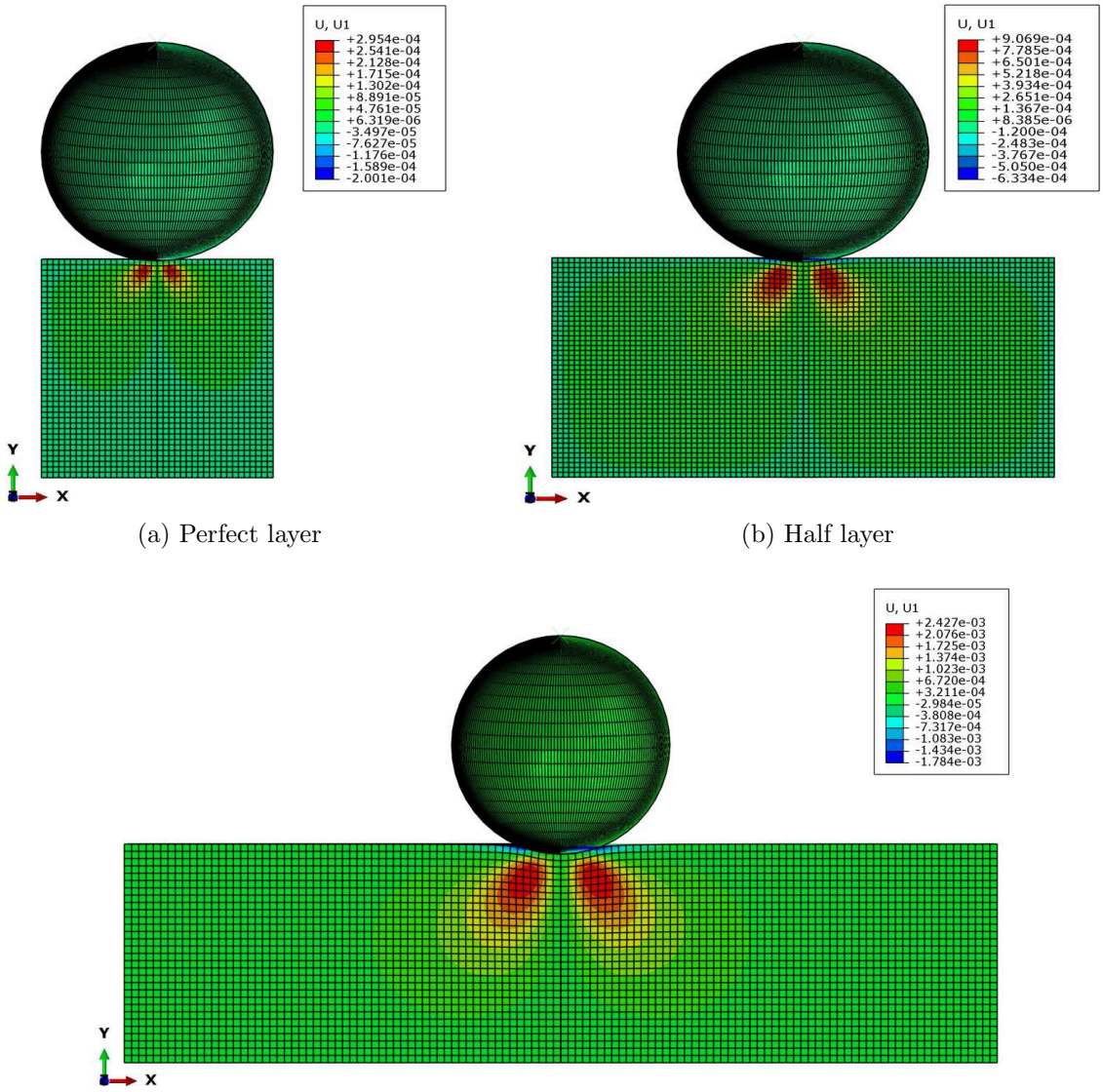

(a) Perfect layer

(b) Half layer

(c) Quarter layer

Figure C.3: Variation of the deformation along X axis for the three layers with mineralogical composition of zone Z2.

© 2018 Tous droits réservés.

lilliad.univ-lille.fr

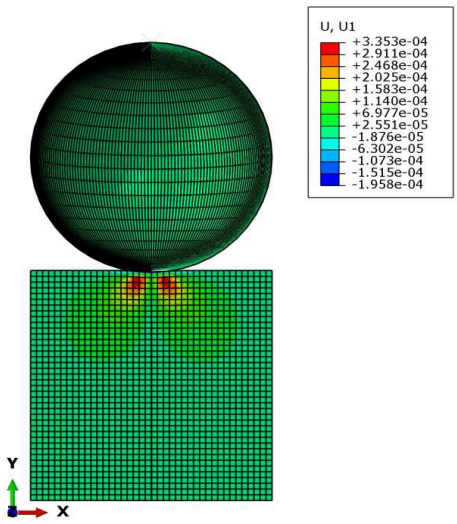

(a) Perfect layer

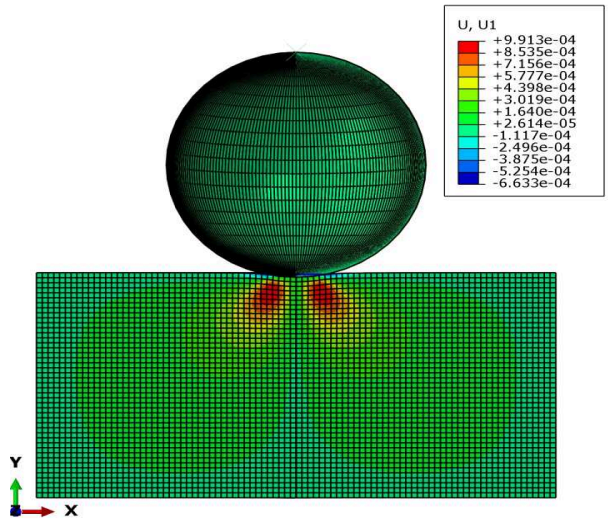

(b) Half layer

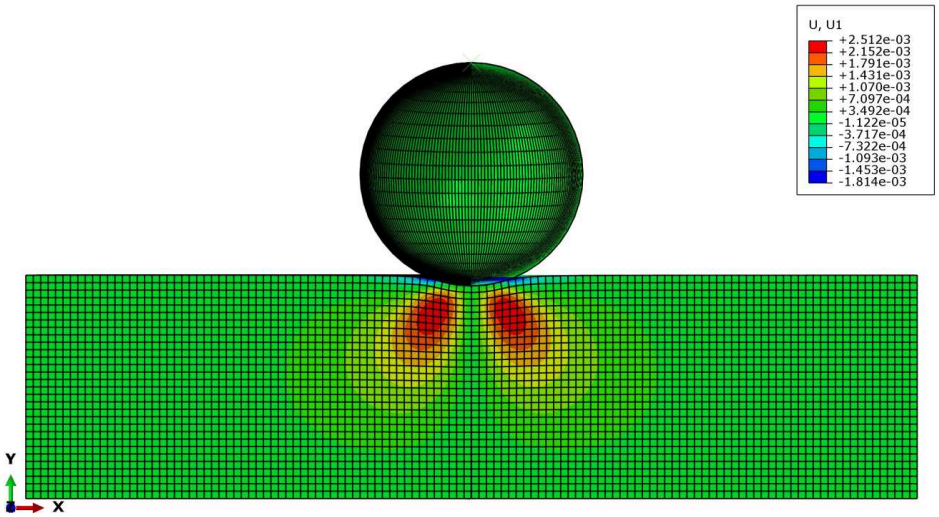

(c) Quarter layer

Figure C.4: Variation of the deformation along X axis for the three layers with mineralogical composition of zone Z3.

© 2018 Tous droits réservés.

lilliad.univ-lille.fr

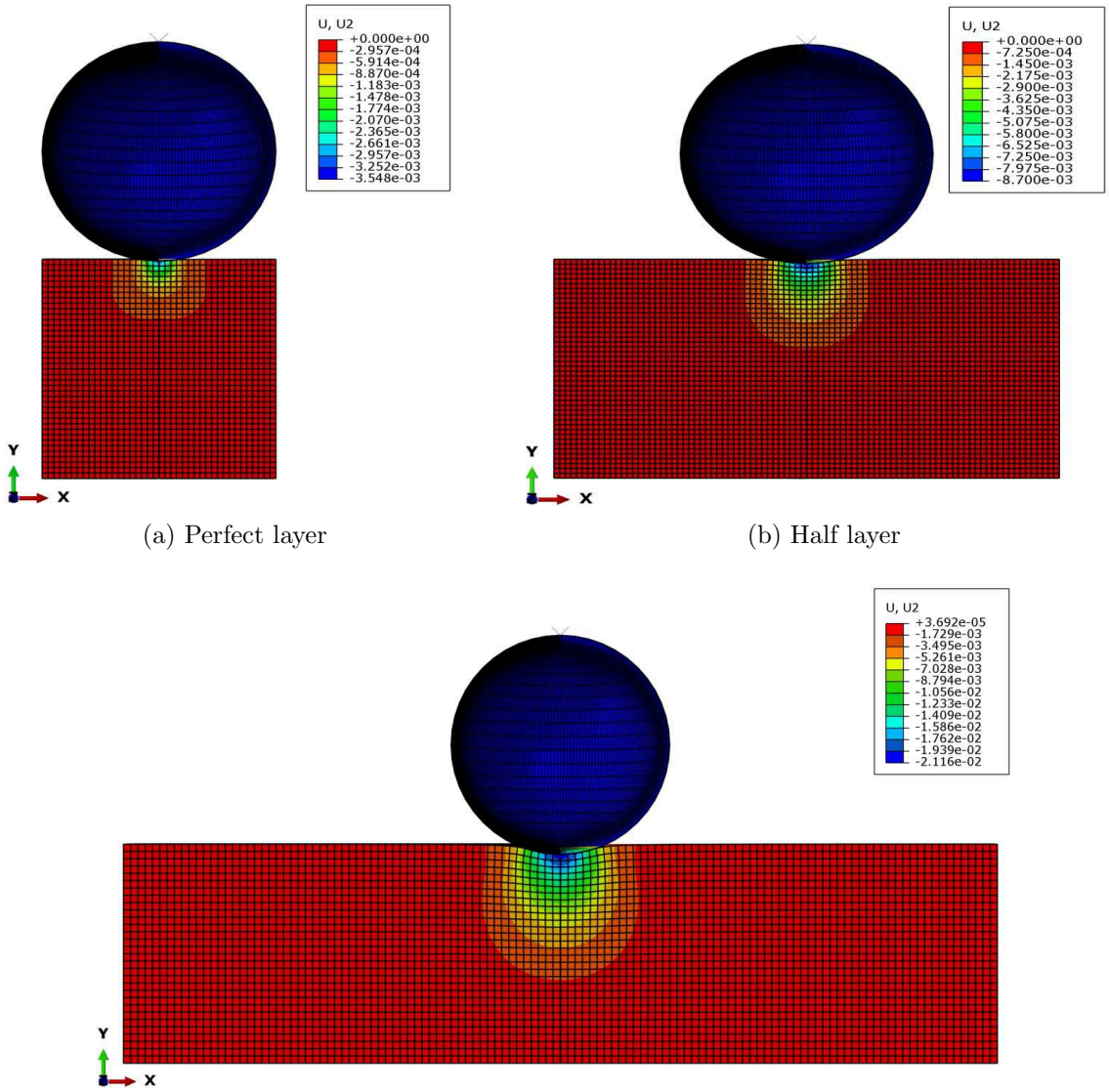

(a) Perfect layer

(b) Half layer

(c) Quarter layer

Figure C.5: Variation of the deformation along Y axis for the three layers with mineralogical composition of zone Z2.

© 2018 Tous droits réservés.

lilliad.univ-lille.fr

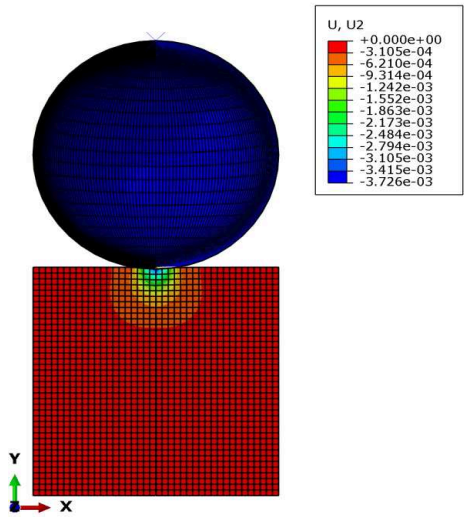

(a) Perfect layer

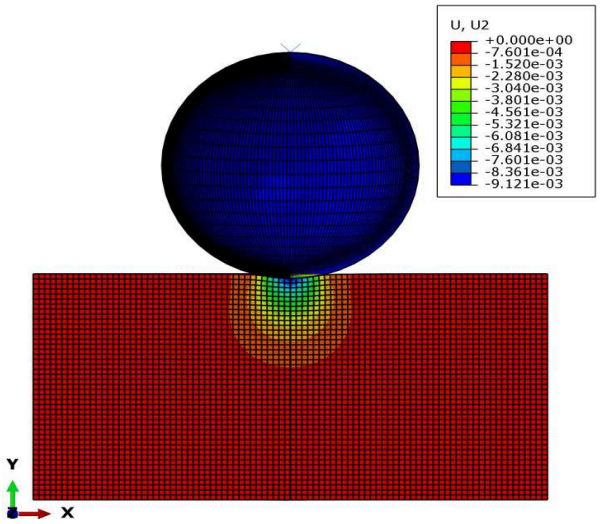

(b) Half layer

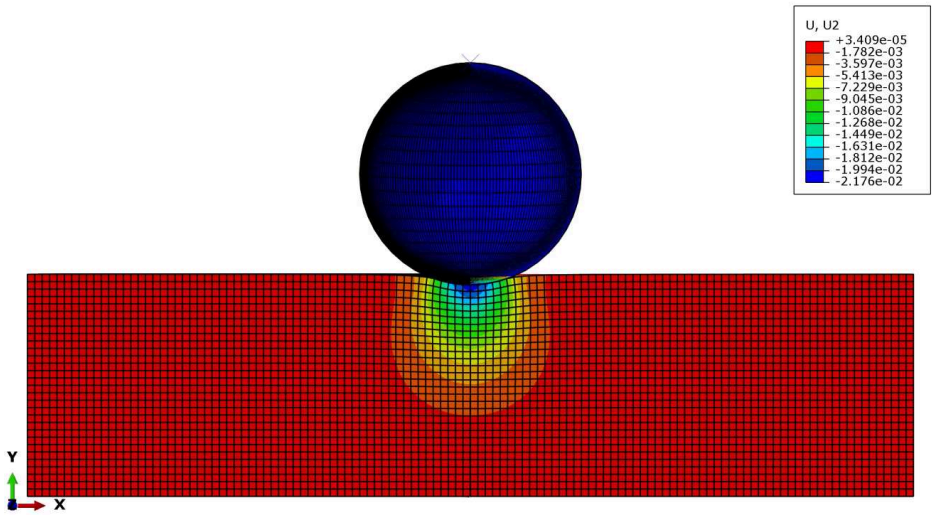

(c) Quarter layer

Figure C.6: Variation of the deformation along Y axis for the three layers with mineralogical composition of zone Z3.

© 2018 Tous droits réservés.

lilliad.univ-lille.fr

Thèse de Faten Farhat, Université de Lille, 2018

Bibliography

S. Abedi, M. Slim, R. Hofmann, T. Bryndzia, and F.J. Ulm. Nanochemo-mechanical signature of organic-rich shales: a coupled indentation-edx analysis. *Acta Geotechnica*, 11:559–572, 2016a.

S. Abedi, M. Slim, and F.J. Ulm. Nanomechanics of organic-rich shales: the role of thermal maturity and organic matter content on texture. *Acta Geotechnica*, 11: 775–787, 2016b.

A. Abou-Chakra Guéry, F. Cormery, J. F. Shao, and D. Kondo. A micromechanical model of elastoplastic and damage behaviour of a cohesive geomaterial. *International journal of solids and structures*, 45:1406–1429, 2008.

A. Abou-Chakra Guéry, F. Cormery, J. F. Shao, and D. Kondo. A multiscale modeling of damage and time-dependent behavior of cohesive rocks. *Int. J. for numerical and analytical methods in Geomechanics*, 33(5):567–589, 2009.

Y. Abousleiman, M.H. Tran, S. Hoang, A. Ortega, and F.J. Ulm. Geomechanics field characterization of the two prolific u.s. mid-west gas plays with advanced wire-line logging tools. New Orleans, Louisiana, 4-7 October, 2009. SPE Annual Technical Conference and Exhibition, Society of Petroleum Engineers.

Y.N. Abousleiman, K.L. Hull, Y. Han, G. Al-Muntasheri, P. Hosemann, S. Parker, and C.B. Howard. The granular and polymer composite nature of kerogen-rich shale. *Acta Geotechnica*, 11:573–594, 2016.

R.S.O Ahmadov. *Microtextural, elastic and transport properties of source rocks*. PhD thesis, Standford university, 2011.

A.T. Akono and P. Kabir. Microscopic fracture characterization of gas shale via scratch testing. *Mechanics Research Communications*, 78:86–92, 2016.

A.M. Allan, A.C. Clark, and T. Vanorio. Pyrolysis-induced evolution of the elastic and transport properties of the barnett shale. New Orleans, Louisiana, 18-23 October, 2015. SEG Annual Meeting.

© 2018 Tous droits réservés.

lilliad.univ-lille.fr

B. Alramahi and M.I. Sundberg. Proppant embedment and conductivity of hydraulic fractures in shales. Chicago, Illinois, 24-27 June, 2012. 46th U.S. Rock Mechanics/Geomechanics Symposium, ARMA.

R.J. Ambrose, R.C. Hartman, M. Diaz-Campos, I.Y. Akkutlu, and C.H. Sondergeld. New pore-scale considerations for shale gas-in-place calculations. Pittsburgh, PA, 23-25 February, 2010. Unconventional Gas Conference, SPE.

A. Askenazi, P. Biscayart, M. Cneva, S. Montenegro, and M. Moreno. Analoga entre la formacin vaca muerta y shale gas/oil plays de eeuu. Society of Petroleum Engineers JJPP0003, 2013.

B.K. Atkinson. Subcritical crack growth in geological materials. *Journal of Geophysical Research-Solid earth*, 89:4077–4114, 1984.

K.C. Bennett, L.A. Berla, W.D. Nix, and R.I. Borja. Instrumented nanoindentation and 3d mechanistic modeling of a shale at multiple scales. *Acta Geotechnica*, 10: 1–14, 2015.

R.H. Bennett, N.R. O'Brien, and M.H. Hulbert. Determinants of clay and shale microfabric signatures: processes and mechanisms. In R.H. Bennett, N.R. O'Brien, and M.H. Hulbert, editors, *Microstructure of fine grained sediments: from mud to shale*, pages 5–32. Springer, New York, 1991.

C. Bikong, D. Hoxha, and J. F. Shao. A micro-macro model for time-dependent behavior of clayey rocks due to anisotropic propagation of microcracks. *International Journal of Plasticity*, 69:73–88, 2015.

C.P. Bobko. *Assessing the Mechanical Microstructure of Shale by Nanoindentation: The Link Between Mineral Composition and Mechanical Properties*. PhD thesis, Massachusetts Institute of Technology, Cambridge MA, 2008.

M. Bornert, T. Bretheau, and P. Gilormini. *Homogénéisation en mécanique des matétriaux 1. Matériaux aléatoires élastiques et milieux périodiques.* Hermes Sciences Europe Ltd, 2001a.

A. Boulenouar, S. Mighani, H. Pourpak, Y. Bernabé, and B. Evans. Mechanical properties of vaca muerta shales from nano-indentation tests. San Francisco, CA, 2017. 51th U.S. Rock Mechanics/Geomechanics Symposium, ARMA.

C. Boyer, B. Clark, V. Jochen, R. Lewis, and J.K. Miller. Shale gas: A global resource. *Schlumberger, Oilfield Review*, 3(3), 2011.

J.M. Brown, E.H. Abramson, and R.J. Angel. Triclinic elastic constants for low albite. *Physics and Chemistry of Minerals*, 33:256–265, 2006.

© 2018 Tous droits réservés.

lilliad.univ-lille.fr

R. Brown and J. Cadenhead. Argentine operations shift to unconventional plays, 2014.

M. Byrne, E. Rojas, R. Kandasamy, and A. Gibb. Fines migration in oil and gas reservoirs: Quantification and qualification through detailed study. Lafayette, Louisiana, USA, 26-28 February, 2014. SPE International Symposium and Exhibition on Formation Damage Control, Society of Petroleum Engineers.

S. Chanchole. *Experimental study of time-dependent behavior of East claystone with sample tests of long duration (in French).* Andra report, DRP0G3S2004-01/A, vol21(7), 1409-1434, Paris, 2004.

L. Cheng, G. de Saxcé, and D. Kondo. A stress-based variational model for ductile porous materials. *International Journal of Plasticity*, 55:133–151, 2014.

N. Conil and G. Armand. *Complementary tests on the time-dependent behavior of the Callovo-Oxfordian argillites.* Andra report in French, Paris, 2015.

N.D. Cristescu. *Rock rheology.* Kluwer Academic, 1989.

N.D. Cristescu. A general constitutive equation for transient and stationary creep of rock salt. *International Journal of Rock Mechanics and Mining Sciences & Geomechanics Abstracts*, 30:125–140, 1993.

M.E. Curtis, R.J. Ambrose, C.H. Sondergeld, and C.S. Rai. Structural characterization of gas shales on the micro- and nano-scales. Calgary, Alberta, Canada, 19-21 October, 2010. Canadian Unconventional Resources and International Petroleum Conference, CSUG/SPE.

A. Dahou, J.F. Shao, and M. Bederiat. Experimental and numerical investigations on transient creep of porous chalk. *Mechanics of Materials*, 21:147–158, 1995.

L.H. Dai and G.J. Huang. An incremental micromechanical scheme for nonlinear particulate composites. *International Journal of Mechanical Sciences*, 43:1179–1193, 2001.

Les Amis de la Terre. `http://www.amisdelaterre.org/rapportargentine`, 2014.

A. Delafargue. *Material invariant properties of shales: nanoindentation and microporoelastic analysis.* PhD thesis, Massachusetts Institute of Technology, Cambridge, MA, 2004.

I. Doghri and A. Ouaar. Homogenization of two-phase elastoplastic composite materials and structures: study of tangent operators, cyclic plasticity and numerical algorithms. *International Journal of Solids and Structures*, 40:1681–1712, 2003.

© 2018 Tous droits réservés.

lilliad.univ-lille.fr

L. Dormieux, D. Kondo, and F.J. Ulm. *Microporomechanics*. Wiley, Chichester, 2006.

D.C. Drucker and W. Prager. Soil mechanics and plastic analysis or limit design. *Quarterly of Applied Mathematics*, 10:157–175, 1952.

R.J. Duenckel, M.W. Conway, B. Eldred, and M.C. Vincent. Proppant diagenesis - integrated analyses provide new insights into origin, occurrence, and implications for proppant performance. The Woodlands, Texas, USA, 24-26 January, 2011. SPE Hydraulic Fracturing Technology Conference, Society of Petroleum Engineers.

H.U. Dusterloh. Rock mechanical investigations into the creep behavior of claystone samples., 2015.

Energy Information Administration EIA. *Annual Energy Outlook*. Washington DC, 2013.

C. Fialips. Argentina neuquén basin san roque block sr.xp-1010 exploration well quantitative mineralogy and petrography from cores, vaca muerta fm., 2014.

A. Fodil, W. Aloulou, and P. Y. Hicher. Viscoplastic behaviour of soft clay. *Geotechnique*, 43(3):581–591, 1997.

F. Gassmann. On elasticity of porous media: classics of elastic wave theory. SEG, 1951.

B. Gathier. *Multiscale strength homogenization-Application to shale nanoindentation*. PhD thesis, Massachusetts Institute of Technology, Cambridge, MA, 2008.

B. Gerard, G. Pijaudier-Cabot, and C. Laborderie. Coupled diffusion-damage modeling and the implications on failure due to strain localizations. *International Journal of Solids and Structures*, 35:4107–4120, 1998.

A. Abou-Chakra Guéry. *Contribution la modélisation micromécanique u comportement non-linéaire de l'argilite du Callovo-Oxfordien*. PhD thesis, University of Lille, France, 2007.

T. Guo, J. Faleskog, and C. Shih. Continuum modeling of a porous solid with pressure-sensitive dilatant matrix. *Journal of the Mechanics and Physics of Solids*, 56: 2188–2212, 2008.

A. Gurson. Continuum theory of ductile rupture by void nucleation and growth: Part 1-yield criteria and flow rules for porous ductile media. *Journal of Engineering Materials and Technology*, 99:2–15, 1977.

E. Hansen, D. Mulvaney, and M. Betcher. Water resource reporting and water footprint from marcellus shale development in west virginia and pennsylvania, downstream strateing, 2013.

© 2018 Tous droits réservés.

lilliad.univ-lille.fr

Z. Hashin and S. Shtrikman. A variational approach to the elastic behavior of multiphase minerals. *Journal of the Mechanics and Physics of Solids*, 11:127–140, 1963.

R. Hill. Continuum micro-mechanicsof elastoplastic polycrystals. *Journal of the Mechanics and Physics of Solids*, 13:89–101, 1965.

B. Hornby, L. Schwartz, and J. Hudson. Anisotropic effective medium modeling of the elastic properties of shales. *Geophysics*, 59:1570–1583, 1994.

Y. Huang and J.F. Shao. A micromechanical analysis of time-dependent behavior based on subcritical damage in claystone. *International Journal of Damage Mechanics*, 22:773–790, 2012.

U. Hunsche and A. Hampel. Rock salt-the mechanical properties of the host rock material for a radioactive waste repository. *Engineering Geology*, 52:271–291, 1999.

IHS Global Insight Inc. IHS. *The economic and employment contributions of shale gas in the United States*. Washington DC, 2011.

ISS/RGM. Microstructure of Vaca Muerta shales, Neuquén basin., 2016.

M. Jakobsen, J.A. Hudson, and T.A. Johansen. T-matrix approach to shale acoustics. *Geophysical Journal International*, 154:533–558, 2003.

T. Jiang, A. Abou-Chakra Guéry, D. Kondo, and J.F. Shao. Multi-scale modeling for inelastic behavior of a cohesive geomaterial. *Mechanics Research Communications*, 36:673–681, 2009.

J. Jin and N. Cristescu. An elastic viscoplastic model for transient creep of rock salt. *International Journal of Plasticity*, 14:85–107, 1998.

L.E.A. Jones and H.F. Wang. Ultrasonic velocities in cretaceous shales from the williston basin. *Geophysics*, 46:288–297, 1981.

J.W. Ju and H.K. Lee. A micromechanical damage model for effective elastoplastic behavior of ductile matrix composites considering evolutionary complete particle debonding. *Computer methods in applied mechanics and engineering*, 183:201–222, 2000.

H.E. King, A.P.R. Eberle, C.C. Walters, C.E. Kliewer, D. Ertas, and C. Huynh. Pore architecture and connectivity in gas shale. *Energy Fuels*, 29:1375–1390, 2015.

M. Kopycinska-Müller, M. Prasad, U. Rabe, and W. Arnold. *Elastic Properties of Clay Minerals Determined by Atomic Force Acoustic Microscopy Technique*, pages 409–416. Springer Netherlands, Dordrecht, 2007.

© 2018 Tous droits réservés.

lilliad.univ-lille.fr

V. Kumar, M.E. Curtis, N. Gupta, C.H. Sondergeld, and C.S. Rai. Estimation of elastic properties of organic matter in woodford shale through nanoindentation measurements. Calgary, Alberta, Canada, 30 October-1 November, 2012. SPE Canadian Unconventional Resources Conference, Society of Petroleum Engineers.

R.F. LaFollette and P.S. Carman. Proppant diagenesis: Results so far. Pittsburgh, Pennsylvania, USA, 23-25 February, 2010. SPE Unconventional Gas Conference, Society of Petroleum Engineers.

B. Lecampion, S. Abbas, and R. Prioul. Competition between transverse and axial hydaulic fractures in horizontal wells. SPE 163848, 2013.

J. Lemaitre and J. L. Chaboche. *Mechanics of solid materials*. Cambridge University Press, London, 1998.

T. Lhomme, E. Detournay, and R. Jeffrey. Effect of fluid compressibility and borehole radius on the propagation of a fluid-driven fracture. Turin, Italy, 2005. 11th International Conference on Fracture.

Y. Li and C. Xia. Time-dependent tests on intact rocks in uniaxial compression. *International Journal of Rock Mechanics and Mining Sciences*, 37:467–475, 2000.

D.R. Lide. *Handbook of Chemistry and Physics*. CRC Press, 2004.

I. Lonardelli, H.R. Wenk, and Y. Ren. Preferred orientation and elastic anisotropy in shales. *Geophysics*, 72:D33–D40, 2007.

R.G. Loucks, R.M. Reed, S.C. Ruppel, and U. Hammes. Spectrum of pore types and networks in mudrocks and a descriptive classification for matrix-related mudrock pores. *AAPG Bull*, 96:1071–1098, 2012.

A.M. Lucier, R. Hofmann, and L.T. Bryndzia. Evaluation of variable gas saturation on acoustic log data from the haynesville shale gas play, nw louisiana, usa. *The Leading Edge*, 30:300–311, 2011.

D. Lydzba and J. F. Shao. Stress equivalence principle for saturated porous media. *Comptes Rendus Mecanique*, 330:297–303, 2002.

D. Lydzba, S. Pietruszczak, and J.F. Shao. Intergranular pressure solution in chalk: a multiscale approach. *Computers and Geotechnics*, 34(4):291 – 305, 2007.

S. Maghous, L. Dormieux, and J.F. Barthélémy. Micromechanical approach to the strength properties of frictional geomaterials. *European Journal of Mechanics - A/Solids*, 28(1):179 – 188, 2009.

© 2018 Tous droits réservés.

lilliad.univ-lille.fr

E. Maranini and M. Brignoli. Creep behavior of a weak rock: experimental characterization. *International Journal of Rock Mechanics and Mining Sciences*, 36: 127–138, 1999.

E. Maranini and T. Yamaguchi. A non-associated viscoplastic model for the behaviour of granite in triaxial compression. *Mechanics of Materials*, 33:283–293, 2001.

C.D. Martin and N.A. Chandler. The progressive failure of lac du bonnet granite. *International Journal of Rock Mechanics and Mining Sciences*, 31:643–659, 1994.

G. Mavko, T. Mukerji, and J. Dvorkin. *The Rock Physics Handbook*. Cambridge University Presss, UK, 1998.

R.H. Morales, R. Suarez-Rivera, and E. Edelman. Experimental evaluation of hydraulic fracture impairment in shale reservoirs. San Francisco, California, 26-29 June, 2011. 45th U.S. Rock Mechanics/Geomechanics Symposium, ARMA.

T. Mori and K. Tanaka. Average stress in a matrix and average elastic energy of materials with misfitting inclusions. *Acta Metallurgica et Materialia*, 42:597–629, 1973.

Q.R. Passey, K.M. Bohacs, W.L. Esch, R. Klimentidis, and S. Sinha. From oil-prone source rock to gas-producing shale reservoir-geologic and petrophysical characterization of unconventional shale gas reservoirs. Beijing, China, 8-10 June, 2010. International Oil and Gas Conference and Exhibition in China, SPE.

F. Pastor and D. Kondo. Limit analysis and lower/upper bounds to the macroscopic criterion of drucker-prager materials with spheroidal voids. *Comptes Rendus Mecanique*, 342:96–105, 2014.

J. Pastor, Ph. Thoré, and F. Pastor. Limit analysis and numerical modeling of spherically porous solids with Coulomb and DruckerPrager matrices. *Journal of Computational and Applied Mathematics*, 234:2162–2174, 2010.

P. Perzyna. Fundamental problems in viscoplasticity. *Advances in Applied Mechanics*, 9:243 – 377, 1966.

S. Pietruszczak, D. Lydzba, and J. F. Shao. Modeling of inherent anisotropy in sedimentary rocks. *International Journal of Solids and Structures*, 39:637–648, 2002.

S. Pietruszczak, D. Lydzba, and J.F. Shao. Description of creep in inherently anisotropic frictional materials. *Journal of Engineering Mechanics*, 130:681–690, 2004.

© 2018 Tous droits réservés.

lilliad.univ-lille.fr

P. Ponte-Castaneda. New variational principles in plasticity and their application to composite materials. *Journal of the Mechanics and Physics of Solids*, 40:1757–1788, 1992.

P. Ponte-Castaneda. Exact second-order estimates for the effective mechanical properties of non-linear composite materials. *Journal of the Mechanics and Physics of Solids*, 44:827–862, 1996.

M. Prasad, M. Kopycinska, U. Rabe, and W. Arnold. Measurement of young's modulus of clay minerals using atomic force acoustic microscopy. *Geophysical Research Letters*, 29:13–1–13–4, 2002.

X. Qin, D.H. Han, and L.Zhao. Rock physics modeling of organic-rich shales with different maturity levels. SEG Technical Program Expanded Abstracts, 2014.

A. Sameni, P. Pourafshary, M. Ghanbarzadeh, and S. Ayatollahi. Effect of nanoparticles on clay swelling and migration. *Egyptian Journal of Petroleum*, 24:429–437, 2015.

J. Schieber, R. Lazar, K. Bohacs, R. Klimentidis, M. Dumitrescu, and J. Ottmann. An SEM study of porosity in the Eagle Ford shale of Texas-Pore types and porosity distribution in a depositional and sequence-stratigraphic context. In J.A. Breyer, editor, *The Eagle Ford shale: a renaissance in U.S. oil production*, pages 167–186. AAPG Memoir 110, 2016.

J.F. Shao, Q.W. Zhu, and K. Su. Modeling of creep in rock materials in terms of material degradation. *Computers and Geotechnics*, 30:549–555, 2003.

J.F. Shao, K.T. Chau, and X.T. Feng. Modeling of anisotropic damage and creep deformation in brittle rocks. *International Journal of Rock Mechanics and Mining Sciences*, 43:582–592, 2006.

W.Q. Shen and J.F. Shao. A micro-macro model for porous geomaterials with inclusion debonding. *International Journal of Damage Mechanics*, 24:1026–1046, 2015.

W.Q. Shen, J.F. Shao, D. Kondo, and B. Gatmiri. A micro-macro model for clayey rocks with a plastic compressive porous matrix. *International Journal of Plasticity*, 36:64–85, 2012.

W.Q. Shen, D. Kondo, L. Dormieux, and J.F. Shao. A closed-form three scale model for ductile rocks with a plastically compressible porous matrix. *Mechanics of Materials*, 59:73–86, 2013.

W.Q. Shen, A. Oueslati, and G. de Saxcé. Macroscopic criterion for ductile porous materials based on a statically admissible microscopic stress field. *International Journal of Plasticity*, 70:60–76, 2015a.

© 2018 Tous droits réservés.

lilliad.univ-lille.fr

W.Q. Shen, J. Zhang, J.F. Shao, and D. Kondo. Approximate macroscopic yield criteria for Drucker-Prager type solids with shperoidal voids . *International Journal of Plasticity*, 99:221–247, 2017.

J.C. Simo and T.J.R Hughes. *Computational inelasticity*. Springer, New York, 1998.

M. Slim. *Creep properties of source rocks using indentation: the role of organic matter on texture and creep rates*. PhD thesis, Massachusetts Institute of Technology, Cambridge MA, 2008.

C.H. Sondergeld, R.J. Ambrose, C.S. Rai, and J. Moncrieff. Microstructural studies of gas shales. Pittsburgh, PA, 23-25 February, 2010. Unconventional Gas Conference, SPE.

H. Sone. *Mechanical properties of shale gas reservoir rocks and its relation to the in-situ stress variation observed in shale gas reservoirs*. PhD thesis, Stanford University, USA, 2012.

S. Stevens and K. Moodhe. Shale gas and shale oil resource assessment methodology. Advanced Resources International Inc., 2013.

K. Su, A. Onaisi, and S. Galeazzi. Geomechanical characterization and fracability assessmanet of the vaca muerta shale play. Mendoza City, Argentina, 3-7 November, 2014. CONEXPLO.

P. Suquet. Overall properties of non-linear composites: a modified secant moduli theory and its link with ponte castaneda's non-linear variationalprocedure. *C.R. Acad. Sci. Paris*, 320:563–571, 1995.

D. Tiab and E.C. Donaldson. *Petrophysics: Theory and Practice of Measuring Reservoir Rock and Fluid Transport Properties*. Gulf Professional Pub., 2015.

K. Tohgo and G.J. Weng. A progress damage mechanics in particle-reinforced metal-matrix composites under high triaxial tension. *Journal of Engineering Materials and Technology*, 116:414–420, 1994.

TOTAL. `http://csr-analysts.total.com`,.

TOTAL. Geomechanical characterization of Vaca Muerta gas shale formation in view of hydraulic fracturing stimulation., 2012.

F.J. Ulm and Y. Abousleiman. The nanogranular nature of shale. *Acta Geotechnica*, 1:77–88, 2006.

F.J. Ulm, A. Delafargue, and G. Constantinides. Experimental microporomechanics. In L. Dormieux and F.J. Ulm, editors, *Applied micromechanics of porous materials*. Springer, 2005.

© 2018 Tous droits réservés.

lilliad.univ-lille.fr

A. Vallade. *Modélisation multi-échelles des shales: influence de la microstructure sur les propriétés macroscopiques et le processus de fracturation.* PhD thesis, University of Lille, France, 2016.

T. Vanorio, M. Prasad, and A. Nur. Elastic properties of dry clay mineral aggregates, suspensions and sandstones. *Geophysical Journal International*, 155:319–326, 2003.

T. Vanorio, T. Mukerji, and G. Mavko. Elastic anisotropy, maturity, and maceral microstructure in organic-rich shales. pages 1635–1639. 78th Annual International Meeting, SEG, Expanded abstracts, 2008.

G.D. Veiga, L.A. Spalleti, J.A. Howell, and E. Schwarz (eds). The neuquén basin, argentina: A case study in sequence stratigraphy and basin dynamics. *Geological Society Special Publication*, 252:1–14, 2005.

G. Z. Voyiadjis, A. Shojaei, and Li G. Q. A generalized coupled viscoplastic viscodamage viscohealing theory for glassy polymers. *International Journal of Plasticity*, 28: 21–45, 2012.

F.P. Wang and R.M. Reed. Pore networks and fluid flow in gas shales. New Orleans, LA, 4-7 October, 2009. Annual Technical Conference and Exhibition, SPE.

Z. Wang, H. Wang, and M.E. Cates. Effective elastic properties of solid clays. *Geophysics*, 66:428–440, 2001.

W. Weibull. A statistical distribution function of wide applicability. *Journal of Applied Mechanics*, 18:293–297, 1951.

H.R. Wenk, I. Lonardelli, H. Franz, K. Nihei, and S. Nakagawa. Preferred orientation and elastic anisotropy of illite-rich shale. *Geophysics*, 72:E69–E75, 2007.

T.M. Wilkinson, S. Zargari, M. Prasad, and C.E. Packard. Optimizing nano-dynamic mechanical analysis for high-resolution, elastic modulus mapping in organic-rich shales. *Journal of Material Science*, 50:1041–1049, 2015.

S. Xie. *Contribution à l'étude du comportement mécanique d'une roche poreuse.* PhD thesis, University of Lille, France, 2005.

S. Y. Xie and J. F. Shao. Experimental investigation and poroplastic modeling of saturated porous geomaterials. *International Journal of Plasticity*, 39:27–45, 2012.

S. Y. Xie and J. F. Shao. An experimental study and constitutive modeling of saturated porous rocks. *Rock Mechanics and Rock Engineering*, 48:223–234, 2015.

T. Xu, G. L. Zhou, M.J. Heap, W. C. Zhu, C. F. Chen, and P. Baud. The influence of temperature on time-dependent deformation and failure in granite: a mesoscale modeling approach. *Rock Mechanics and Rock Engineering*, 50:2345–2364, 2017.

© 2018 Tous droits réservés.

lilliad.univ-lille.fr

F. Yan and D. Han. Measurement of elastic properties of kerogen. 83rd Annual International Meeting, SEG, 2013.

A. Zaoui. *Matériaux hétérogènes et composites*. cours l'École Polytechnique, 2000.

S. Zargari, M. Prasad, K.C. Mba, and E.D. Mattson. Organic maturity, elastic properties, and textural characteristics of self resourcing reservoirs. *Geophysics*, 78:223–235, 2013.

J.C. Zeszotarski, R.R. Chromik, R.P. Vinci, M.C. Messmer, R. Michels, and J.W. Larsen. Imaging and mechanical property measurements of kerogen via nanoindentation. *Geochimica et Cosmochimica Acta*, 68:4113–4119, 2004.

J. Zhang, L. Ouyang, D. Zhu, and A.D. Hill. Experimental and numerical studies of reduced fracture conductivity due to proppant embedment in the shale reservoir. *Journal of Petroleum Science and Engineering*, 130:37–45, 2015.

L.Y. Zhao, Q.Z. Zhu, W.Y. Xu, F. Dai, and J.F. Shao. A unified micromechanics-based damage model for instantaneous and time-dependent behaviors of brittle rocks. *International Journal of Rock Mechanics and Mining Sciences*, 84:187–196, 2016.

Y.H. Zhao and G.J. Weng. A theory of inclusion debonding and its influence on the stressstrain relations of a ductile matrix. *International Journal of Damage Mechanics*, 4:196–211, 1995.

H. Zhou, Y. Jia, and J. F. Shao. A unified elastic-plastic and viscoplastic damage model for quasi-brittle rocks. *International Journal of Rock Mechanics and Mining Sciences*, 45:1237–1251, 2008.

H. R. Zhu and L. Sun. A viscoelastic-viscoplastic damage constitutive model for asphalt mixtures based on thermodynamics. *International Journal of Plasticity*, 40:81–100, 2013.

© 2018 Tous droits réservés.

lilliad.univ-lille.fr